論文 / 著書情報
Article / Book Information

題目(和文)	
Title(English)	Cyclic behaviors of square hollow section columns under small inelastic cycles
著者(和文)	DONG Yang
Author(English)	Yang Dong
出典(和文)	学位:博士（工学）, 学位授与機関:東京工業大学, 報告番号:甲第12236号, 授与年月日:2022年9月22日, 学位の種別:課程博士, 審査員:吉敷 祥一,元結 正次郎,石原 直,西村 康志郎,佐藤 大樹,山田 哲
Citation(English)	Degree:Doctor (Engineering), Conferring organization: Tokyo Institute of Technology, Report number:甲第12236号, Conferred date:2022/9/22, Degree Type:Course doctor, Examiner:,,,,,
学位種別(和文)	博士論文
Type(English)	Doctoral Thesis

A thesis submitted for the degree of

Doctor of Engineering

Cyclic behaviors of square hollow section columns under small inelastic cycles

Yang DONG

Supervisor: Prof. Kishiki Shoichi

Department of Architecture and Building Engineering

Tokyo Institute of Technology

Sep. 2022

CONTENTS

Appendices

Publications

ABSTRACT

Structural components can be subjected to a limited number of cyclic large drifts during strong earthquakes (e.g., Northridge earthquake, 1994; Kobe earthquake, 1995), as well as many cyclic small amplitude loading during long-duration earthquake excitations (e.g., Tohoku earthquake, 2011). Traditional studies on cyclic behaviors of structural components mainly focused on large drifts and neglected small amplitude loading, rendering them inadequate to represent different seismic loading cases. Square hollow section (SHS) columns are widely used in low- and middle-rise steel building structures in Japan. The bottoms of the first story columns yield under severe earthquakes, even though the strong-column-weak-beam concept is adopted during building design. To better understand the deformation capacities and hysteretic behaviors of steel columns under cyclic small amplitude loading and fill in this knowledge gap, tests on 26 SHS columns were first carried out in this study. The width-to-thickness, axial force, shear span ratios, and loading history of the columns were the main test parameters. The loading histories consisted of monotonic loading, variable amplitude loading, and several constant small amplitude loadings. All specimens exhibited local buckling at the bottom of the columns. Under small amplitude loading, it was observed that the strength of the specimens deteriorated slightly within a certain number of cycles, while the restoring force decreased rapidly afterwards. The stability limit concept was proposed to represent the point when the column’s strength starts to deteriorate rapidly; it is based on the axial deformation in the flange in the local buckling region. The concept combines the monotonic and cyclic behaviors together. Accurate prediction methods for the stability limit values and the numbers of cycles until the stability limits were reached were also proposed, which can be applied to SHS columns under random amplitude loading. The concept of the stability limit was also applied to the inelastic time history response analyses to check the damage progress in the steel columns in the structural system level. The concept of stability limit was proved to be a conservative and better damage evaluation index. Based on the relationship of lateral residual strength and deformation in the flange of local buckling zone, a method to determine the residual strength with local buckling deformation was developed for approximate strength deterioration prediction.

In practical engineering, the probability for occurrence of major earthquake (can cause severe damage to structures) is much lower than that of earthquakes with relatively small intensity (may cause minor damage to structures). The accumulated damage caused by earthquakes with small intensity is unignorable when the cumulative cycles reach a large number, which can cause both structural and functionality problems. These have arisen the research interest in the low cycle fatigue behaviors of the steel structures under this condition. Previous research mainly focused on the low cycle fatigue (LCF) behaviors of beam-to-column connections while usually ignored column components. To investigate this scenario, loading tests were further carried on 22 cold-roll-formed SHS columns with smaller width-to-thickness ratio, axial force ratio and loading amplitude. The axial force ratio, shear span ratio and loading amplitude were studied as the main test parameters. Both cyclic variable and constant amplitude loading (i.e., rotation angle of the column ranging from 0.54% to 2.11%) were carried out. All of the specimens failed due to flange fracture. The axial force ratio was found to have minor influence on the fatigue life of the SHS columns under one specific loading amplitude, while the shear span ratio was found to have unignorable influence. The methods to predict the fatigue life were developed based on the empirical regression functions for the specimens under constant amplitude loading. They can also be applied to evaluate the fatigue life of specimens under variable amplitude loading by combining with the rainflow method and Miner's rule. The strength deterioration behaviors were laid great emphasis in this study and two methods to predict the strength deterioration behavior for specimens failed owing to flange fracture were proposed. One was based on the empirical function of strength deterioration rates for the tested specimens and the other one was based on the crack propagation in the section of the column end. They can be further applied to hysteretic model and practical engineering, respectively. Furthermore, transformation boundaries for different failure modes (i.e., local buckling and flange fracture) were developed based on the test database of the current study.

Based on this research, local buckling and flange fracture followed by rapid strength deterioration could occur after a certain number of cycles even though the steel columns were subjected to small amplitude loadings. This stressed the necessity to consider the damage caused by the small inelastic cycles in the design of and analyses for structural components under seismic loading in the future.

Chapter 1 Introduction

1.1 Research background

Several severe earthquakes happened around the world in recent years (e.g., Wenchuan Earthquake in China (Fig. 1-1 (a)), and Tohoku Earthquake (Fig. 1-1 (b))). These earthquakes have caused considerable damage to structures, resulting in severe economic loss and casualties. These massive earthquakes subject structures to many cyclic small amplitude loadings, due to their characteristic long-duration ground motions (compared with the seismic records for Kobe Earthquake 1995, Fig. 1-1 (c)); this is not usually considered in current seismic designs. The cyclic behavior and strength deterioration performance of structural components are crucially affected by the loading protocol. Classical loading protocols (i.e., the ATC-24 [1-1], SAC [1-2], FEMA 461 protocols [1-3] and the loading protocol recommended by the Building Research Institute and the Japan Iron and Steel Federation [1-4]) are widely used in experimental studies on cyclic behaviors of steel components, as shown in Fig. 1-2. However, such protocols are incremental, with limited cycle counts and are inadequate for representing different seismic loadings (i.e., long-duration earthquakes). Powell et al. [1-5] suggested that many small inelastic excursions are probably less damaging than fewer large excursions. Krawinkler et al. [1-6] mentioned that small inelastic cycles can have unneglectable effect on damage when they occur in great numbers. Although the damage accumulation and deterioration behavior for structural components subjected to small amplitude loadings have been recognized for a long time, there is no consensus on how to deal with the damage accumulation and deterioration behavior; therefore, studies that build a consensus are needed.

Steel moment resisting frames (SMRFs) are widely used as a lateral load resisting system in the seismic regions around the world. In the SMRFs, the strong column-weak beam design concept is commonly used to achieve the stable seismic performance under earthquakes. In this concept, the plastic hinges are expected to appear in the beam ends during the sway of the structures. The input energy is expected to be dissipated by the plastic deformation in the beam components, and avoid the plastic hinge from forming in the column ends, as shown in Fig. 1-3. Therefore, many researchers have built proven methods and clarified mechanisms for the beams under a large number of cyclic loadings. However, even though the strong column-weak beam concept has been applied to the seismic design of the SMRFs, plastic hinges still form in the column ends during the severe earthquakes, as shown in Fig. 1-3. Damage is concentrated at the bottoms of the first story columns when SMRFs are under seismic loadings [1-7], which is generated by story drift. In other words, the loss of the restoring force of columns, due to local buckling, largely determines the seismic performance of these buildings. Furthermore, there is a high risk for the collapse of the structures when the cumulative damage in the columns reaches a high level. Therefore, only focus on the hysteretic behaviors of the beam components under a large number of cyclic loadings is not enough, great emphasis should be laid on the plastic hysteretic behaviors of column components as well.

Based on the concerns discussed above (i.e., loading protocols to simulate the long-duration earthquakes and the hysteretic behaviors of the steel column components under this kind of loading condition), the current study was carried out to fill in the knowledge gap.

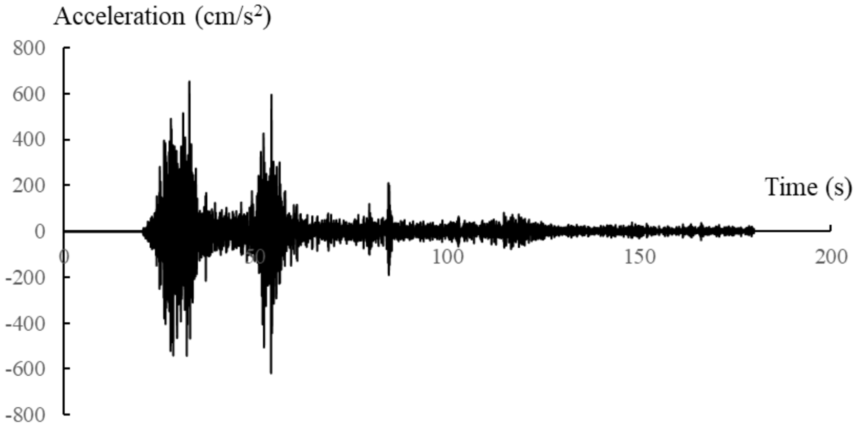

(a) Wenchuan Earthquake, ground motion records at Wolong (2008), NS component

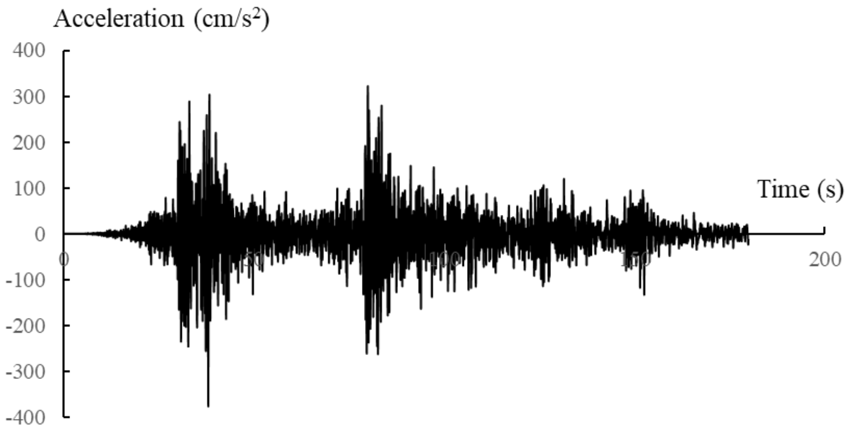

(b) Tohoku Earthquake, ground motion records at JMA Sendai (2011), NS component

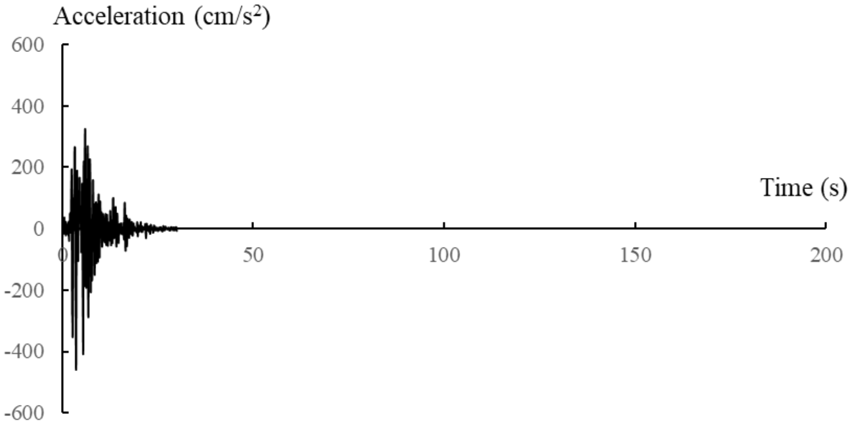

(c) Hyogoken-Nanbu Earthquake, ground motion records at Kobe (1995), NS component

Fig. 1-1 Representative earthquake acceleration time histories

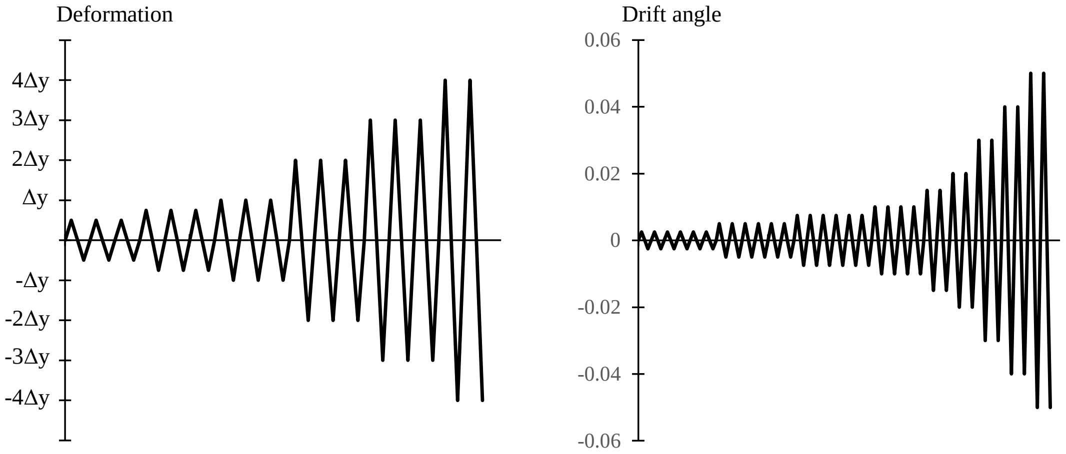

(a) ATC-24 loading protocol [1-1]

(b) SAC loading protocol [1-2]

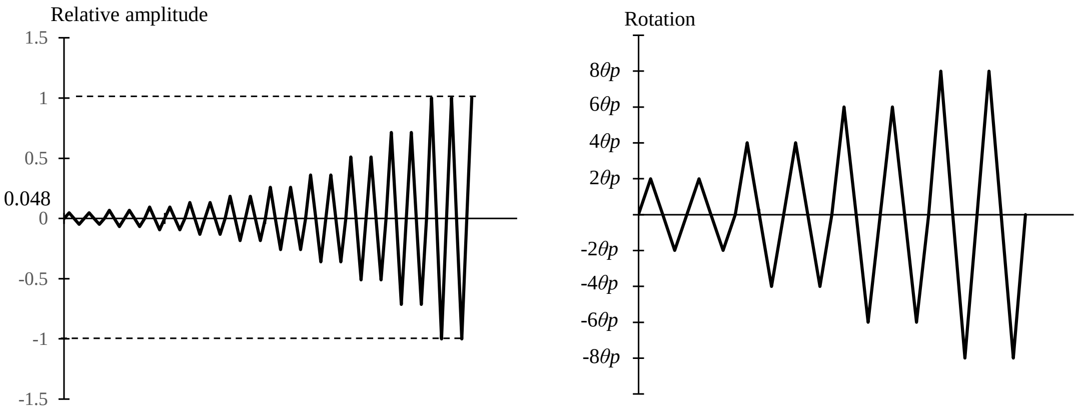

(c) FEMA 461 loading protocol[1-3]

(d) Japanese Design Recommendation loading protocol [1-4]

Fig. 1-2 Classical loading protocols

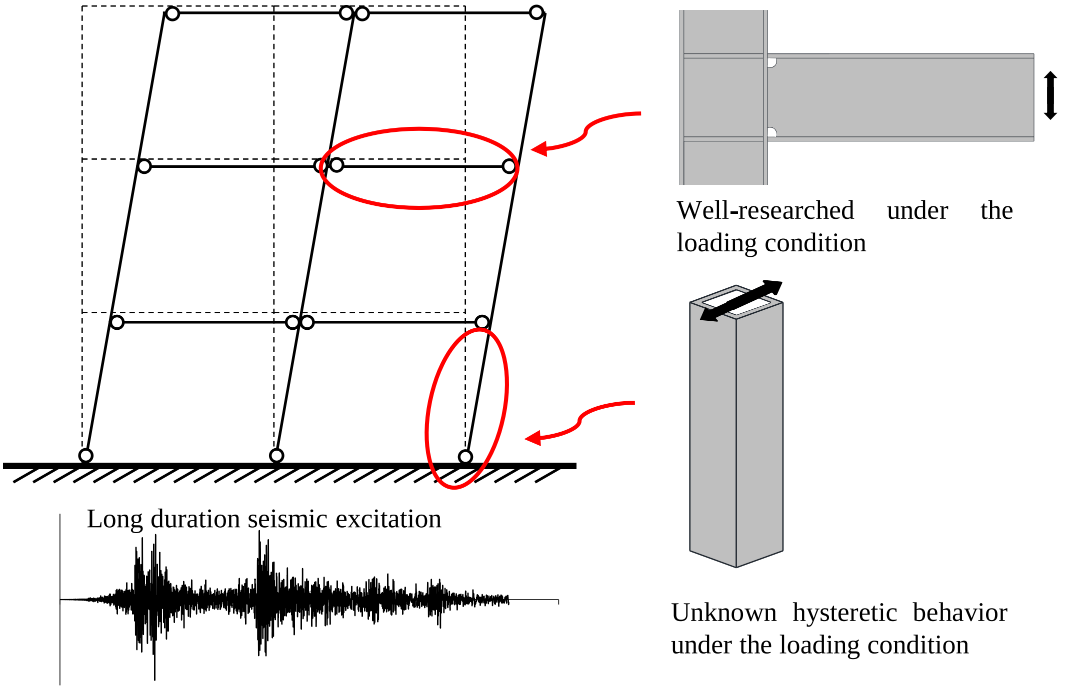

Fig. 1-3 Distribution of plastic hinges for structures under long-duration seismic excitation.

1.2 Previous research

Major earthquakes can cause great damage to structures, lead to the loss of vertical load bearing capacity or the horizontal resistance, and subsequently decrease the safety margin [1-8][1-9]. These earthquakes can cause considerable damage to structures, resulting in severe economic loss and casualties to the society. To avoid these severe problems, scholars have placed considerable emphasis on studying major earthquakes, with significant progress made in the design of current seismic codes. Due to the frequent long-term earthquakes happened in recent years and the concerns on the cumulative damage in the structural components during several minor or moderate earthquake events, the behavior of structural members subjected to cyclic loading with relatively small amplitudes has garnered substantial research interest. Researchers in Japan have investigated the cyclic behaviors of structural components in tall buildings under long-period ground motions. They noted that the buildings exhibit significant resonance under this loading condition.

The plastic deformation capacity for beam-to-column connections and column ends are critical in the seismic design of the steel moment-resisting frame (SMRF) system. In recent years, considerable studies [1-6][1-10][1-11][1-12][1-13][1-14][1-15][1-16][1-17][1-18][1-19] have been conducted on the fatigue endurance of beam-to-column connections under cyclic loadings. Proven prediction methods have been proposed both experimentally and numerically (i.e., low fatigue life prediction based on the stress range[1-15][1-16][1-19], strain range[1-14], rotation angle[1-13][1-14][1-18] and normalized rotation angle[1-11][1-12], and the crack propagation progress[1-6][1-14][1-17]). The behaviors of beam-to-column connections were mainly governed by fractures, and the potential low cycle fatigue (LCF) mechanisms for these connections have been clarified. The proposed methods by the scholars can be applied to the steel beams under random loading as well.

As the most important structural component in the SMRFs, the steel columns under compression and bending have been researched for a long time experimentally, analytically and numerically. The seismic performance of the steel columns is usually governed by the local buckling behaviors, which are focused on by most of the researchers. Experimental study on the steel columns under large constant amplitude loadings [1-20][1-21] have been carried out to investigate the strength deterioration behaviors. However, the research on the cyclic behaviors of the steel columns usually focused on the classical loading protocols with limited number of cycles (i.e., incremental loading) [1-22][1-23][1-24][1-25][1-26][1-27][1-28]. Researchers always focused on the strength deterioration behaviors of the steel columns on the basis of the hysteretic curves and proposed the damage index based on the strength deterioration, energy dissipation [1-22] and cumulative deformation [1-22][1-25]. Deformation capacity is also an important index in the practical engineering besides the strength deterioration behaviors. It also rises the research interest of the researchers, i.e., local buckling deformation [1-26][1-29] and axial shortening behaviors of the steel columns [1-27][1-28][1-30][1-31]. The nonlinear structural analyses were also carried out on structural system level considering the axial shortening in the steel columns [1-30][1-31].

Based on the experimental results, researchers started to develop hysteretic models for the steel columns to predict the strength deterioration behaviors under seismic loadings, i.e., the rotational spring model [1-32][1-33][1-34] in the macroscopic component level (moment-displacement relationship), curve approximated model built on the shape of hysteresis curves [1-35], fiber models [1-36][1-37][1-38] with the hysteretic properties occupied in the fiber elements, and model based on artificial neural network [1-39] with parameters calibration based on huge database. Numerical simulation methods were also applied widely to simulate the strength deterioration behaviors [1-40][1-41][1-42][1-43], ductility[1-44] of the columns and calibrate the important parameters in the hysteretic models [1-36][1-38][1-45].

Besides the local buckling behaviors in the steel columns, fracture was the dominant failure mode in previous studies [1-46][1-47][1-48] on the extreme LCF behavior of steel column components. Ge et al. [1-46] conducted extreme LCF tests on thick-walled steel piers with box sections. Cyclic lateral loading was applied with constant vertical compression and governed by ductile crack initiation and propagation, accompanied by local buckling. Tateishi et al. [1-47] conducted cyclic loading tests on cantilever box-section columns to develop the assessment method for extreme LCF behaviors. No axial force was applied on the specimens; they were governed by fracture without any local buckling. Myers et al. [1-48] studied the effect of weld details on the ductility of connections between steel columns and baseplates. Crack initiation and propagation were observed in the bottom of the columns; the final failure mode was a fracture in the bottom. These studies[1-46][1-47][1-48] focused on column components subjected to limited number of cycles with relatively large amplitude and illustrated the possibility of fractures being the dominant failure mode of SHS columns.

The previous research has already built a solid knowledge on the strength deterioration behaviors and deformation capacity of steel columns subjected a limited number of large amplitude loadings. Furthermore, they are predictable with the proposed models in an acceptable accuracy. However, to the best knowledge of the author, research on the behaviors of column components under long duration earthquakes (e.g., built-up box section columns and concrete-filled steel tube (CFT) columns [1-52][1-53][1-54]) are very limited.

The studies on column components subjected to a large number of small amplitude loadings are introduced as below. For the studies on built-up box section columns [1-52], the researchers focused on the strength deterioration behaviors (relationship of strength and the number of cycles), strain progress in the flange and buckling length progress in the local buckling region. For the studies on CFT columns, the researchers focused on the strength deterioration trend (relationship of strength and the number of cycles) [1-53][1-54], axial deformation progress [1-53] and damage evaluation [1-53]. Due to insufficient data and information, the deterioration behaviors of column components after peak strength (e.g., CFT and SHS columns) while subjected to many small inelastic cycles remain unknown, and there is still no determinate way to evaluate the deterioration behavior.

Square hollow section (SHS) columns are widely used in Japanese SMRFs and few studies focused on the deterioration behaviors of these columns when strained by many small inelastic cycles. The actual mechanism is not well understood. Only Kido et al. [1-54] conducted experiments to study the strength deterioration of cantilever SHS columns by applying many cyclic small amplitude loadings (rotation angle ranging from 0.75% to 1.5%) to several columns. However, they only tested a few SHS columns since the study’s focus was on CFT columns. The influence of different important parameters on deterioration behaviors of SHS columns was still unknown. They stopped stressing the columns when their bearing capacity was 80% of their maximum bearing capacity. Therefore, the final failure modes of most of the SHS columns were not observed, and the strength deterioration behaviors of the columns remains ambiguous. More investigation is needed to flesh out our knowledge of deformation capacities, the hysteretic behaviors (including the strength deterioration range), and final failure modes of SHS columns subjected to cyclic small amplitude loads.

1.3 Objectives of this study

Based on the aforementioned research background, the study on the SHS columns under a large number of small inelastic cycles was rarely carried out. With the insufficient data, the hysteretic behaviors of the SHS columns under this loading condition is still not clear. Whether the hysteretic behaviors of the columns (including strength deterioration behaviors and deformation capacities) under a large number of small amplitude loadings are the same as those under a limited number of large incremental loadings remain unknown. Whether it's a dangerous case that the researchers have ignored or a safe case for practical engineering is not clear either. Whether the different critical design parameters can have an influence on the hysteretic behaviors and what are they remain unclear. How should researchers or engineers evaluate the seismic performance of the steel columns under this loading condition also cause confusion (i.e., using the previous methods for steel columns under large amplitude loading or some new indices). These may bring a lot of uncertainties to the designers considering the structures under long-duration earthquakes, which happened frequently during the recent years. Furthermore, the safety of the structures and human lives can be challenged.

Therefore, to solve these problems, this study was carried out to fill in the knowledge gap in this research field based on the experimental study of SHS columns under many small inelastic cycles. The potential differences between the hysteretic behaviors of the SHS columns under small and large amplitude loadings are investigated. The failure mode of the SHS columns under this loading condition is aimed to figure out. The influences of the important design parameters (i.e., width-to-thickness ratio, shear span ratio and axial force ratio) on the hysteretic behaviors are aimed to clarify. The regular patterns for the strength deterioration and deformation capacity are investigated. The limit status for SHS columns is aimed to be proposed based on the test database, and can be further applied to the design in practice. Inelastic response analyses are also carried out with these proposed indices to find out the potential limitations in structural analysis that are based on the hysteretic models from large amplitude loading. Furthermore, the residual strength evaluation methods were investigated for the structural retrofitting works post the earthquakes.

A database has been built based on previous research [1-20][1-23][1-25][1-28][1-33][1-47][1-49][1-50][1-51][1-54], as Fig. 1-4. The circles represent the specimens under cyclic constant amplitude loading; while the triangles stand for the specimens under incremental or decremental loading, and the maximum loading amplitudes in the loading histories are marked. The current study mainly focused on the red region marked in the figure, termed as "small inelastic cycles". The rotation range is rare researched, thus it's meaningful to clarify the hysteretic behaviors of the SHS columns in this range.

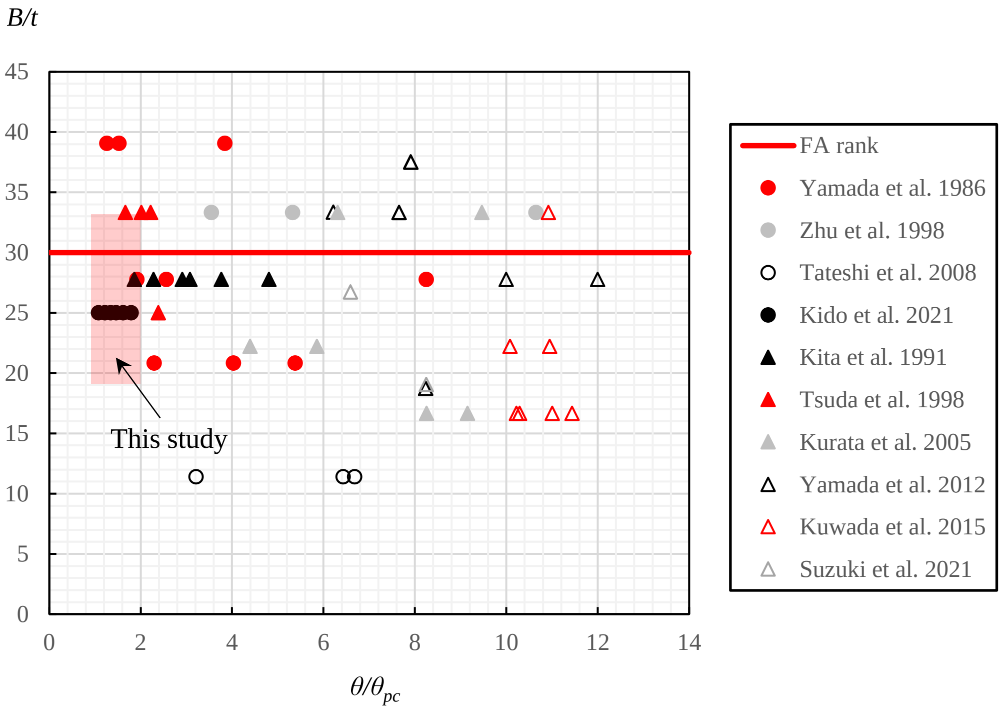

Fig. 1-5 Database for the SHS columns under cyclic lateral loads.

1.4 Structure of dissertation

The dissertation consists of 4 chapters, and describes an experimental and analytical investigation on the hysteretic behaviours of SHS columns under a large number of small inelastic cycles. The knowledge gap of seismic performance for SHS columns under long-duration earthquake was filled in.

Chapter 2 discussed an experimental study on the hysteretic behaviours of SHS columns under a large number of small inelastic cycles. The failure mode was clarified as local buckling. The influences of the width-to-thickness ratio, axial force ratio, shear span ratio and loading amplitude were investigated. The strength deterioration behaviour and deformation capacity of SHS columns were mainly focused on. A concept of the stability limit was proposed based on the pushover test, and the corresponding prediction methods for it have been developed as well. It was further applied to the structural analyses to identify the damage accumulative in the column components. A method to predict the residual lateral resistance was proposed based on the deformation in the local buckling zone for practical use.

Chapter 3 discussed an experimental study on the hysteretic behaviours of SHS columns under a large number of small amplitude loadings (smaller loading amplitude and lower axial force ratio compared to the test results in **Chapter 2**). The failure mode was clarified as flange fracture. The influences of the axial force ratio, shear span ratio and loading amplitude were investigated. The fatigue life and strength deterioration behaviours were mainly focused on. A series of methods to predict the fatigue life of SHS columns were proposed. A method to predict the residual lateral resistance was proposed based on the crack length. The failure modes transformation boundaries for local buckling and flange fracture were summarized based on the test results.

Chapter 4 summarized the research work reported in this dissertation. Main conclusions were summarized, and directions for future research were also suggested. Furthermore, some recommendations based on the current research findings were offered.

References

[1-1] Krawinkler H. Guidelines for cyclic seismic testing of components of steel structures. Report No. ATC-24, Applied Technology Council, Redwood City, CA, 1992.

[1-2] Clark P, Frank K, Krawinkler H, Shaw R. Protocol for fabrication, inspection, testing, and documentation of beam-column connection tests and other experimental specimens. SAC Steel Project Background Document, Report No. SAC/BD-97/02, 1997.

[1-3] Federal Emergency Management Agency. Interim testing protocols for determining seismic performance characteristics of structural and nonstructural components. FEMA 461 Draft Document, Applied Technology Council, Redwood City, CA, 2007.

[1-4] Building Research Institute and the Japan Iron and Steel Federation. Study on Testing method for Structural Performance Evaluation of Steel Structures. 2002. Tokyo.

[1-5] Powell GH, Allahabadi R. Seismic damage prediction by deterministic methods: Concepts and procedures. *Earthquake Engineering and Structural Dynamics*. 1988, 16(5):719-734.

[1-6] Krawinkler H. Performance Assessment of Steel Components. *Earthquake Spectra*. 1987, 3(1):27-41.

[1-7] Tenderan R, Ishida T, Jiao Y, Yamada S. Seismic Performance of ductile steel moment-resisting frames subjected to multiple strong ground motions. *Earthquake Spectra*. 2018, 35: 289-310.

[1-8] Nakashima M, Inoue K, Tada M. Classification of damage to steel buildings observed in the 1995 Hyogoken-Nanbu earthquake. *Engineering Structures*. 1998, 20(s 4-6): 271-281.

[1-9] Mahin SA. Lessons from damage to steel buildings during the Northridge earthquake. *Engineering Structures*. 1998, 20(4-6): 261-270.

[1-10] Jiao Y, Yamada S, Kishiki S, Shimada Y. Evaluation of plastic energy dissipation capacity of steel beams suffering ductile fracture under various loading histories. *Earthquake Engineering and Structural Dynamics*. 2011, 40(14): 1553-1570.

[1-11] Suita K, Manabe Y, Takatsuka K, Tanaka T, Tsukada T. Prediction of fracture of steel moment connection by cyclic loading with various deformation amplitude. In: 15th World Conference on Earthquake Engineering, Lisbon, Portugal; 2012.

[1-12] Takatsuka K, Suita K, Umeda T. Deformation capacity of flange-welded web-bolted moment connection under cyclic loading. In: 16th World Conference on Earthquake Engineering, Santiago, Chile; 2017.

[1-13] Kishiki S, Lee D S, Yamada S, Ishida T, Jiao Y. Low-cycle fatigue performance assessment of current Japanese steel beam-to-column connections determined by ductile fracture. *Engineering Structures*. 2019, 182: 241-250.

[1-14] Krawinkler H, Zohrei M. Cumulative damage in steel structures subjected to earthquake ground motions. *Computers & Structures.* 1983, 16: 531–41.

[1-15] Ballio G, Castglioni CA. A unified approach for the design of steel structures under low and/or cycle fatigue. *Journal of Constructional Steel Research.* 1995, 34: 75-101.

[1-16] Ballio G, Calado L, Castglioni CA. Low cycle fatigue behaviour of structural steel members and connections. *Fatigue & Fracture of Engineering Materials & Structures.* 1997, 20(8): 1129-1146.

[1-17] Iyama J, Ricles JM. Prediction of fatigue life of welded beam-to-column connections under earthquake loading. *Journal of Structural Engineering*. 2009, 135(12): 1472-1480.

[1-18] Zhou H, Wang Y, Yang L, Shi Y. Seismic low-cycle fatigue evaluation of welded beam-to-column connections in steel moment frames through global-local analysis. *International Journal of Fatigue.* 2014, 64: 97-113.

[1-19] Castiglioni CA, Mouzakis HP, Carydis PG. Constant and variable amplitude cyclic behavior of welded steel beam-to-column connections. *Journal of Earthquake Engineering*. 2007, 11(6): 876-902.

[1-20] Yamada M, Kawamura H, Tani A, Yamanaka K. Elasto-plastic deformation and fracture behavior of steel box columns subjected to double curvature cyclic bending under constant axial load (V). 1986, Summaries of Technical Paper of Kinki Branch, Architectural Institute of Japan, 409-412.

(in Japanese)

[1-21] Kuwamura H, Iyama J, Zhu D. Collapse and residual drift during post-local-buckling behaviors under earthquake. *Journal of Structural and Construction Engineering*, AIJ, 1999, 64 (526): 169-176. (in Japanese)

[1-22] Kumar S, Usami T. Damage evaluation in steel box columns by cyclic loading tests. *Journal of Structural Engineering*. 1996, 122(6): 626-634.

[1-23] Ishida T, Jiao Y, Shimada Y, Yamada S. Deterioration behavior of the square hollow section columns under cyclic loading: Part 1 Basic study on three-point bending experiment. Summaries of Technical Paper of Kanto Branch, Architectural Institute of Japan, 457-460. (in Japanese)

[1-24] Kurata M, Nakashima M, Suita K. Test on large cyclic deformation of steel tube columns having fixed column bases. *Journal of Structural and Construction Engineering,* AIJ, 2005, 598: 149-154. (in Japanese)

[1-25] Kuwada R, Koetaka Y, Suita K. Plastic deformation capacity of cold press-formed SHS columns determined by local buckling and fracture. *Journal of Structural and Construction Engineering*, AIJ, 2015, 80 (718): 1961-1970. (in Japanese)

[1-26] Kishiki S, Iwasaki Y. Evaluation of residual strength based on local buckling deformation of steel column——Quick inspection method for steel structures based on the visible damage Part 3, *Journal of Structural and Construction Engineering*, AIJ, 2017, 82 (735):735-743. (in Japanese)

[1-27] Cravero J, Elkady A, Lignos DG. Experimental evaluation and numerical modeling of wide-flange steel columns subjected to constant and variable axial load coupled with lateral drift demands. *Journal of Structural Engineering*. 2020, 146(3): 04019222.

[1-28] Suzuki Y, Lignos DG. Experimental evaluation of steel columns under seismic hazard-consistent collapse loading protocols. *Journal of Structural Engineering*. 2021, 147(4): 04021020.

[1-29] Zhu Y, Kanvinde A. Estimating the evolution of strain induced by inelastic cyclic local buckling in steel beam-columns. *Engineering Structures*. 2020, 215: 110708.

[1-30] MacRae GA, Urmson CR, Walpole WR, Moss P, Hyde K, Clifton C. Axial shortening of steel columns in building subjected to earthquakes. *Bulletin of the New Zealand Society for Earthquake Engineering*. 2009, 42(4): 275-287.

[1-31] Elkady A, Güell G, Lignos DG. Proposed methodology for building-specific earthquake loss assessment including column residual axial shortening. *Earthquake Engineering and Structural Dynamics*. 2020, 49: 339-355.

[1-32] Ibarra LF, Medina RA, Krawinkler H. Hysteretic models that incorporate strength and stiffness deterioration. *Earthquake Engineering and Structural Dynamics*. 2005, 34: 1489-1511.

[1-33] Yamada S, Ishida T, Jiao Y. Hysteretic behavior of RHS columns under random cyclic loading considering local buckling. *International Journal of Steel Structures*. 2018, 18(5):1761-1771.

[1-34] Lignos DG, Hartloper AR, Elkady A, Deierlein GG, Hamburger R. Proposed updates to the ASCE 41 nonlinear modeling parameters for wide-flange steel columns in support of performance-based seismic engineering. *Journal of Structural Engineering*. 2019, 145(9): 04019083.

[1-35] Dang J, Yuan H, Igarashi A, Aoki T. Curve-approximated hysteresis model for steel bridge columns. *Journal of Structural Engineering*. 2014, 140: 04014058.

[1-36] Taniguchi K, Koetaka Y, Chan I, Tanaka K. Mechanical model for deterioration behaviors caused by local buckling of cold press-formed square hollow section columns. *Journal of Structural and Construction Engineering*, AIJ, 2019, 84 (766): 1577-1587. (in Japanese)

[1-37] Kolwankar S, Kanvinde A, Kenawy M, Lignos DG, Kunnath S. Simulating local buckling-induced softening in steel members using an equivalent nonlocal material model in displacement-based fiber elements. *Journal of Structural Engineering*. 2018, 144(10): 04018192.

[1-38] Suzuki Y, Lignos DG. Fiber-based hysteretic model for simulating strength and stiffness deterioration of steel hollow structural section columns under cyclic loading. *Earthquake Engineering and Structural Dynamics*. 2020, 49: 1702-1720.

[1-39] Yang C, Fan J. Artificial neural network-based hysteresis model for circular steel tubes. *Structures.* 2021, 30: 418-439.

[1-40] Goto Y, Wang Q, Obata M. FEM analysis for hysteretic behavior of thin-walled columns. *Journal of Structural Engineering*. 1998, 124(11): 1290-1301.

[1-41] Usami T, Ge H. Cyclic behavior of thin-walled steel structures—numerical analysis. *Thin Walled Structures*. 1998, 32: 41-80.

[1-42] Cao T, Shan L, Xiao Y. Numerical studies on full-scale steel columns under complex seismic loading. *Journal of Constructional Steel Research*. 2020, 172: 106227.

[1-43] Fogarty J, El-Tawil S. Collapse resistance of steel columns under combined axial and lateral loading. *Journal of Structural Engineering*. 2016, 142(1): 04015091.

[1-44] Gao S, Usami T, Ge H. Ductility of steel short cylinders in compression and bending. *Journal of Engineering Mechanics*. 1998, 124(2): 176-183.

[1-45] Chen S, Xie X, Zhuge H. Hysteretic model for steel piers considering the local buckling of steel

plates. *Engineering Structures.* 2019, 183: 303-318.

[1-46] Ge H, Kang L, Tsumura Y. Extremely low-cycle fatigue tests of thick-walled steel bridge piers. *Journal of Bridge Engineering.* 2013, 18(9): 858-870.

[1-47] Tateishi K, Chen T, Hanji T. Extremely low cycle fatigue assessment method for un-stiffened cantilever steel columns. *Journal of Structural and Construction Engineering*, AIJ, 2008, 64 (2): 288-296.

[1-48] Myers AT, Kanvinde AM, Deierlein GG, Fell BV. Effect of weld details on the ductility of steel column baseplate connections. *Journal of Constructional Steel Research*, 2009, 65: 1366-1373.

[1-49] Zhu D, Iyama J, Takada K, Kuwamura H. Relationship between hysteresis loop and monotonic loading curve of steel member: Part 2 In case of local buckling. Summaries of Technical Paper of Kanto Branch, Architectural Institute of Japan, 1998, 89-92. (in Japanese)

[1-50] Tsuda K, Matsui C. Strength of square steel tubular beam-columns under constant vertical and horizontal loads. *Journal of Structural and Construction Engineering*, AIJ, 1998, 63(512): 149-156. (in Japanese)

[1-51] Kita Y, Tsuji B. Elastic plastic behavior of beam-columns with square hollow section. Summaries of Technical Paper of AIJ annual meeting, Architectural Institute of Japan, 1991, 1305-1306. (in Japanese)

[1-52] Kiyokawa T. et al. (2011) (2012): Study on safety assessment methods for super-high-rise steel buildings against long-period earthquake ground motions Part 6 – 7, Part 13 – 14. Summaries of Technical Paper of Annual Meeting, Architectural Institute of Japan, 1023-1026, 1057-1060. (in Japanese)

[1-53] Narihara H. et al. (2014): Study on safety assessment methods for super-high-rise steel buildings against long-period earthquake ground motions Part 27 – 31. Summaries of Technical Paper of Annual Meeting, Architectural Institute of Japan, 1251 – 1260. (in Japanese)

[1-54] Kido M, Tsuda K, Fukumoto T, Ichinohe Y, Morita K. Behavior of square concreate filled steel tubular beam-columns subjected to lateral load with constant cyclic displacement, *Japan Architecture Review.* 2020, 4: 41-55.

Chapter 2 Local buckling behaviors of SHS columns subjected to small inelastic cycles

2.1 Introduction

As introduced in Chapter 1, the steel columns can be subjected to a large number of small amplitude loadings due to the long-duration earthquakes that happened frequently in recent years. Furthermore, the damage concentration in the column end [2-1][2-2] was still found even though the strong column-weak beam design concept was used. Under the specific loading condition (a large number of small inelastic cycles), the following questions remained uncertain and needed to be clarified. Whether the hysteretic behaviors of the columns (including failure mode, strength deterioration and deformation capacities) are the same as those under a limited number of large incremental loadings; Whether it’s a dangerous case that have not been paid enough attention or it can be generally ignored for practical engineering; Whether the different critical design parameters (e.g., axial force ratio, width-to-thickness ratio, and shear span ratio) can have an influence on the hysteretic behaviors and what are the influences; How should researchers or engineers evaluate the seismic performance of the steel columns under this loading condition and what indices they should focus on.

In this Chapter, cyclic tests of 26 SHS columns under small amplitude loadings were conducted to investigate the effects of loading amplitude, width-to-thickness ratio, axial force ratio, and shear span ratio on the deterioration behavior. Failure mode for the columns in the experiment was also verified (i.e., local buckling). The concept of stability limit was proposed to represent the beginning of the rapid deterioration. The prediction method was also proposed for the number of cycles until the stability limit was reached. Additionally, this Chapter verified that the deterioration behavior due to local buckling under small amplitude loadings were different from that under large amplitude loadings because of the different deformation progress mechanisms in the local buckling region prior to the stability limit. The proposed concept of the stability limit was also applied in the inelastic earthquake response analysis to judge the critical status of the cumulative damage. The stability limit can be a conservative and better damage evaluation index for steel columns and SMRFs. A simple method to determine the residual lateral resistance was also proposed based on the deformation in the local buckling zone. The details of the specimens, testing method, and primary findings are summarized in the following subchapters.

2.2 Test program

2.2.1 Material test

In this study, cold-roll-formed SHS columns were loaded cyclically. These columns were made of BCR295 steel (nominal yield strength: 295 N/mm^2; nominal tensile strength: 400 N/mm^2) and they are widely used in SMRFs in Japan. The outer radius of the corner was made 2.5 times the plate thickness, and the nitrogen content was limited in chemical composition to restrict the influence of cold forming, as shown in Table 2-1 [2-3]. The test coupons designed based on the tensile test pieces specified by JIS Z 2241[2-4] are shown in Fig. 2-1. The test coupons were manufactured from the three surfaces without weld, as Fig. 2-1. During the coupon test, both the strain and the displacement in the middle section were measured. The material test results are summarized in Table 2-2, and the stress-strain relationships from tensile coupon test for each series of specimens are plotted in Fig. 2-2. Since the steel was cold-formed and the yielding was gradual, 0.2% proof stress was employed as the yield stress. Due to the cold-forming process, the yield strength of the steel was increased, and subsequently led to the high yield ratio for the cold-formed steel. The yield strength, tensile strength and yield ratio in Table 2-2 satisfy the regulated values in the specification [2-5]. This can show the BCR 295 steel columns used in current study are qualified.

The material test results are used in the analytical work in Chapters 2 and 3, as well as in the numerical simulation.

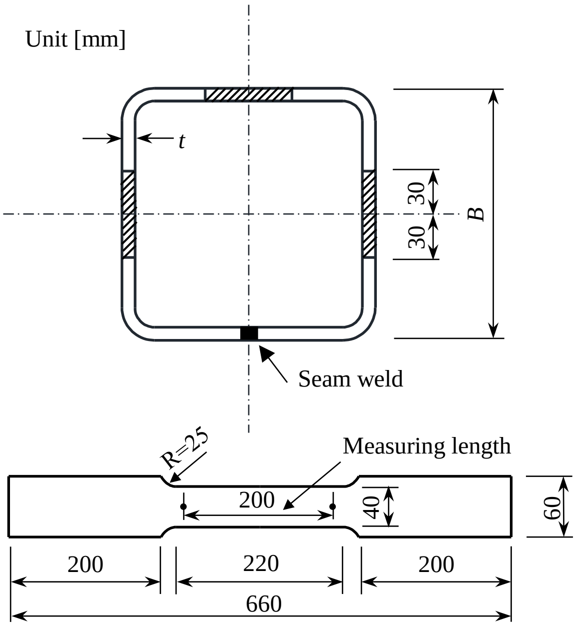

Fig. 2-1 Sampling position and configuration of the coupons for the material tests.

Table 2-1 Chemical composition of BCR295 steel.

Chemical composition (%)						Carbon equivalent (%)	Weld crack susceptibility composition (%)
C	Mn	Si	P	S	N		
<0.20	<1.40	<0.35	<0.030	<0.015	<0.006	<0.36	<0.26

Table 2-2 Tensile coupon test results

Lot	Dimension	Yield stress [N/mm^2]	Tensile strength [N/mm^2]	Yield ratio
A	□-175×175×9	371	418	0.89
B	□-175×175×9	383	425	0.90
C	□-175×175×9	382	440	0.87
D	□-175×175×6	391	454	0.86
E	□-200×200×9	392	430	0.91
F	□-200×200×9	380	446	0.85
G	□-200×200×6	345	403	0.86

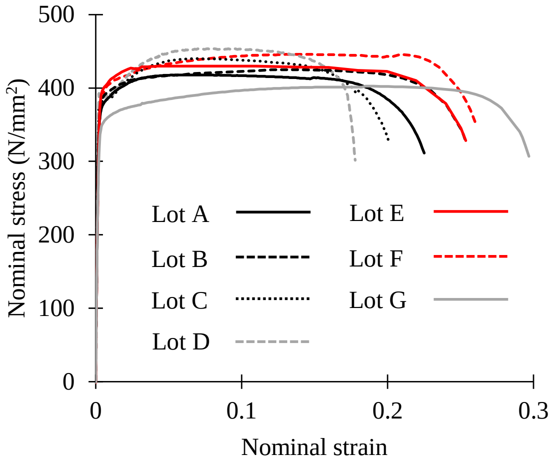

Fig. 2-2 Stress-strain relationships for test coupons.

2.2.2 Measuring plan

The SHS columns in this study were loaded as a cantilever system as shown in Fig. 2-3. Constant axial force and cyclic lateral load were applied to the top of the columns. End plates are connected to each end of the columns via full-penetration welds that confirm to JASS 6 [2-6]. The upper end plate of the SHS column is connected to a pin jig via bolts. The jig can rotate around the center of the circle freely as a pin. The upper end is free, while the lower end is fixed for this cantilever system. There were three different lengths for all the column specimens in this study, i.e., L=525mm, 860mm, and 1225mm. Plastic strain gauges were glued 20 mm above the bottom base plate of the column. The configuration of the gauges is shown in Fig. 2-4. The plastic strain gauges were used for obtaining the strain data of the column end, judging the horizontal of the loading head, and monitoring crack initiation and propagation. The measuring plan for obtaining each deformation is introduced in detail as follows.

The loading direction is the east-west direction, as shown in Fig. 2-5. Fig. 2-5 also illustrated, in detail, how the rotation angle of the column end was measured. Two potentiometers on either side of the frame measured the changes in the horizontal and vertical positions of the center of the pin, as shown in Fig. 2-5(a). Six displacement transducers on the baseplate of the specimen measured the horizontal and vertical displacements (i.e., 4 of them measured the axial deformation, and two of them measured the horizontal deformation), as shown in Fig. 2-5(b). The naming scheme for these displacement transducers was “measuring target, deformation direction, position”. For example, “${}_{bp}\delta_{v\_en}$” stands for the displacement transducer measuring vertical displacement on the northeast side of the base plate; “${}_{pin}\delta_h$” stands for the horizontal displacement of the center of the pin. Fig. 2-6 provides the schematic illustration for the deformation of the specimens. The positive deformation directions were also marked in a coordinate in Fig. 2-6. The rotation angle of the column end is represented below. Each quantity was defined in detail previously (i.e., Eqs. (2-1)–(2-5)).

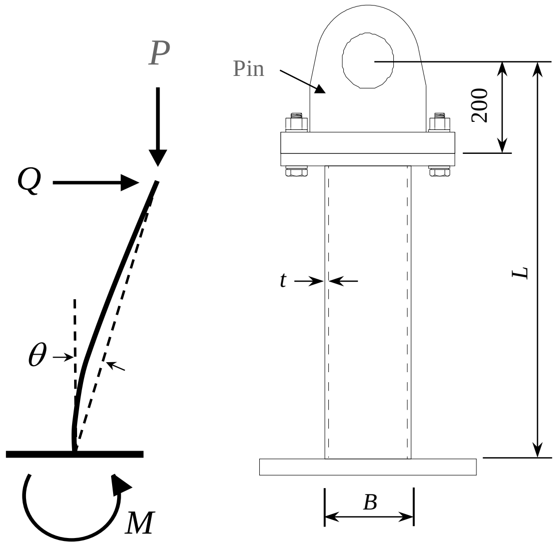

Fig. 2-3 Configuration and boundary condition of test pieces.

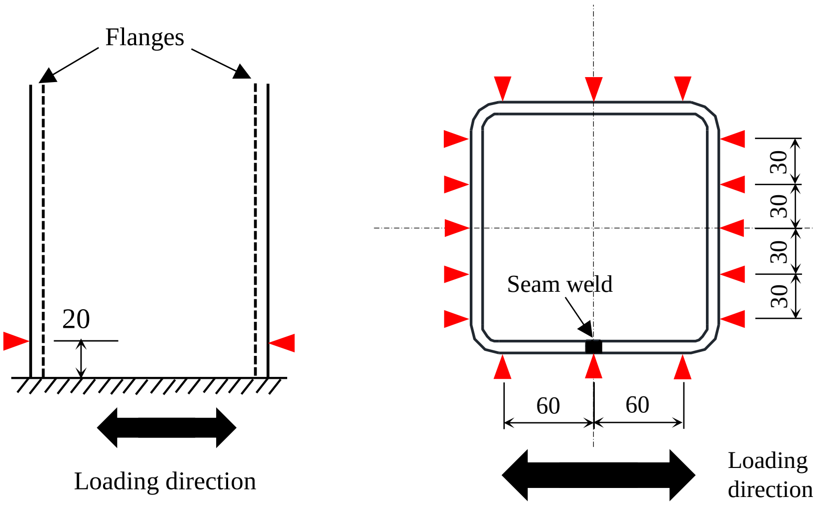

(a) Gauge position. (b) Gauge configuration in column ends.

Fig. 2-4 Configuration of the strain gauges in column end.

$$\theta = \arctan\left(\frac{{}_{pin}\delta_h - {}_{bp}\delta_h}{L - \delta_v}\right) - {}_{bp}\theta \tag{2-1}$$

$$ {}_{bp}\delta_h = \frac{1}{2}({}_{bp}\delta_{h\_es} + {}_{bp}\delta_{h\_en}) \tag{2-2} $$

$$ \delta_v = {}_{pin}\delta_v - {}_{bp}\delta_v \tag{2-3} $$

$$ {}_{bp}\delta_v = \frac{1}{4}({}_{bp}\delta_{v\_es} + {}_{bp}\delta_{v\_en} + {}_{bp}\delta_{v\_ws} + {}_{bp}\delta_{v\_wn}) \tag{2-4} $$

$$ {}_{bp}\theta = \arctan\left[\frac{\left({}_{bp}\delta_{v\_ws} + {}_{bp}\delta_{v\_wn}\right) - \left({}_{bp}\delta_{v\_es} + {}_{bp}\delta_{v\_en}\right)}{2L_{bp}}\right] \tag{2-5} $$

where ${}_{bp}\theta$ is the rotation angle of the baseplate, δ_v is the axial deformation of the column, and L_{bp} is the distance between the two transducers on the east-west side, as shown in Fig. 2-5(b).

The deformation of the local buckling region was measured to ascertain the deterioration behavior of the columns under cyclic loading, as shown in Fig. 2-7. Displacement transducers were set 1.25*B* from the upper surface of the baseplate, in accordance with findings from a previous study [2-11] that determined that the length of local buckling region for SHS columns ranged from 0.4*B* to 0.8*B*. *B* is the width of the column. The rotation angle, θ_b, and the axial deformation of the flange plate, δ_b, of the local buckling zone can be subsequently calculated using Eqs. (2-6) and (2-7), respectively. In Eq. (2-7), the former part is the axial deformation part and the latter part is the rotational deformation part in the local buckling zone.

$$ \theta_b = \frac{d_2 - d_1}{L_b} \tag{2-6} $$

$$ \delta_b = \frac{d_2 + d_1}{2} + \frac{B}{2}\theta_b \tag{2-7} $$

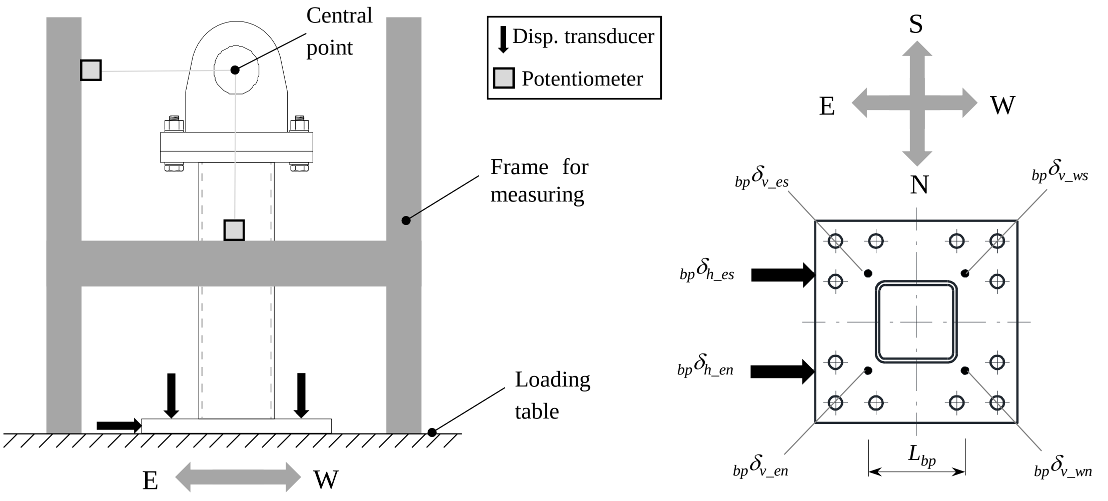

(a) Positions of the transducers. (b) Configuration of the transducers on baseplate.

Fig. 2-5 Measuring method for the rotation angle of the column end.

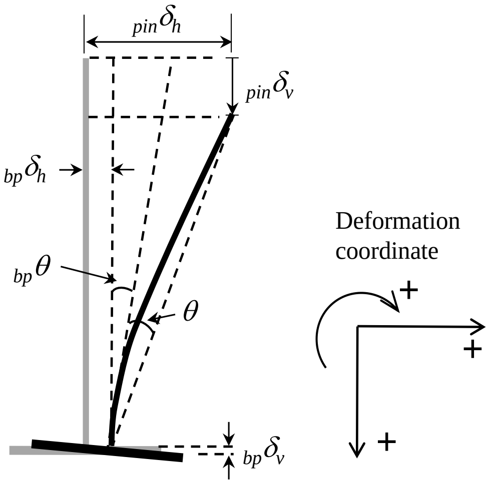

Fig. 2-6 Deformation mechanism for the specimens.

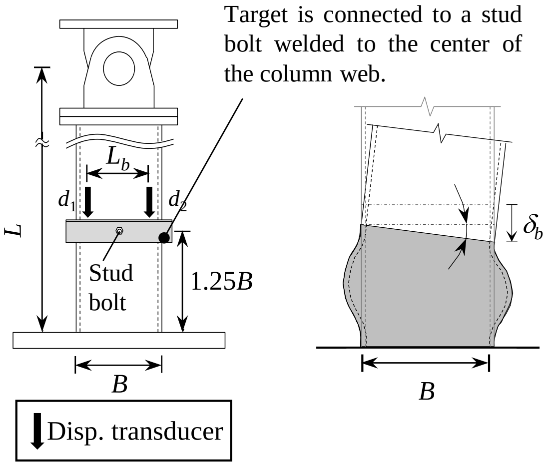

Fig. 2-7 Measuring deformation in the local buckling zone.

2.2.3 Test setup

The test setup is illustrated in Fig. 2-8. The specimens were connected to the pin at the top and fixed to the loading table, via bolts, at the bottom. The plate with the seam weld was used as the web plate to eliminate its influence on the cyclic behavior of the specimens. The specimens were loaded as a cantilever loading system. Constant compressive axial force (P) was applied to the specimens through the three vertical jacks (P_1, P_2 and P_3) and the vertical jacks were controlled to keep the reaction frame horizontal. The axial force (P) can be calculated as below. Lateral load was applied to the specimens via the horizontal jack. The horizontal jack can both contract and extend, and control the movement of the loading table. The displacement of the horizontal jack was controlled manually referring to the calculated rotation angle of the column end, θ, as introduced above. Q is the shear force in the horizontal support; F is the friction under loading table. The horizontal support is non deformable, and its length is a fixed value. It acts as a support to transfer the horizontal force from the reaction block to the loading frame. The moment for each specimen, M, was calculated based on the quantities obtained from the measuring system as follows:

$$P = P_1 + P_2 + P_3 \tag{2-8}$$

$$M = Q \cdot (L - \delta_v) + P \cdot ({}_{pin}\delta_h - {}_{bp}\delta_h) \tag{2-9}$$

2.2.4 Test parameters

The study's test parameters were the width-to-thickness ratio, shear span ratio, axial force ratio and loading protocol. Four different section sizes were employed (i.e., □–175×175×9, □–175×175×6, □–200×200×9, and □–200×200×6). The width-to-thickness ratio is defined as the quotient of the width divided by the thickness of the section. In other words, four width-to-thickness ratios were investigated (i.e., B/t=19.4, 22.2, 29.2, and 33.3). The shear span ratio is defined as the quotient of the column length divided by the width of the section. Four shear span ratios were employed (i.e., L/B=3.0, 4.3, 4.9, and 7.0), which covered the general shear span ratios of columns used in low and middle-rise SMRFs in Japan. The length of the columns (L) is the distance from the rotation center of the pin connection to the upper surface of the bottom base plate, as shown in Fig. 2-3. The axial force ratios (i.e., the applied axial force divided by axial yield strength of the section) ranged from 0.15 to 0.35. The axial yield strength of the section was calculated with the measured material properties in Table 2-2. The designed axial force ratios can be assumed to correspond to the dead load of the first-floor columns of low- and middle-rise buildings.

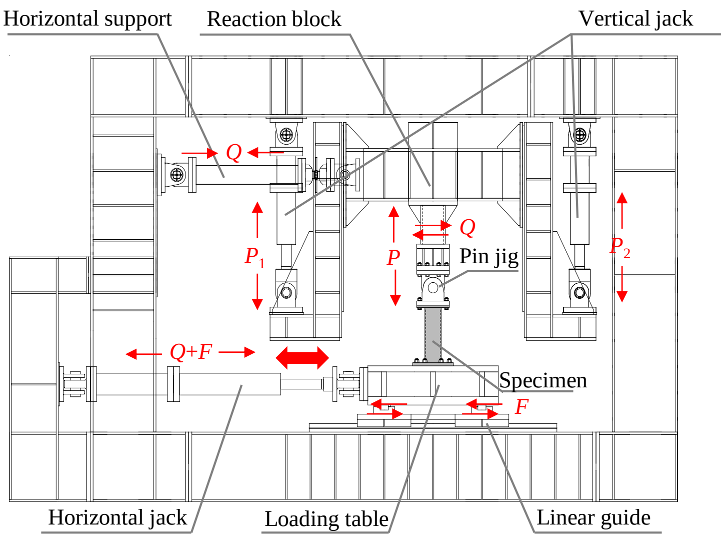

(a) Plain view for the test setup.

(b) Photograph of the test setup.

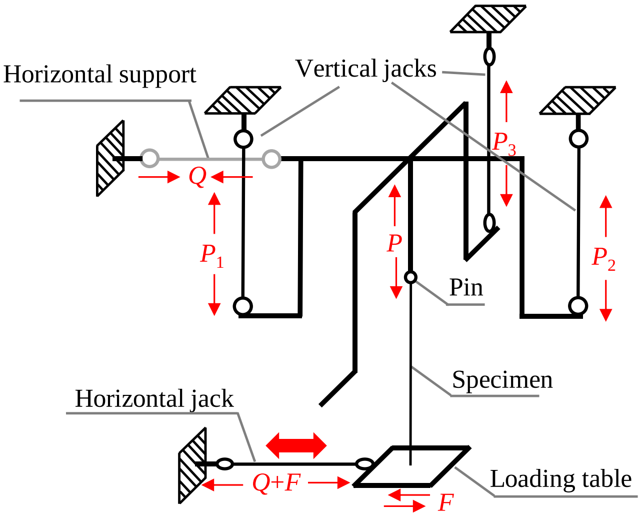

(c) Diagram for the test setup (3D view).

Fig. 2-8 Test setup.

Both monotonic and cyclic loading were employed in this study. Both constant and variable amplitude loadings were applied to specimens under cyclic loading. Fig. 2-9 illustrates how rotation angle of the column end, θ, and loading amplitude are defined. θ_{pc} is the calculated elastic rotation angle of the column corresponding to the plastic moment (M_{pc}) when the effect of the axial force is considered [2-7]. The detailed calculation methods are illustrated in the Appendix 1. The constant amplitude loading ranged from $1.0\theta_{pc}$ to $3.5\theta_{pc}$ with the rotation angle ranging from 0.71% to 1.85%, as shown in Fig. 2-10(a). Incremental and random amplitude loadings were used for variable amplitude loading. The absolute peak amplitude of incremental loading consisted of a set of four cycles of $1.5\theta_{pc}$, two cycles of $2.0\theta_{pc}$, and one cycle of $2.5\theta_{pc}$, as shown in Fig. 2-10(b). The random amplitude loading set was designed based on a response analysis of a 3-story SMRF [2-1] excited by the 1952 Kern County Earthquake Taft Record East-West (EW) component, which can make the large responses of columns with relatively small differences compared to the maximum one, as shown in Fig. 2-10 (c). The detailed information of the 3-story SMRF can be referred to in the Appendix 2. The rotation response of the first-floor columns was converted into a random loading protocol and named Taft. A proper scale factor was used during the response analysis to limit the maximum loading amplitude for each half cycle in the random loading (Fig. 2-10 (c)) within $2.75\theta_{pc}$. In addition, all cycles with a peak-to-peak amplitude less than $2\theta_{pc}$ were removed because the columns remained mostly elastic under these rotation ranges. Once determined, the variable amplitude loading set was reused in the subsequent loading cycles.

Table 2-3 lists the tested specimens in detail. The specimens were named in accordance with a “loading protocol_width-to-thickness ratio_axial force ratio_shear span ratio” naming scheme. The loading protocol “M” stands for monotonic loading, “V” means variable amplitude loading, and “Cn” means $n{\cdot}\theta_{pc}$ constant amplitude loading.

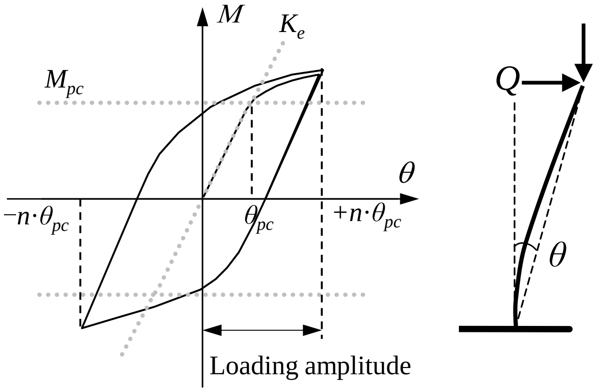

Fig. 2-9 Definition of loading amplitude.

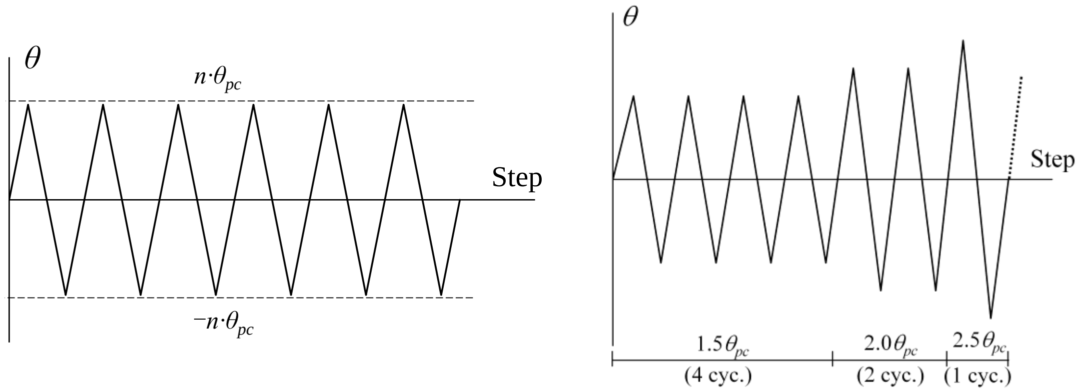

(a) Constant amplitude loading.

(b) Incremental loading.

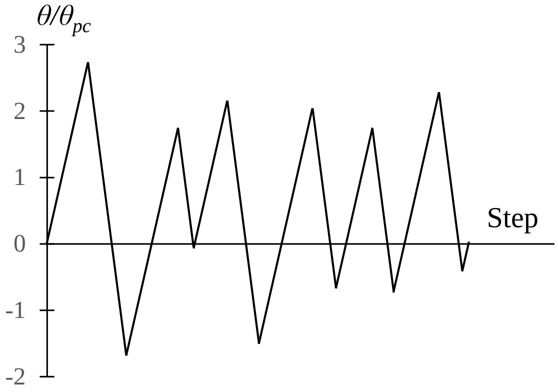

(c) Random loading.

Fig. 2-10 Loading protocol.

Table 2-3 List of the specimens

Lot	Dimension	Specimen	B/t	P/P_y	L/B	Loading history	Loading amplitude	N_{cr}	$N_{peak(+)}$	$N_{peak(-)}$	M_{cr}/M_{peak}
A	□-175×175×9 (BCR295)	M_19.4_0.3_7.0	19.4	0.3	7.0	Monotonic	n/a	n/a	n/a	n/a	n/a
		C1.5_19.4_0.3_7.0				Const. amp. 1.5θ_{pc}	0.0136	169	4	3	0.87
		C2.0_19.4_0.3_7.0				Const. amp. 2.0θ_{pc}	0.0185	15	2	2	0.91
B		M_19.4_0.3_4.9	19.4	0.3	4.9	Monotonic	n/a	n/a	n/a	n/a	n/a
		C1.5_19.4_0.3_4.9				Const. amp. 1.5θ_{pc}	0.0106	234	3	2	0.83
		C1.75_19.4_0.3_4.9				Const. amp. 1.75θ_{pc}	0.0123	52	3	3	0.89
		C2.0_19.4_0.3_4.9				Const. amp. 2.0θ_{pc}	0.0141	24	3	2	0.90
C		M_19.4_0.3_3.0	19.4	0.3	3.0	Monotonic	n/a	n/a	n/a	n/a	n/a
		C2.0_19.4_0.3_3.0				Const. amp. 2.0θ_{pc}	0.0103	22	4	4	0.87
		C2.5_19.4_0.3_3.0				Const. amp. 2.5θ_{pc}	0.0121	11	3	3	0.89
		C3.5_19.4_0.3_3.0				Const. amp. 3.5θ_{pc}	0.0172	5	2	1	0.87
D	□-175×175×6 (BCR295)	M_29.2_0.15_4.9	29.2	0.15	4.9	Monotonic	n/a	n/a	n/a	n/a	n/a
		C1.5_29.2_0.15_4.9				Const. amp. 1.5θ_{pc}	0.0117	52	3	2	0.76
		M_29.2_0.3_4.9	29.2	0.3	4.9	Monotonic	n/a	n/a	n/a	n/a	n/a
		C1.0_29.2_0.3_4.9				Const. amp. 1.0θ_{pc}	0.0071	283	2	3	0.84
		C1.5_29.2_0.3_4.9				Const. amp. 1.5θ_{pc}	0.0106	1	2	2	n/a

E	□-200×200×9 (BCR295)	M_22.2_0.35_4.3	22.2	0.35	4.3	Monotonic	n/a	n/a	n/a	n/a	n/a
		C1.5_22.2_0.35_4.3				Const. amp. 1.5θ_{pc}	0.0085	284	4	4	0.89
		C2.0_22.2_0.35_4.3				Const. amp. 2.0θ_{pc}	0.0123	21	4	3	0.91
		V_22.2_0.35_4.3				Variable	n/a	27	7	7	n/a
F		M_22.2_0.2_4.3	22.2	0.2	4.3	Monotonic	n/a	n/a	n/a	n/a	n/a
		Taft_22.2_0.2_4.3				Variable	n/a	30	1	1	n/a
G	□-200×200×6 (BCR295)	M_33.3_0.2_4.3	33.3	0.2	4.3	Monotonic	n/a	n/a	n/a	n/a	n/a
		C1.5_33.3_0.2_4.3				Const. amp. 1.5θ_{pc}	0.0085	168	2	2	0.78
		C2.0_33.3_0.2_4.3				Const. amp. 2.0θ_{pc}	0.0117	3	2	1	0.96
		V_33.3_0.2_4.3				Variable	n/a	7	6	5	n/a

Notes: B/t: Width-to-thickness ratio; P/P_y: Axial force ratio; L/B: Shear span ratio; N_{cr}: Number of cycles until the stability limit as defined in Section 4; θ_{pc}: The calculated elastic rotation angle of the column that corresponds to the plastic moment considering the effect of axial force; “Const.” is the abbreviation for “Constant”; “amp.” is the abbreviation for “amplitude”; $N_{peak(+)}$: Number of cycles reaching the maximum moment in the positive side; $N_{peak(-)}$: Number of cycles reaching the maximum moment in the negative side; M_{cr}/M_{peak}: the ratio of strength until the stability limit to the maximum moment.

2.3 Test results

2.3.1 Failure mode

Local buckling was observed in all specimens, as shown in Fig. 2-11 (photographs of Specimen C1.0_29.2_0.3_4.9 and C2.0_19.4_0.3_4.9, respectively). Local buckling occurred at the bottoms of all the specimens. The local buckling mode for each specimen has been listed in Appendix 13 in detail. The extended local buckling mode was observed for limited specimens with relatively small width-to-thickness ratio (i.e., □–175×175×9) under cyclic loading; while the non-extended local buckling mode was observed in the other specimens.

The local buckling deformation was measured manually at intervals during the experiment process, as shown in Fig. 2-12. The maximum strength and the strength deterioration processes for all specimens were governed by the local buckling deformation. For the specimens under monotonic loading, the deformation in the local buckling is minor before reaching the maximum strength; the deformation progressed rapidly after reaching the maximum strength. For the specimens under cyclic amplitude loading, once local buckling deformation progress rapidly, the strength bearing capacity decreased fast.

(a) Non-extended mode.

(b) Extended mode.

Fig. 2-11 Failure mode (i.e., local buckling) in the experiment.

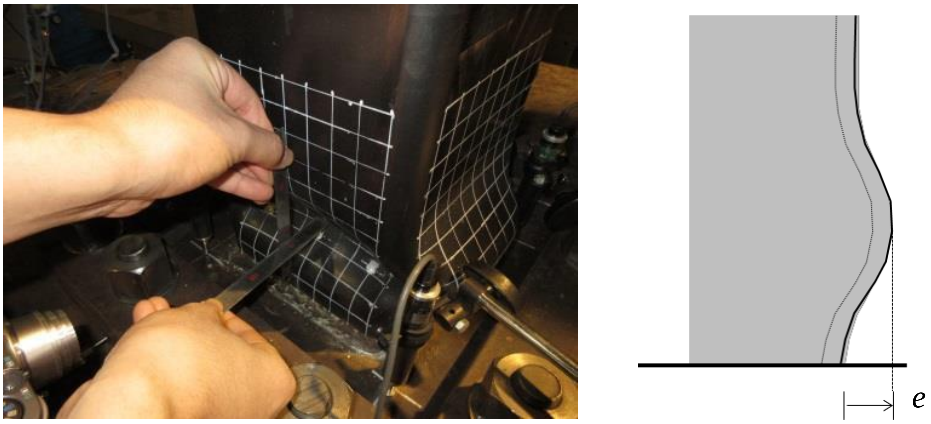

Fig. 2-12 Measuring for the local buckling deformation.

2.3.2 Hysteretic curves

The moment-rotation angle relationships for the specimens under monotonic loading were shown in Fig. 2-13. For all the specimens, the strength increased linearly during the elastic stage, the strength increasing rate decreased in the plastic stage, and started to deteriorate after reaching the maximum strength. M_{pc} is the calculated plastic moment considering the effect of the axial force. K_e represents the calculated elastic stiffness of the columns, which are always compared with the measuring one to make sure the measuring system work well before carrying out the loading process in the experiment. The solid, black line represents the moment-rotation angle relationship prior to the stability limit, while the dashed, red line represents that relationship after the stability limit. The concept of stability limit will be illustrated in Chapter 2.4 in detail.

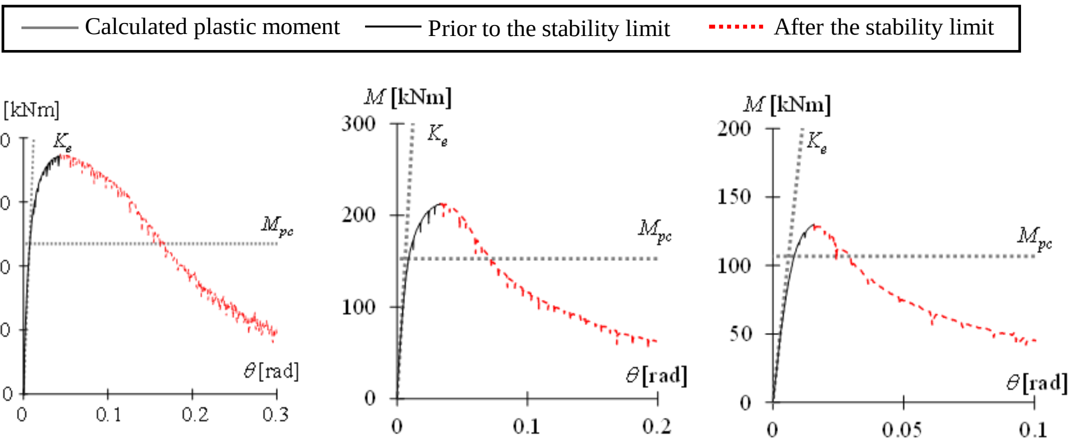

(a) M_19.4_0.3_4.9 (b) M_22.2_0.35_4.3 (c) M_33.3_0.2_4.3

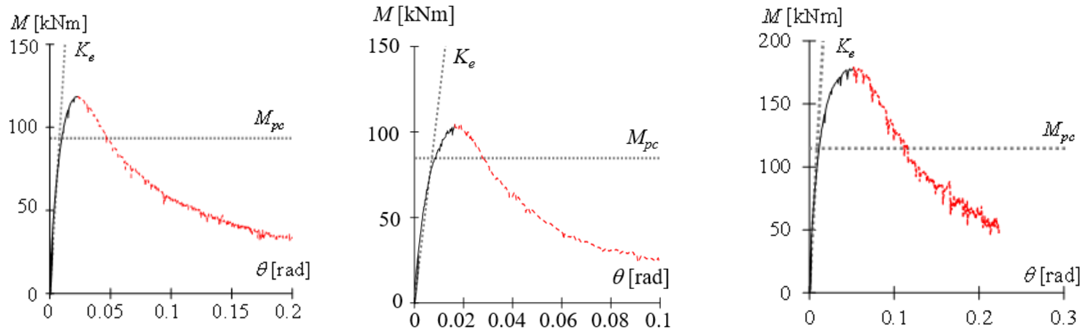

(d) M_29.2_0.15_4.9 (e) M_29.2_0.3_4.9 (f) M_19.4_0.3_7

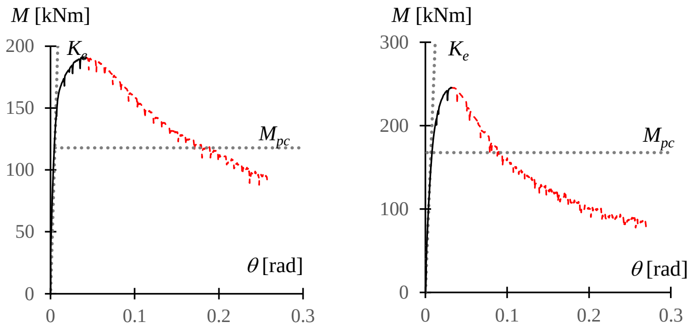

(g) M_19.4_0.3_3 (h) M_22.2_0.2_4.3

Fig. 2-13 Moment-rotation angle relationship for SHS columns under monotonic loading

For the specimens under cyclic constant amplitude loading, all the specimens can reach the calculated plastic moment considering the axial force, M_{pc}. The peak strength always appeared in the first several cycles, and could never reach the maximum strength of the specimens under monotonic loading. Furthermore, slight strength decrease can be observed before reaching the stability limit. This phenomenon can be explained in two aspects. In one way, the strength decrease was caused by the cyclic softening behavior in the material property of the cold-formed column components [2-8][2-9] , which can lead to the decrease in the stress of the column section and subsequently decrease the moment bearing capacity. In the other way, there was already slight residual deformation accumulating in the flanges of the columns before the stability limit, which could also lead to the strength decrease after first few cycles. Both the number of cycles to the maximum strength in the positive and negative sides were summarized in Table 2-3. Prior to the stability limit, minor strength and stiffness deterioration was observed from the hysteretic curves in Fig. 2-14; After the stability limit, rapid decrease was observed in bearing capacity and unloading stiffness for the columns.

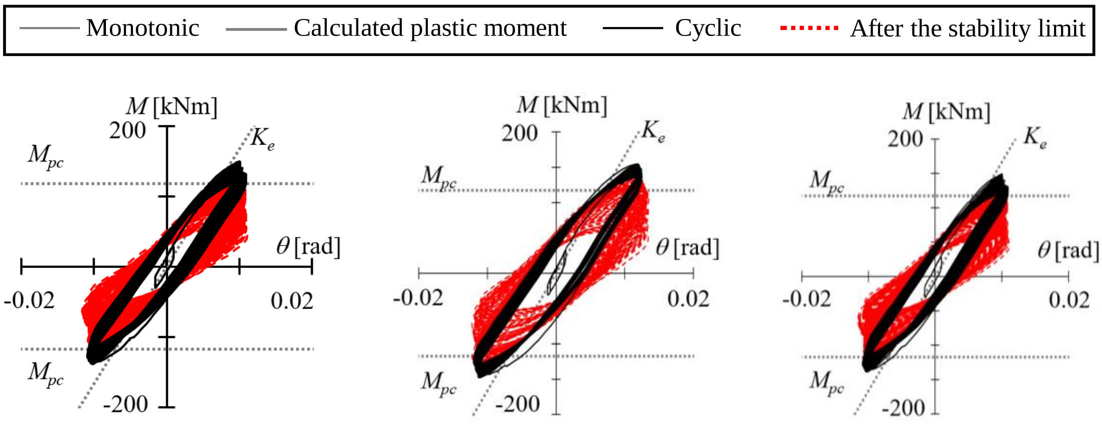

(a) C2.0_19.4_0.3_4.9 (b) C1.75_19.4_0.3_4.9 (c) C1.5_19.4_0.3_4.9

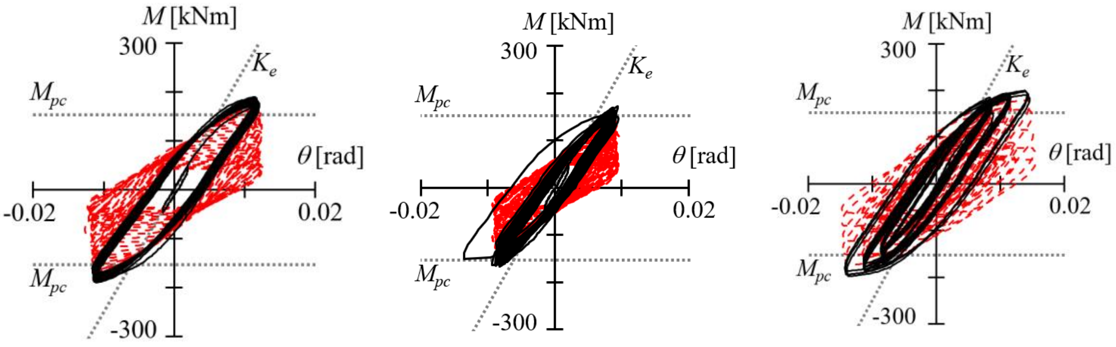

(d) C2.0_22.2_0.35_4.3 (e) C1.5_22.2_0.35_4.3 (f) V_22.2_0.35_4.3

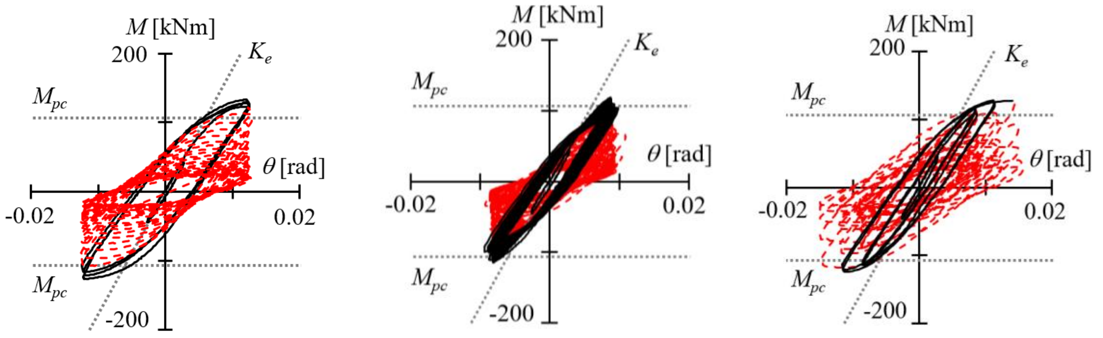

(g) C2.0_33.3_0.2_4.3 (h) C1.5_33.3_0.2_4.3 (i) V_33.3_0.2_4.3

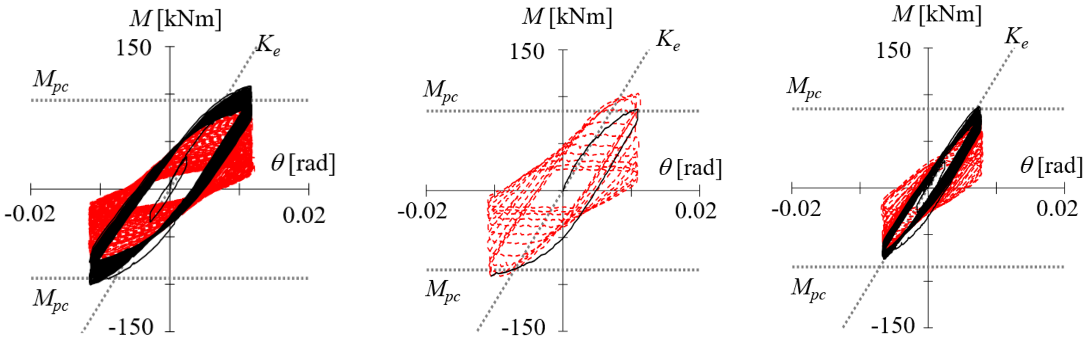

(j) C1.5_29.2_0.15_4.9 (k) C1.5_29.2_0.3_4.9 (l) C1.0_29.2_0.3_4.9

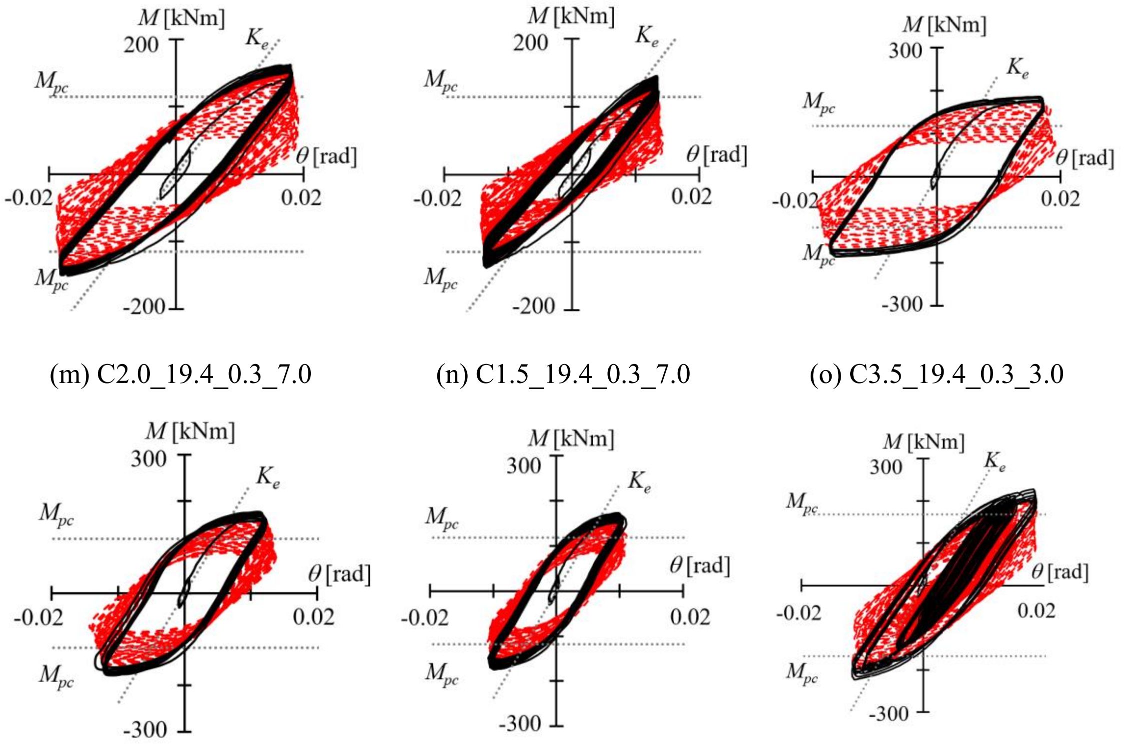

(m) C2.0_19.4_0.3_7.0 (n) C1.5_19.4_0.3_7.0 (o) C3.5_19.4_0.3_3.0

(p) C2.5_19.4_0.3_3.0 (q) C2.0_19.4_0.3_3.0 (r) Taft_22.2_0.2_4.3

Fig. 2-14Moment-rotation angle relationship for SHS columns under cyclic loading

2.3.3 Extended skeleton curves

In this study, the extended skeleton curve [2-10] was employed to depict the strength deterioration behaviors of the specimens subjected to cyclic small amplitude loading. It is the envelope of the cumulative hysteresis curve based on the hysteresis rule (i.e., hysteresis curve can be decomposed into three parts before maximum strength: skeleton part, Baushiger part and elastic unloading part [2-11]). The extended skeleton curve is obtained by connecting the skeleton curve before the maximum strength (M_{max}) and the hysteresis curve of each half cycle after the maximum strength, as shown in Fig. 2-15. It can show the cumulative deformation and the strength deterioration behaviors clearly during the whole loading process for specimens under cyclic constant amplitude loading. For specimens under large plastic loading, the extended skeleton curve is empirically known to approximately correspond to the moment-rotation angle curve under monotonic loading [2-10]. This regular pattern is stated as “empirical rule” throughout this paper. Test data from previous study [2-12] were also shown in Appendix 3 to illustrate the empirical rule.

Fig. 2-16 shows the extended skeleton curves for the specimens under cyclic loading, as well as their moment-rotation angle relationship under monotonic loading (solid, grey line). In the figure, θ_s is the cumulative rotation angle of the extended skeleton curve. Similar to Fig. 2-14, the solid, black line in Fig. 2-16 represents the extended skeleton curve prior to the stability limit, and the dashed, red line represents the extended skeleton curve after the stability limit.

The extended skeleton curves of most of the specimens under small amplitude loading displayed different trends compared to the moment-rotation angle relationship of specimens under monotonic loading. Exceptions were Specimens C1.5_29.2_0.3_4.9 (Fig. 2-16 (k)), V_33.3_0.2_4.3(Fig. 2-16 (i)), C2.0_33.3_0.2_4.3 (Fig. 2-16 (g)), C2.5_19.4_0.3_3.0 (Fig. 2-16 (p)) and C3.5_19.4_0.3_3.0 (Fig. 2-16 (o)). These specimens roughly followed the empirical rule [2-10]. (A column under limited number of cyclic large amplitude loadings was shown as an example in Appendix 3 to explain the empirical rule). In other words, the cumulative rotation angle from maximum strength to the point when obvious strength deterioration initiated increased. In addition, the negative slope of the envelope curve of those specimens after obvious strength deterioration was shallower relative to the slopes of the specimen subjected to monotonic load.

The test results confirmed that, for columns under small amplitude loading, the extended skeleton curves do not necessarily correspond to the moment-rotation angle relationship of corresponding columns under monotonic loading [2-6]. The specimens can obtain higher stabilities and better cumulative plastic deformation capacities relative to specimens under monotonic or large amplitude loading, as shown in Fig. 2-16. That is similar to the findings in [2-13] (i.e., the rate of strength reduction due to local buckling slows down as the loading amplitude decreases).

According to the experimental results, the width-to-thickness ratio, axial force ratio, shear span ratio, and loading history have non-negligible effects on the deterioration behavior of the columns. The influences of those parameters were compared in Fig. 2-17. For all specimens, the rate of strength deterioration slowed as the loading amplitude decreased, as shown in Fig. 2-17 (a). Increasing the width-to-thickness ratio resulted in faster bearing capacity deterioration, as shown in Fig. 2-17 (b). This is because the width-to-thickness ratio significantly influences local buckling behavior. Decreasing the axial force ratio, strength of the specimens deteriorates slower, as shown in Fig. 2-17 (c). Additional bending moment caused by the axial force has an obvious effect on the strength deterioration behavior. Differences in shear span ratio had relatively minor influence on the deterioration behaviors of specimen prior to the stability limit. However, increased shear span ratios resulted in faster strength deterioration after the stability limit, as shown in Fig. 2-17 (d). Specimen with larger shear span ratios also reached the stability limits earlier. The influence of different parameters on the stability limit can also be compared and observed directly in Fig. 2-18.

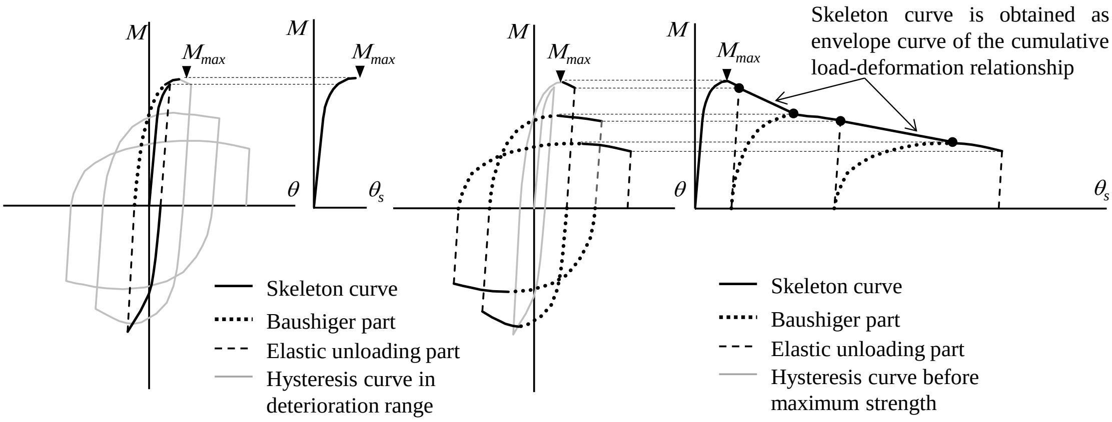

(a) Before reaching the maximum strength M_{max}. (b) After reaching the maximum strength M_{max}.

Fig. 2-15 Definition of the extended skeleton curve

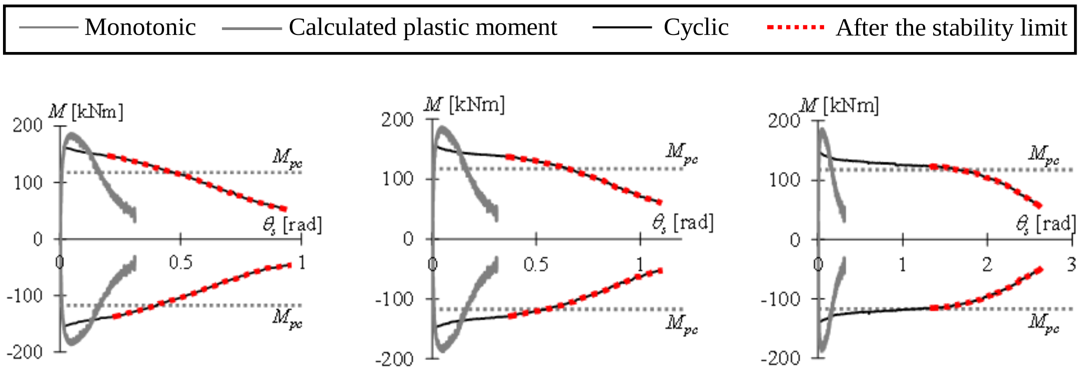

(a) C2.0_19.4_0.3_4.9 (b) C1.75_19.4_0.3_4.9 (c) C1.5_19.4_0.3_4.9

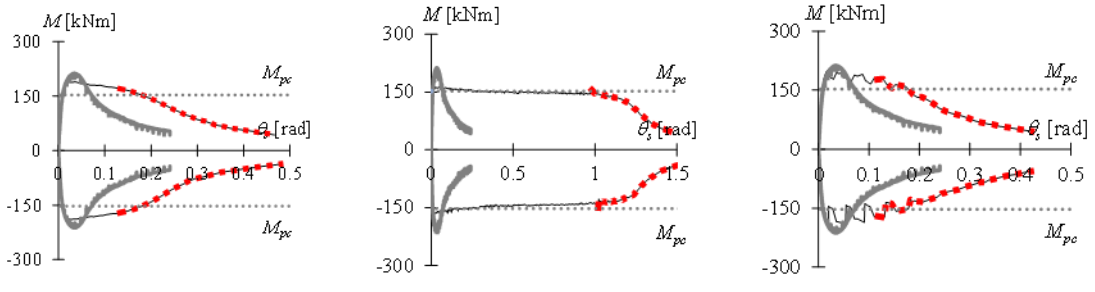

(d) C2.0_22.2_0.35_4.3 (e) C1.5_22.2_0.35_4.3 (f) V_22.2_0.35_4.3

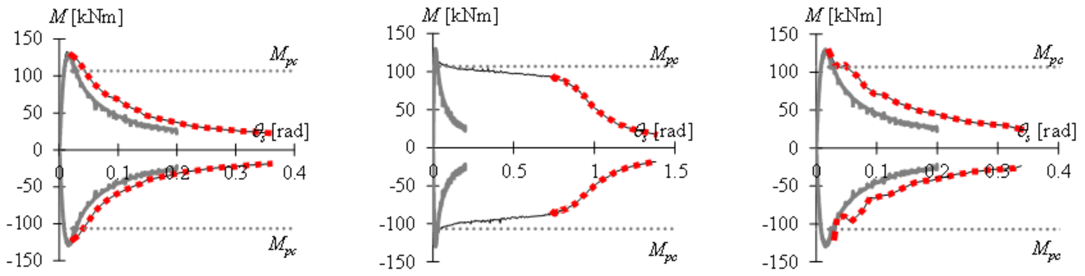

(g) C2.0_33.3_0.2_4.3 (h) C1.5_33.3_0.2_4.3 (i) V_33.3_0.2_4.3

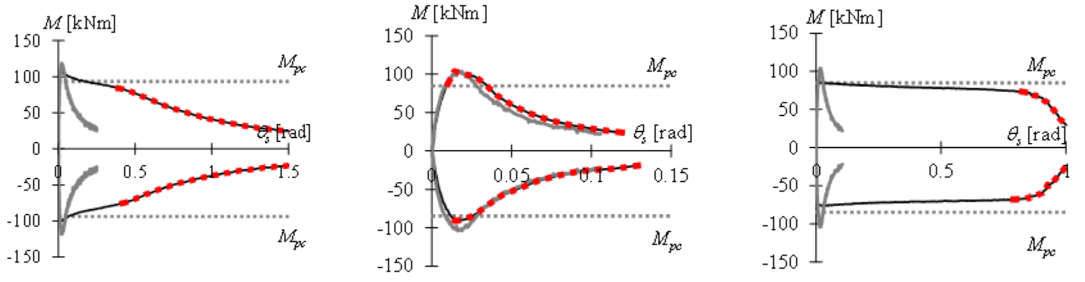

(j) C1.5_29.2_0.15_4.9 (k) C1.5_29.2_0.3_4.9 (l) C1.0_29.2_0.3_4.9

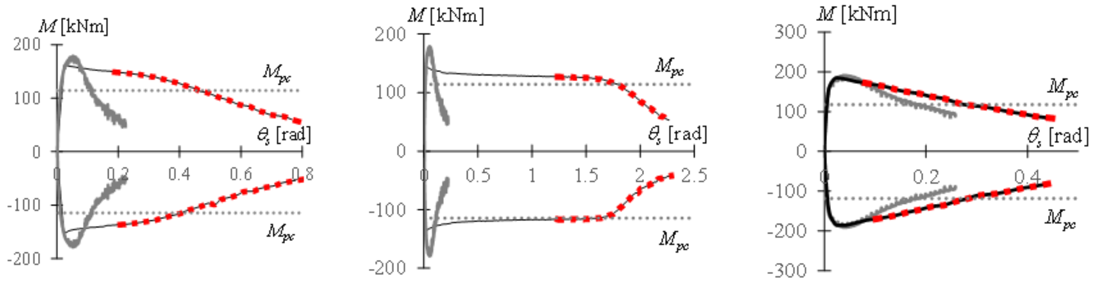

(m) C2.0_19.4_0.3_7.0 (n) C1.5_19.4_0.3_7.0 (o) C3.5_19.4_0.3_3.0

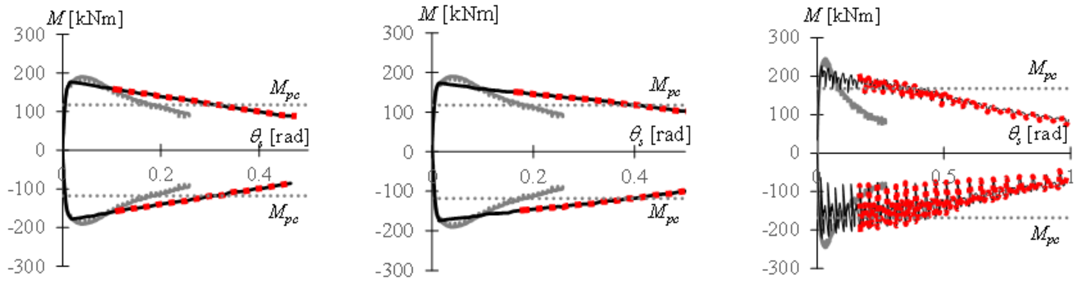

(p) C2.5_19.4_0.3_3.0 (q) C2.0_19.4_0.3_3.0 (r) Taft_22.2_0.2_4.3

Fig. 2-16 Comparison of the extended skeleton curves

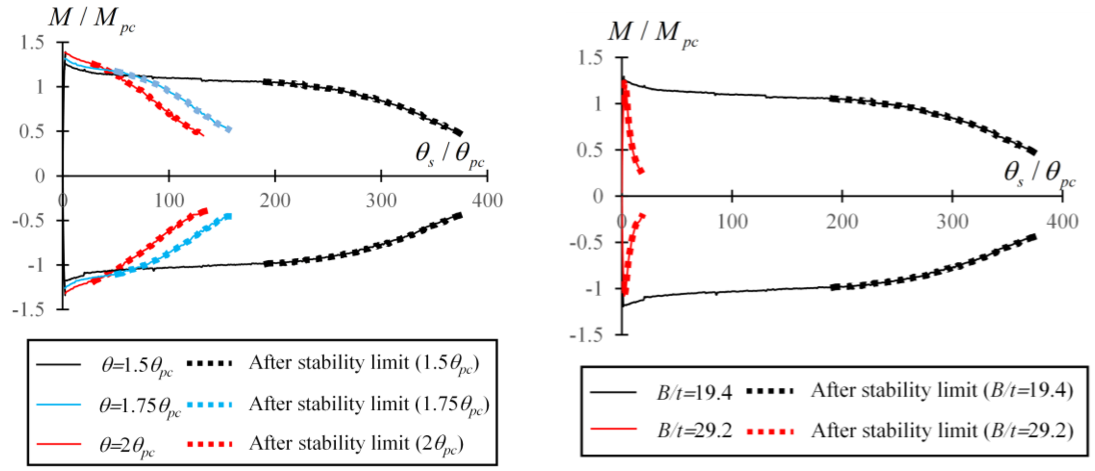

(a) Influence of loading amplitude.

(B/t=19.4, P/P_y=0.3, L/B=4.9)

(b) Influence of width-to-thickness ratio.

(Constant amplitude 1.5θ_{pc}, P/P_y=0.3, L/B=4.9)

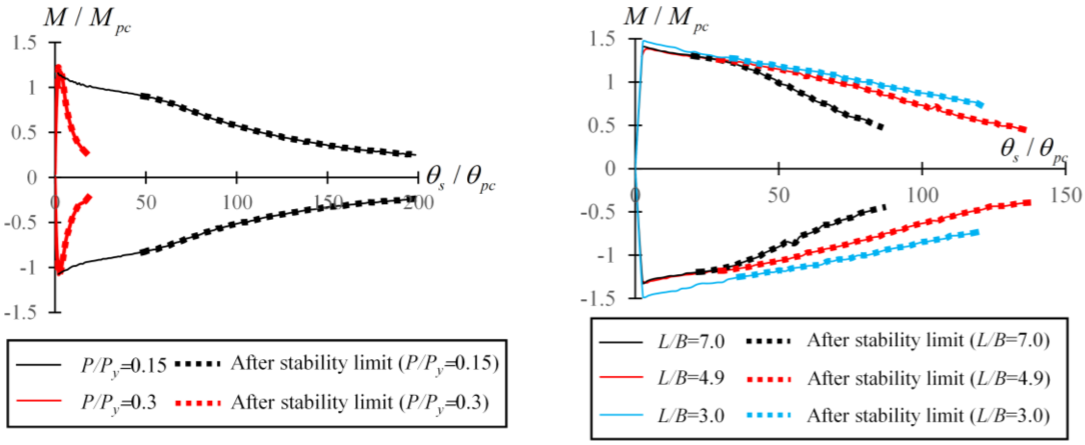

(c) Influence of axial force ratio.

(Constant amplitude 1.5θ_{pc}, B/t=29.2, L/B=4.9)

(d) Influence of shear span ratio.

(Constant amplitude 2θ_{pc}, B/t=19.4, P/P_y=0.3)

Fig. 2-17 Influence of different parameters on strength deterioration behavior.

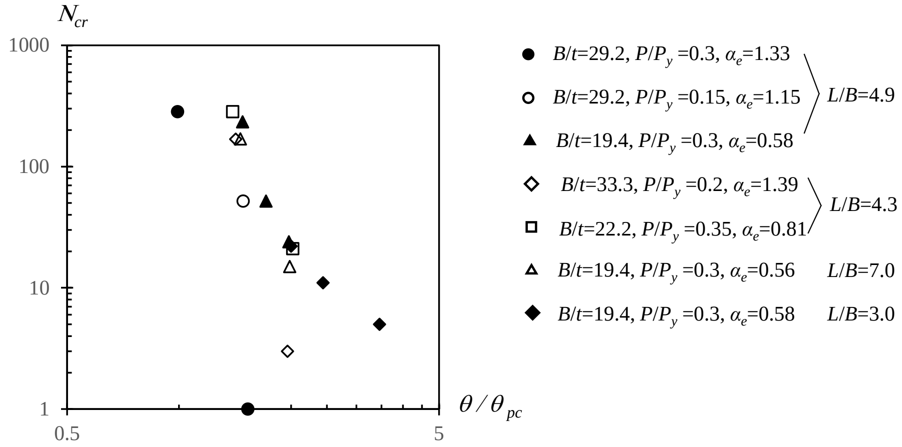

Fig. 2-18 Influence of different parameters on the number of cycles to the stability limit.

2.3.4 Stiffness deterioration

In the Chapter 2.3.3, the strength deterioration behavior caused by the local buckling has been investigated based on the concept of the extended skeleton curve. The stiffness of the steel columns was closely related to the deformed shape. When severe local buckling appeared, the stiffness of the steel columns would decrease as well. Therefore, the stiffness deterioration behavior of all the specimens were investigated based on the relationship of K/K_e and N, as in Fig. 2-19. K/K_e represents the ratio of current stiffness to the initial one, and N stands for the number of cycles. The stiffness was calculated with the maximum rotation angle and its corresponding strength in each cycle, and the rotation angle when the strength decreases to zero. During the experiment process, when the actuators were stopped, there can be some strength drop, which caused the fluctuations in Fig. 2-19. According to Fig. 2-19, the stiffness started to deteriorate rapidly since the point "stability limit" mentioned in previous section; while there are always plateaus in the stiffness prior to the "stability limit" point for most of the specimens, except for Specimens C1.5_29.2_0.3_4.9 (Fig. 2-19 (k)), V_33.3_0.2_4.3 (Fig. 2-19 (i)), and C2.0_33.3_0.2_4.3 (Fig. 2-19 (g)). This is because the number of cycles to the stability limit for these specimens are small. Once there is any fluctuation, a stable trend for the stiffness deterioration prior to the stability limit cannot be obtained.

Based on the discussions in Chapters 2.3.3 and 2.3.4, severe strength and stiffness deterioration can be considered to happen simultaneously due to the local buckling progress.

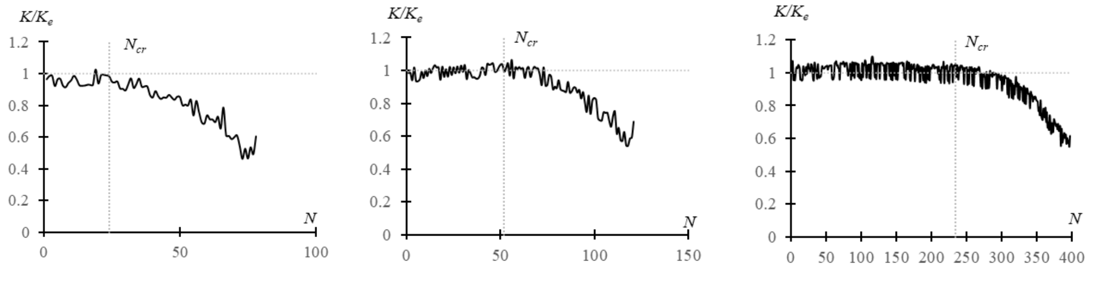

(a) C2.0_19.4_0.3_4.9 (b) C1.75_19.4_0.3_4.9 (c) C1.5_19.4_0.3_4.9

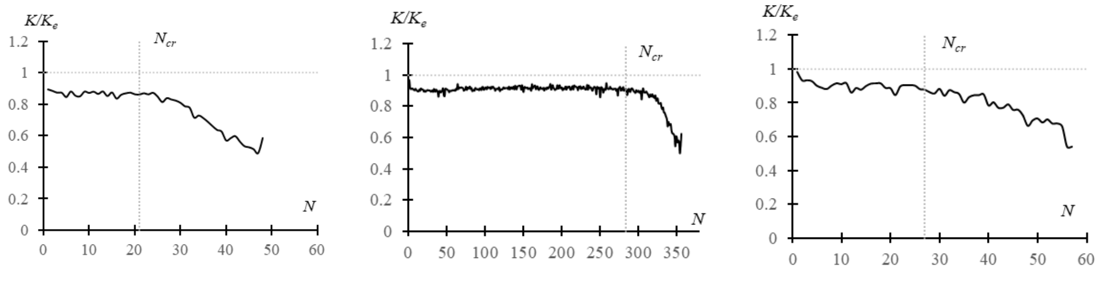

(d) C2.0_22.2_0.35_4.3 (e) C1.5_22.2_0.35_4.3 (f) V_22.2_0.35_4.3

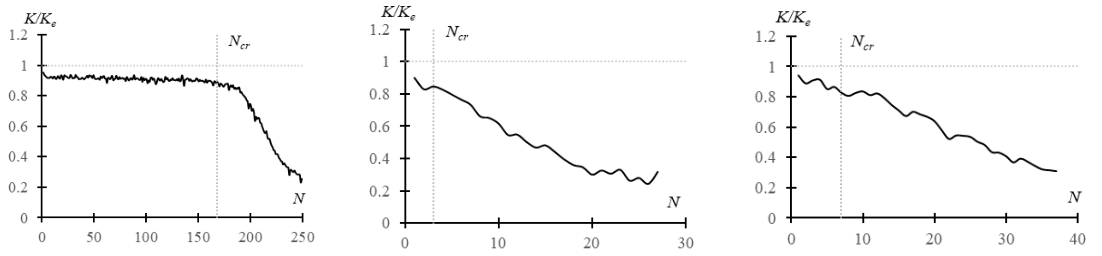

(g) C2.0_33.3_0.2_4.3 (h) C1.5_33.3_0.2_4.3 (i) V_33.3_0.2_4.3

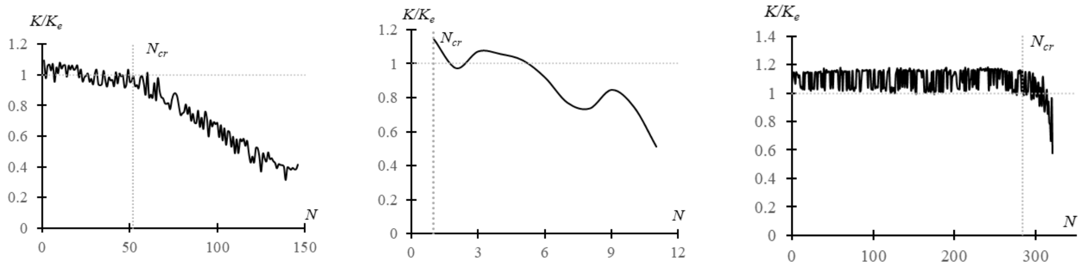

(j) C1.5_29.2_0.15_4.9 (k) C1.5_29.2_0.3_4.9 (l) C1.0_29.2_0.3_4.9

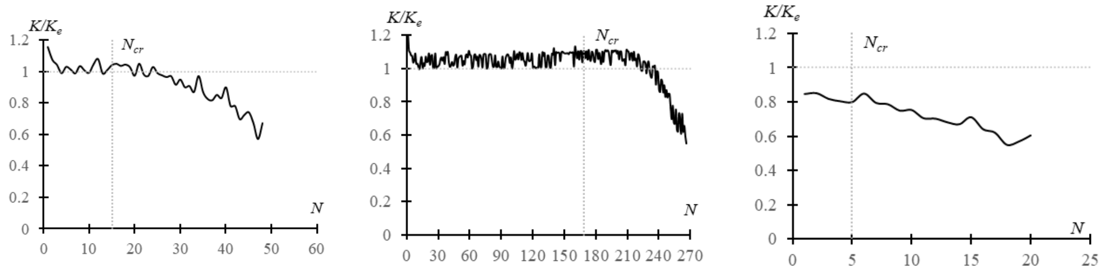

(m) C2.0_19.4_0.3_7.0 (n) C1.5_19.4_0.3_7.0 (o) C3.5_19.4_0.3_3.0

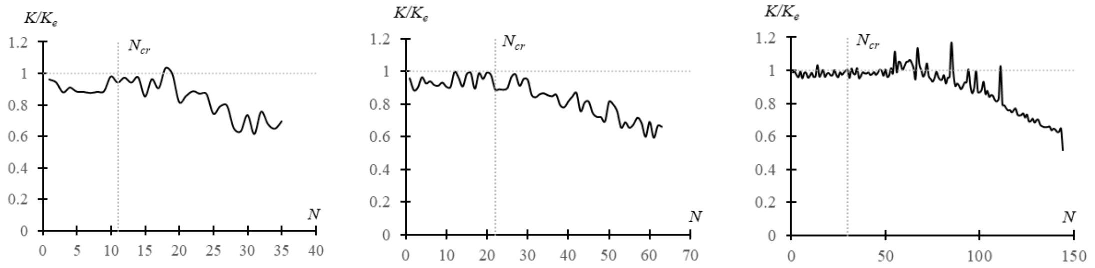

(p) C2.5_19.4_0.3_3.0 (q) C2.0_19.4_0.3_3.0 (r) Taft_22.2_0.2_4.3

Fig. 2-19 Unloading stiffness deterioration behavior

2.4 Proposal of the stability limit

2.4.1 Concept of the stability limit

A close relationship between the progress of the axial deformation of the flange plate in the local buckling region (δ_b) and the strength deterioration of the columns was observed. After local buckling has occurred, plastic deformation concentrates and progresses in that region.

Meanwhile, other parts exhibit elastic behaviors. In particular, when the value of δ_b exceeded $\delta_{b,cr}$, (i.e., δ_b has reached maximum strength under monotonic loading) while under cyclic loading, the strength deteriorated significantly, as schematically illustrated in Fig. 2-20. In the figure, points A to D were determined one by one and in order. The point where δ_b reaches $\delta_{b,cr}$ is the "stability limit". Each specimen obviously weakened under cyclic loading upon reaching the stability limit, as shown by the dashed, red line in Fig. 2-20.

The concept of the stability limit combines the behaviors of the steel columns under monotonic loading and cyclic loading together. The concept also combines the strength deterioration behavior and deformation progress together, which considers the over strength deterioration and excessive deformation cases in practice. Furthermore, the concept tries to depict the complicated cyclic behaviors with only simple pushover test, which has already been well researched. It can bring much convenience to the practical engineering.

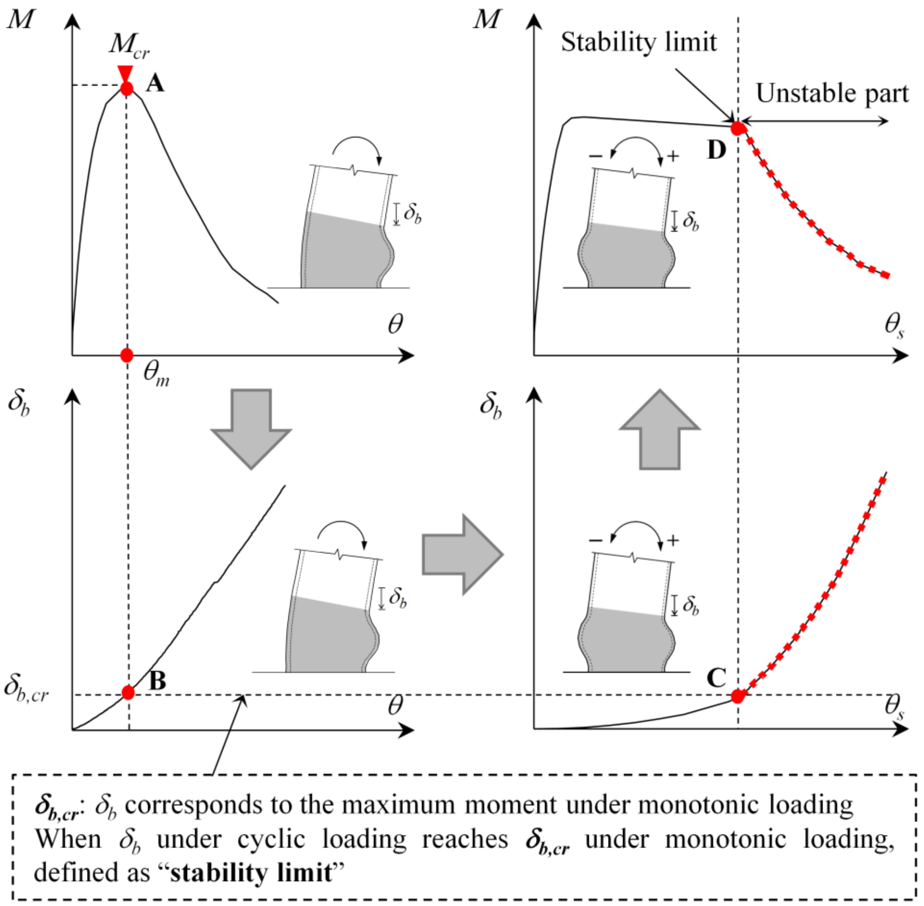

$\boldsymbol{\delta_{b,cr}}$: δ_b corresponds to the maximum moment under monotonic loading
When δ_b under cyclic loading reaches $\boldsymbol{\delta_{b,cr}}$ under monotonic loading, defined as "**stability limit**"

(a) Monotonic (b) Cyclic

Fig. 2-20 Definition of the stability limit.

2.4.2 Investigation of the axial deformation of the flange plate in the local buckling region

The relationships between δ_b (i.e., the axial deformation of the flange plate in the local buckling region) and θ_s (i.e., the cumulative rotation angle) for specimens under monotonic and cyclic loadings are shown in Fig. 2-21. It should be noted that a measuring problem occurred in the buckling region for Specimen C1.5_29.2_0.3_4.9. Consequently, the axial deformation of the column, δ_z, was used to evaluate the deformation progress of the column. According to Fig. 2-21, all specimens under cyclic constant amplitude loading saw slow, linear increases to δ_b prior to reaching the stability limit. In contrast, δ_b increased rapidly after the stability limit ($\delta_{b,cr}$) was exceeded. That corresponded to the fast strength deterioration in the extended skeleton curves in Chapter 2.3.3, and the rapid stiffness decrease in Chapter 2.3.4. For specimens under variable amplitude loading, the increases to δ_b prior to reaching the stability limit was rather slow; after the stability limit, rapid δ_b increase and fast strength deterioration were also observed. These phenomena were similar to those under constant amplitude loading. Prior to the stability limit, the δ_b increase of each cycle varied with the variation in loading amplitude; for cycles under the same loading amplitude level, the δ_b increase was basically close to each other; the δ_b increase was positively related to the loading amplitude.

The progress of δ_b for Specimens C1.5_29.2_0.3_4.9, C2.0_33.3_0.2_4.3, V_33.0_0.2_4.3, C2.5_19.4_0.3_3.0 and C3.5_19.4_0.3_3.0 prior to them reaching stability was nearly the same as that of corresponding specimens under monotonic loading. This is consistent with the specimens roughly following the empirical rule. In contrast, the δ_b of the other specimens developed slowly prior to the stability limit relative to the corresponding specimens under monotonic loading. In summary, the different deformation mechanisms in the flange plate of the local buckling region prior to the stability limit being reached caused the differences in the strength deterioration behaviors of the specimens failing due to local buckling. That explains the phenomena from the perspective of physical meaning.

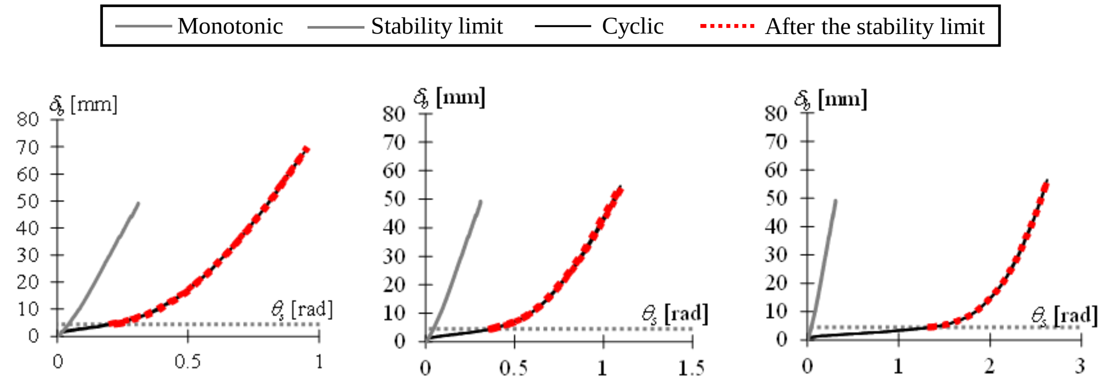

(a) C2.0_19.4_0.3_4.9 (b) C1.75_19.4_0.3_4.9 (c) C1.5_19.4_0.3_4.9

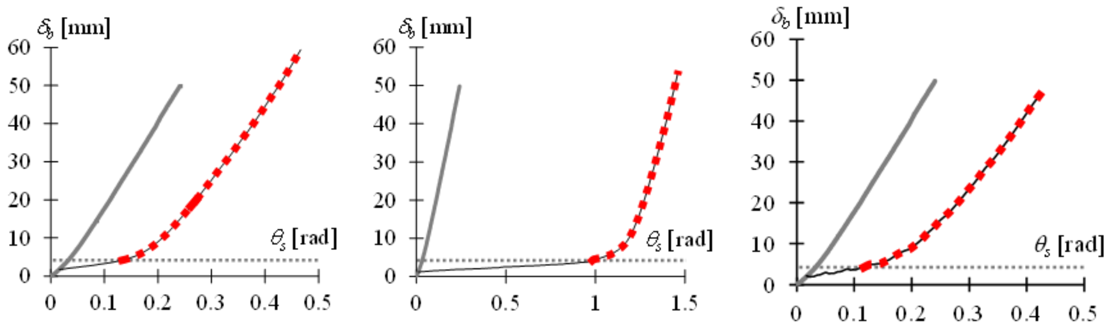

(d) C2.0_22.2_0.35_4.3 (e) C1.5_22.2_0.35_4.3 (f) V_22.2_0.35_4.3

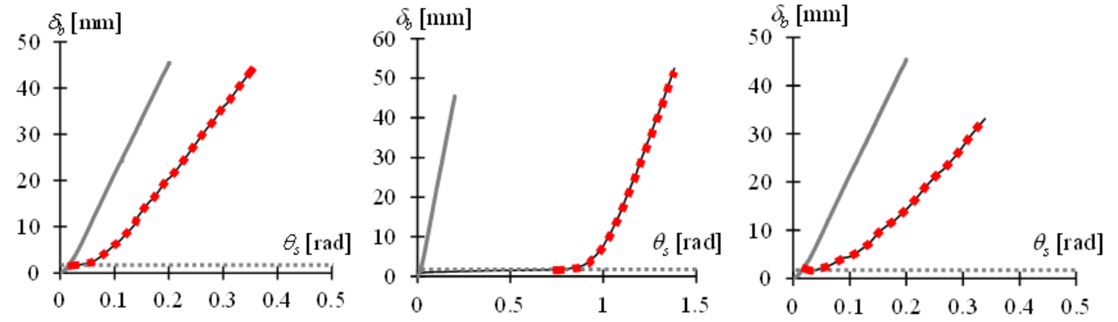

(g) C2.0_33.3_0.2_4.3 (h) C1.5_33.3_0.2_4.3 (i) V_33.3_0.2_4.3

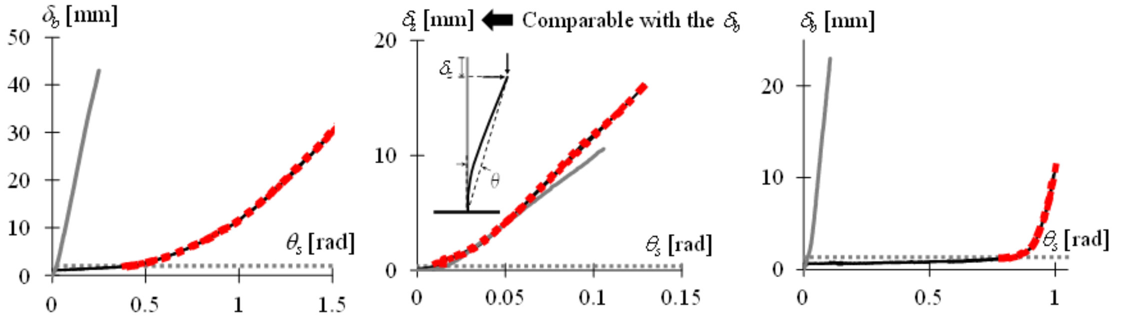

(j) C1.5_29.2_0.15_4.9 (k) C1.5_29.2_0.3_4.9 (l) C1.0_29.2_0.3_4.9

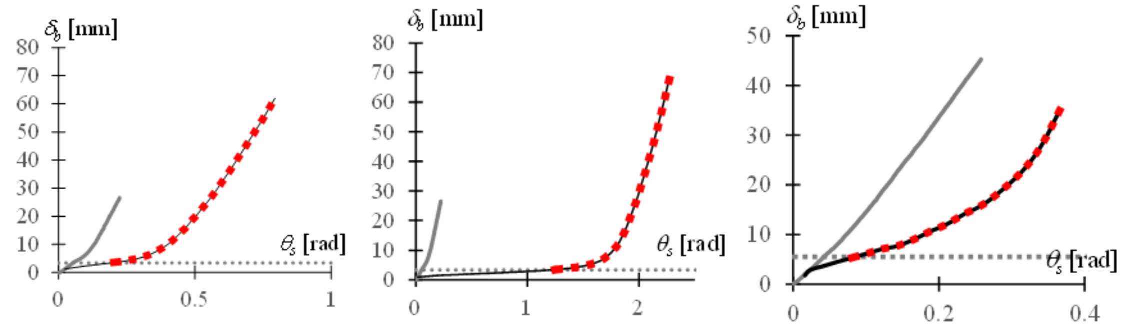

(m) C2.0_19.4_0.3_7.0 (n) C1.5_19.4_0.3_7.0 (o) C3.5_19.4_0.3_3.0

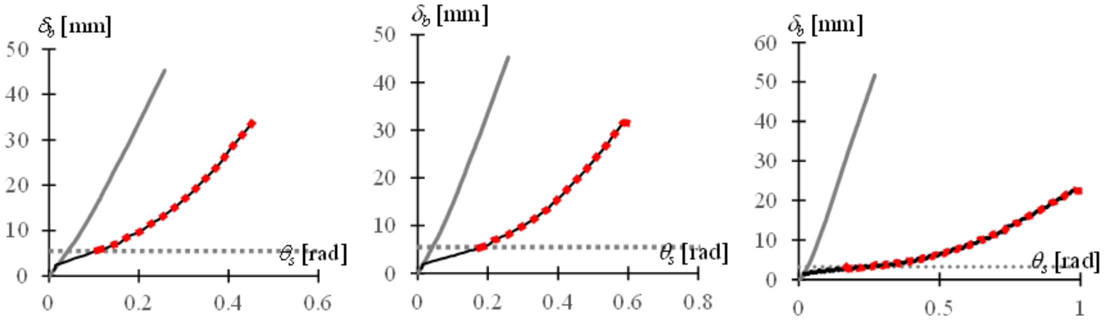

(p) C2.5_19.4_0.3_3.0 (q) C2.0_19.4_0.3_3.0 (r) Taft_22.2_0.2_4.3

Fig. 2-21 Progress of the axial deformation of the flange plate of the local buckling zone.

2.5 Evaluation of deformation capacity in the local buckling zone

Based on the discussion in Chapter 2.4, $\delta_{b,cr}$ (i.e., the stability limit point) is a good index to judge when the rapid deterioration stage begins for columns. Practically, it can be applied to prevent the onset of rapid deterioration in a column's bearing capacity. Based on the test results, prediction methods for the value of stability limit ($\delta_{b,cr}$) and the number of cycles until the stability limit (N_{cr}) is reached were developed and introduced in detail in this section.

2.5.1 Modeling concept for prediction methods of stability limit

By comparing the relationship between δ_b (i.e., axial deformation in the flange of local buckling region) and N (i.e., the number of cycles) for all the specimens under cyclic constant amplitude loading, the regular patterns of deformation progress can be summarized as follows: Before the stability limit, δ_b developed linearly starting with the second cycle. The first 0.25 cycle's deformation increment was larger than the increments of subsequent cycles before the stability limit was reached, as shown in Fig. 2-22. $\delta_{b,0}$ is the axial deformation in the flange of the local buckling region for the first 0.25 cycle, as defined in Fig. 2-22. $\Delta\delta_b$ is the total axial deformation increment in the flange of the local buckling region from the second cycle onwards until the stability limit. It is the difference of $\delta_{b,cr}$ and $\delta_{b,0}$, as Eq. (2-10).

$$\delta_{b,cr} = \delta_{b,0} + \Delta\delta_b \tag{2-10}$$

The physical meanings of $\delta_{b,0}$ and $\Delta\delta_b$ are illustrated as follows. Axial deformation in the flange of the local buckling region (δ_b) was composed of two parts (i.e., axial and rotational deformation in the local buckling region), as shown in Eq. (2-11). Those two parts correspond to the two items in Eq. (2-7). For the rotational deformation, it was found to be approximately a constant value for one specific loading amplitude before the stability limit, as shown in Fig. 2-23 (Specimen C1.5_29.2_0.15_4.9 was listed as an example, and the detailed information for the other specimens can be referred to Appendix 5). In addition, rotational deformation ($\delta_{b,rotation}$) was found to account for the majority of $\delta_{b,0}$ based on the test results, as shown in Fig. 2-24.

Table 2-4 lists the legends for each series of specimens, which will be used through Chapter 2. Since $\delta_{b,rotation}$ accounts for the majority of $\delta_{b,0}$, a simplified deformation process of $\delta_{b,rotation}$ prior to stability limit can be obtained, as shown in Fig. 2-25. The figure also shows the simplified deformation progress for δ_b for comparison. Although $\delta_{b,0}$ consisted of both axial and rotational parts, it can be approximated as the rotational one ($\delta_{b,rotation}$) since the axial part affected it little, based on Fig. 2-24. $\Delta\delta_b$ can be approximated as the axial deformation part ($\delta_{b,axial}$) subsequently.

$$\delta_b = \delta_{b,axial} + \delta_{b,rotation} \tag{2-11}$$

The regular pattern for the development of δ_b prior to the stability limit for specimens under monotonic loading was illustrated as below. The relationship between δ_b and rotation angle θ can be regarded as approximately linear prior to the stability limit. As shown in Fig. 2-26, this applied to all the specimens under monotonic loading that were studied, as Appendix 4. For specimens under cyclic loading, as long as the rotation amplitude was known, the value of $\delta_{b,0}$ mentioned above can be obtained using $\delta_{b,cr}$ and θ_m according to Fig. 2-26. θ_m is for the rotation angle corresponding to the maximum strength for specimens under monotonic loading.

In the following subsections, the modelling concept of the prediction methods was built based on the regular patterns in Fig. 2-22 and Fig. 2-26.

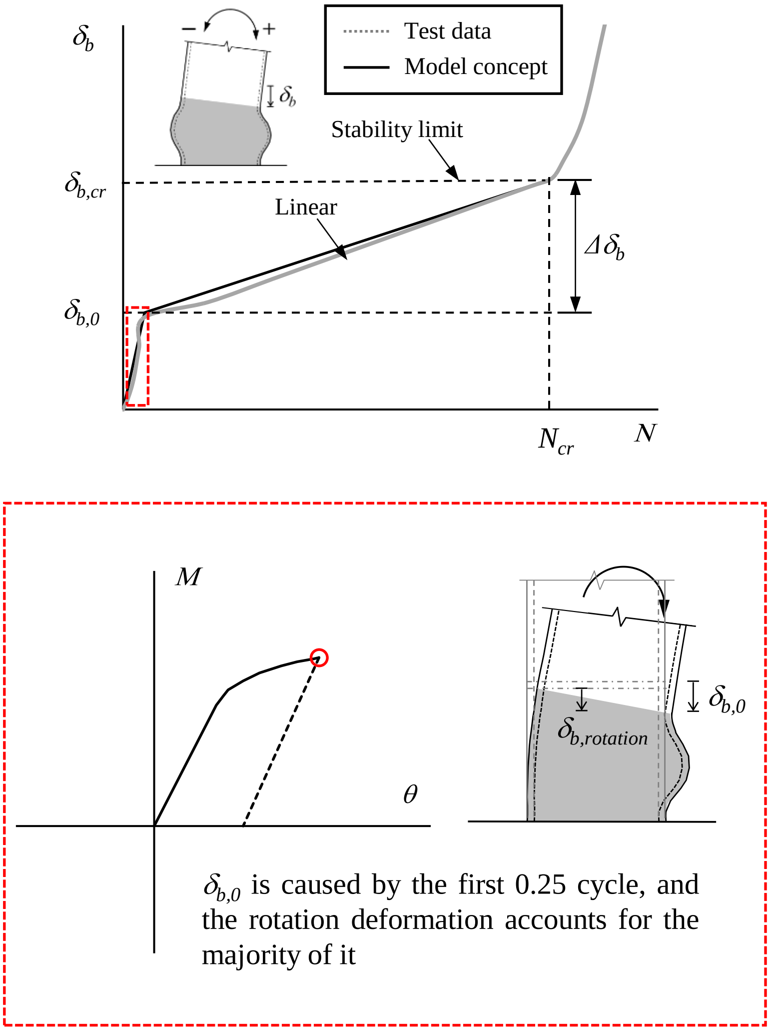

$\delta_{b,0}$ is caused by the first 0.25 cycle, and the rotation deformation accounts for the majority of it

Fig. 2-22 The simplified deformation progress of δ_b for specimens under cyclic loading.

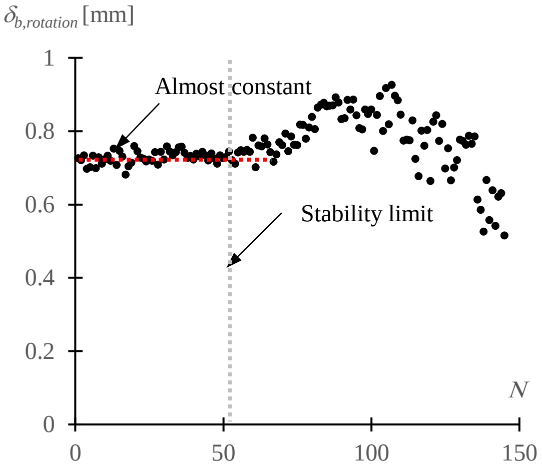

Fig. 2-23 Rotational deformation process in δ_b.

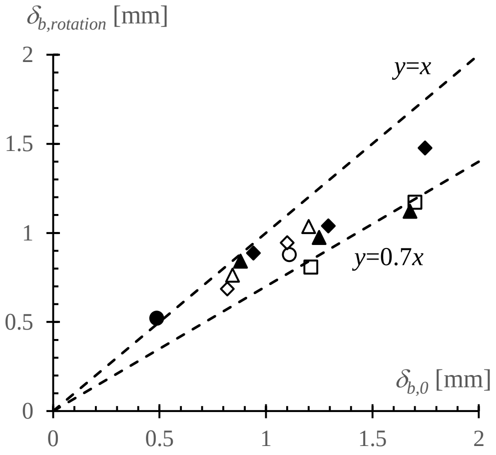

Fig. 2-24 Comparison between $\delta_{b,0}$ and $\delta_{b,rotation}$.

Table 2-4 Legends for the corresponding specimens

	B/t	P/P_y	α_e	L/B
●	29.2	0.3	1.33	4.9
○	29.2	0.15	1.15	4.9
▲	19.4	0.3	0.58	4.9
◇	33.3	0.2	1.39	4.3
□	22.2	0.35	0.81	4.3
■	22.2	0.2	0.68	4.3
◆	19.4	0.3	0.58	3
△	19.4	0.3	0.56	7

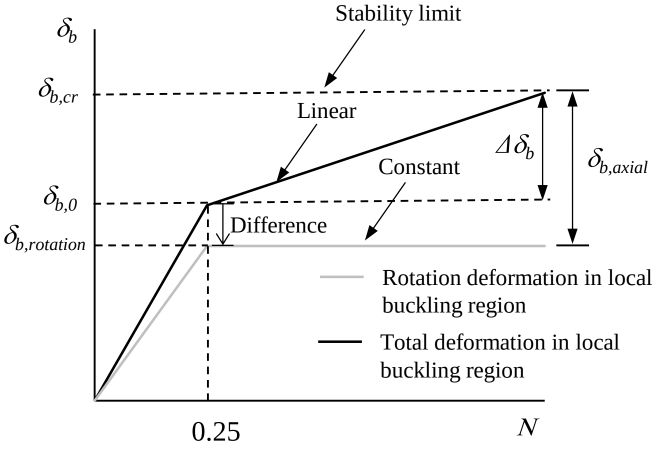

Fig. 2-25 Deformation progress of the rotational part in δ_b.

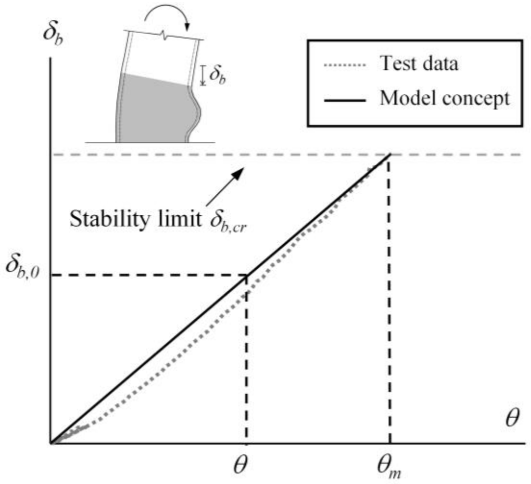

Fig. 2-26 Simplified deformation progress of δ_b prior to stability limit for a specimen under monotonic loading.

2.5.2 Prediction method for the $\delta_{b,cr}$

In this study, experiment for the specimens under monotonic loading were carried out to obtain their stability limit values. The stability limit values were calculated from the measurements made within the local buckling region. However, it is not practical to carry out such experiments for every column with different geometrical features or under different loading conditions. Therefore, a method to predict the stability limit value is needed for further practical use. Using this study's experimental data, such a method by considering geometrical features, loading conditions, and material properties was developed.

From the theoretical solution of the local buckling load for a plate under uniaxial compression within an elastic range [2-18], the standardized width-to-thickness ratio, α, was developed. σ_y is the yield stress, and E is Young's modulus. The detailed theoretical derivation process can be referred to Appendix 6.

$$\alpha = \frac{\sigma_y}{E}(B/t)^2 \tag{2-12}$$

In a previous study [2-14], the standardized width-to-thickness ratio, α, was used to evaluate the post-buckling and deterioration behavior of box steel columns under uniaxial load. A highly accurate stress-strain prediction model was also developed, which can be referred to Appendix 7. Yamada et al. [2-12][2-14] proposed an equivalent standardized width-to-thickness ratio, α_e, for members under a combination of axial force and bending moment. It was employed to consider the influence of the axial force ratio, as follows.

$$\alpha_e = \frac{1+k^2}{2}\frac{\sigma_y}{E}(B/t)^2 \tag{2-13}$$

where k is the ratio of the area of the compressive part of the web plate to the whole area of the web plate under plastic moment, and it can be expressed as

$$k = \begin{cases} 0.5 + P/P_y & P/P_y < 0.5 \\ 1 & P/P_y \geq 0.5 \end{cases} \tag{2-14}$$

In this study, α_e was also used to predict the value of $\delta_{b,cr}$. In order to ascertain the influence of different parameters on the stability limit value (i.e., width-to-thickness ratio, axial force ratio, and material property), a regression function that fitted (R^2=0.935) the experimental data for specimens under monotonic loading was obtained, as shown in Eq. (2-15) and Fig. 2-27. The predicted and experimental results for $\delta_{b,cr}$ are compared in Fig. 2-29, where the error of the prediction method can be controlled within ±15%. In the proposed relationship, the value of $\delta_{b,cr}$ is largely dependent on α_e, which considers the influence of width-to-thickness ratio and axial force ratio. When the value of α_e is small (compact section and/or low axial force ratio), the value of $\delta_{b,cr}$ tends to be large (high deformation capacity). The extended local buckling tends to happen to this type of specimens under cyclic loading (as Table A.13-1), which can explain the high deformation capacity in a view of local buckling mode.

$$\frac{\delta_{b,cr}}{B\varepsilon_y} = \frac{10.23}{\alpha_e} - 2.86 \qquad (0.56 \le \alpha_e \le 1.39) \tag{2-15}$$

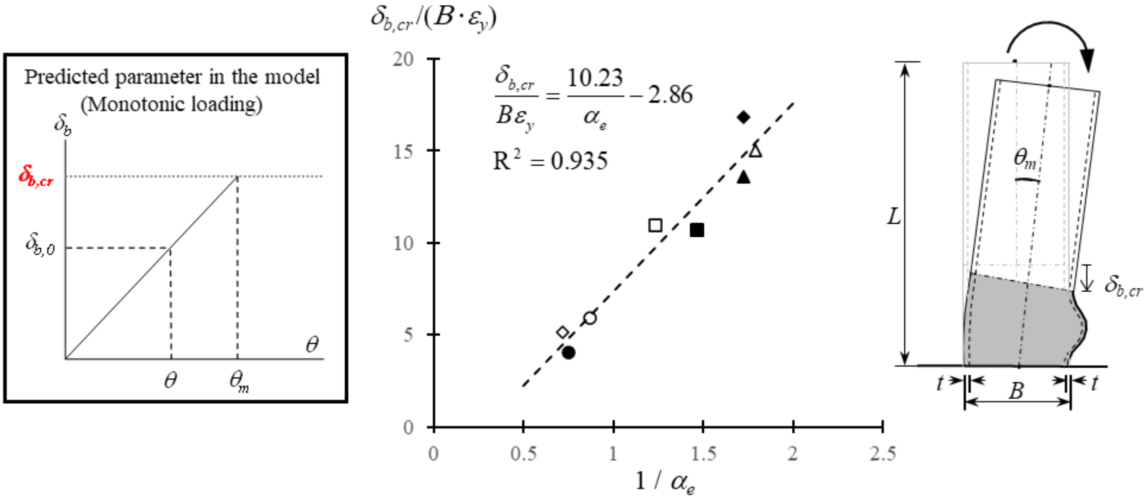

Fig. 2-27 The relationship between $(\delta_{b,cr}/B)/\varepsilon_y$ and $1/\alpha_e$.

A previous study [2-14] put forward an empirical function that predicted the strain when local buckling occurred for specimens under monotonic uniaxial loading, ε_u. The function was based on the relationship of $\varepsilon_u / \varepsilon_y$ and $1 / \alpha$, as shown in Appendix 7. Similar concept was also applied in Eq. (2-15) normalizing the stability limit ($\delta_{b,cr}$) with the width of column (B) multiplied by the yield strain (ε_y). The independent variable was $1 / \alpha_e$. $\delta_{b,cr}$ was calculated with the measurements from the measuring system (Fig. 2-7). The system was fixed at 1.25 column widths above the baseplate. Hence, the normalized $\delta_{b,cr}$ is equivalent to 1.25 times the average strain in the flange of the compressive side in the local buckling region, which was close to the role of ε_u in [2-14]. Based on the experiment data, the effective range of Eq. (2-15) was $0.56 \le \alpha_e \le 1.39$.

In Chapter 2.5.1, the rotation angle corresponding to the maximum strength for specimens under monotonic loading, θ_m, was an important parameter in the modeling concept as well. A method to predict the value of θ_m was also developed. It was an important parameter in Chapter 2.5.3. A previous study [2-15] also looked for a way to predict θ_m. In that study, the standardized width-to-thickness and slenderness ratios (α and λ, respectively) were employed as the independent variables. The detailed information of the model is shown in Appendix 8. Similar independent variables were chosen in this study (i.e., the equivalent standardized width-to-thickness ratio, α_e, and shear span ratio, L/B). The dependent variable θ_m was normalized with θ_p, where θ_p is the calculated elastic rotation angle which corresponds to the plastic moment without considering the effect of axial force. As shown in Fig. 2-28 and Eq. (2-16), a regression function from the variables discussed above fits the test data well ($R^2=0.95$). Whereas $\delta_{b,cr}$ is mainly determined by the behavior of local buckling region, θ_m is determined by both the local buckling region and elastic part. That explains the difference in the independent parameters in Eqs. (2-15) and (2-16). Based on the experimental data, the effective range of Eq. (2-16) was $0.56 \le \alpha_e \le 1.39$, $3 \le L/B \le 7$. The predicted and experimental results for θ_m are compared in Fig. 2-30, where the error of the prediction method can be controlled within ±15%.

$$\begin{gathered}\frac{\theta_m}{\theta_p} = -1.03\left(\alpha_e \cdot L/B\right) + 8.66 \\ (0.56 \le \alpha_e \le 1.39,\ 3 \le L/B \le 7)\end{gathered} \tag{2-16}$$

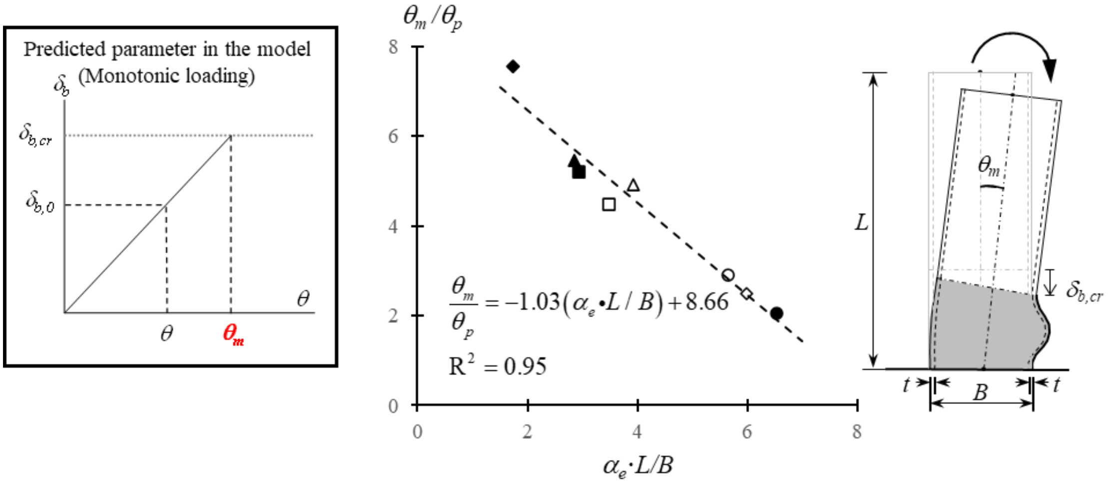

Fig. 2-28 The relationship between θ_m/θ_p and $\alpha_e \cdot L/B$.

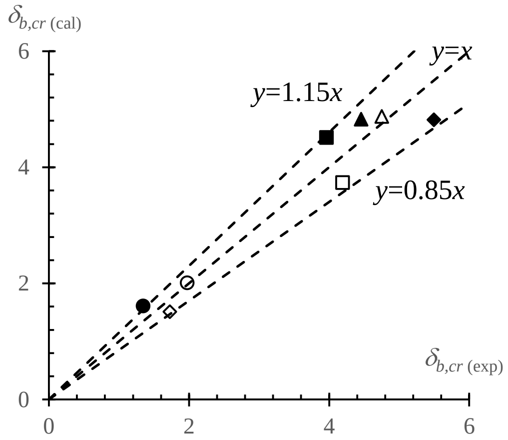

Fig. 2-29 Comparison between the calculated and experimental value of $\delta_{b,cr}$

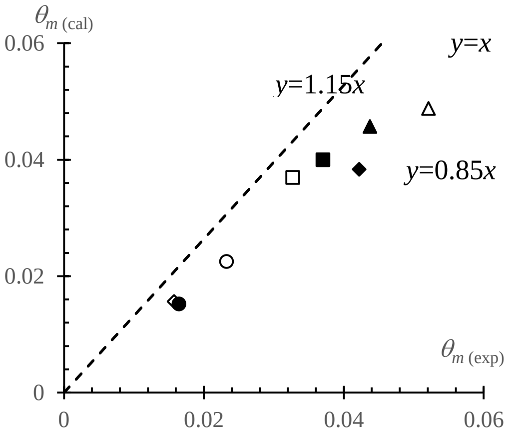

Fig. 2-30 Comparison between the calculated and experimental value of θ_m

2.5.3 Prediction of N_{cr} for specimens under cyclic constant amplitude loading

The method to predict the $\delta_{b,cr}$ has been illustrated in detail above. In order to prevent rapid strength deterioration in column components, it is important to know when δ_b reaches the stability limit point for SHS columns under cyclic loading. Towards this goal, the method to predict number of cycles to stability limit, N_{cr}, is studied as follows.

The relationship between the normalized increment rate of $\Delta\delta_b$ and normalized rotation angle was investigated based on the experimental results. The normalized rotation angle was employed as the independent variable in building up the relationship to only consider the influence of the loading amplitude and ignore that of other parameters. The loading history was considered to have an important influence on the progress of $\Delta\delta_b$. Therefore, the increment rate of $\Delta\delta_b$ was employed as the dependent variable and normalized with width of the section and yield strain to eliminate the minor influence of geometrical features and material property. The normalized increment rate of $\Delta\delta_b$ and normalized rotation angle can be represented as a power function. The function fits the data well (R^2=0.87), as shown in Fig. 2-31.

$$\frac{\dfrac{\Delta\delta_b}{N_{cr}}}{B\varepsilon_y} = 0.0079\left(\frac{\theta}{\theta_{pc}}\right)^{5.36} \tag{2-17}$$

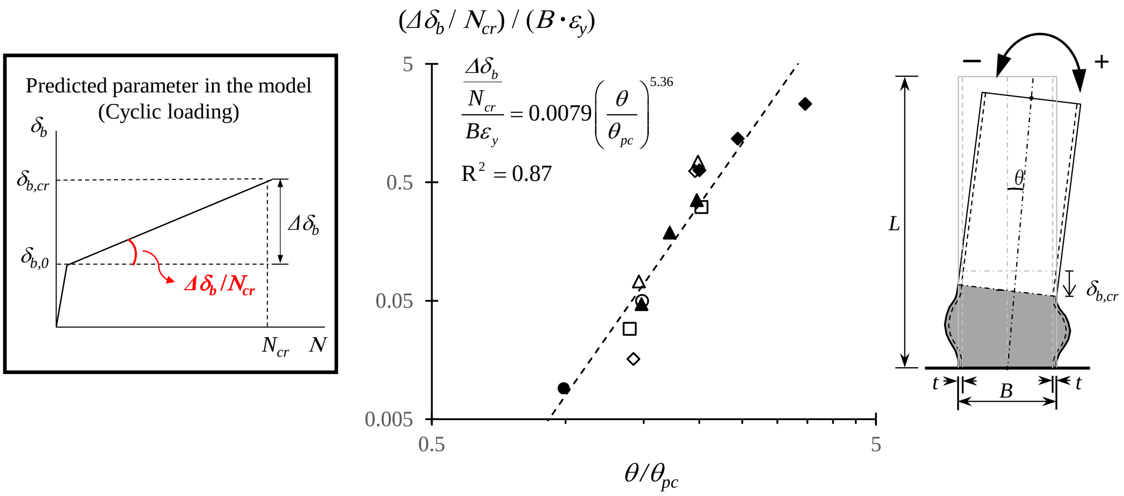

Fig. 2-31 The relationship between the normalized $\Delta\delta_b/N_{cr}$ and θ/θ_{pc}.

The relationship mentioned above was established based on the experimental data. However, when one specific loading amplitude is known, N_{cr} cannot be predicted without first knowing the value of $\Delta\delta_b$. Therefore, the method to predict $\Delta\delta_b$ is developed as follows to predict the value of N_{cr}.

In Chapter 2.5.2, the methods to predict the stability limit, $\delta_{b,cr}$, and the rotation angle corresponding to the maximum moment for specimens under monotonic loading, θ_m, were developed. Based on Fig. 2-26, the deformation in the flange of the local buckling region for the first cycle, $\delta_{b,0}$, for one specific rotation angle, θ, can be calculated by combining Eqs. (2-15) and (2-16), as follows.

$$\delta_{b,0} = \theta \cdot \frac{\delta_{b,cr}}{\theta_m} = \theta \cdot \frac{B\varepsilon_y}{\alpha_e \theta_p}\left[\frac{10.23 - 2.86\alpha_e}{-1.03\left(\alpha_e \cdot L/B\right) + 8.66}\right] \tag{2-18}$$

By predicting the stability limit $\delta_{b,cr}$, as described in Chapter 2.5.2, we can subsequently predict the value of $\Delta\delta_b$ for one specific rotation angle, as follows:

$$\begin{aligned} \Delta\delta_b &= \delta_{b,cr} - \delta_{b,0} \\ &= \frac{B\varepsilon_y}{\alpha_e}\left(10.23 - 2.86\alpha_e\right)\left[1 - \frac{\theta}{\theta_p}\left(\frac{1}{-1.03\left(\alpha_e \cdot L/B\right) + 8.66}\right)\right] \end{aligned} \tag{2-19}$$

Based on the expression above, the predicted and experimental results for $\Delta\delta_b$ are calculated and compared in Fig. 2-32, where the error of the prediction method can be controlled within ±30%.

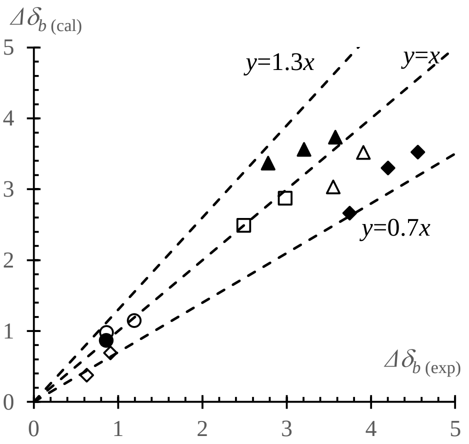

Fig. 2-32 Comparison between the calculated and experimental value of $\Delta\delta_b$

Once $\Delta\delta_b$ has been predicted, the N_{cr} for specimens under cyclic constant amplitude loading can be predicted and compared with the experimental values. Fig. 2-33 shows the prediction results that have acceptable errors. Hence, the validity of the prediction method for specimens under cyclic constant amplitude loading was proved.

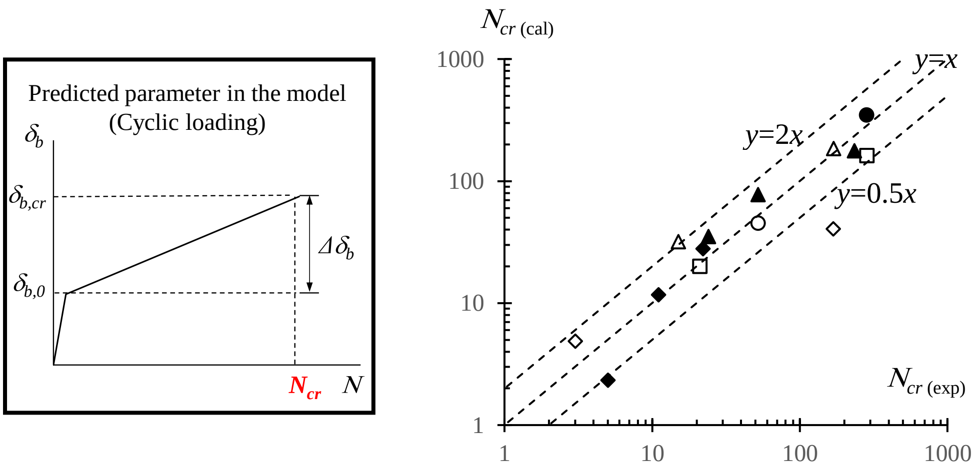

Fig. 2-33 Comparison between $N_{cr(exp)}$ and $N_{cr(cal)}$ for specimens under constant amplitude loading.

2.5.4 Prediction of N_{cr} for specimens under cyclic variable amplitude loading

The applicability of the method developed in Section 2.5.3 to specimens under variable amplitude loading, i.e., V_22.2_0.35_4.3, V_33.3_0.2_4.3 and Taft_22.2_0.2_4.3, was investigated by combining it with the rainflow method [2-16] and Miner's rule [2-17].

In this study, it is assumed that the damage accumulation is linear prior to reaching the stability limit and the damage index D is equivalent to the unity (1.0) upon reaching the stability limit. The damage is assumed to be caused by the axial part of δ_b (i.e., $\Delta\delta_b$), as mentioned in Chapter 2.5.1. Based on assumptions prior, the damage caused by the corresponding rotation ranges can be calculated with Eq. (2-20), where m_i is for the number of cycles for one specific loading amplitude-*i* (θ_i).

$$D = \sum_{i=1} \frac{m_i}{N_{cr(i)}} \tag{2-20}$$

The rotation ranges for specimens under variable amplitude loading can be obtained using the rainflow method. The number of cycles until the stability limit for the corresponding rotation angle, $N_{cr(i)}$, can be calculated using Eq. (2-17) after obtaining the corresponding values of $\Delta\delta_b$ with Eq. (2-19). The process to determine the number of cycles until the stability limit for specimens under variable amplitude is:

1. Predict the value of $\delta_{b,cr}$;

2. Use the rainflow method to get the rotation range, $2\theta_i$ (i=1, 2…, n);

3. Calculate the deformation of first cycle $\delta_{b,0(i)}$ (i=1, 2…, n) for the corresponding loading amplitude θ_i;

4. Calculate the total axial deformation increment $\Delta\delta_{b(i)}$ for each corresponding loading amplitude θ_i;

5. Calculate $N_{cr(i)}$ for corresponding loading amplitude θ_i;

6. Calculate the damage index with Eq. (2-20). When the damage index reaches 1.0, the specimen reaches the stability limit and N_{cr} can be determined.

The above process is also illustrated in Fig. 2-34.

With the process summarized above, the N_{cr} for the three specimens under variable amplitude loading were predicted. The predicted values were 7 (Specimen V_33.3_0.2_4.3), 32 (Specimen V_22.2_0.35_4.3), and 30 (Specimen Taft_22.2_0.2_4.3), respectively. The comparison between the predicted and experimental results were shown in Fig. 2-35. The predicted values closely aligned with the experimental results with only small errors, providing the validity of the prediction method.

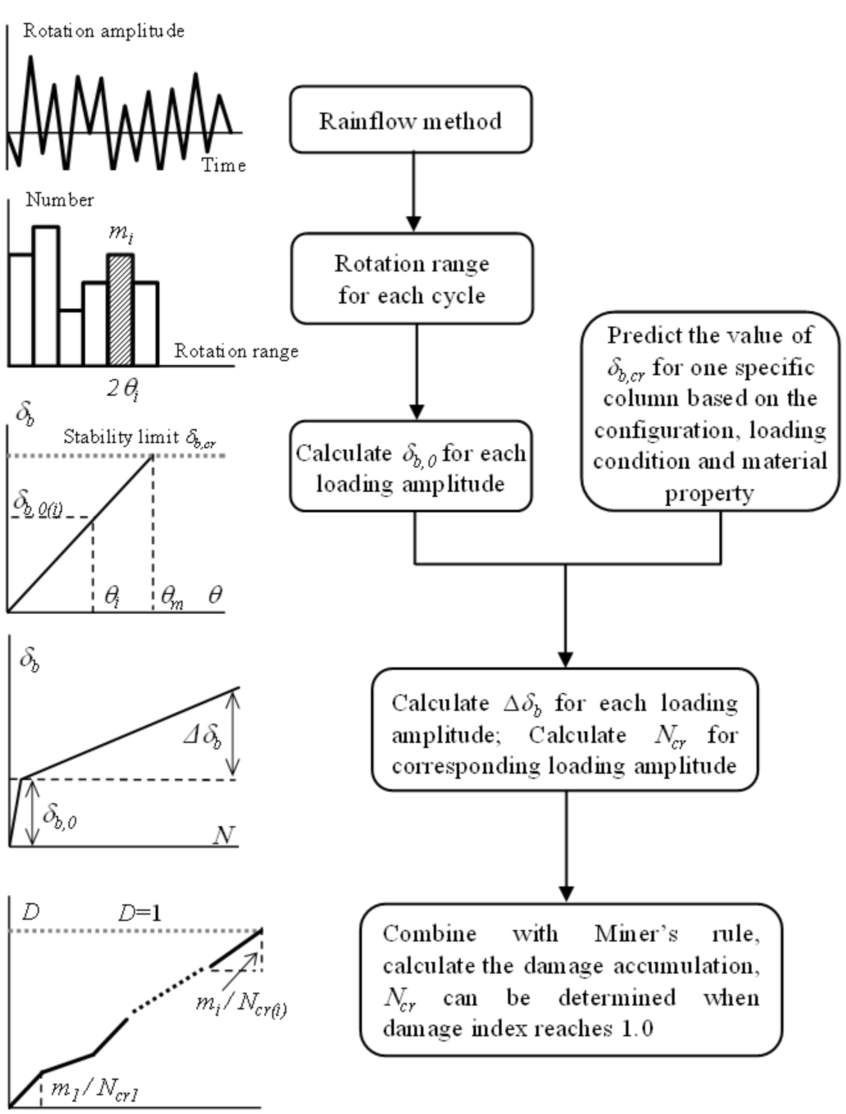

Fig. 2-34 Process to determine the stability limit for specimens under variable amplitude loading.

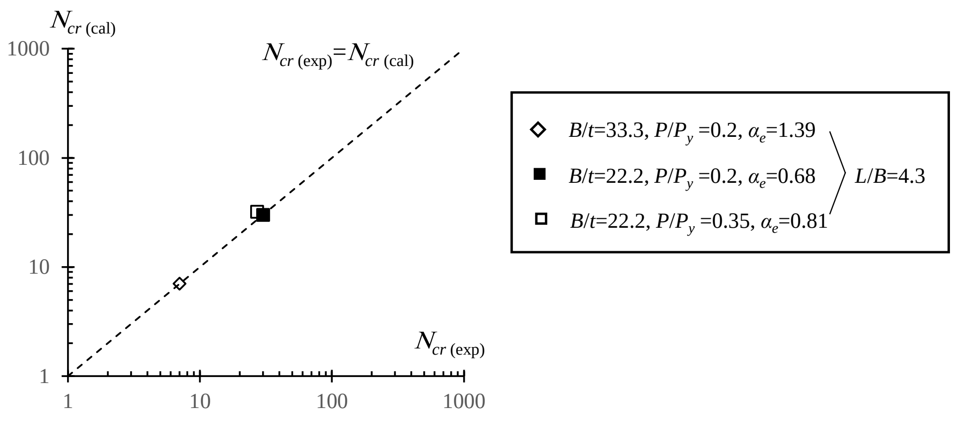

Fig. 2-35 Comparison between $N_{cr(\mathrm{exp})}$ and $N_{cr(\mathrm{cal})}$ for specimens under variable amplitude loading.

2.6 Structural analyses considering the stability limit

2.6.1 Introduction of the models and cases

In Chapter 2.5, the prediction methods have been proposed for the stability limit, and verified with the test data in the structural component level. Furthermore, it has been proved to be a good index to evaluate the damage level of the steel columns. In structural system level, many damage indices have been employed to evaluate the damage accumulation in the structural components, e.g., the energy dissipation capacity [2-21], the strength bearing capacity [2-2][2-22], ductility [2-23], and both energy dissipation and deformation capacity [2-24]. In this Chapter, the concept of the stability limit proposed in Chapter 2.4 and the prediction methods in Chapter 2.5 will be further applied to the inelastic structural analysis to evaluate the damage level of the structural system.

Infinite uniform plane model (steel frame) was used as the analytical model. The detailed information for the model (including the basic information for the columns and beams, hysteretic models, and etc.) can be referred in Appendices 2 and 9. The main parameters for the inelastic structural response analysis are the story of the steel frames (i.e., 3 and 6 floors), the width-to-thickness ratio of the steel columns (i.e., *B/t*=22.2, 25, and 29.4), different seismic inputs (as in Table 2-5) with different intensities (PGV=50 cm/s (design level), 75 cm/s and 100 cm/s). Steel frames with 3 and 6 floors can represent the common low- and middle-rise buildings to check the influence of the floor numbers. The width-to-thickness ratios for the columns are first designed as the FA rank according to the design recommendations in Japan [2-25]. The skeleton curve for the steel columns on the 1st floor are compared in Fig. 2-36. Furthermore, the application range of the proposed prediction method for the stability limit was also checked based on the designed axial force ratio of the columns, and the lower boundary of the width-to-thickness ratio can be determined. The seismic waves were selected with both relatively long-duration components and general earthquakes (El Centro and Taft). For the first four seismic waves, they were recorded seismic events in the history. For the last two seismic waves, they were created by the Japanese government considering the long-duration seismic components based on the previous seismic records, seismic intensities, propagation path and site characteristics [2-26]. In the following subchapters, “El Centro” is used for representing the 1940 Imperial Valley Earthquake recorded by El Centro, the NS component for simplification; Similarly, “Taft” stands for the 1952 Kern County Earthquake recorded by Taft, the EW component; “Hachinohe” stands for the 1968

Tokachi-Oki Earthquake recorded by Hachinohe, the EW component; “JMA Sendai” stands for the 2011 Tohoku Earthquake recorded by JMA Sendai, the NS component. All the records are scaled based on the PGV value to control their input energy (i.e., the intensities). The velocity response spectra of the records at the design level were shown in Fig. 2-37. The time histories of the seismic records can be refereed in Fig. 2-38. Both single and multiple seismic inputs were analyzed in the numerical model. The repeated excitations of the same input wave and same intensity were considered to simulate the multiple earthquake sequences to present the results simply and clearly. For models under multiple seismic inputs, the number of inputs were determined based on the damage they caused per cycle to reach the stability limit. The number of inputs was usually limited to around five, since a case including five strong seismic inputs in a short period can be considered extremely rare.

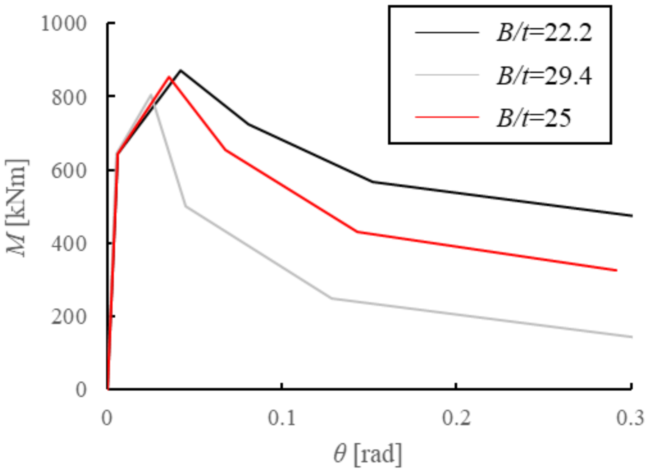

Fig. 2-36 Comparison of the skeleton curves for the columns with different width-to-thickness ratios on the 1st floor of the three-story models

The damage progress was checked for the columns on the 1st floor, because the great damage concentration was found in them [2-1], which can represent the dangerous case in all of the columns in the system. Besides the stability limit, another damage evaluation method used in the previous study [2-2] was also employed in this study for comparison. The concept of the damage evaluation method is briefly introduced as below. The penta-linear hysteretic model including the strength deterioration range was employed for the steel columns in this study (detailed information can be referred in Appendix 2). The skeleton curve used for the hysteretic model is shown as below (Fig. 2-39), where ${}_cM_u$ is the maximum strength, ${}_cM_{pc}$ is the plastic moment considering the axial force, ${}_cM_i$ is the bending moment at the i^{th} step. The damage index based on the strength was defined as:

If $\max\{|{}_cM_i|\} \geq {}_cM_{pc}$,

$$D_M = \frac{\max\{|{}_cM_i|\} - {}_cM_{pc}}{{}_cM_u - {}_cM_{pc}} \tag{2-21}$$

If $\max\{|{}_cM_i|\} < {}_cM_{pc}$,

$$D_M = 0 \tag{2-22}$$

During the inelastic structural response analysis, when the absolute value of the bending moment in each step is smaller than ${}_cM_{pc}$, the column is considered to be in the elastic range, and there is no damage accumulation. When the D_M reaches 1, it is considered already reaching the onset of the strength deterioration. If the negative instant stiffness is observed, the deterioration process starts. During the analyses, both the D obtained from the stability limit and the D_M from the current evaluation method are calculated. The analytical results from each model and primary findings are summarized and discussed in the following subchapters.

Table 2-5 Ground motion records used in the analyses

No.	Earthquake	M_w	Seismic record	Component	PGA (m/s^2)	PGV (m/s)
1	1940 Imperial Valley	6.95	El Centro	NS	3.42	0.38
2	1952 Kern County	7.36	Taft	EW	1.76	0.18
3	1968 Tokachi-Oki	8.2	Hachinohe	EW	1.81	0.37
4	2011 Tohoku	9	JMA Sendai	NS	4.10	0.54
5	Artificial: CH1	8.9	/	/	2.65	0.59
6	Artificial: OS1	8.9	/	/	2.63	0.47

Notes: PGA: peak ground acceleration; PGV: peak ground velocity; Artificial: CH1: The artificial wave for area CH1 in Chukyo circle, intended for the Minato ku in Nagoya; Artificial: OS: The artificial wave for area OS1 in Osaka circle, intended for the Konohana ku in Osaka.

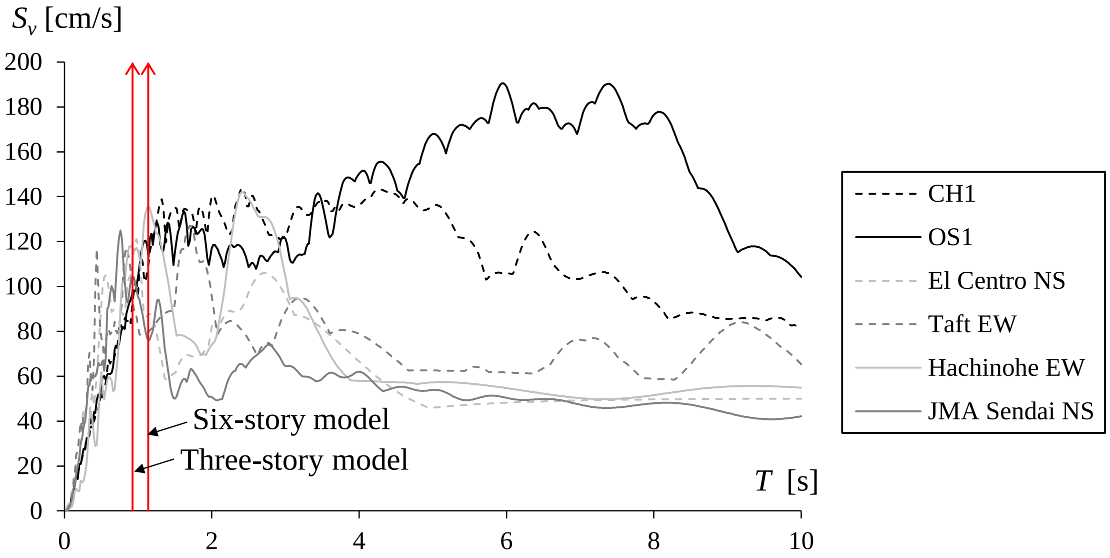

Fig. 2-37 Velocity response spectra of the input ground motion (Damping ratio 5%)

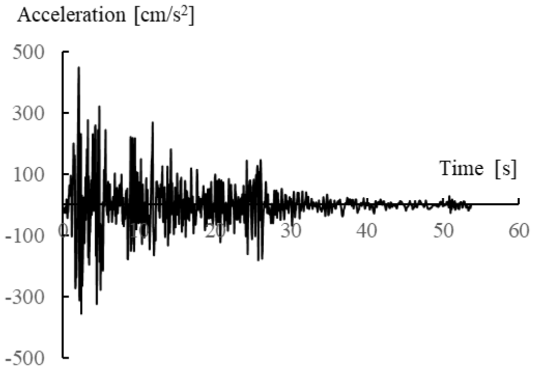

(a) 1940 Imperial Valley, El Centro NS

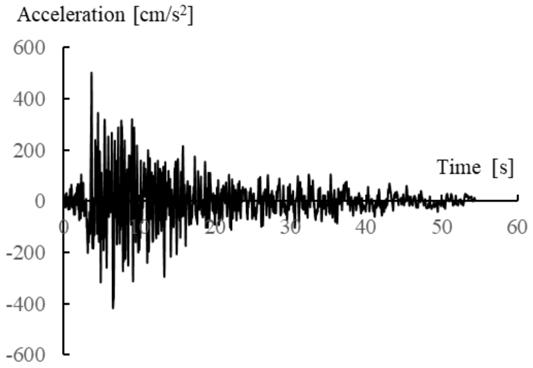

(b) 1952 Kern County, Taft EW

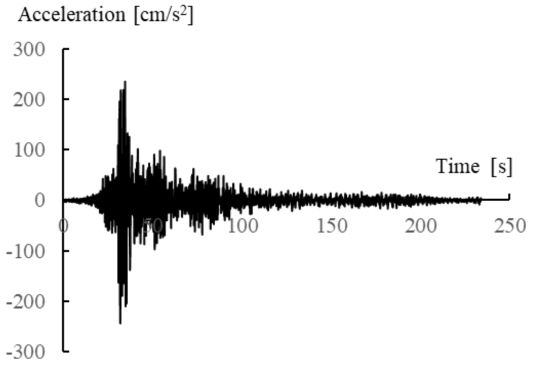

(c) 1968 Tokachi-Oki, Hachinohe EW

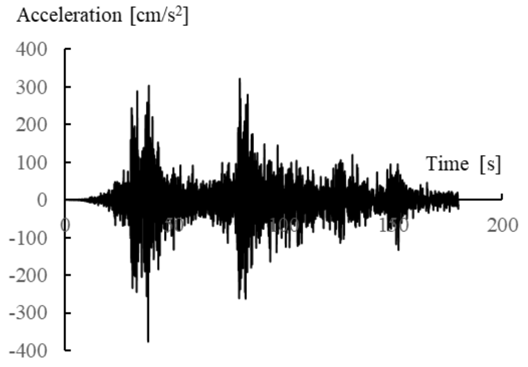

(d) 2011 Tohoku, JMA Sendai, NS

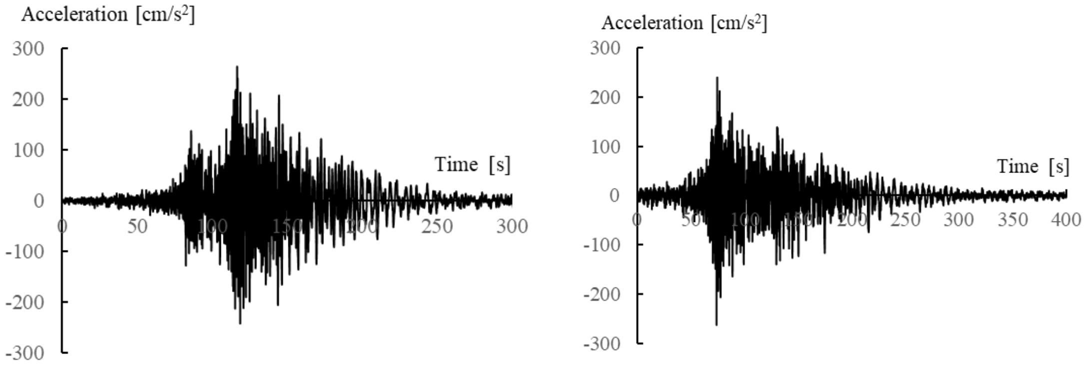

(e) Artificial: CH1 (f) Artificial: OS1

Fig. 2-38 Earthquake acceleration histories of the analyses

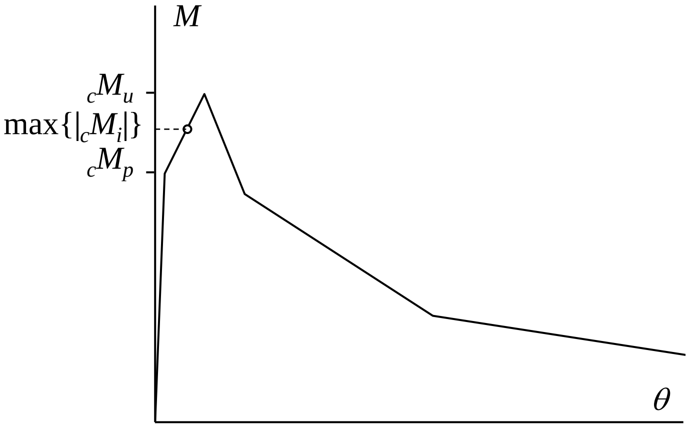

Fig. 2-39 The definition of damage for the columns based on skeleton curve

2.6.2 Analytical results of the 3-story model (*B/t*=29.4 for columns)

The analytical results for the 3-story model (*B/t*=29.4 for columns) are summarized in this Chapter. The damage progress in the columns on the first floor is mainly focused on.

Firstly, the model under single seismic excitation was investigated. The cases with PGV=50cm/s (design level), PGV=75cm/s, and PGV=100cm/s were researched and the analytical results were summarized in Table 2-6. It should be noted that "*D* in the bottoms of columns in 1st story" stands for the value of *D* when reaching the stability limit, and "D_M in 1st story" is the corresponding D_M at the same time step. If the stability limit was not reached, the two columns stood for the values in the last time step. And the same criterion is applied to the rest of the tables, which will not be repeated in the following subchapters.

For the cases with PGV=50cm/s, the limit status (D=1 or D_M=1) was not reached for the model under JMA Sendai, El Centro and Taft. The damage progress (both D and D_M) in the columns on the first floor is plotted in Fig. 2-40. For the cases with PGV=75cm/s, all of the models already reached the limit status and collapse even happened in some cases (i.e., Hachinohe, Artificial wave: CH1, and Artificial wave: OS1). It should be noted that “collapse” represents the frame already loses the horizontal force resistance, and it is one final status of the analytical results. The damage progress in the columns on the first floor is plotted Fig. 2-41 as well. For the cases with PGV=100cm/s, collapse happened in all of the models. The damage progress in the columns on the first floor is plotted as Fig. 2-42.

Next, analyses for the model under multiple seismic excitations were further carried out on the cases with PGV=50cm/s that did not reach the limit status in Table 2-6. The analytical results were summarized in Table 2-7. The damage progress for the analytical model under multiple seismic inputs are shown in Fig. 2-43.

The time when the limit status is reached is the main concentration of this study, and they are summarized in Table 2-7. Based on the analytical results, the limit status was first reached based on the previous damage evaluation method [2-2]. For most of the cases, the limit status was reached basically at the same time by using the concept of the stability limit. For the 3-story model (B/t=29.4 for columns), the two damage evaluation methods can give similar predictions, which can prove the applicability of the stability limit concept. Furthermore, the limit status is not dependent on the earthquake type for this model.

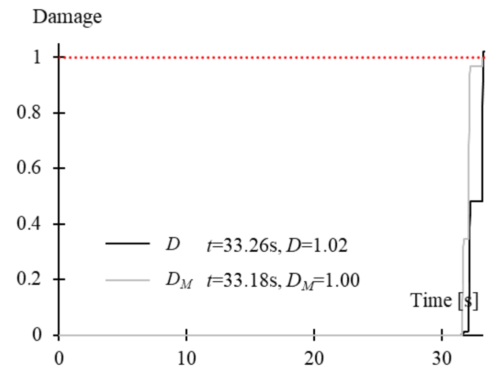

(a) Hachinohe

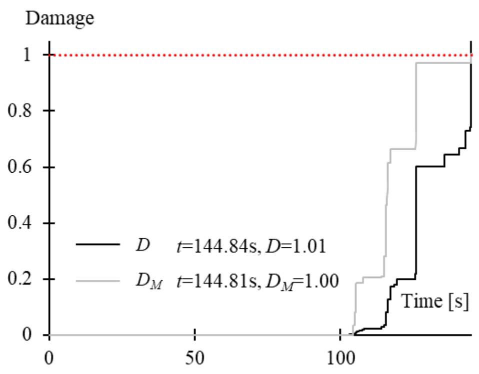

(b) Artificial wave (CH1)

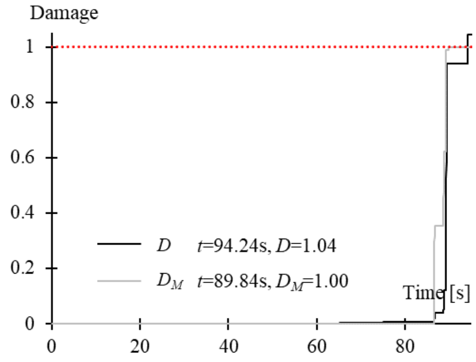

(c) Artificial wave (OS1)

Fig. 2-40 Damage evolution in the columns (in 1st floor) under single seismic excitation (PGV=50cm/s)

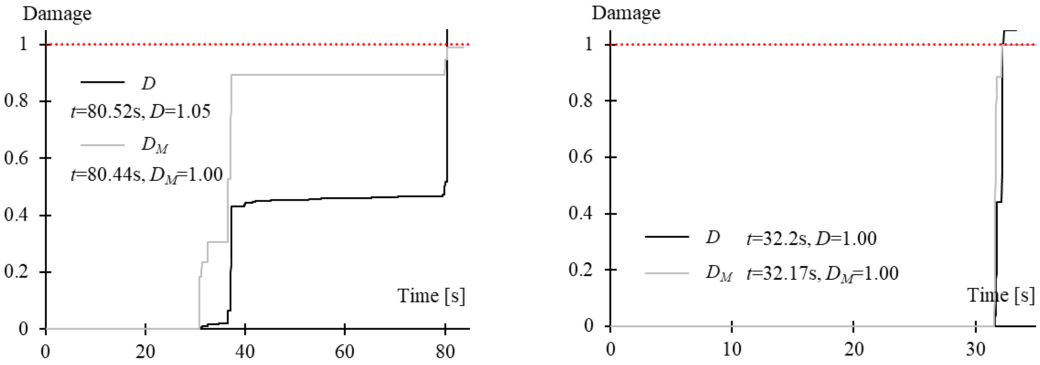

(a) JMA Sendai (b) Hachinohe

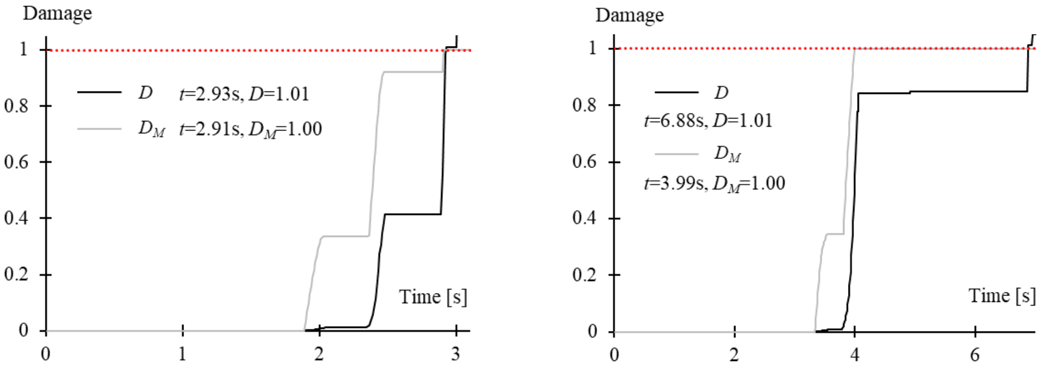

(c) El Centro (d) Taft

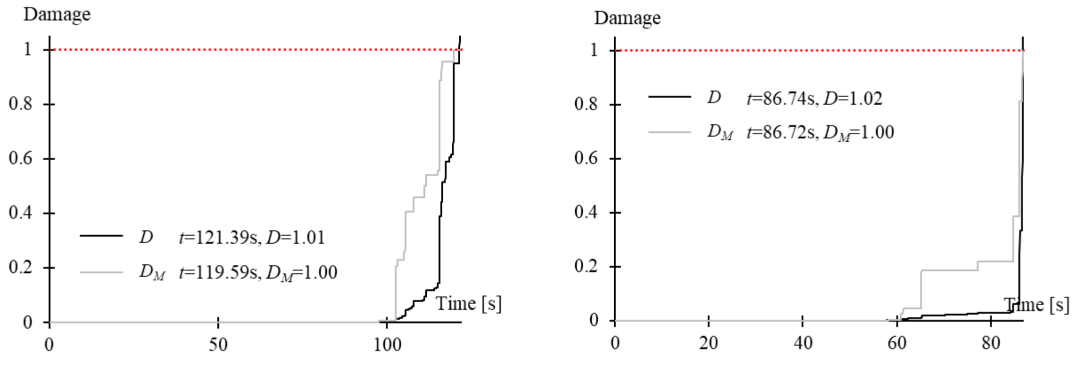

(e) Artificial wave (CH1)

(f) Artificial wave (OS1)

Fig. 2-41 Damage evolution in the columns (in 1st floor) under single seismic excitation (PGV=75cm/s)

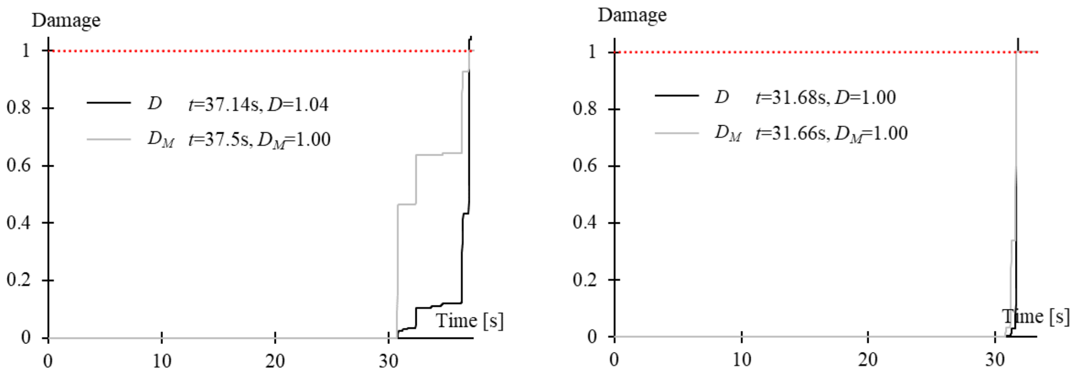

(a) JMA Sendai

(b) Hachinohe

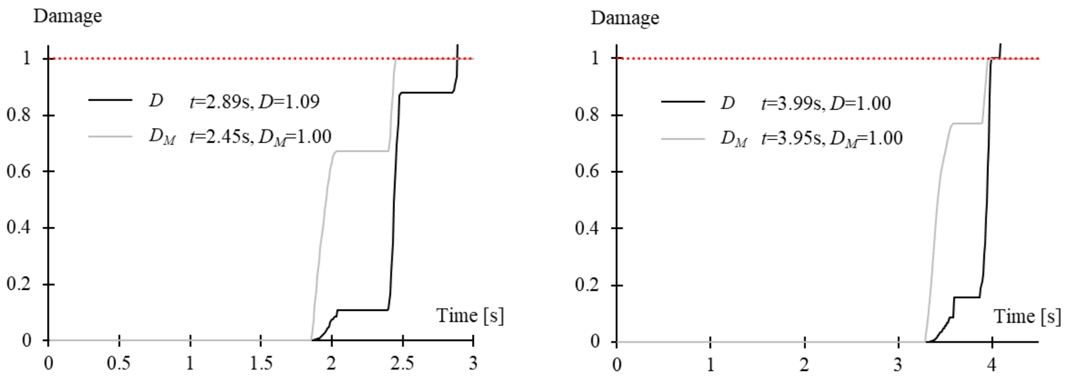

(c) El Centro

(d) Taft

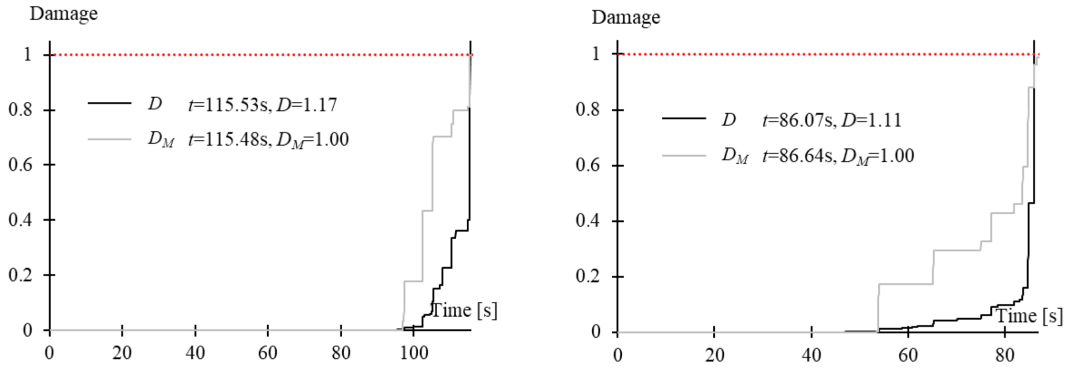

(e) Artificial wave (CH1)

(f) Artificial wave (OS1)

Fig. 2-42 Damage evolution in the columns (in 1st floor) under single seismic excitation (PGV=100cm/s)

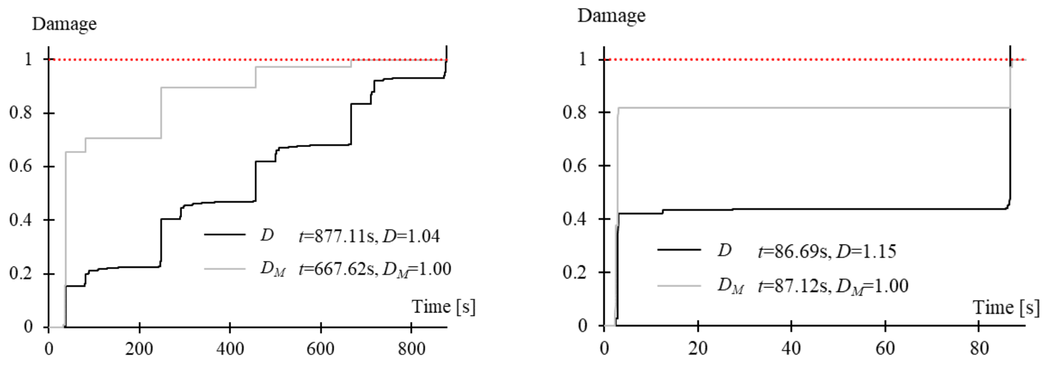

(a) JMA Sendai

(b) El Centro

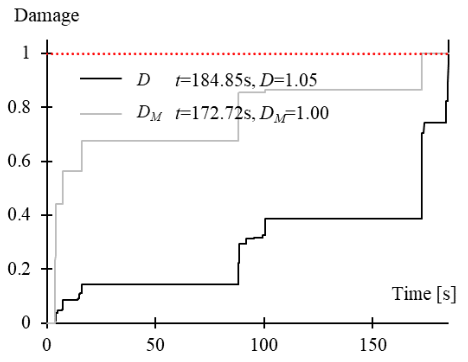

(c) Taft

Fig. 2-43 Damage evolution in the columns (in 1st floor) under multiple seismic excitations (PGV=50cm/s)

Table 2-6 Summary of the analytical results for models subjected to single seismic wave (3-story model, B/t=29.4 for columns)

Seismic wave	PGV [cm/s]	Scale factor	Time reaching the stability limit (Total time)	D in the bottoms of columns in 1st story	D_M in 1st story	D=1 or D_M=1 is first reached	Notes
JMA Sendai	50	0.919	na	0.22	0.71	na	The limit status was not reached
	75	1.378	80.52s (210s)	1.05	1.00	D_M	D_M=1 was reached at 80.44s
	100	1.838	37.14s (83.38s)	1.04	0.98	D	Collapse
Hachinohe	50	1.348	33.26s (264s)	1.02	1.00	D_M	D_M=1 was reached at 33.18s
	75	2.022	32.2s (40.9s)	1.00	1.00	D_M	Collapse
	100	2.696	31.68s (36.28s)	1.00	1.00	D_M	Collapse
El Centro	50	1.311	na	0.44	0.82	na	The limit status was not reached
	75	1.967	2.93s (83.74s)	1.01	1.00	D_M	D_M=1 was reached at 2.91s
	100	2.623	2.89s (33.88s)	1.09	1.00	D_M	Collapse
Taft	50	2.850	na	0.14	0.68	na	The limit status was not reached
	75	4.275	6.88s (84.38s)	1.01	1.00	D_M	D_M=1 was reached at 3.99s
	100	5.700	3.99s (10.50s)	1.00	1.00	D_M	Collapse
Artificial waves (CH1)	50	0.844	144.84s (330s)	1.01	1.00	D_M	D_M=1 was reached at 144.81s
	75	1.266	121.39s (141.67s)	1.01	1.00	D_M	Collapse
	100	1.688	115.53s (125s)	1.17	1.00	D_M	Collapse
Artificial waves (OS1)	50	1.073	94.24s (430s)	1.04	1.00	D_M	D_M=1 was reached at 89.84s
	75	1.609	86.74s (104.46s)	1.02	1.00	D_M	Collapse
	100	2.146	86.07s (91.47s)	1.11	0.96	D	Collapse

Table 2-7 Summary of the analytical results for models subjected to multiple seismic waves (3-story model, B/t=29.4 for columns)

Seismic wave	PGV [cm/s]	Scale factor	Number of input waves	Time reaching the stability limit (Total time)	D in the bottoms of columns in 1st story	D_M in 1st story	D=1 or D_M=1 is first reached	Notes
JMA Sendai	50	0.919	5	877.11s (1050s)	1.04	1.00	D_M	D_M=1 was reached at 667.62s
El Centro	50	1.311	2	86.69s (167.48s)	1.15	1.00	D	D_M=1 was reached at 87.12s
Taft	50	2.850	3	184.85s (253.14s)	1.05	1.00	D_M	D_M=1 was reached at 172.72s

2.6.3 Analytical results of the 6-story model (*B/t*=29.4 for columns)

The influence of the number of floors was investigated in this Chapter subsequently. Compared with the 3-story model in Chapter 2.6.2, not only the number of floors is different, but also the detailed information of the beams and columns, and the designed axial force ratio are different (refer to Appendix 2). Only the width-to-thickness ratios of the columns are the same.

Similarly, the model under single seismic excitation was first investigated. The cases with PGV=50cm/s (design level), PGV=75cm/s, and PGV=100cm/s were researched and the analytical results were summarized in Table 2-8. Compared with the 3-story model in Chapter 2.6.2, the damage caused by the single seismic excitation with PGV=50cm/s is relatively small. None of the cases with PGV=50cm/s (under single seismic excitation) reached the limit status (either D=1 or D_M=1). For the cases with larger PGV (i.e., PGV=75cm/s and 100cm/s), only limited cases reached the limit status (i.e., Hachinohe, Artificial wave: CH1, and Artificial wave: OS1). The damage process for the cases reaching the limit status was plotted in Fig. 2-44.

Next, analyses for the model under multiple seismic excitations were further carried out on the cases with PGV=75cm/s and 100cm/s that have not reached the limit status in Table 2-8. The cases with PGV=50cm/s (under multiple seismic excitations) were not carried out because the damage caused by singe seismic excitation (as in Table 2-8) was very small and the number of the cycles to the limit status can be large (extremely rare) for some specific cases (i.e., JMA Sendai, El Centro, and Taft). The damage progress for the analytical models under multiple seismic inputs are plotted in Fig. 2-45.

The time when the limit status was reached are summarized in Table 2-8 and Table 2-9. Based on the analytical results, the limit status (D=1) was first reached based on the concept of stability limit for analytical models under both single and multiple seismic inputs. For most of the cases (single seismic input), the limit status (D_M=1) can be reached after the stability limit in a short period of time. However, there are still some cases that only the stability limit was reached and the strength deterioration never happened (i.e., Hachinohe (PGV=75cm/s) and Artificial waves (OS1) (PGV=75cm/s)) for the analytical model under single seismic input. Furthermore, the same phenomenon (i.e., D=1 and D_M<1) can be observed in all the cases under multiple seismic inputs. These cases showed the conservative damage evaluation of the stability limit concept and the possibility of overestimation of the strength bearing capacity in the previous damage evaluation method [2-2] under long-duration earthquakes. Under the single seismic input, the stability limit will never be reached for the 6-story model under general earthquake (i.e., El Centro and Taft) regardless of the intensities. However, when the multiple earthquakes happen, the stability limit will always be reached regardless the type of the earthquakes.

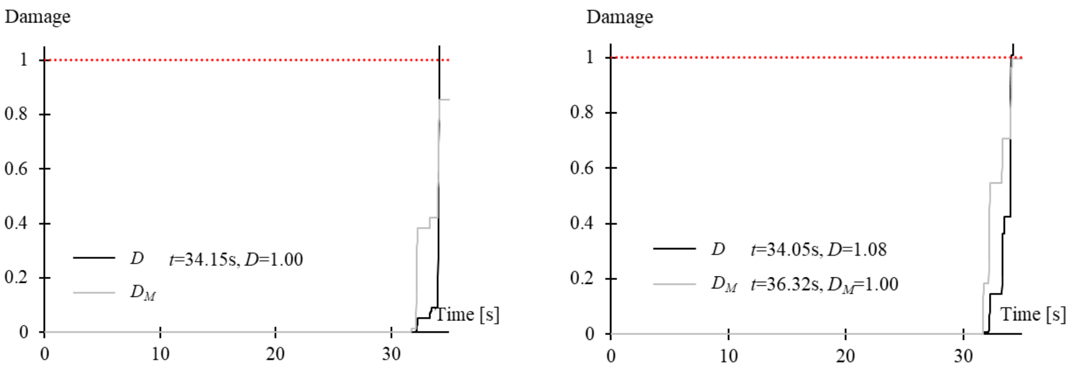

(a) Hachinohe, PGV=75cm/s (b) Hachinohe, PGV=100cm/s

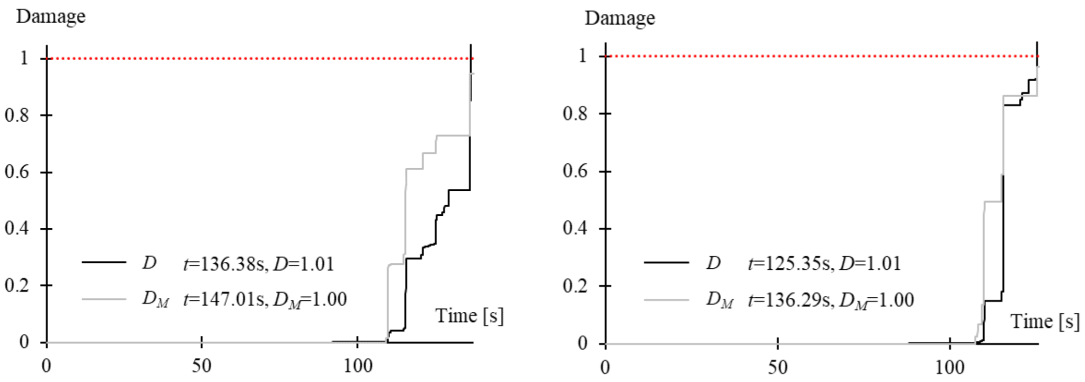

(c) Artificial wave (CH1), PGV=75cm/s (d) Artificial wave (CH1), PGV=100cm/s

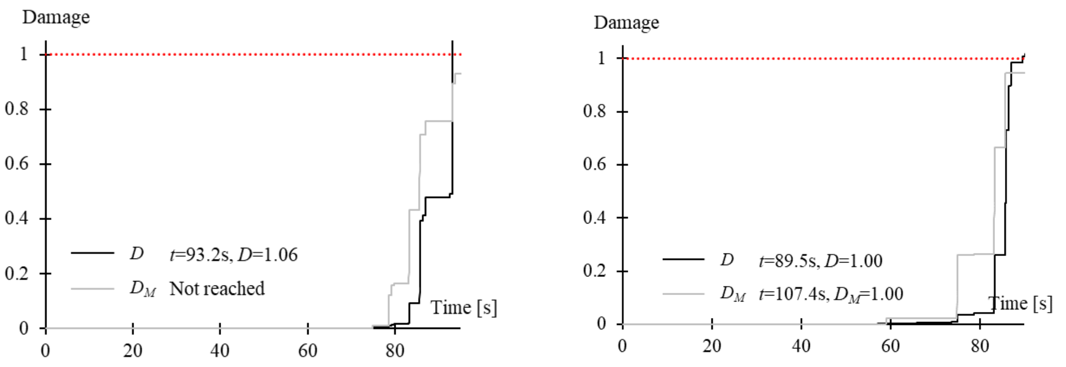

(e) Artificial wave (OS1), PGV=75cm/s (f) Artificial wave (OS1), PGV=100cm/s

Fig. 2-44 Damage evolution in the columns (in 1st floor) under single seismic excitation

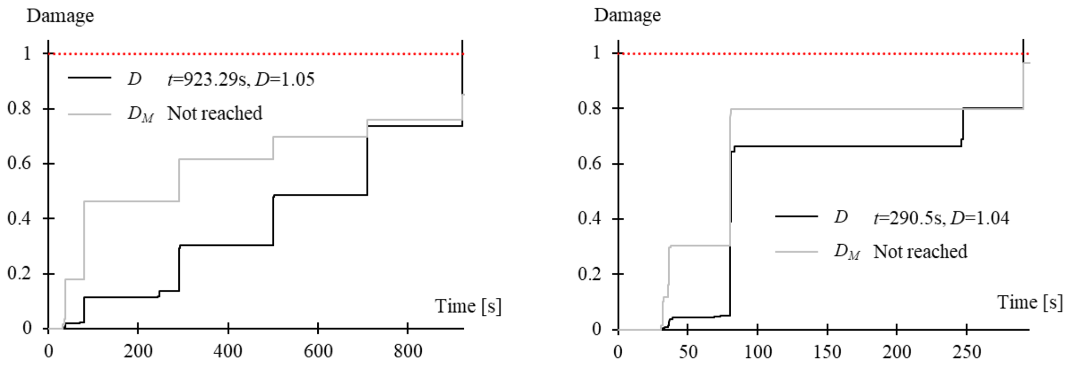

(a) JMA Sendai, PGV=75cm/s (b) JMA Sendai, PGV=100cm/s

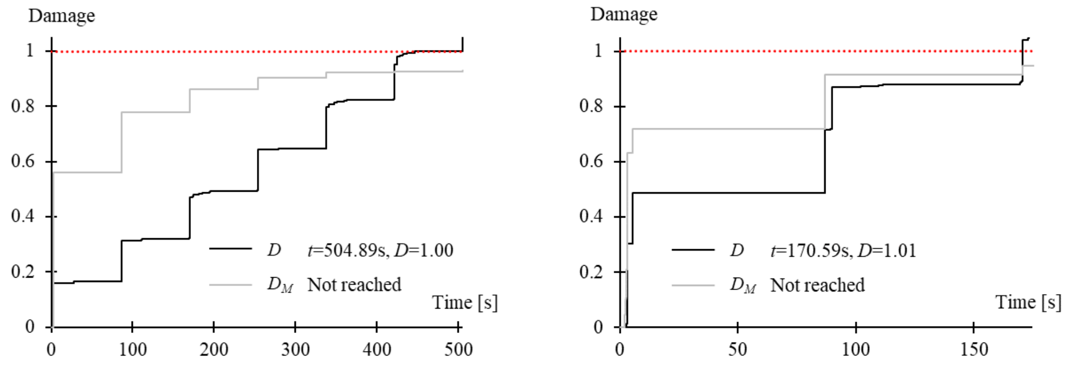

(c) El Centro, PGV=75cm/s (d) El Centro, PGV=100cm/s

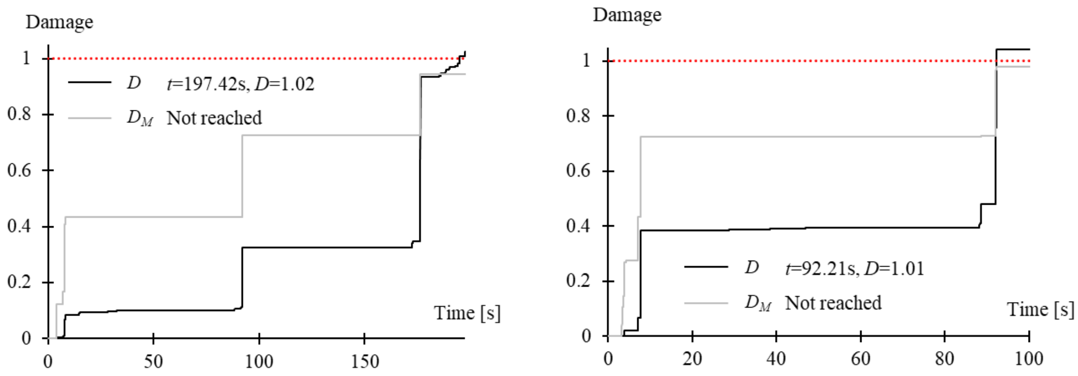

(e) Taft, PGV=75cm/s (f) Taft, PGV=100cm/s

Fig. 2-45 Damage evolution in the columns (in 1st floor) under multiple seismic excitations

Table 2-8 Summary of the analytical results for models subjected to single seismic wave (6-story model, B/t=29.4 for columns)

Seismic wave	PGV [cm/s]	Scale factor	Time reaching the stability limit (Total time)	D in the bottoms of columns in 1st story	D_M in 1st story	D=1 or D_M=1 is first reached	Notes
JMA Sendai	50	0.919	na	0.04	0.17	na	The limit status was not reached
	75	1.378	na	0.17	0.46	na	The limit status was not reached
	100	1.838	na	0.42	0.80	na	The limit status was not reached
Hachinohe	50	1.348	na	0.28	0.68	na	The limit status was not reached
	75	2.022	34.15s (264s)	1.00	0.82	D	D_M=1 was not reached
	100	2.696	34.05s (264s)	1.08	0.85	D	D_M=1 was reached at 36.32s
El Centro	50	1.311	na	0.03	0.32	na	The limit status was not reached
	75	1.967	na	0.11	0.56	na	The limit status was not reached
	100	2.623	na	0.57	0.72	na	The limit status was not reached
Taft	50	2.850	na	0.01	0.13	na	The limit status was not reached
	75	4.275	na	0.10	0.43	na	The limit status was not reached
	100	5.700	na	0.39	0.73	na	The limit status was not reached
Artificial waves (CH1)	50	0.844	na	0.59	0.81	na	The limit status was not reached
	75	1.266	136.38s (330s)	1.01	0.95	D	D_M=1 was reached at 147.01s
	100	1.688	125.35s (330s)	1.01	0.88	D	D_M=1 was reached at 136.29s
Artificial waves (OS1)	50	1.073	na	0.36	0.64	na	The limit status was not reached
	75	1.609	93.2s (430s)	1.06	0.87	D	D_M=1 was not reached
	100	2.146	89.5s (430s)	1.00	0.94	D	D_M=1 was reached at 107.4s

Table 2-9 Summary of the analytical results for models subjected to multiple seismic waves (6-story model, B/t=29.4 for columns)

Seismic wave	PGV [cm/s]	Scale factor	Number of input waves	Time reaching the stability limit (Total time)	D in the bottoms of columns in 1st story	D_M in 1st story	D=1 or D_M=1 is first reached	Notes
JMA Sendai	75	1.378	6	923.29s (1260s)	1.05	0.85	D	D_M=1 was not reached
	100	1.838	2	290.5s (420s)	1.04	0.96	D	D_M=1 was not reached
El Centro	75	1.967	7	504.89s (586.18s)	1.00	0.93	D	D_M=1 was not reached
	100	2.623	3	170.59s (251.22s)	1.01	0.94	D	D_M=1 was not reached
Taft	75	4.275	3	197.42s (253.14s)	1.02	0.95	D	D_M=1 was not reached
	100	5.700	2	92.21s (168.76s)	1.01	0.98	D	D_M=1 was not reached

2.6.4 Analytical results of the 3-story model (*B/t*=22.2 for columns)

In Chapter 2.6.3, the damage evaluation method [2-2] based on the current hysteretic model [2-10] of the columns can overestimate their bearing capacity in some cases, which can be dangerous in the inelastic structural response analysis. In 3-story model (*B/t*=29.4 for columns), D=1 and D_M=1 was found to occur basically at the same time. If the width-to-thickness ratio is reduced (SHS column with a higher strength bearing capacity), whether similar cases to 6-story model (*B/t*=29.4 for columns) can be observed is still unknown. In the following two subchapters, the influence of the width-to-thickness ratio of the columns on the damage evolution was further investigated.

The only difference between the model in this Chapter and that in 3-story model (*B/t*=29.4 for columns) is the thickness of the columns, which changes the width-to-thickness ratio. The same seismic loading cases as those in 3-story model (*B/t*=29.4 for columns) were carried out.

For the analytical model under single seismic excitation (PGV=50cm/s), none of the cases reached the limit status. Compared with the 3 cases reaching the limit status in 3-story model (*B/t*=29.4 for columns), the decrease in the width-to-thickness ratio of the columns improved the seismic performance of the system a lot. For the analytical under single seismic excitation (PGV=75cm/s), the time when the stability limit appeared was delayed compared with the results in Table 2-6. And no collapse happens in these cases. For all the cases (PGV=75cm/s), the stability limit (D=1) was first reached, and D_M=1 was not reached, which was totally different from the results in 3-story model (*B/t*=29.4 for columns). For the cases with PGV=100cm/s, collapse happened in only 1 case (i.e., Artificial wave OS1). Some of the cases only reached the stability limit, while the others reached both limit status (the stability limit was always first reached).

Based on the results in Table 2-10, some of the cases were carried out as multiple seismic excitations (PGV=50cm/s), while the others were carried out as multiple seismic excitations (PGV=75cm/s). Because the number of the seismic inputs can be large for some cases (i.e., JMA Sendai, El Centro and Taft) compared with those in Table 2-7 (within 5 seismic inputs), which is considered as impractical. The cases subjected to the multiple seismic waves are summarized in Table 2-11. For the analytical model under seismic excitations (PGV=50cm/s or 75cm/s), the number of seismic inputs to reach the stability limit was increased, i.e., the structure becomes more durable with the smaller width-to-thickness ratio. Similar to the cases in the 6-story model, even though the stability limit was reached, $D_M=1$ was not reached for all of the cases. For the model with relatively small width-to-thickness ratio, the damage evaluation method based on the current hysteretic model of the columns can also overestimate their bearing capacities under the long-duration seismic loadings, which is a rather dangerous case.

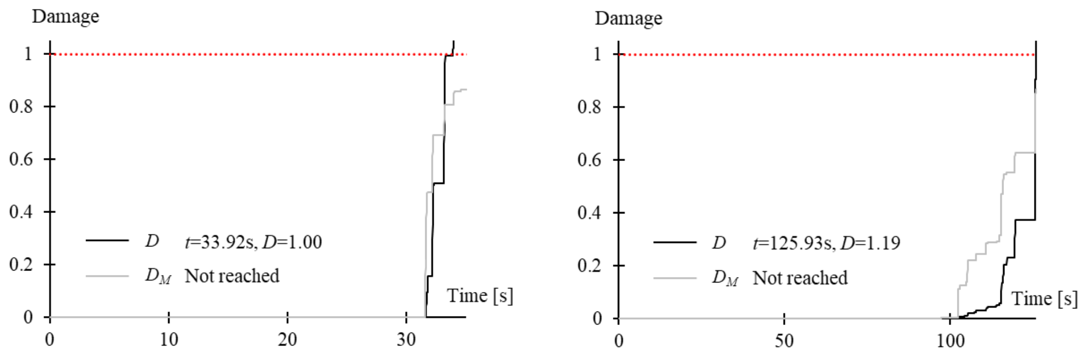

(a) Hachinohe, PGV=75cm/s

(b) Artificial wave (CH1), PGV=75cm/s

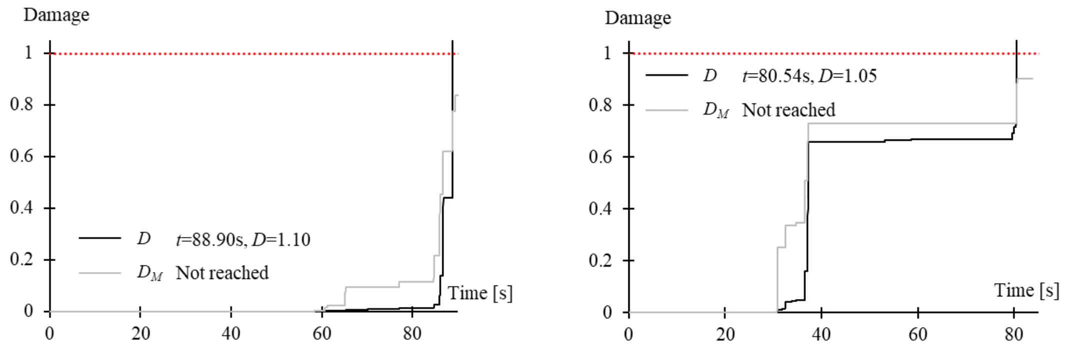

(c) Artificial wave (OS1), PGV=75cm/s

(d) JMA Sendai, PGV=100cm/s

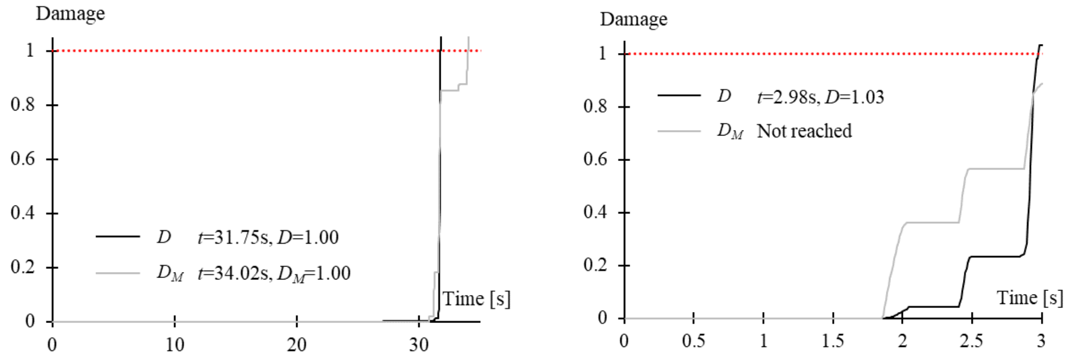

(e) Hachinohe, PGV=100cm/s

(f) El Centro, PGV=100cm/s

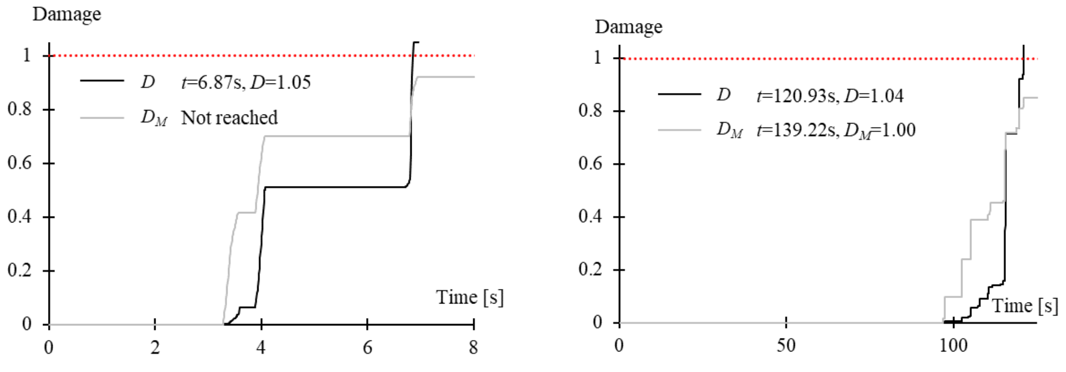

(g) Taft, PGV=100cm/s

(h) Artificial wave (CH1), PGV=100cm/s

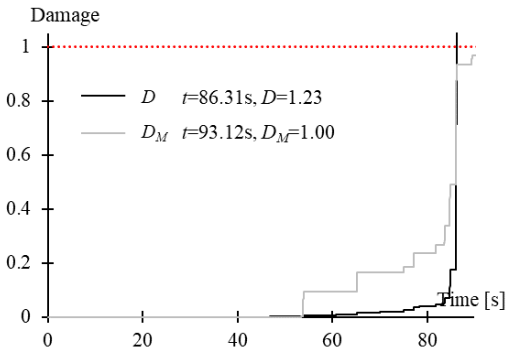

(i) Artificial wave (OS1), PGV=100cm/s

Fig. 2-46 Damage evolution in the columns (in 1st floor) under single seismic excitation

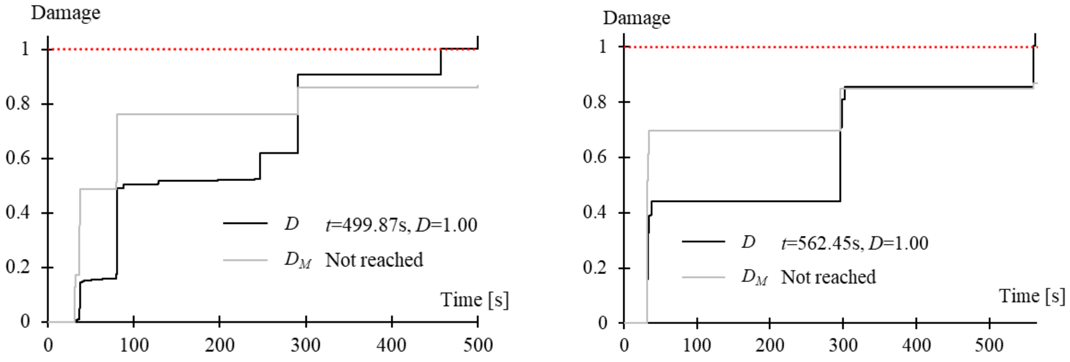

(a) JMA Sendai, PGV=75cm/s

(b) Hachinohe, PGV=50cm/s

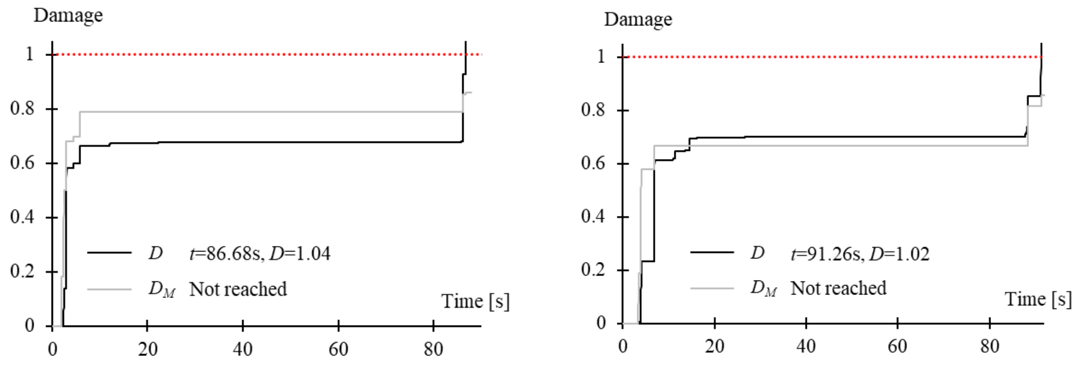

(c) El Centro, PGV=75cm/s (d) Taft, PGV=75cm/s

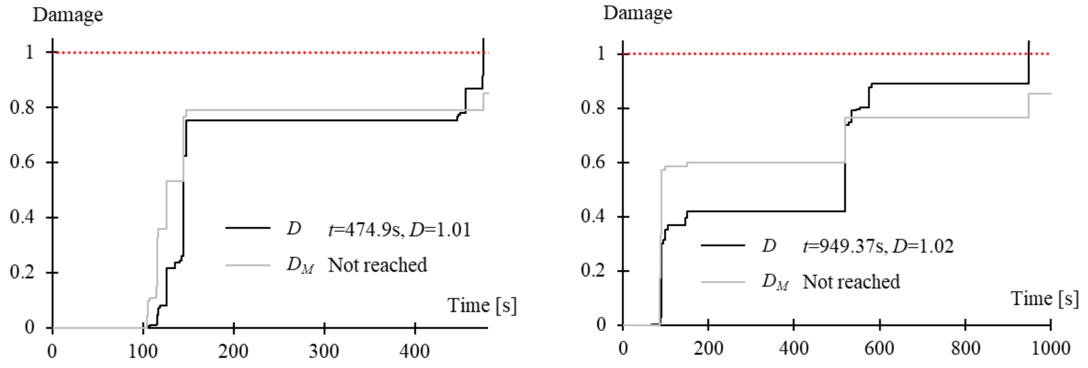

(e) Artificial wave (CH1), PGV=50cm/s (f) Artificial wave (OS1), PGV=50cm/s

Fig. 2-47 Damage evolution in the columns (in 1st floor) under multiple seismic excitations

Table 2-10 Summary of the analytical results for models subjected to single seismic wave (3-story model, B/t=22.2 for columns)

Seismic wave	PGV [cm/s]	Scale factor	Time reaching the stability limit (Total time)	D in the bottoms of columns in 1st story	D_M in 1st story	D=1 or D_M=1 is first reached	Notes
JMA Sendai	50	0.919	na	0.08	0.39	na	The limit status was not reached
	75	1.378	na	0.52	0.76	na	The limit status was not reached
	100	1.838	80.54s (210s)	1.05	0.86	D	D_M=1 was not reached
Hachinohe	50	1.348	na	0.43	0.70	na	The limit status was not reached
	75	2.022	33.92s (264s)	1.00	0.69	D	D_M=1 was not reached
	100	2.696	31.75s (264s)	1.00	0.80	D	D_M=1 was reached at 34.02s
El Centro	50	1.311	na	0.15	0.44	na	The limit status was not reached
	75	1.967	na	0.68	0.79	na	The limit status was not reached
	100	2.623	2.98s (83.74s)	1.03	0.88	D	D_M=1 was not reached
Taft	50	2.850	na	0.06	0.37	na	The limit status was not reached
	75	4.275	na	0.70	0.67	na	The limit status was not reached
	100	5.700	6.87s (84.38s)	1.05	0.87	D	D_M=1 was not reached
Artificial waves (CH1)	50	0.844	na	0.75	0.79	na	The limit status was not reached
	75	1.266	125.93s (430s)	1.19	0.87	D	D_M=1 was not reached
	100	1.688	120.93s (158.20s)	1.04	0.85	D	Collapse
Artificial waves (OS1)	50	1.073	na	0.40	0.60	na	The limit status was not reached
	75	1.609	88.90s (430s)	1.10	0.78	D	D_M=1 was not reached
	100	2.146	86.31s (430s)	1.23	0.93	D	D_M=1 was reached at 93.12s

Table 2-11 Summary of the analytical results for models subjected to multiple seismic waves (3-story model, B/t=22.2 for columns)

Seismic wave	PGV [cm/s]	Scale factor	Number of input waves	Time reaching the stability limit (Total time)	D in the bottoms of columns in 1st story	D_M in 1st story	D=1 or D_M=1 is first reached	Notes
JMA Sendai	75	1.378	3	499.87s (630s)	1.00	0.86	D	D_M=1 was not reached
Hachinohe	50	1.348	3	562.45s (792s)	1.00	0.87	D	D_M=1 was not reached
El Centro	75	1.967	2	86.68s (167.48s)	1.04	0.85	D	D_M=1 was not reached
Taft	75	4.275	2	91.26s (168.76s)	1.02	0.82	D	D_M=1 was not reached
Artificial wave (CH1)	50	0.844	2	474.9s (660s)	1.01	0.83	D	D_M=1 was not reached
Artificial wave (OS1)	50	1.073	3	949.37s (1290s)	1.02	0.85	D	D_M=1 was not reached

2.6.5 Analytical results of the 3-story model (*B/t*=25 for columns)

The 3-story model (*B/t*=25 for columns) was also checked with the same aim of 3-story model (*B/t*=22.2 for columns). Similarly, the only difference between the model in this Chapter and that in 3-story model (*B/t*=29.4 for columns) is the thickness of the columns. The same cases as those for 3-story model (*B/t*=29.4 for columns) together with some additional ones were carried out in this Chapter.

For the analytical model under single seismic excitation (PGV=50cm/s), only one case reached the limit status (i.e., Artificial waves (CH1)), which is the only difference with the results of 3-story model (*B/t*=22.2 for columns). Similarly, the decrease in the width-to-thickness ratio of the columns improved the seismic performance of the system. For the analytical under single seismic excitation (PGV=75cm/s), the time when the stability limit appeared was delayed compared with the results in Table 2-6, but a little earlier than the results in Table 2-10. No collapse happens in these cases as well, which is the same as results of 3-story model (*B/t*=22.2 for columns). The stability limit (D=1) was first reached except for JMA Sendai. For most of the cases reaching the stability limit, D_M=1 was not reached, except for the following cases with PGV=75cm/s (Hachinohe and Artificial waves (CH1)). For the analytical under single seismic excitation (PGV=100cm/s), collapse happened for 3 cases. While for the other 3 cases, 2 of them only reached the stability limit (JMA Sendai and El Centro) and one of them reached both limit status (Taft).

For the analytical model under multiple seismic excitations (PGV=50cm/s), the number of seismic inputs to reach the stability limit were increased compared with the results in 3-story model (*B/t*=29.4 for columns), but was decreased compared with the results in 3-story model (*B/t*=22.2 for columns). Similarly, even though the stability limit was reached, D_M=1 was not reached for all of the cases under multiple seismic inputs. The damage evaluation method based on the current hysteretic model of the columns can also overestimate their bearing capacities under the long-duration seismic loadings, but the number of the overestimated cases is reduced with the increase in width-to-thickness ratio (from *B/t*=22.2 to *B/t*=25).

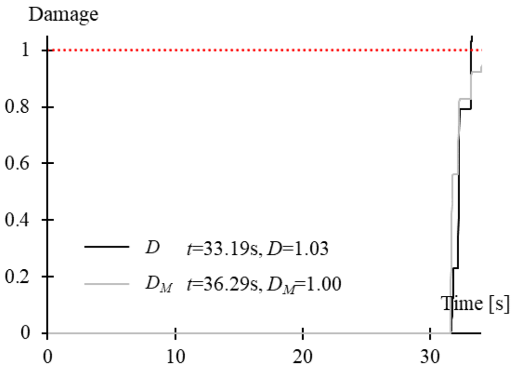

(a) Hachinohe, PGV=75cm/s

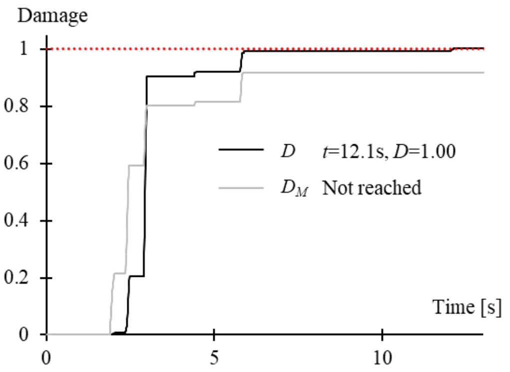

(b) El Centro, PGV=75cm/s

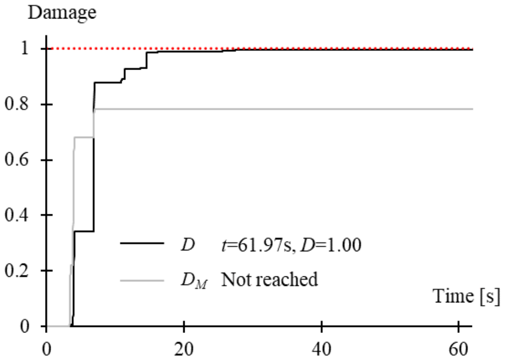

(c) Taft, PGV=75cm/s

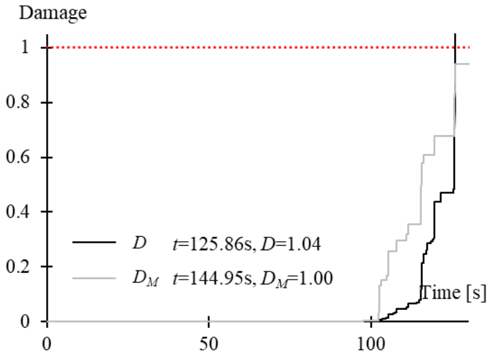

(d) Artificial wave (CH1), PGV=75cm/s

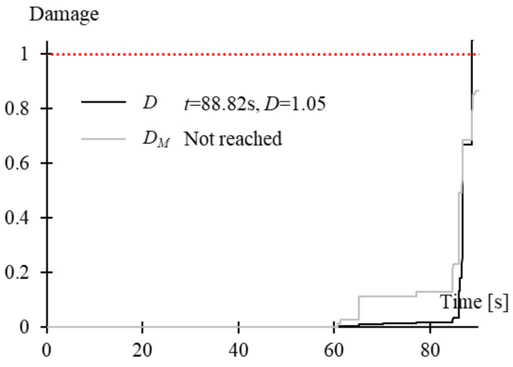

(e) Artificial wave (OS1), PGV=75cm/s

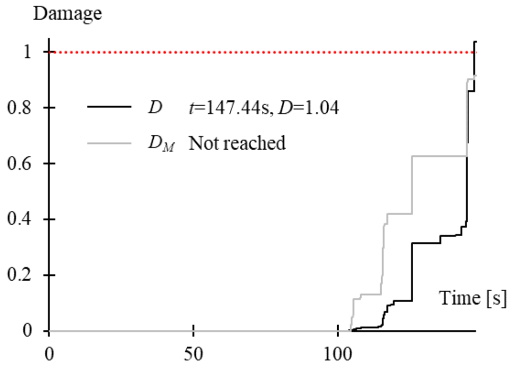

(f) Artificial wave (CH1), PGV=50cm/s

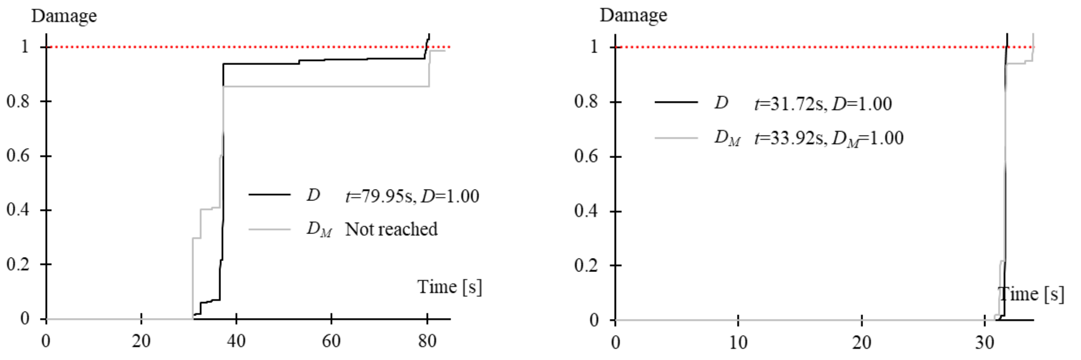

(g) JMA Sendai, PGV=100cm/s (h) Hachinohe, PGV=100cm/s

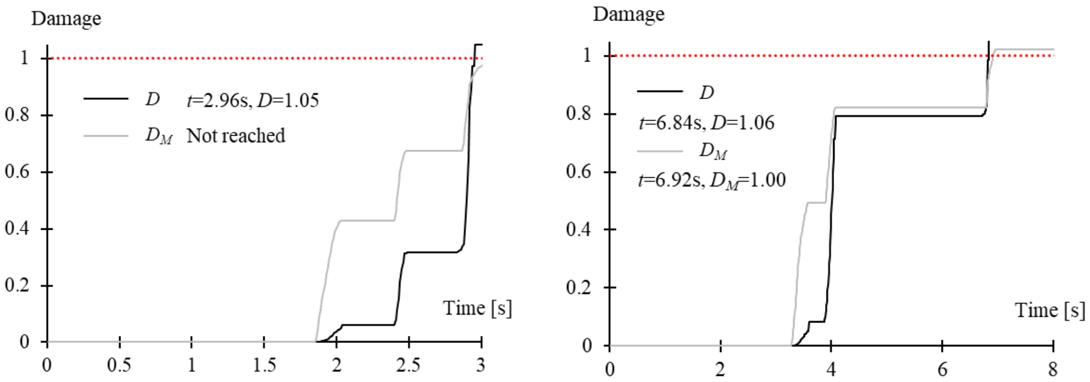

(i) El Centro, PGV=100cm/s (j) Taft, PGV=100cm/s

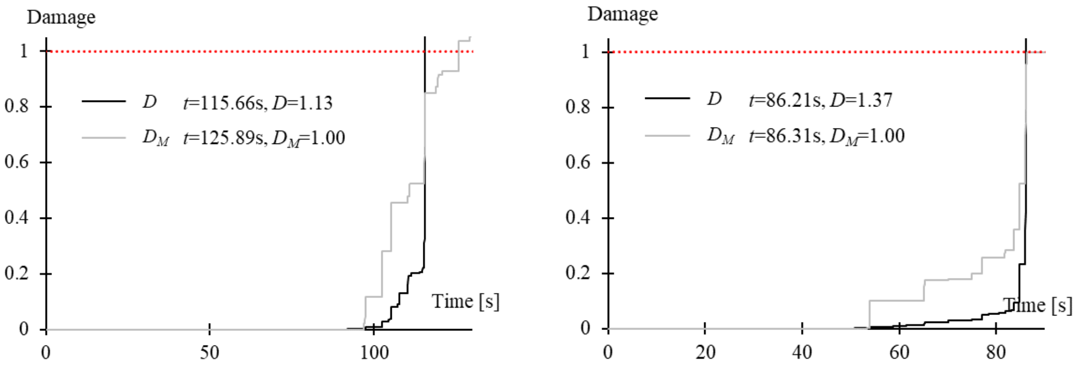

(k) Artificial wave (CH1), PGV=100cm/s (l) Artificial wave (OS1), PGV=100cm/s

Fig. 2-48 Damage evolution in the columns (in 1st floor) under single seismic excitation

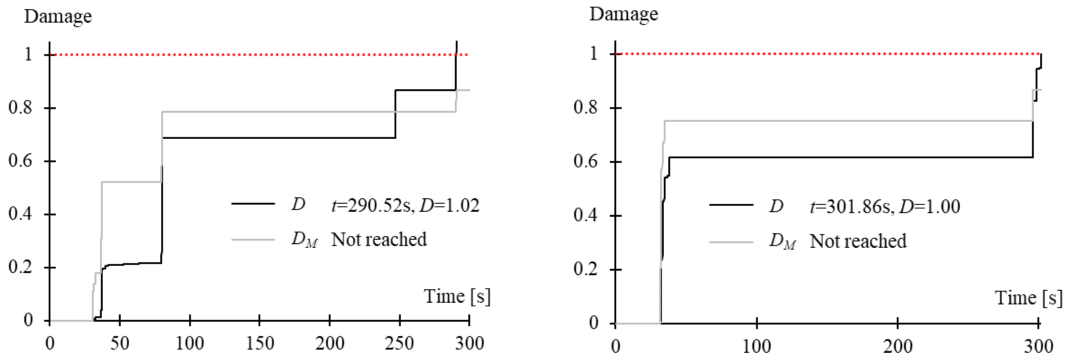

(a) JMA Sendai (PGV=75cm/s)

(b) Hachinohe (PGV=50cm/s)

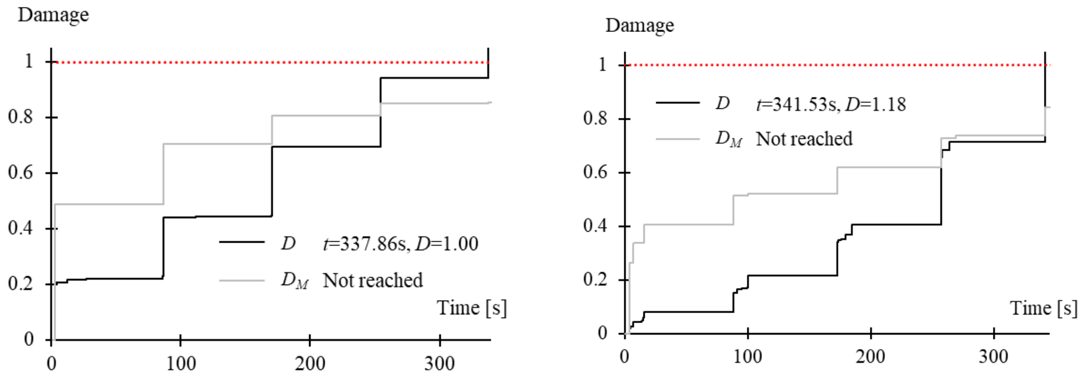

(c) El Centro (PGV=50cm/s)

(d) Taft (PGV=50cm/s)

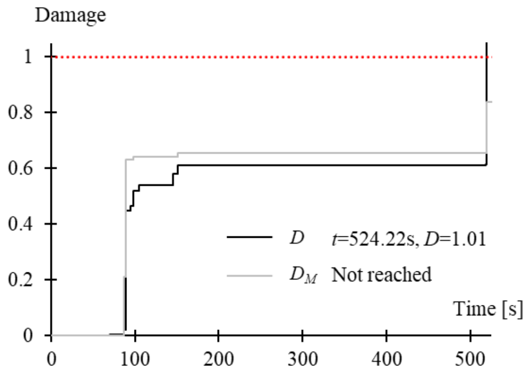

(e) Artificial wave (OS1) (PGV=50cm/s)

Fig. 2-49 Damage evolution in the columns (in 1st floor) under multiple seismic excitations

Table 2-12 Summary of the analytical results for models subjected to single seismic wave (3-story model, B/t=25 for columns)

Seismic wave	PGV [cm/s]	Scale factor	Time reaching the stability limit (Total time)	D in the bottoms of columns in 1st story	D_M in 1st story	D=1 or D_M=1 is first reached	Notes
JMA Sendai	50	0.919	na	0.12	0.45	na	The limit status was not reached
	75	1.378	na	0.63	0.84	na	The limit status was not reached
	100	1.838	79.95s (210s)	1.00	0.85	D	D_M=1 was not reached
Hachinohe	50	1.348	na	0.61	0.81	na	The limit status was not reached
	75	2.022	33.19s (264s)	1.03	0.87	D	D_M=1 was reached at 36.29s
	100	2.696	31.72s (44.24s)	1.00	0.87	D	Collapse
El Centro	50	1.311	na	0.22	0.52	na	The limit status was not reached
	75	1.967	12.1s (83.74s)	1.00	0.92	D	D_M=1 was not reached
	100	2.623	2.96s (83.74s)	1.05	0.95	D	D_M=1 was not reached
Taft	50	2.850	na	0.08	0.41	na	The limit status was not reached
	75	4.275	61.97s (84.38s)	1.00	0.78	D	D_M=1 was not reached
	100	5.700	6.84s (84.38s)	1.06	0.93	D	D_M=1 was reached at 6.92s
Artificial waves (CH1)	50	0.844	147.44s (330s)	1.04	0.92	D	D_M=1 was not reached
	75	1.266	125.86s (330s)	1.04	0.93	D	D_M=1 was reached at 144.95s
	100	1.688	115.66s (155.72s)	1.13	0.85	D	Collapse
Artificial waves (OS1)	50	1.073	na	0.58	0.66	na	The limit status was not reached
	75	1.609	88.82s (430s)	1.05	0.79	D	D_M=1 was not reached
	100	2.146	86.21s (108.33s)	1.37	0.94	D	Collapse

Table 2-13 Summary of the analytical results for models subjected to multiple seismic waves (3-story model, *B/t*=25 for columns)

Seismic wave	PGV [cm/s]	Scale factor	Number of input waves	Time reaching the stability limit (Total time)	*D* in the bottoms of columns in 1st story	D_M in 1st story	*D*=1 or D_M=1 is first reached	Notes
JMA Sendai	75	1.378	2	290.52s (420s)	1.02	0.84	*D*	D_M=1 was not reached
Hachinohe	50	1.348	2	301.86s (528s)	1.00	0.87	*D*	D_M=1 was not reached
El Centro	50	1.311	5	337.86s (418.7s)	1.00	0.85	*D*	D_M=1 was not reached
Taft	50	2.850	5	341.53s (421.9s)	1.18	0.84	*D*	D_M=1 was not reached
Artificial wave (OS1)	50	1.073	2	524.22s (860s)	1.01	0.84	*D*	D_M=1 was not reached

2.6.6 Discussions

In Chapter 2.6, four different models were analyzed to investigate the influence of the number of stories, the width-to-thickness ratio of the columns, seismic wave types and intensities on the damage evolution in the column components. In Fig. 2-50 and Fig. 2-51, the influence of the seismic intensities is reflected the darkness of the pie chart. In addition, the cases under single and multiple seismic waves were considered separately. The blue series represent the safe cases, the grey series represent the cases that the two damage evaluation methods give the similar prediction results, and the orange series represent the cases that the stability limit is necessary to be considered. Based on the summarized results in previous subchapters (as shown in Fig. 2-50 and Fig. 2-51), the following discussions were made.

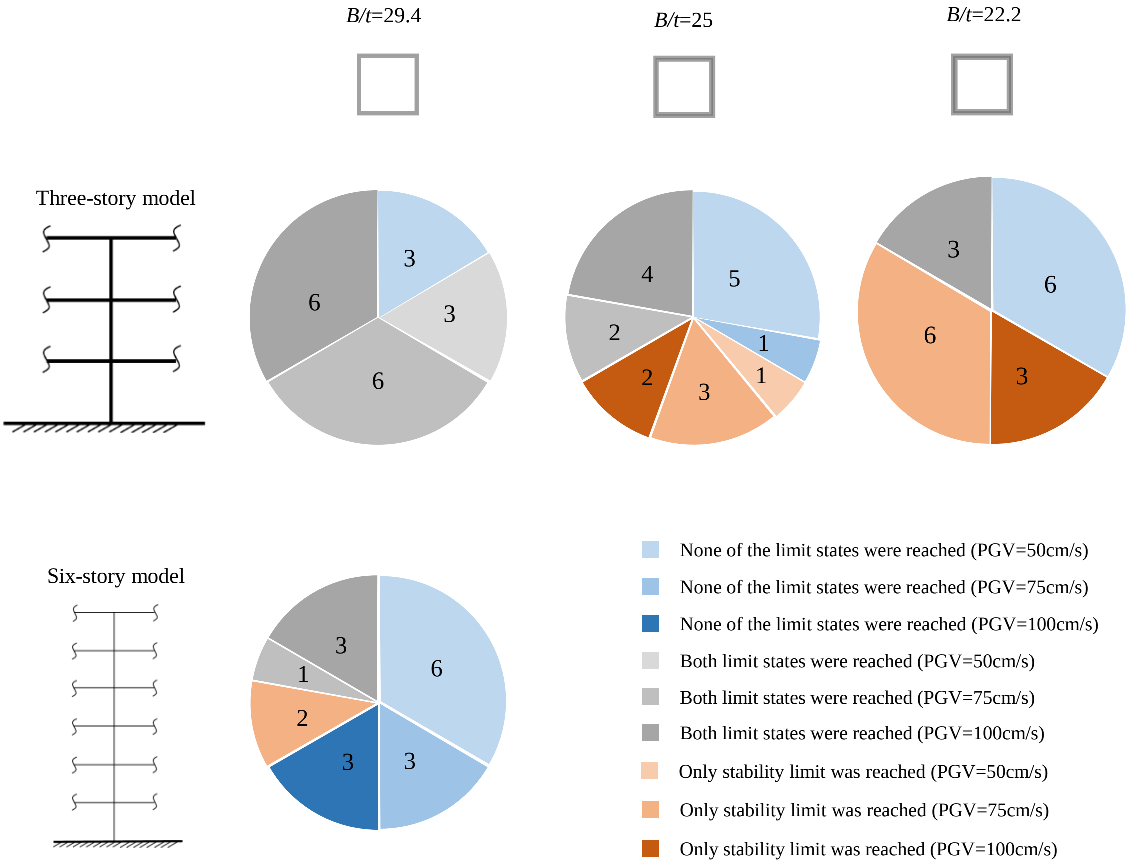

Fig. 2-50 The summarized analytical results of the current research (under single seismic input)

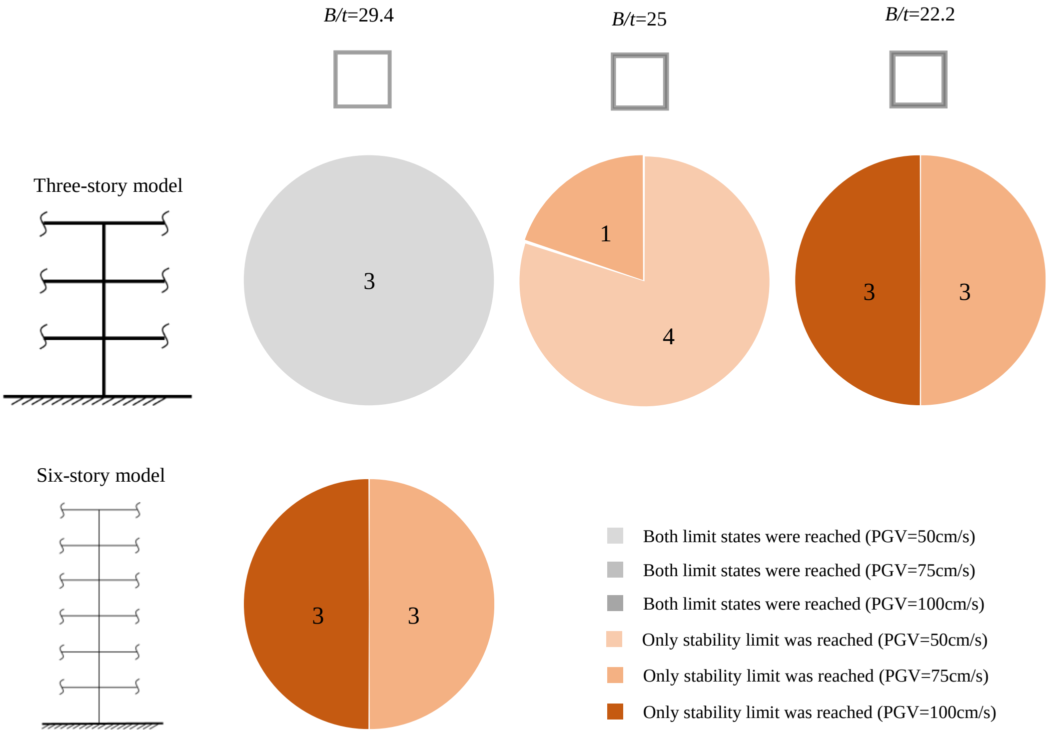

Fig. 2-51 The summarized analytical results of the current research (under multiple seismic inputs)

The six-story model exhibits a more stable seismic performance compared with the three-story model having the same width-to-thickness ratio. In the previous study [2-2], similar findings were also observed, i.e., the low-rise buildings are more vulnerable to the strong seismic inputs. This is caused by the concentration of the dissipated energy in the 1st floor for the three-story model [2-2]. When subjected to the seismic inputs, the 6-story model can always be safe under the design level (PGV=50cm/s). Under the single seismic input, the stability limit will never be reached for the 6-story model under general earthquake (i.e., El Centro and Taft) regardless of the intensities. However, when the multiple earthquakes happen, the stability limit will always be reached regardless the type of the earthquakes. For the 6-story model, the stability limit (D=1) is first reached, and the damage evaluation method (D_M=1) is not reached for most of the cases (expect for some cases under extremely severe earthquakes with PGV=100cm/s, but always later than the stability limit). These results stressed the necessity to consider the stability limit as the damage evaluation index in the middle-rise buildings under the following conditions: 1. Single seismic wave (long-duration earthquake) with moderate or large PGV (PGV=75cm/s and 100cm/s in this study); 2. Multiple seismic waves. Furthermore, the deterioration range in the hysteretic model for the columns [2-10] should be modified to decrease the strength when the limit status is already reached.

For the 3 three-story models, the time for reaching the stability limit will be delayed with the decreasing in the width-to-thickness ratio. For the cases under single seismic excitation, the time when reaching the stability limit is close to each other. Because the stability limit in these cases is usually determined by the main pulse in the seismic inputs, which will cause relatively large damage. But great difference can be observed in the D_M values for the cases of three-story models with different width-to-thickness ratios. For the cases under multiple seismic excitations, the number of seismic inputs increase with the decrease in width-to-thickness ratio. The damage evaluation method (D_M=1) in previous study can be applicable and give similar damage evaluation results to those from the stability limit concept for the models with relatively large width-to-thickness ratio (i.e., B/t=29.4). However, the damage evaluation method is not suggested to apply to the models with more compact sections (i.e., B/t=22.2 or 25), which will underestimate the damage accumulation in the structure and lead to the unexpected disasters. For the 3-story models, the stability limit will be reached with the increase of intensities (PGV=75cm/s or 100cm/s) regardless the earthquake type. For the cases with extremely large PGV (PGV=100cm/s), some of them reached both limit status (i.e., D_M=1 and D=1), while there are still many cases only reached the stability limit. Based on the discussion above, the stability limit is suggested to be applied to the columns with relatively small width-to-thickness ratio (B/t=22.2 or 25 in this study) as follows: 1. Multiple seismic waves; 2. Seismic waves with intensities over the design level. Similarly, the necessity to further modify the deterioration stage of the current hysteretic model is stressed.

Based on the analytical results, the following conclusions can be drawn. The stability limit can be a good concept to evaluate the cumulative damage in the column components in a broad range. The damage evaluation method proposed in the previous study [2-2] will overestimate the seismic performance of the structures in the following conditions: 1. Steel frame with more stories; 2. The columns with small width-to-thickness ratios (i.e., compact sections).

In summary, the main focus in this study is the time when the rapid deterioration initiates, while there are still limitations for the current analytical work. The analytical results can be considered as accurate prior to the stability limit; while the results are not reliable after the stability limit point due to the limitation in the strength deterioration part. The hysteretic model

[2-10] in the previous analyses [2-2] has to be further modified in the deterioration range (in the extended skeleton curve) by considering the stability limit in the future study to provide a more accurate strength deterioration prediction.

2.7 Residual lateral resistance prediction with local buckling deformation

After severe earthquake happens, there is usually damage accumulation in the structural components. Without carrying out inelastic response analyses for the specific structure, it's hard to obtain the loading history and the residual lateral resistance of the column components cannot be estimated, which is not possible for the engineers and researchers to evaluate the residual strength of the columns in a short time. The visible damage can hardly be related to the damage of steel structural components directly, while crack width has been used as a clear damage index for RC structures. It is very important to establish a visible damage index for quick damage estimation of steel structures.

In the previous study [2-19], Kishiki et al. proposed a method to predict the residual strength of the steel columns via measuring the out-of-plane deformation of the local buckling zone, and developed residual strength prediction lines based on test data. Due to the limited number of specimens, the method was not verified in some aspects. For example, the method did not try to find out the potential connection between the local buckling deformation of steel columns under cyclic loading and monotonic loading. The method did not find out the potential connection for the specimens under cyclic loading with the only difference in loading amplitude. In addition, a solid prediction method for the deformation progress without experiment is also in need.

Based on the discussion above, the possible visible damage indices were investigated; potential connection between the local buckling deformation of steel columns under monotonic and cyclic loading was researched; The method to provide deformation progress for the steel columns was also determined.

As mentioned in Chapter 2.3.1, the out-of-plane deformation of the steel columns was measured manually in this study at intervals. Firstly, the relationship between the out-of-plane deformation and residual strength was investigated based on the concept in [2-19], as shown in Fig. 2-52. The strength deterioration trends for both monotonic and cyclic loading were plotted and compared. The deterioration trends for the steel column under monotonic loading and cyclic loading seems to be similar. Considering the measuring error caused manually, the relationship of deteriorated strength and out-of-plane deformation in local buckling zone for the columns under monotonic loading can roughly represent those under cyclic loading.

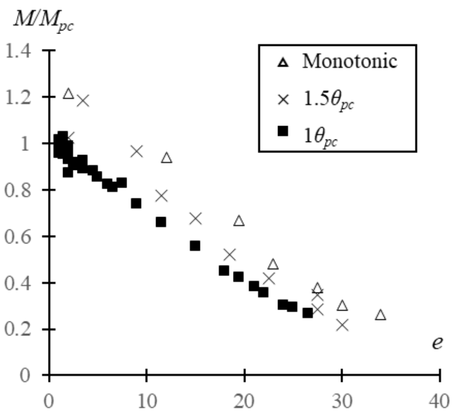

(a) 175-6-0.3P_y-4.9

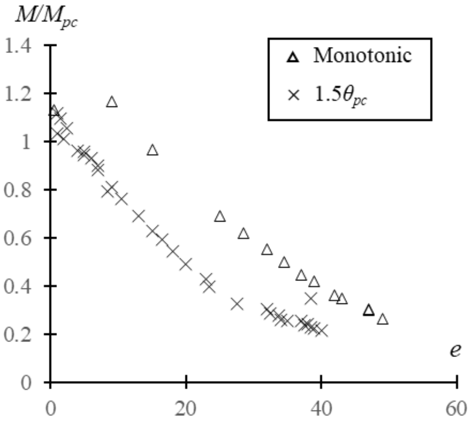

(b) 175-6-0.15P_y-4.9

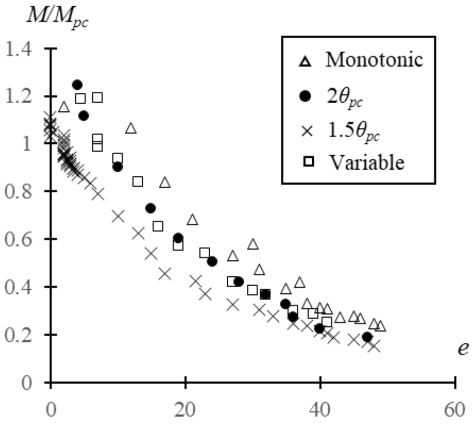

(c) 200-6-0.2P_y-4.3

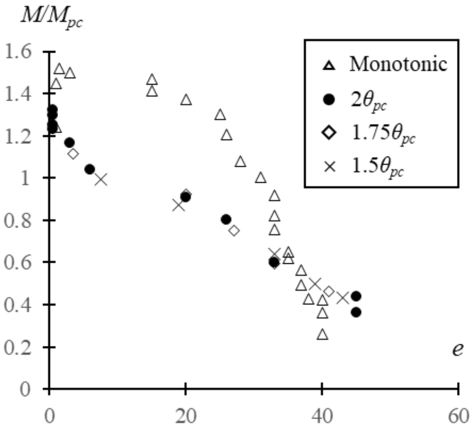

(d) 175-9-0.3P_y-4.9

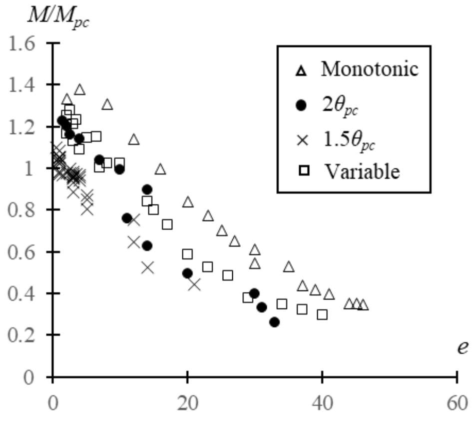

(e) 200-9-0.35P_y-4.3

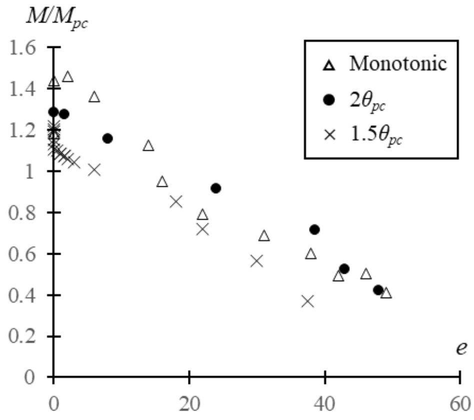

(f) 175-9-0.3P_y-7

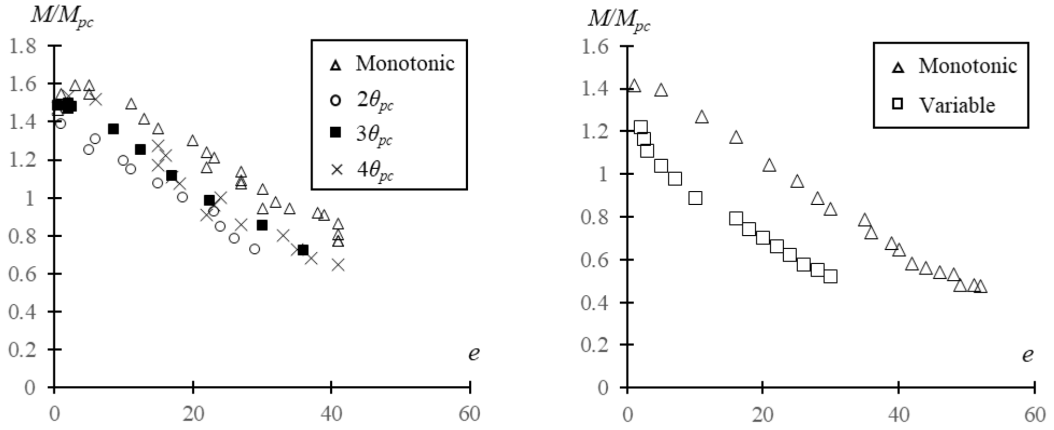

(g) 175-9-0.3P_y-3 (h) 200-9-0.2P_y-4.3

Fig. 2-52 The relationships between M and e

The regular pattern of the strength deterioration and out-of-plane deformation e was investigated above. The following defect still exists for the conclusion above. The out-of-plane deformation was measured manually and discontinuously, where the measuring data were not totally objective. In the previous study [2-19], the relationship between the axial deformation in the flange and out-of-plane deformation in the local buckling zone was built with a three-pin model simply. Therefore, the relationship of the strength deterioration and the axial deformation in the flange of local buckling zone, δ_b, was further investigated. The value of δ_b was measured by the displacement transducers with high accuracy continuously in this research, which is objective. Similarly, the strength deterioration trends for both monotonic and cyclic loading were plotted and compared in Fig. 2-53. According to the comparison, the relationship of M and δ_b under monotonic loading can also represent those specimens under cyclic loading with acceptable accuracy. One of the fastest ways to obtain the relationship (M-δ_b) without pushover test is to carry out the numerical simulation (ABAQUS) on the steel columns under monotonic loading. The simulation skill for the steel columns under monotonic loading is quite proven and time-saving. The simulated results for the moment-rotation angle relationship and δ_b-rotation angle relationship can be referred in Appendix 10, where acceptable accuracy can be obtained. With the corresponding simulation results, the residual lateral resistance can be roughly predicted by only measuring the deformation in the local buckling zone.

The suggested procedures for the potential practice use are listed as below. After the earthquake happened, the engineers should first determine the story and the bay that suffer the most severe damage [2-20]. Then the geometrical details for the steel column components should be made sure. Next, numerical model should be built based on the information and the pushover test should be carried out subsequently. By measuring the deformation in the local buckling zone, i.e., out-of-plane deformation *e* and axial deformation in the flange δ_b, and comparing with the numerical simulation results, the residual lateral resistance of the steel columns can be roughly predicted. This can be a time-saving method with acceptable accuracy in practice.

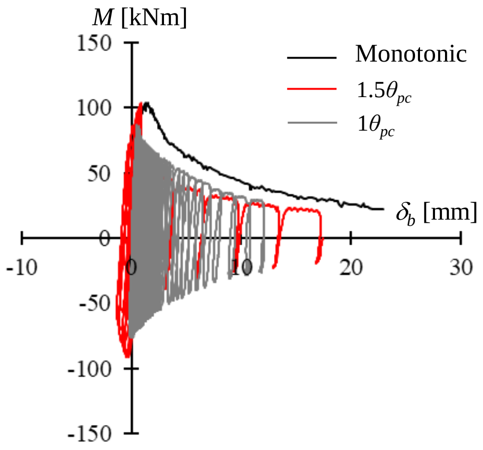

(a) 175-6-0.3P_y-4.9

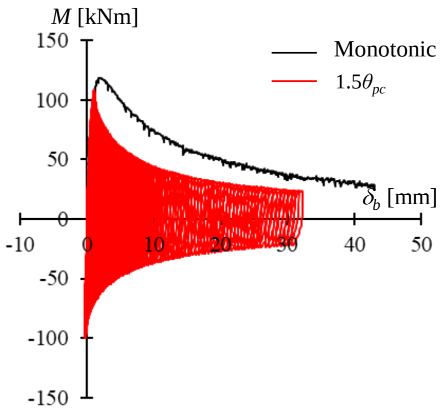

(b) 175-6-0.15P_y-4.9

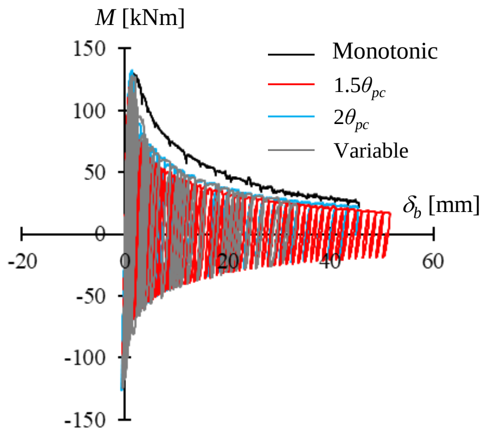

(c) 200-6-0.2P_y-4.3

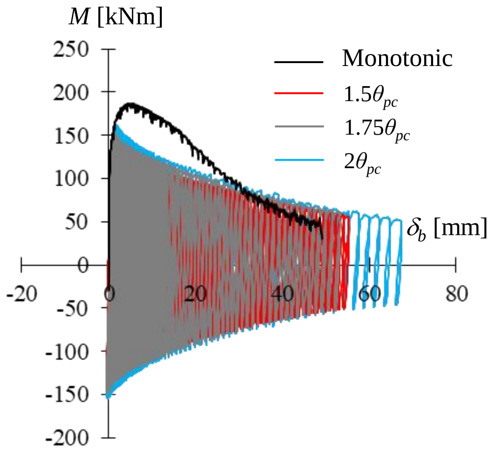

(d) 175-9-0.3P_y-4.9

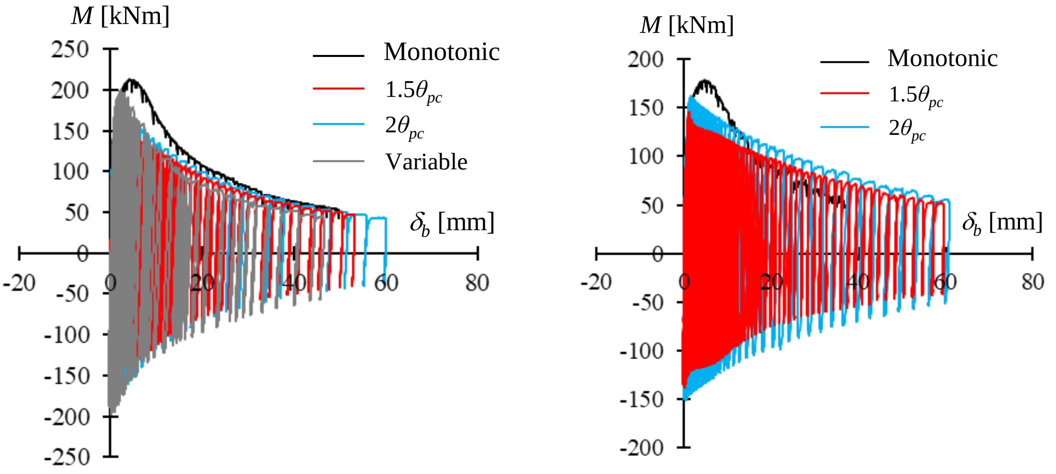

(e) 200-9-0.35P_y-4.3 (f) 175-9-0.3P_y-7

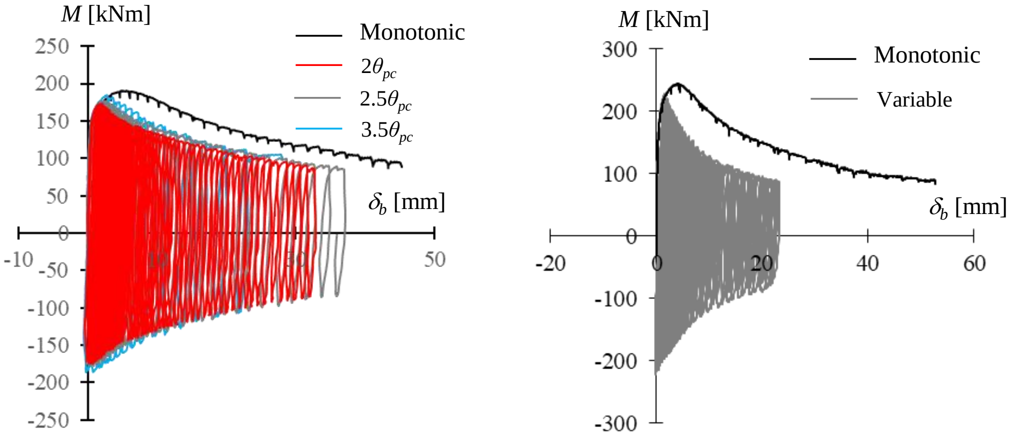

(g) 175-9-0.3P_y-3 (h) 200-9-0.2P_y-4.3

Fig. 2-53 The relationships between M and δ_b

2.8 Summary

In this Chapter, SHS columns subjected to cyclic small amplitude loads were carried out to investigate how width-to-thickness ratio, axial force ratio, shear span ratio, and loading histories influence deterioration behavior due to local buckling. The hysteretic behaviors (including the strength deterioration and deformation capacities) were researched in detail. Important damage index was proposed, predicted and applied in the practice. Based on the experimental and analytical study, the following conclusions were drawn:

The extended skeleton curves for most specimens under small amplitude loading showed different trends relative to the moment-rotation angle relationship of specimen under monotonic loading, which was different from the empirical rule from previous studies. This study confirmed that the extended skeleton curve of columns under small inelastic cycles did not correspond to the moment-rotation angle relationship of columns under monotonic loading.

For specimens under small amplitude loading, they behaved steadily for a certain number of cycles and then rapidly deteriorated. The concept of a stability limit was proposed based on the axial deformation of the flange plate in the local buckling region. Upon reaching the stability limit, deformation of the local buckling region of and the strength deterioration of the columns increased rapidly. That can explain the phenomena observed in experiment. Two different strength deterioration behaviors were observed in the test results. They were caused by the different deformation mechanisms in the local buckling region prior to the stability limit.

Increases in the width-to-thickness ratio, axial force ratio, or loading amplitude results in quicker strength deterioration for specimens under cyclic small amplitude loading. The shear span ratio had a minor influence on the deterioration behavior of the specimens before the stability limit; However, increases in shear span ratio resulted in faster strength deterioration after the stability limit has been reached.

A method to accurate and directly predict the stability limit value using the geometrical features, loading conditions and material property was proposed. Additionally, a method to predict the number of cycles until the stability limit is reached was also proposed. The method was accurate and applicable to specimens under both constant and variable amplitude loading.

The residual strength of the SHS columns with local buckling can be predicted with the deformation in the local buckling zone. The strength deterioration trend of the columns under cyclic loading can be simply represented with that obtained from pushover test.

Based on the experimental results, local buckling and rapid strength deterioration could occur after a certain number of cycles even though the steel columns were subjected to small inelastic cycles. This stressed the necessity to consider the damage caused by the small inelastic cycles in the design of and analyses for structural components under seismic loading.

The proposed concept of the stability limit and its corresponding prediction methods were further applied into the seismic analyses. The stability limit was regarded a damage evaluation index in the view of deformation due to local buckling for the structures subjected to seismic loading. In the seismic analyses, the columns are regarded as a safe status before the stability limit is reached; when the stability limit is reached, the deformation of the columns starts to progress rapidly, and leads to the large drift in the structure. In this condition, the functionality for the structure barely exists and there is a great possibility of the structure to collapse. Furthermore, the hysteretic model[2-10] for the column components in the inelastic response analyses tends to overestimate the bearing capacity for the structures with smaller width-to-thickness ratios and more floors, which is an unsafe case. The deterioration range of the model should be further modified in the future study.

References

[2-1] Tenderan R, Ishida T, Jiao Y, Yamada S. Seismic Performance of ductile steel moment-resisting frames subjected to multiple strong ground motions. *Earthquake Spectra*. 2018, 35: 289-310.

[2-2] Tenderan R, Ishida T, Yamada S. Effect of column strength deterioration on the performance of steel moment-resisting frames subjected to multiple strong ground motions. *Engineering Structures*. 2021, 252(1): 113579.

[2-3] Japan Iron and Steel Federation (JISF). 2017. Cold roll formed square steel pipe for building structure (BCR295), MDCR0002-2017. (in Japanese).

[2-4] Japanese Standards Association: JIS Z 2241: Metallic materials-Tensile testing-Method of test at room temperature, 2011.

[2-5] Japan Iron and Steel Federation (JISF). 2017. Cold roll formed square steel pipe for building structure (BCR295), MDCR0002-2017. (in Japanese).

[2-6] Architectural Institute of Japan: Japanese Architectural Standard Specification (JASS) 6 Steel Work, 2018

[2-7] Architectural Institute of Japan, AIJ recommendations for plastic design of steel structures, 2017. (in Japanese)

[2-8] Shimada Y, Jiao Y, Kim J, Yamada S. Effects of Strain-Rate on the Hysteretic Behavior of Structural Steels. In: 15th World Conference on Earthquake Engineering, Lisbon, Portugal; 2012.

[2-9] Tseng NT, Lee GC. Simple Plasticity Model of Two-Surface Type. *Journal of Engineering Mechanics*. 1983, 109(3): 795-810.

[2-10] Yamada S, Ishida T, Jiao Y. Hysteretic behavior of RHS columns under random cyclic loading considering local buckling. *International Journal of Steel Structures*. 2018, 18(5): 1761-1771.

[2-11] Kato B, Akiyama H, Yamanouchi H. Predictable properties of structural steels subjected to incremental cyclic loading. 1973. In *Preliminary Publication of IABSE Symposium on Resistance and Ultimate Deformability of Structures Acted on by Well Defined Loads.*

[2-12] Yamada M, Kawamura H, Tani A, Yamanaka K. Elasto-plastic deformation and fracture behavior of steel box columns subjected to double curvature cyclic bending under constant axial load (V). 1986, Summaries of Technical Paper of Kinki Branch, Architectural Institute of Japan, 409-412. (in Japanese)

[2-13] Kuwamura H, Iyama J, Zhu D. Collapse and residual drift during post-local-buckling behaviors under earthquake. *Journal of Structural and Construction Engineering.* AIJ, 1999, 64 (526):169-176. (in Japanese)

[2-14] Yamada S, Akiyama H, Kuwamura H. Post-buckling and deteriorating behavior of box-section steel members, *Journal of Structural and Construction Engineering.* AIJ, 1993, 444: 135-143. (in Japanese).

[2-15] Akiyama H. Earthquake-resistant limit-state design for buildings. First Edition, University of Tokyo Press, 1985.

[2-16] Matsuishi M, Endo T. Fatigue of metals subjected to varying stress. Japan Society of Mechanical Engineering, 1968.

[2-17] Miner MA. Cumulative damage in fatigue. *Journal of Applied Mechanics*, 1948.

[2-18] Timoshenko SP, Gere J.M. Theory of elastic stability. Second Edition, McGraw-Hill, 1963.

[2-19] Kishiki S, Iwasaki Y. Evaluation of residual strength based on local buckling deformation of steel column——Quick inspection method for steel structures based on the visible damage Part 3, *Journal of Structural and Construction Engineering*. AIJ, 2017, 82 (735):735-743. (in Japanese)

[2-20] Japan Building Disaster Prevention Association. Damage classification criteria and restoration technical guidelines for earthquake-damaged buildings to determine the possibility of reuse and restore, 2016. (in Japanese)

[2-21] Ibarra LF, Medina RA, Krawinkler H. Hysteretic models that incorporate strength and stiffness deterioration. *Earthquake Engineering and Structural Dynamics*. 2005, 34: 1489-1511.

[2-22] Kamaris GS, Hatzigeorgiou GD, Beskos DE. A new damage index for plane steel frames exhibiting strength and stiffness degradation under seismic motion. *Engineering Structures*. 2013, 46: 727-736.

[2-23] Cosenza E, Manfredi G, Ramasco R. The use of damage functionals in earthquake engineering: a comparison between different methods. *Earthquake Engineering and Structural Dynamics*. 1993, 22(10): 855-868.

[2-24] Park YJ, Ang AHS. Mechanistic seismic damage model for reinforced concrete. *Journal of Structural Engineering*. 1985, 111: 722-739.

[2-25] Building Center of Japan. Stipulation of methods of calculating D_s and F_{es}. In The Building Standard Law of Japan: Notifications of Ministry of Land, Infrastructure, Transport, and Tourism (MLIT) NO. 596. 2013, Tokyo, Japan.

[2-26] Ministry of Land, Transport and Tourism. Measures against long-period ground motion caused by a huge earthquake along the Nankai Trough in skyscrapers etc. https://www.mlit.go.jp/jutakukentiku/build/jutakukentiku_house_fr_000080.html

Chapter 3 Low cycle fatigue behaviors of SHS columns subjected to small inelastic cycles

3.1 Introduction

Major earthquakes can cause great damage to structures, lead to the loss of vertical load bearing capacity or the horizontal resistance, and subsequently decrease the safety margin. To avoid these problems, scholars have placed considerable emphasis on studying major earthquakes, with significant progress made in the design of current seismic codes. Generally, earthquakes with relatively smaller excitations happen more frequently than major ones in earthquake-prone areas. The accumulated damage caused by a large number of small-amplitude loadings is non-neglectable [3-1][3-2]. Therefore, research on the remaining fatigue endurance of structural components under repeated small-amplitude loadings in future seismic events (i.e., aftershocks or main shocks) is important. Scholars have become interested in the security risks for structures in earthquake-prone areas subjected to several earthquakes since they create a large number of small inelastic cycles that affect structural components. In Chapter 1, many studies [3-3][3-4][3-5][3-6][3-7][3-8][3-9][3-10][3-11] on the low cycle fatigue problem of beam-to-column connection have been introduced, and the dominant failure mode is fracture. In previous limited studies [3-12][3-13][3-14], fracture dominant failure mode was also found in the steel column components.

In Chapter 2, all of the specimens failed due to local buckling. If the width-to-thickness ratio, axial force ratio or loading amplitude is decreased, whether the dominant failure mode is still local buckling remains unknown. There will be a possibility for fracture to happen under a large number of small amplitude loadings. The deterioration evaluation method developed based on local buckling can be inapplicable to specimens failing due to fracture. Therefore, the methods to evaluate the column components dominant by the fracture failure mode have to be developed. The residual lateral resistance should also be assessed with ease. Furthermore, a failure mode transformation boundary should be considered to distinguish the steel columns fail due to different failure modes. These unknown cases had to be investigated further under complex conditions in practical engineering. Data on steel columns subjected to small amplitude loadings in a relatively large amount need to be collected to fill existing gaps in research.

In Chapter 3, cyclic tests of 22 SHS columns subjected to many small inelastic cycles were carried out to investigate the effects of loading amplitude, axial force ratio, and shear span ratio on the strength deterioration behavior and fatigue life of the columns. The failure mode for the columns subjected to repeated small-amplitude loadings (with relatively small axial force and width-to-thickness ratio) was verified as flange fracture. LCF life prediction methods were established based on the empirical regression functions of specimens under constant amplitude loading and used in combination with the rainflow counting method [3-15] and Miner's rule [3-16] for specimens under variable amplitude loading. Strength deterioration prediction methods based on empirical regression functions on deterioration rates in experiments and propagation of cracks have been proposed. The failure modes transformation boundaries were built based on the experiment database in this study. The details of the specimens, testing method, and primary findings are reported in the following subsections.

3.2 Test program

3.2.1 Material test

SHS columns made of BCR 295 (nominal yield strength: 295 N/mm2; nominal tensile strength: 400 N/mm2) are still used in this Chapter. The chemical composition can be referred to Table 2-1 in Chapter 2. The test coupons were also designed based on the tensile test pieces specified by JIS Z 2241[3-17] are shown in Fig. 2-1. The manufacturing method was the same as previous test coupons, as Fig. 2-1. The material test results are summarized in Table 3-1, and the stress-strain relationships from tensile coupon test for each series of specimens are plotted in Fig. 3-1. 0.2% proof stress was employed as the yield stress in Table 3-1.

The material test results are further used in the analytical work in Chapter 3, as well as in the numerical simulation.

Table 3-1 Test results for tensile coupons.

Lot	Dimension	Yield stress [N/mm^2]	Tensile strength [N/mm^2]	Yield ratio	Elongation (%)
A	□-175×175×9 (BCR295)	371	418	0.89	23.4
C	□-175×175×9 (BCR295)	382	440	0.87	20.7
D	□-175×175×6 (BCR295)	391	454	0.86	18.3
H	□-175×175×9 (BCR295)	369	413	0.89	22.1

Notes: The Lot in Table 3-1 is the same definition as that in Table 2-2.

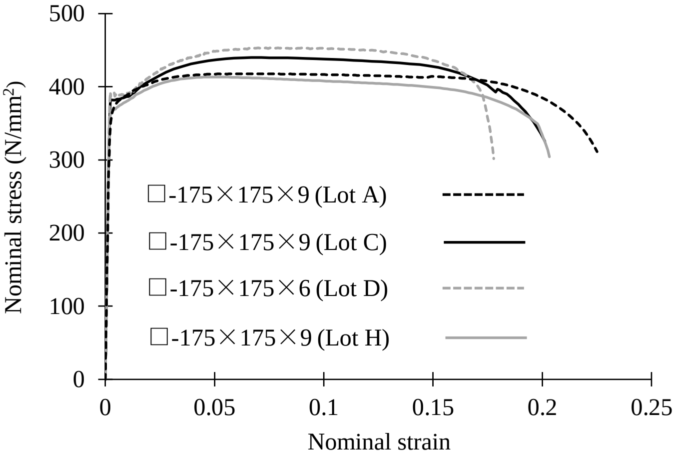

Fig. 3-1 Stress-strain relationships for material test.

3.2.2 Test parameters

The effects of width-to-thickness ratio, shear span ratio, axial force ratio, and loading history on the LCF life of cold-roll-formed SHS columns were also investigated in this Chapter. Two different width-to-thickness ratios were employed: 29.2 for a single specimen and 19.4 for the remaining 21 specimens. The influence of this ratio was not our main focus in this study since there was only one specimen with a different width-to-thickness ratio. Three different shear span ratios were employed: 3, 4.9, and 7. The axial force ratio is defined as the quotient of the axial force divided by the axial yield strength of the section. Four different axial forces ratios were employed: -0.15, 0, 0.15, and 0.3. The negative axial force ratio indicates the specimen under tensile axial force.

The loading histories employed in this study were categorized into three groups: constant, variable, and random amplitude loading; each type is shown in Fig. 3-2. The constant amplitude loading ranged from 1.0 to 2.0 θ_{pc} for corresponding specimens. For variable and random amplitude loading, once a set was determined for each loading history, the same set would be repeated until fracture. The peak loading amplitude of variable loading consisted of 6 cycles of 1.0, 4 cycles of 1.5, and 2 cycles of 2.0 θ_{pc}; incremental loading was followed for each set. The random loading sets were designed based on the response analyses of a 3-story SMRF excited by the 2011 Tohoku Earthquake JMA Sendai Record North-South (NS) component and the 1952 Kern County Earthquake Taft Record East-West (EW) component. The detailed information for the frame can be referred to in Appendix 2. The rotation responses of the columns on the first floor were converted into random loading histories, named JMA Sendai and Taft. Proper scale factors were selected for the response analyses to control the maximum loading amplitude of each half-cycle within 2.3 θ_{pc}. Local buckling around 1 mm was observed in the column end during the experiment process when the peak loading amplitude for the half-cycle of 2.3 θ_{pc}. Local buckling was avoided in the specimens under random amplitude loading to eliminate the combined effect of different failure modes on the cyclic behaviors. In addition, all cycles with a peak-to-peak amplitude less than 1.5 θ_{pc} were removed to improve the efficiency in the loading process since the columns were basically elastic under these conditions. The detailed information of the tested specimens in this study is shown in Table 3-2. The naming rule for the specimens: "loading history_width-to-thickness ratio_axial force ratio_shear span ratio." For the loading history, "Cn" refers to $n\cdot\theta_{pc}$ (constant amplitude loading), and "Inc," "Sendai," and "Taft" refer to the form of the variable loading.

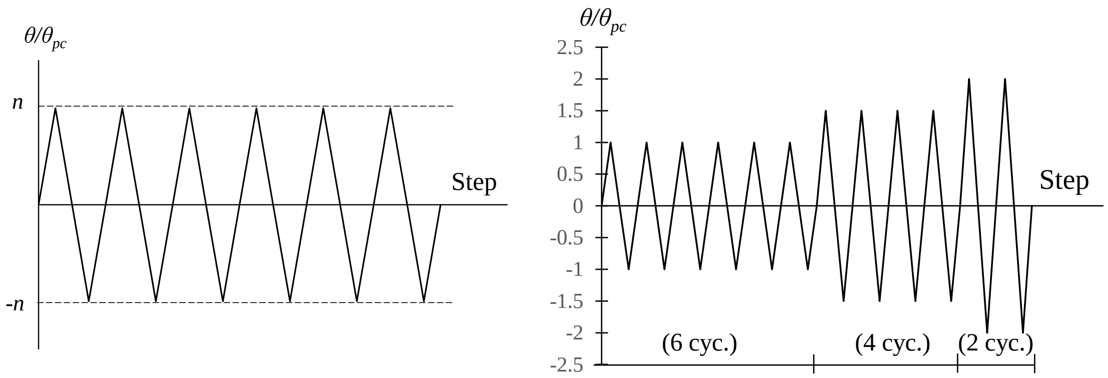

(a) Constant amplitude loading.

(b) Variable amplitude loading-Incremental loading.

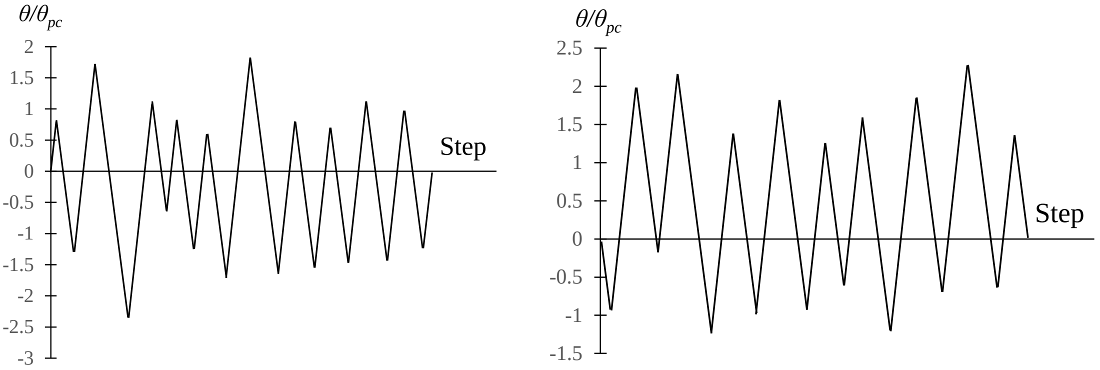

(c) Random amplitude loading-JMA Sendai.

(d) Random amplitude loading-Taft.

Fig. 3-2 Loading protocol.

Table 3-2 List of the specimens

Lot	Dimension	Specimen	B/t	P/P_y	L/B	Loading history	Loading amplitude	N_f	N_{ini}
A	□-175×175×6 (BCR295)	C1.0_29.2_0.15_4.9	29.2	0.15	4.9	Const. amp. 1.0θ_{pc}	0.0076	1332	402
B	□-175×175×9 (BCR295)	C1.0_19.4_0.3_7.0	19.4	0.3	7.0	Const. amp. 1.0θ_{pc}	0.0093	2335	560
		C1.0_19.4_0.15_4.9	19.4	0.15	4.9	Const. amp. 1.0θ_{pc}	0.0072	1732	134
		C1.5_19.4_0.15_4.9				Const. amp. 1.5θ_{pc}	0.0107	477	118
		C2.0_19.4_0.15_4.9				Const. amp. 2.0θ_{pc}	0.0142	271	118
		Inc_19.4_0.15_4.9				Variable Inc.	n/a	528	120
C		C1.0_19.4_0_4.9	19.4	0	4.9	Const. amp. 1.0θ_{pc}	0.0077	1316	450
		C1.5_19.4_0_4.9				Const. amp. 1.5θ_{pc}	0.0116	380	25
		C2.0_19.4_0_4.9				Const. amp. 2.0θ_{pc}	0.0150	170	20
		Taft_19.4_0_4.9				Random Taft	n/a	495	45
		Sendai_19.4_0_4.9				Random JMA Sendai	n/a	680	80
		Inc_19.4_0_4.9				Variable Inc.	n/a	324	48

	C1.0_19.4_-0.15_4.9	19.4	-0.15	4.9	Const. amp. 1.0θ_{pc}	0.0075	1170	180
	C1.5_19.4_-0.15_4.9				Const. amp. 1.5θ_{pc}	0.0113	441	135
	C2.0_19.4_-0.15_4.9				Const. amp. 2.0θ_{pc}	0.0151	116	24
	C1.0_19.4_0.3_4.9	19.4	0.3	4.9	Const. amp. 1.0θ_{pc}	0.0068	1850	500
D	C1.5_19.4_0.3_3.0	19.4	0.3	3.0	Const. amp. 1.5θ_{pc}	0.0078	270	80
	C1.0_19.4_0.15_3.0	19.4	0.15	3.0	Const. amp. 1.0θ_{pc}	0.0054	638	120
	C2.0_19.4_0.15_3.0				Const. amp. 2.0θ_{pc}	0.0111	105	20
	C1.0_19.4_0.15_7.0	19.4	0.15	7.0	Const. amp. 1.0θ_{pc}	0.0106	905	460
	C1.5_19.4_0.15_7.0				Const. amp. 1.5θ_{pc}	0.0158	337	30
	C2.0_19.4_0.15_7.0				Const. amp. 2.0θ_{pc}	0.0211	250	15

Notes: B/t: Width-to-thickness ratio; P/P_y: Axial force ratio; L/B: Shear span ratio; N_f: Number of cycles until the cracks propagate through one of the flanges; N_{ini}: Number of cycles when the crack initiates in the corners; θ_{pc}: The calculated elastic rotation angle of the column that corresponds to the plastic moment considering the effect of axial force; “Const.” is the abbreviation for “Constant”; “amp.” is the abbreviation for “amplitude”.

3.3 Test results

3.3.1 Failure mode

Flange fracture was the final failure mode for all the specimens in the test, as shown in Fig. 3-3. The crack initiated at the corners of the specimens and propagated to the center of the flanges for all the specimens, as illustrated in Fig. 3-4. The loading process was stopped until the crack propagated through either side of the flange for each specimen. The crack propagation was monitored by both photographs at intervals and the data in the strain gauges. According to the photographs, the crack propagation from the corners to the middle of the flange was quite slow at the beginning; when the crack propagates through the second and fourth black tapes in Fig. 3-3, the crack grows rapidly and propagates through the flange, which only takes several cycles. One representative example for the strain gauge data progress is illustrated in Fig. 3-5. The definition of the strain range is defined in Fig. 3-6, which is the difference of the maximum and minimum peak values. The strain ranges of the strain gauges keep in a constant value before the crack propagates the strain gauge; when the crack approaches the strain gauge, the value of the strain range increases rapidly; when the crack propagates through the strain gauge, the strain range drops rapidly.

Moderate local buckling was observed in Specimens C2.0_19.4_0.15_4.9 and C2.0_19.4_0.15_7.0; minor local buckling was observed in Specimens C2.0_19.4_0.15_3.0 and Sendai_19.4_0_4.9. This buckling could influence the strain concentration in the column end and lead to an increase in the number of cycles to fracture.

Fig. 3-3 Failure mode (flange fracture) in the experiment.

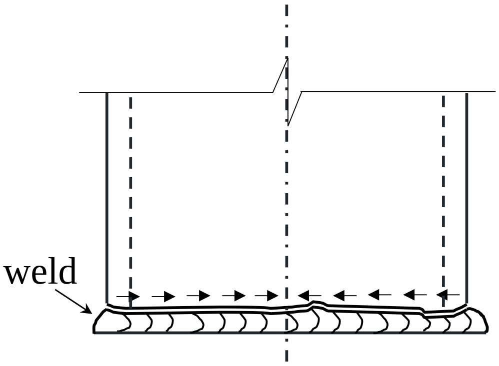

Fig. 3-4 Schematic illustration of crack propagation.

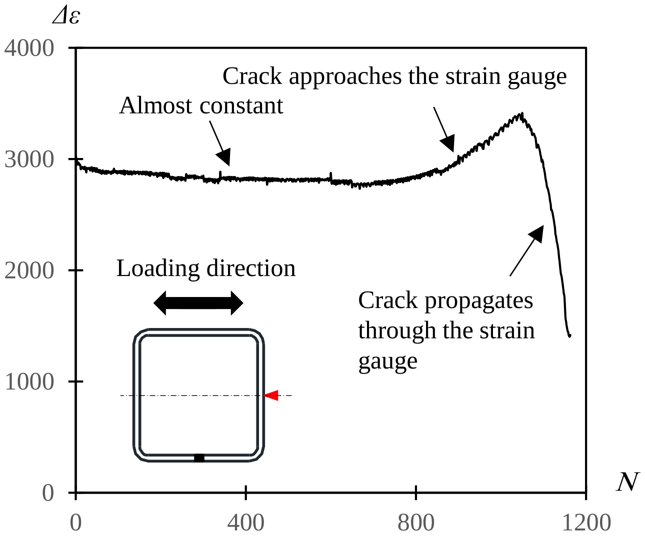

Fig. 3-5 Illustration of strain range progress (Specimen C1.0_19.4_-0.15_4.9).

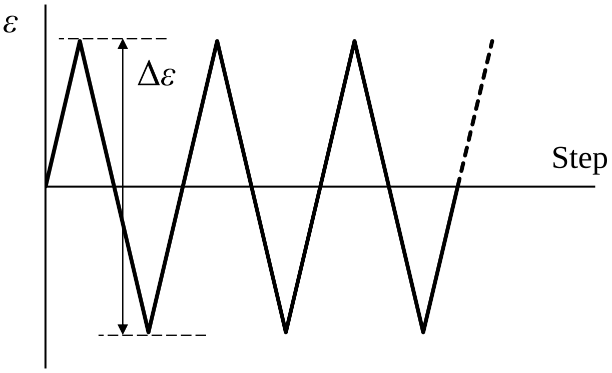

Fig. 3-6 Definition of strain range.

3.3.2 Hysteretic curves

The hysteretic curves of all the specimens are plotted in Fig. 3-7. M_{pc} represents the plastic moment, considering the effect of the axial load, and K_e represents the elastic stiffness of the columns. A remarkable decrease in strength was observed in the hysteretic loops. Combining with the results in Chapter 3.3.1, the lateral load-bearing capacity for the columns deteriorated smoothly before crack propagation was completed; this capacity was mainly governed by the level of crack propagation for all the specimens in the experiment. Once the crack propagated through in either flange, the lateral load-bearing capacity dropped suddenly.

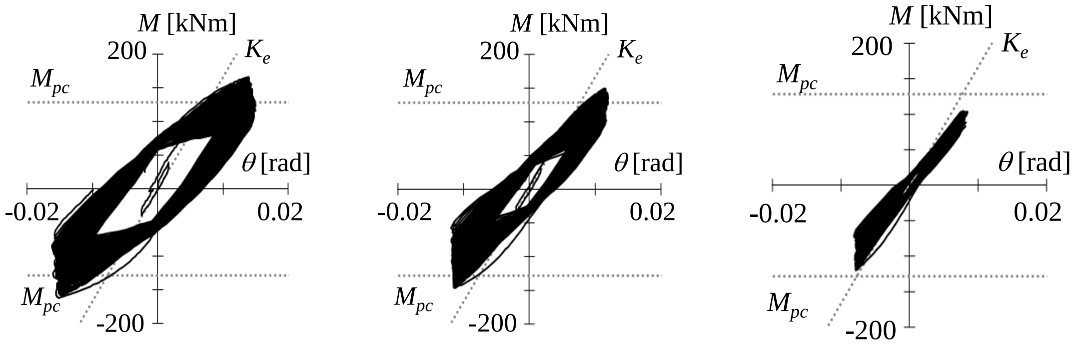

(a) C2.0_19.4_0_4.9 (b) C1.5_19.4_0_4.9 (c) C1.0_19.4_0_4.9

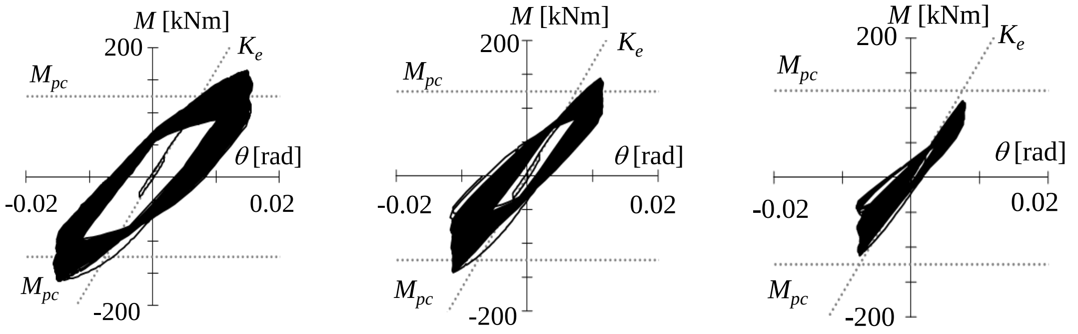

(d) C2.0_19.4_-0.15_4.9 (e) C1.5_19.4_-0.15_4.9 (f) C1.0_19.4_-0.15_4.9

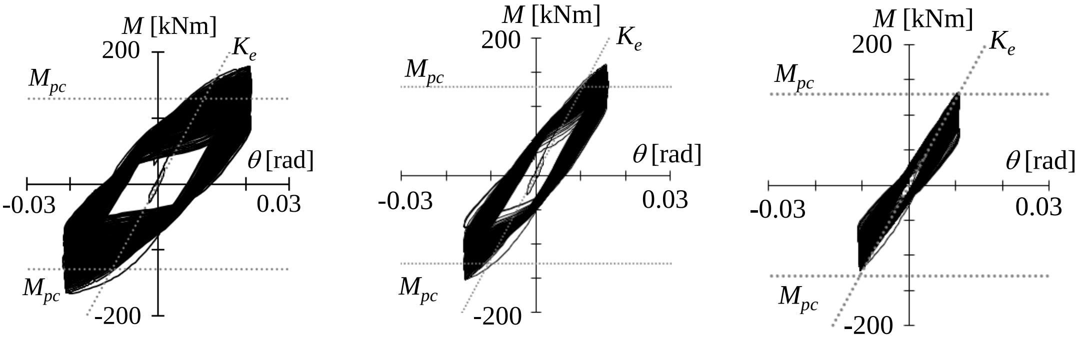

(g) C2.0_19.4_0.15_7 (h) C1.5_19.4_0.15_7 (i) C1.0_19.4_0.15_7

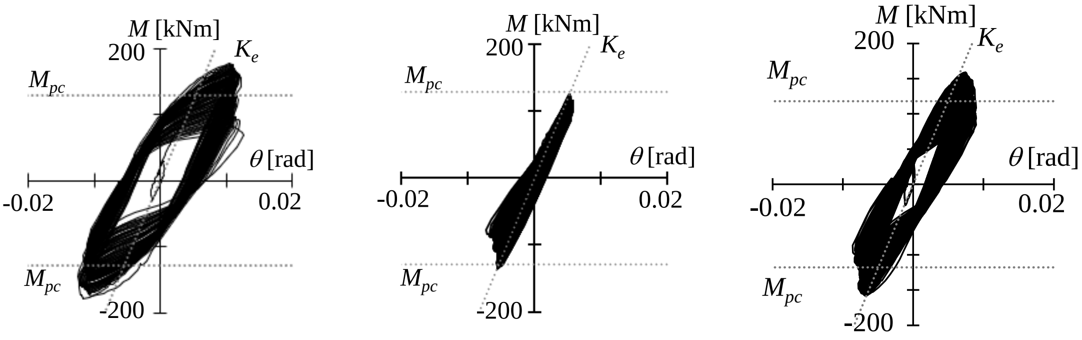

(j) C2.0_19.4_0.15_3 (k) C1.0_19.4_0.15_3 (l) C1.5_19.4_0.3_3

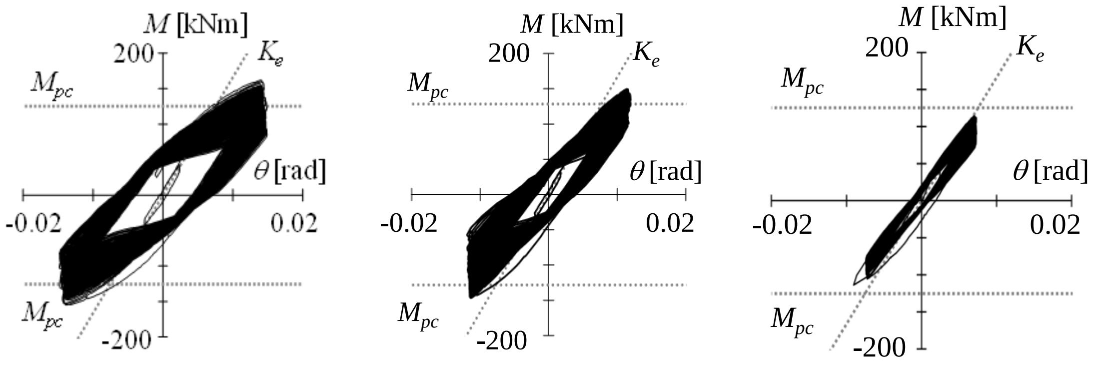

(m) C2.0_19.4_0.15_4.9 (n) C1.5_19.4_0.15_4.9 (o) C1.0_19.4_0.15_4.9

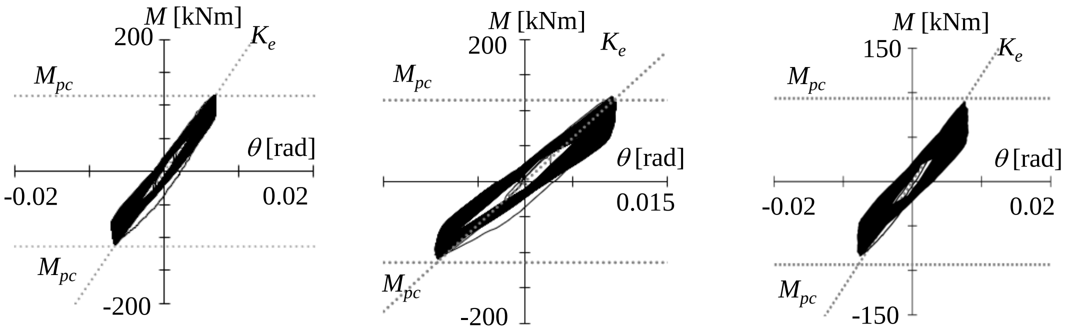

(p) C1.0_19.4_0.3_4.9 (q) C1.0_19.4_0.3_7 (r) C1.0_29.2_0.15_4.9

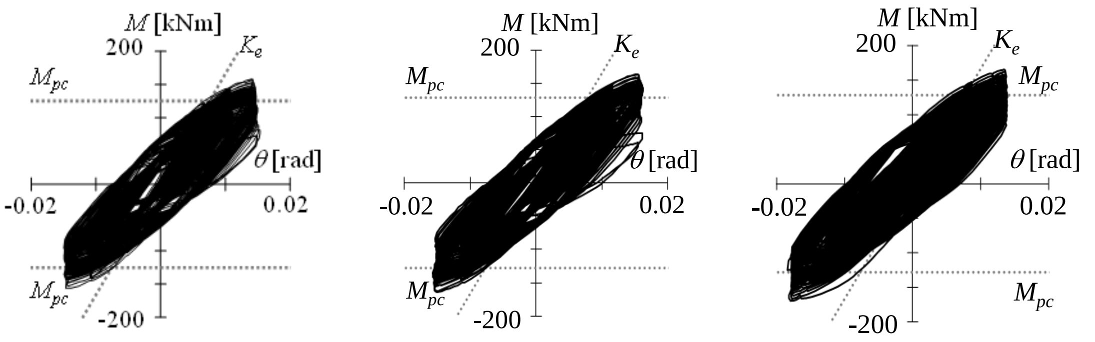

(s) Inc_19.4_0.15_4.9 (t) Inc_19.4_0_4.9 (u) Sendai_19.4_0_4.9

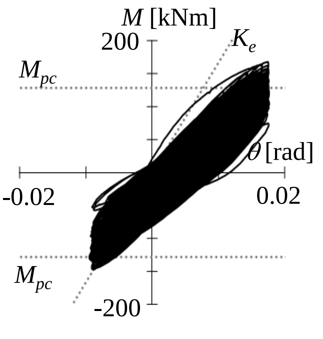

(v) Taft_19.4_0_4.9

Fig. 3-7 Moment-rotation angle relationship for SHS columns under cyclic loading

3.3.3 Strength deterioration process

To have a better knowledge of the strength deterioration behavior of the SHS columns failed due to flange fracture, the relationships between the maximum moment for each cycle (M) and the number of cycle (N) are plotted for all the specimens (the maximum strength in the whole loading process was taken as the strength deterioration starting point), as in Fig. 3-8. According to the figure, the strength started to decrease from the first several cycles for most of the specimens. Exceptions are the Specimens C1.0_19.4_0.15_3 and C1.0_19.4_0.15_4.9. The two specimens were under constant amplitude loading 1 θ_{pc}, which is rather small and the strength deterioration process is rather slow. Once there is any fluctuation in the operation during the loading process, the strength can be influenced a lot (e.g., when the actual rotation angle is larger than the target one, there will be strain hardening and the moment will increase). According to the information listed in Table 3-2, there are a certain number of cycles before the crack initiates in the corners. Strength deterioration can be observed in this range before crack initiates. Similarly, this is also caused by the cyclic softening behavior of the cold-formed steel [3-18][3-19], which is the same as the strength deterioration behavior prior to the stability limit. All the specimens saw a smooth and linear strength deterioration before approaching the flange fracture, while the strength decreases sharply in the last several cycles. This phenomenon corresponds to the crack propagation behavior mentioned in Chapter 3.3.1.

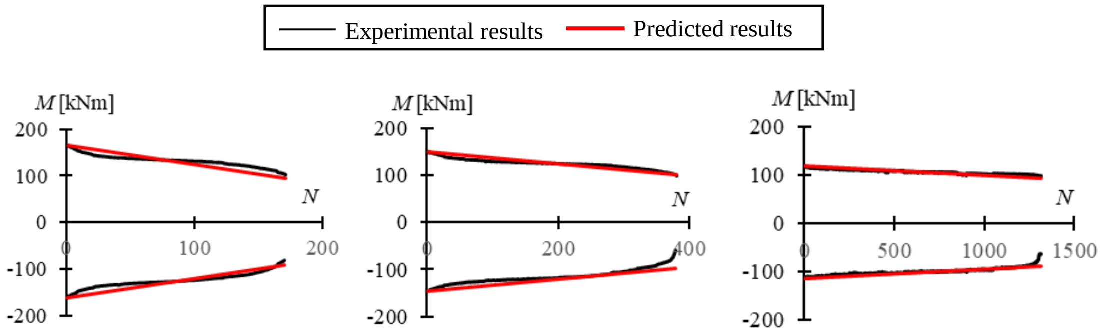

(a) C2.0_19.4_0_4.9 (b) C1.5_19.4_0_4.9 (c) C1.0_19.4_0_4.9

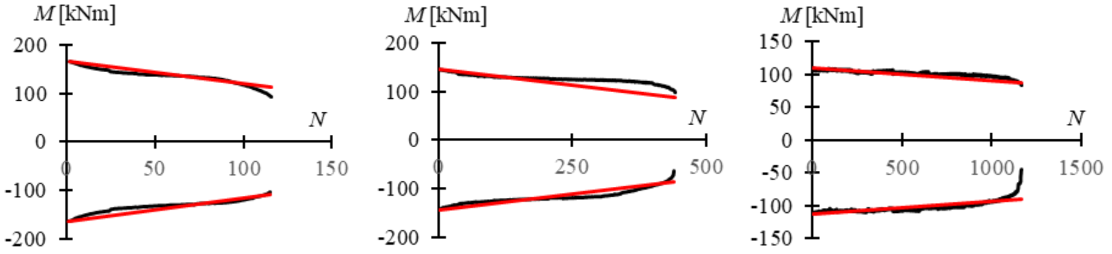

(d) C2.0_19.4_-0.15_4.9 (e) C1.5_19.4_-0.15_4.9 (f) C1.0_19.4_-0.15_4.9

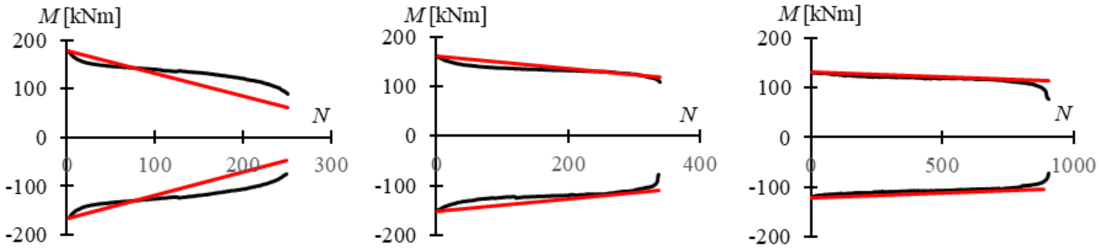

(g) C2.0_19.4_0.15_7 (h) C1.5_19.4_0.15_7 (i) C1.0_19.4_0.15_7

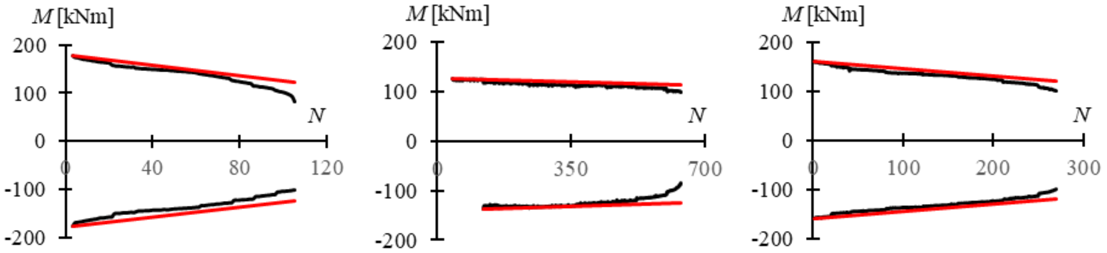

(j) C2.0_19.4_0.15_3 (k) C1.0_19.4_0.15_3 (l) C1.5_19.4_0.3_3

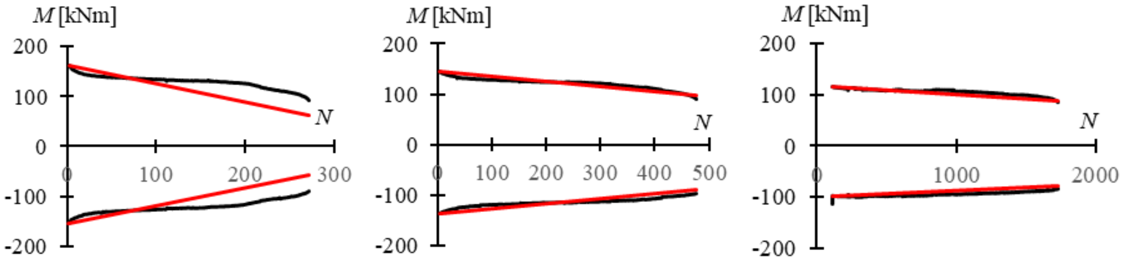

(m) C2.0_19.4_0.15_4.9 (n) C1.5_19.4_0.15_4.9 (o) C1.0_19.4_0.15_4.9

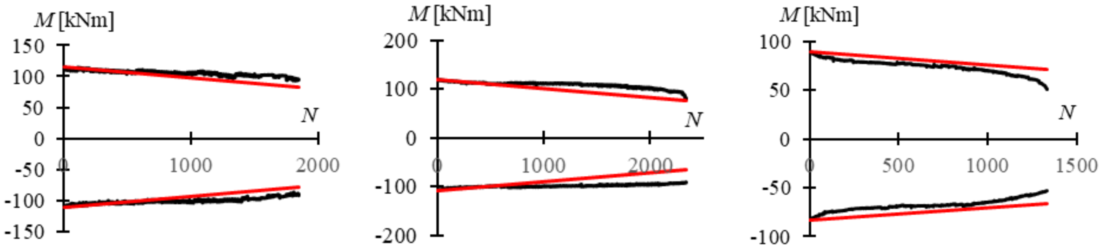

(p) C1.0_19.4_0.3_4.9 (q) C1.0_19.4_0.3_7 (r) C1.0_29.2_0.15_4.9

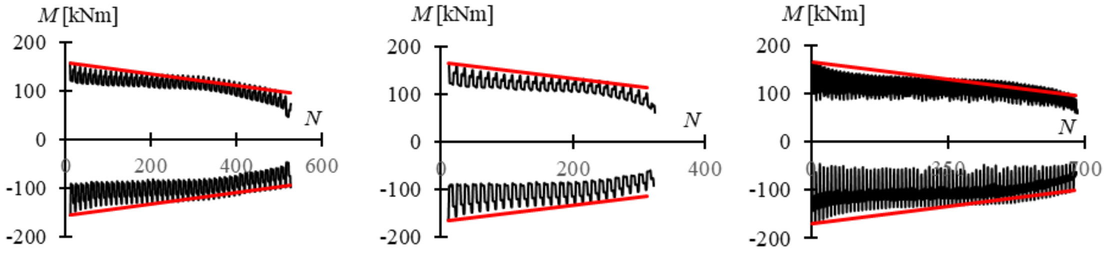

(s) Inc_19.4_0.15_4.9 (t) Inc_19.4_0_4.9 (u) Sendai_19.4_0_4.9

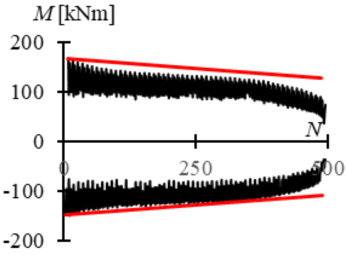

(v) Taft_19.4_0_4.9

Fig. 3-8 Strength deterioration behaviors for SHS columns failed due to low cycle fatigue

3.3.4 Stiffness deterioration

In Chapter 2.3.4, the stiffness deterioration behavior for the SHS columns failed due to local buckling has been investigated. In this Chapter, the stiffness deterioration behavior for the SHS columns failed due to flange fracture will be investigated as well.

The relationship between K/K_e and N was illustrated to study the stiffness deterioration behavior, as in Fig. 3-9. K/K_e represents the ratio of current stiffness to the initial one, and N stands for the number of cycles. According to Fig. 3-9, the stiffness of the SHS columns seem to be a constant value before the flange fracture happens. Only when the crack propagates through the flange, there is an obvious drop in the stiffness. The stiffness drop is caused by the lift-up of the cracked section in the column ends.

The stiffness deterioration behavior of the SHS columns failed due to flange fracture is quite different from those failed due to local buckling. The stiffness of the steel columns was closely related to the deformed shape caused by local buckling rather than the crack propagation in the column end. Based on the comparisons with the results in Chapter 2.3.4, stiffness deterioration can be ignorable during the crack propagation process. Only when it's close to flange fracture, the stiffness deterioration should be stressed.

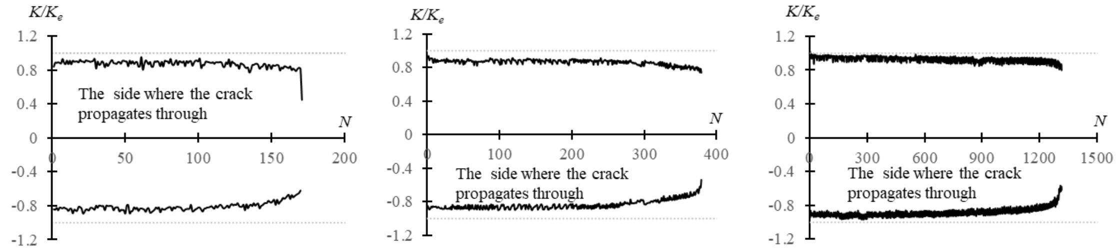

(a) C2.0_19.4_0_4.9 (b) C1.5_19.4_0_4.9 (c) C1.0_19.4_0_4.9

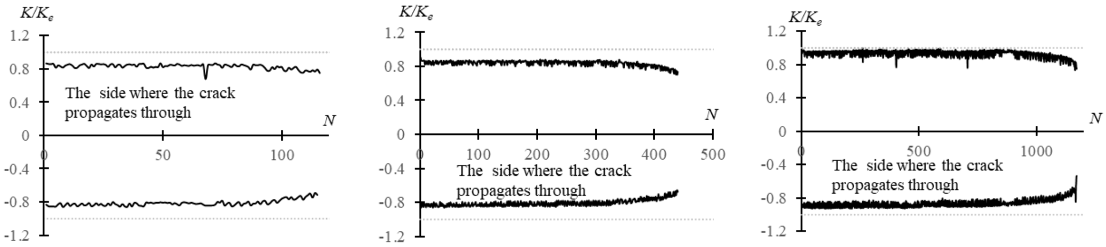

(d) C2.0_19.4_-0.15_4.9 (e) C1.5_19.4_-0.15_4.9 (f) C1.0_19.4_-0.15_4.9

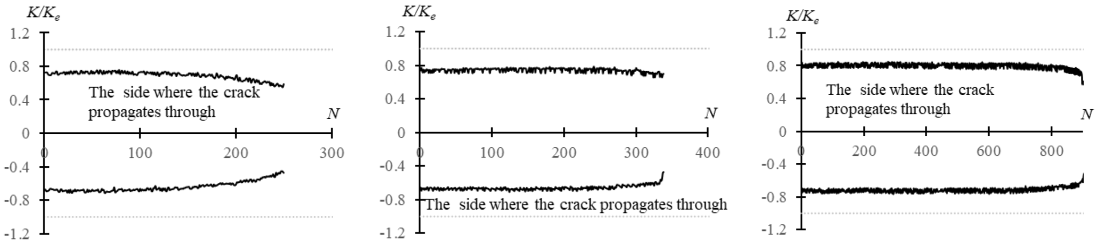

(g) C2.0_19.4_0.15_7 (h) C1.5_19.4_0.15_7 (i) C1.0_19.4_0.15_7

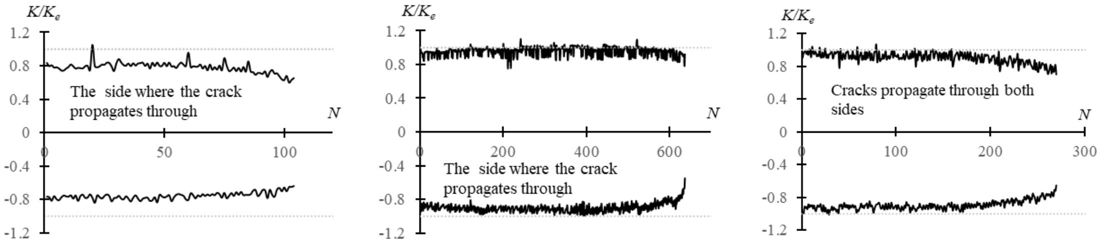

(j) C2.0_19.4_0.15_3 (k) C1.0_19.4_0.15_3 (l) C1.5_19.4_0.3_3

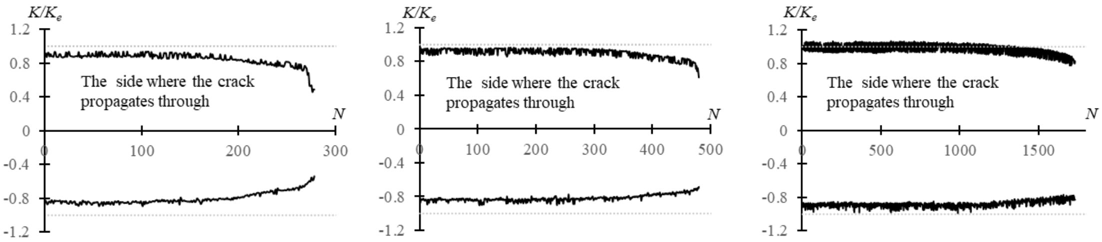

(m) C2.0_19.4_0.15_4.9 (n) C1.5_19.4_0.15_4.9 (o) C1.0_19.4_0.15_4.9

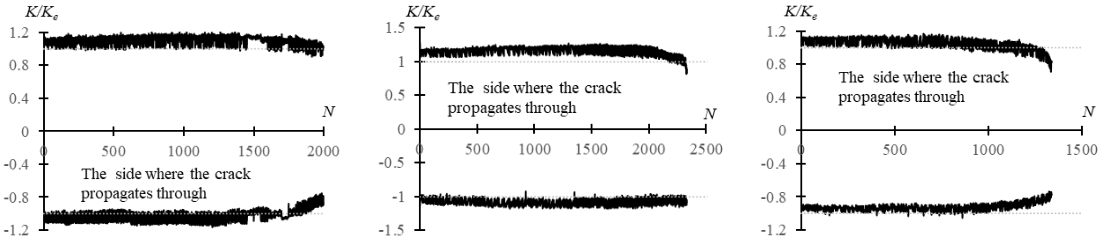

(p) C1.0_19.4_0.3_4.9 (q) C1.0_19.4_0.3_7 (r) C1.0_29.2_0.15_4.9

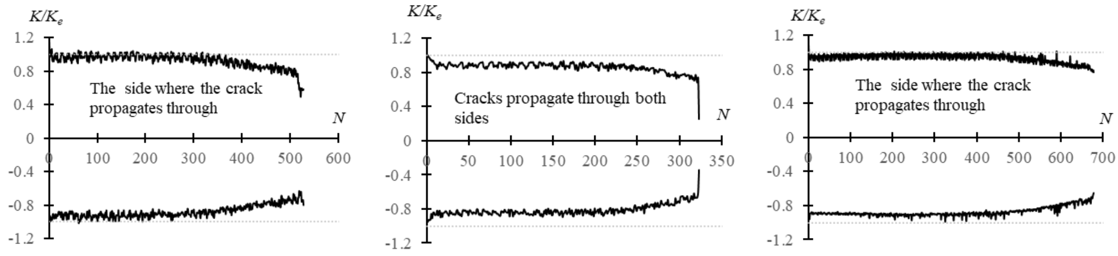

(s) Inc_19.4_0.15_4.9 (t) Inc_19.4_0_4.9 (u) Sendai_19.4_0_4.9

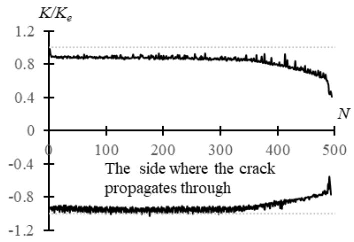

(v) Taft_19.4_0_4.9

Fig. 3-9 Stiffness deterioration behaviors for SHS columns failed due to low cycle fatigue

3.4 Fatigue life of columns subjected to small inelastic cycles

3.4.1 Fatigue life prediction based on Mason-Coffin law

The Manson–Coffin law [3-20][3-21] is a common method for predicting fatigue life (N_f) in LCF research. It is usually represented in a power function using the relationship between strain range ($\Delta\varepsilon$) and fatigue life. The definition of strain range is the same in Chapter 3.3.1, as Fig. 3-6.

The strain range was obtained from the data of the strain gauges in the test. The selection criteria for strain gauge data in this study are listed as follows:

(1) The gauge data for the flange plates of the first 20 cycles were selected, and the strain range, $\Delta\varepsilon$, for each gauge was then calculated, as shown in Fig. 3-10. According to the experimental data, strain ranges for the gauges seemed constant before the crack initiated; the strain ranges started to change when the crack propagated through the gauges, as shown inFig. 3-5. In the first 20 cycles, no crack initiation was observed for most cases.

(2) Five strain gauges were attached in each flange, as shown in Fig. 2-4. Comparing the calculated results in step 1 (strain concentration first happened in the corners of the specimens, leading to crack initiation), the strain ranges of the two gauges in the corner were always much larger than those of the middle three strain gauges, and those of the middle three gauges of both sides were quite similar. The strain distribution in the first 20 cycles for Specimen C1.0_19.4_-0.15_4.9 (Fig. 3-10) was listed as an example to

support this observation. Therefore, the average value of the strain ranges of the middle three strain gauges in the flanges of both sides was employed to represent the strain range for each specific specimen.

(3) The strain ranges from the six middle strain gauges were compared with one other to check for any incorrect measurements. If any inappropriate result was produced, the corresponding strain range would be excluded after comparison. The average value of the strain ranges of the other gauges are considered the strain range for the corresponding specimen.

Using this selection method, the empirical fatigue ductility coefficients were subsequently calibrated. The relationship between N_f and $\Delta\varepsilon$ is plotted in Fig. 3-11; the legends for the specimens are also shown. The regression function was applicable within the range of $0.003 \leq \Delta\varepsilon \leq 0.0088$:

$$N_f = 0.0017(\Delta\varepsilon)^{-2.41} \tag{3-1}$$

With the regression function developed above, the calculated and experimental N_f were compared in Fig. 3-12, where good correspondence can be obtained.

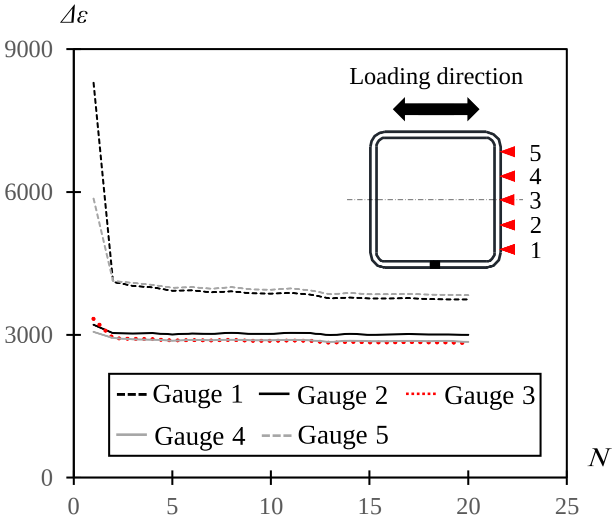

Fig. 3-10 Strain range progress of first 20 cycles for 5 strain gauges on the flange (Specimen C1.0_19.4_-0.15_4.9).

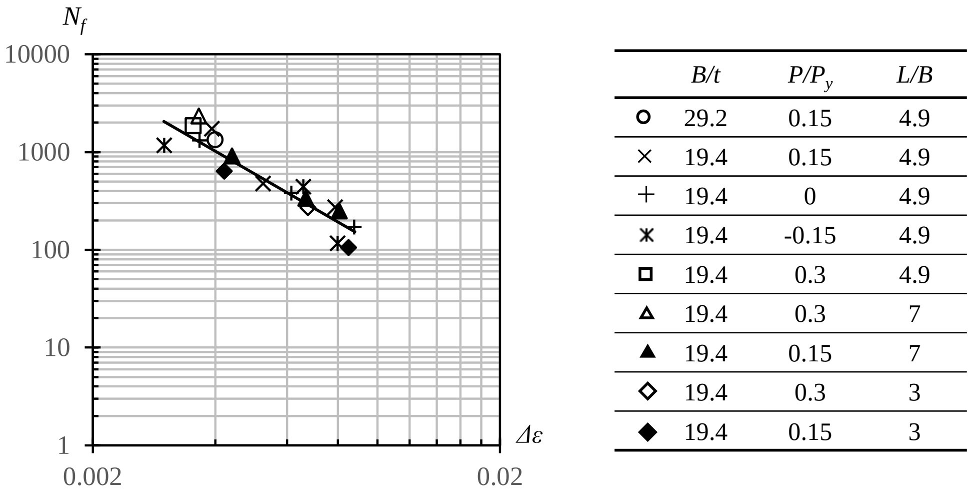

	B/t	P/P_y	L/B
○	29.2	0.15	4.9
×	19.4	0.15	4.9
+	19.4	0	4.9
✳	19.4	-0.15	4.9
□	19.4	0.3	4.9
△	19.4	0.3	7
▲	19.4	0.15	7
◇	19.4	0.3	3
◆	19.4	0.15	3

Fig. 3-11 Number of cycles to fracture N_f versus strain range $\Delta\varepsilon$.

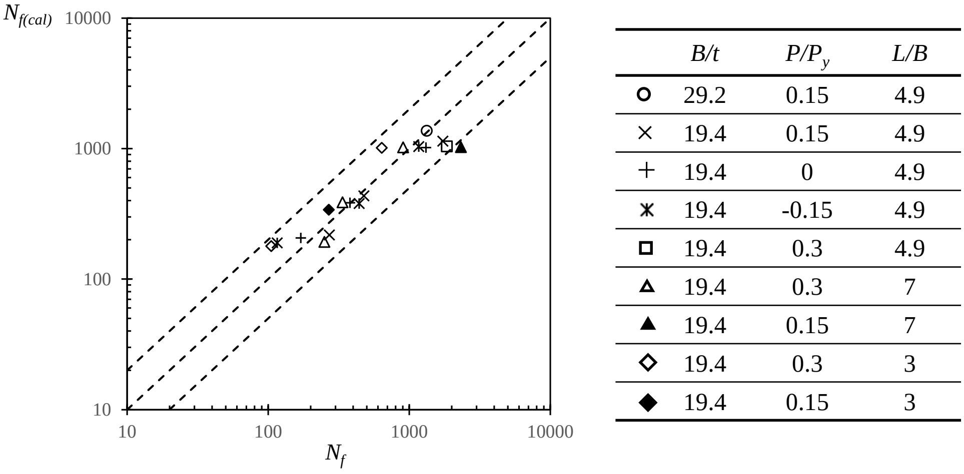

	B/t	P/P_y	L/B
○	29.2	0.15	4.9
×	19.4	0.15	4.9
+	19.4	0	4.9
✳	19.4	-0.15	4.9
□	19.4	0.3	4.9
△	19.4	0.3	7
▲	19.4	0.15	7
◇	19.4	0.3	3
◆	19.4	0.15	3

Fig. 3-12 Comparison between the experimental and calculated N_f (with strain range $\Delta\varepsilon$.).

3.4.2 Influences of different parameters on strain range

In practical engineering, as the actual strain data for structural components is generally difficult to obtain, different representative deformation parameters are chosen to establish the fatigue deformability curves for structural components under cyclic loading, i.e., the total rotation range including the elastic deformation [3-3], or only the plastic rotation range [3-4]. In this study, the rotation angle of the columns, θ, was selected as the deformation parameter for the fatigue curve, easily obtained through cyclic tests, and acted as a representative for the global deformation of the specimens.

Before creating the deformation-based fatigue curves, the relationship between $\Delta\varepsilon$ and θ, and the influence of different parameters (i.e., axial force ratio and shear span ratio) on $\Delta\varepsilon$ were clarified.

For specimens with a shear span ratio of 4.9, the axial force ratio was investigated as the main test parameter on their LCF behaviors. The strain range is 0 when there was no rotation in the column component. Therefore, the relationship between $\Delta\varepsilon$ and θ needed to start from the original point. This relationship was considered linear for specimens with the same axial force ratio based on the test data, as shown in Fig. 3-13. According to Fig. 3-13., the relationship between the strain range and rotation angle for specimens with different axial force ratios is close, and their regression functions are summarized in

Table 3-3; the slopes of these functions were found to be approximately similar. The data on the strain gauges in the center of the flange (first 20 cycles, specimens under cyclic constant amplitude 1 θ_{pc}) are also compared in Fig. 3-14. As seen in Fig. 3-14, the different axial force ratios can only influence the strain range of the first cycle for specimens failing due to LCF. The strain range for the following cycles remained a constant value. Since the specimens were subjected to small-amplitude loading, the damage caused by the first cycle was considered to have a negligible effect on the entire fatigue life of the specimens. In summary, for a specific loading amplitude, the axial force ratio has a negligible influence on the strain range during the whole loading process.

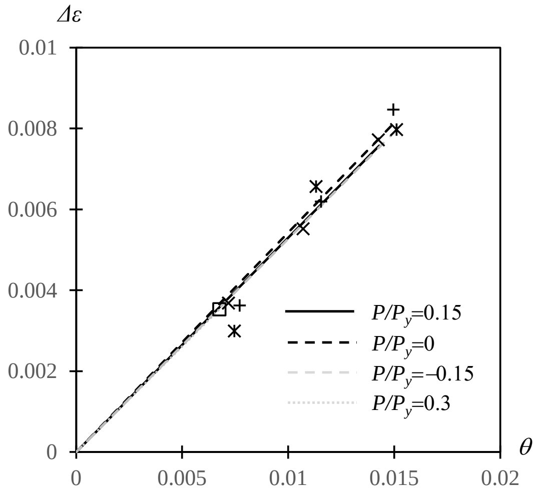

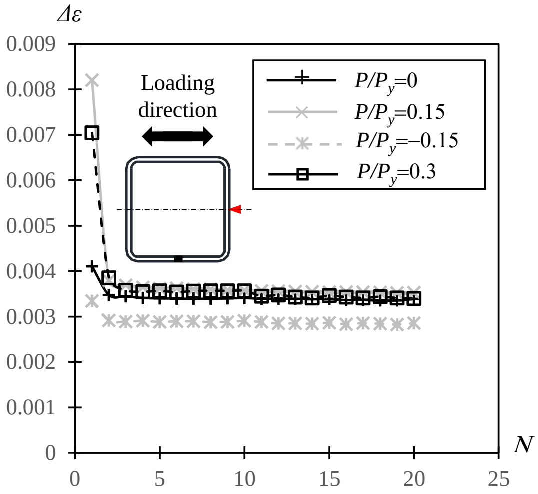

Fig. 3-13 Relationship between strain range and rotation angle for specimens with different axial force ratios.

Fig. 3-14 Strain range development process for specimens with different axial force ratios.

Table 3-3 Summary of regression functions for specimens with different axial force ratios (B/t=19.4, L/B=4.9).

Axial force ratio (P/P_y)	Regression function	Effective range	Goodness of fit (R^2)
-0.15	$\Delta\varepsilon = 0.5269\theta$	$0 \leq \theta \leq 0.0151$	R^2=0.989
0	$\Delta\varepsilon = 0.5427\theta$	$0 \leq \theta \leq 0.0150$	R^2=0.996
0.15	$\Delta\varepsilon = 0.5298\theta$	$0 \leq \theta \leq 0.0143$	R^2=0.999
0.3	$\Delta\varepsilon = 0.5227\theta$	$0 \leq \theta \leq 0.0068$	R^2=1

Based on the above discussion, the specimens with different axial force ratios were categorized into the same group (minor influence) when the LCF behaviors are investigated. Then the influence of shear span ratio on strain range was investigated as follows. The relationship between $\Delta\varepsilon$ and θ for specimens with different shear span ratios is shown in Fig. 3-15, wherein they seem to be approximately linear for a specific shear span ratio. For a specific loading amplitude, the strain range decreased as the shear span ratio increased. With the change in shear span ratio, the moment in the bottom end was different even though it was subjected to the same loading amplitude, consequently causing the differences in the strain ranges. The regression functions for the specimens with different shear span ratios are summarized in Table 3-4. These functions were used to predict the strain range using only the rotation angle. Based on the test data, the effective ranges for the regression functions (☐–175×175×9, *L*/*B*=3), (☐–175×175×9, *L*/*B*=4.9), and (☐–175×175×9, *L*/*B*=7) were $0 \leq \theta \leq 0.011$, $0 \leq \theta \leq 0.015$, and $0 \leq \theta \leq 0.021$, respectively.

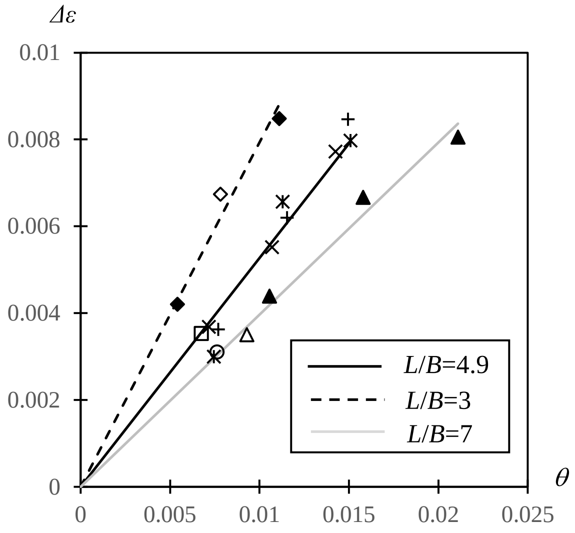

	B/t	P/P_y	*L/B*
○	29.2	0.15	4.9
×	19.4	0.15	4.9
+	19.4	0	4.9
⋇	19.4	-0.15	4.9
□	19.4	0.3	4.9
△	19.4	0.3	7
▲	19.4	0.15	7
◇	19.4	0.3	3
◆	19.4	0.15	3

Fig. 3-15 Relationship between strain range and rotation angle for specimens with different shear span ratios.

Table 3-4 Summary of regression functions for specimens with different shear span ratios.

Shear span ratio (*L/B*)	Regression function	Effective range	Goodness of fit (R^2)
3	$\Delta\varepsilon = 0.7933\theta$	$0 \leq \theta \leq 0.011$	$R^2=0.997$
4.9	$\Delta\varepsilon = 0.5272\theta$	$0 \leq \theta \leq 0.015$	$R^2=0.993$
7	$\Delta\varepsilon = 0.3965\theta$	$0 \leq \theta \leq 0.021$	$R^2=0.998$

3.4.3 Relationship between fatigue life and rotation angle

Based on the discussion in Chapter 3.4.2, the strain range can be replaced with the rotation angle in the fatigue curves. The relationship between the N_f and θ is discussed below. The empirical regression functions for specimens with different shear span ratios are represented as follows. The effective ranges for Eqs. (3-2), (3-3) and (3-4) are $0.0054 \leq \theta \leq 0.011$, $0.0068 \leq \theta \leq 0.015$, and $0.0093 \leq \theta \leq 0.021$, respectively. Based on the regression functions obtained above, the N_f was calculated with them and compared with the experimental ones, as shown in Fig. 3-17, where good prediction accuracy can be obtained for the fatigue life.

As seen in Fig. 3-16, the N_f for the specimens with moderate local buckling (Specimens C2.0_19.4_0.15_4.9 and C2.0_19.4_0.15_7.0, enclosed in red squares) were usually higher than those predicted with regression functions, indicating that local buckling had an unignorable influence on the LCF life (i.e., increase in the LCF life). For specimens without local buckling, the strain was concentrated in the flanges of the column bottom sections; for those with local buckling, it was concentrated in the local buckling region, making it more difficult for crack initiation and propagation in the flanges, subsequently increasing the LCF life.

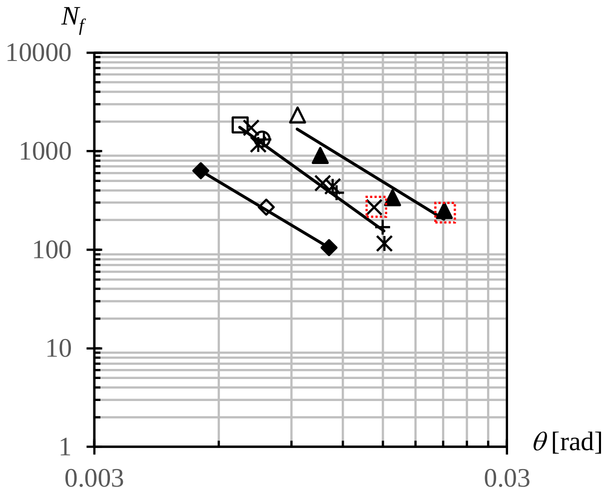

	B/t	*P/P$_y$*	*L/B*
○	29.2	0.15	4.9
×	19.4	0.15	4.9
+	19.4	0	4.9
✱	19.4	-0.15	4.9
□	19.4	0.3	4.9
△	19.4	0.3	7
▲	19.4	0.15	7
◇	19.4	0.3	3
◆	19.4	0.15	3

Fig. 3-16 Number of cycles to fracture N_f versus rotation angle θ.

$$N_f = 0.0013(\theta)^{-2.51},\ \mathrm{R}^2=1,\ L/B = 3 \tag{3-2}$$

$$N_f = 0.0005(\theta)^{-3.02},\ \mathrm{R}^2=0.98,\ L/B = 4.9 \tag{3-3}$$

$$N_f = 0.0101(\theta)^{-2.57},\ \mathrm{R}^2=0.91,\ L/B = 7 \tag{3-4}$$

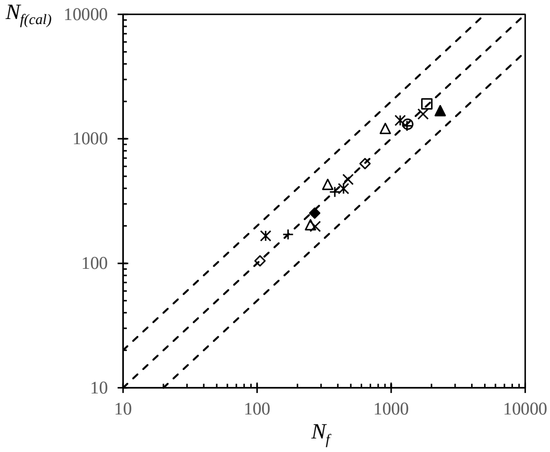

	B/t	P/P_y	L/B
○	29.2	0.15	4.9
×	19.4	0.15	4.9
+	19.4	0	4.9
✱	19.4	-0.15	4.9
□	19.4	0.3	4.9
△	19.4	0.3	7
▲	19.4	0.15	7
◇	19.4	0.3	3
◆	19.4	0.15	3

Fig. 3-17 Comparison between the experimental and calculated N_f (with rotation angle θ).

Based on the discussion above, the relationship between the number of cycles to fracture and strain range can predict fatigue life regardless of the parameters used; however, it is difficult to get data on the strain for each structural component in practical engineering. Although the independent variable θ in the N_f–θ relationship can be easily obtained, clarifying this relationship for each specimen with each specific shear span ratio is infeasible. A method that can predict fatigue life with only the rotation angle will be highly convenient for practical application. The relationship between N_f and θ/θ_{pc} was also applied in other research [3-5][3-6], and its efficiency was proved. Therefore, the relationship between the strain range $\Delta\varepsilon$ and normalized rotation angle θ/θ_{pc} was investigated. Similar to the relationship between $\Delta\varepsilon$ and θ, this relationship had to be formed from the original point. Then, a linear relationship with a high goodness of fit (R^2=0.994) was calibrated as shown in Eq. (3-5) and Fig. 3-18. The independent variable $\Delta\varepsilon$ in the relationship between N_f and $\Delta\varepsilon$ was replaced with θ/θ_{pc} subsequently, as shown in Fig. 3-19. The relationship between N_f and θ/θ_{pc} was calibrated as Eq. (3-6), obtaining an acceptable goodness of fit (R^2=0.75). Within the scope of the test results in this study, the effective range for Eq. (3-6) is $0.96 \le \theta/\theta_{pc} \le 2.1$. Based on the regression functions obtained above, the N_f was calculated with it and compared with the experimental ones, as shown in Fig. 3-20, where good prediction accuracy can be obtained for the fatigue life.

In summary, the fatigue life for specimens under cyclic constant amplitude loading can be predicted with relatively high accuracy with only a normalized rotation angle.

$$\Delta\varepsilon = 0.004(\theta / \theta_{pc}) \tag{3-5}$$

$$N_f = 1284.6(\theta / \theta_{pc})^{-3} \tag{3-6}$$

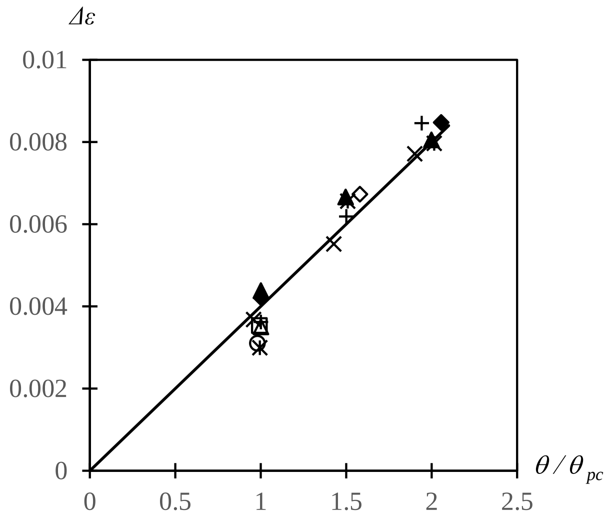

	B/t	P/P_y	*L/B*
○	29.2	0.15	4.9
×	19.4	0.15	4.9
+	19.4	0	4.9
*	19.4	-0.15	4.9
□	19.4	0.3	4.9
△	19.4	0.3	7
▲	19.4	0.15	7
◇	19.4	0.3	3
◆	19.4	0.15	3

Fig. 3-18 Relationship between strain range $\Delta\varepsilon$ and normalized rotation angle θ/θ_{pc}.

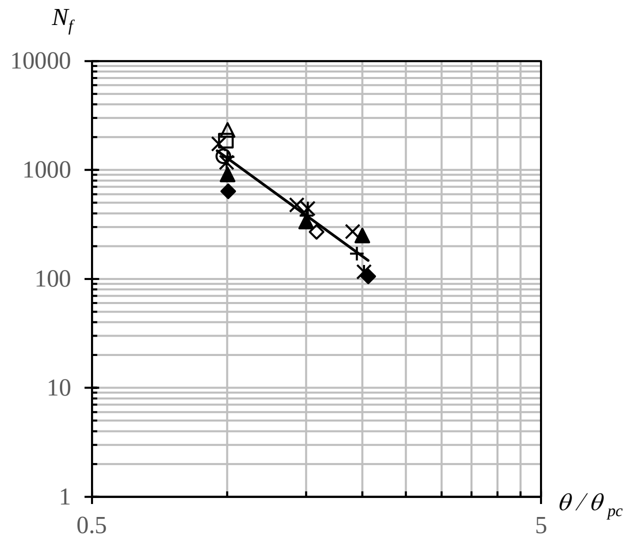

	B/t	P/P_y	*L/B*
○	29.2	0.15	4.9
×	19.4	0.15	4.9
+	19.4	0	4.9
*	19.4	-0.15	4.9
□	19.4	0.3	4.9
△	19.4	0.3	7
▲	19.4	0.15	7
◇	19.4	0.3	3
◆	19.4	0.15	3

Fig. 3-19 Number of cycles to fracture N_f versus normalized rotation angle θ/θ_{pc}.

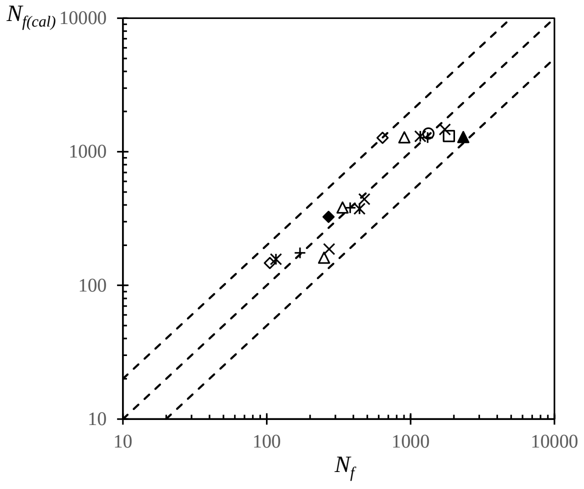

	B/t	P/P_y	L/B
○	29.2	0.15	4.9
×	19.4	0.15	4.9
+	19.4	0	4.9
⁎	19.4	-0.15	4.9
□	19.4	0.3	4.9
△	19.4	0.3	7
▲	19.4	0.15	7
◇	19.4	0.3	3
◆	19.4	0.15	3

Fig. 3-20 Comparison between the experimental and calculated N_f (with normalized rotation angle θ/θ_{pc}).

3.4.4 Fatigue life prediction under random loading

The relationships in Chapter 3.4.3 were established for SHS columns under cyclic constant amplitude loading and could be further extended to cyclic variable amplitude loading in combination with the rainflow counting method and Miner's rule. The damage was assumed to accumulate linearly until the fracture propagated through the flange of the column bottoms. It was assumed that no obvious local buckling would occur in the whole loading process. Based on the above assumptions, the damage caused by each rotation range was calculated as below:

$$D = \sum_{i=1} \frac{n_i}{N_{f(i)}} \tag{3-7}$$

where n_i is the number of cycles for a specific loading amplitude-i (θ_i). When the damage index D reached 1.0, the specimen reached its fatigue life. The steps to predict the number of cycles to fracture for SHS columns under random loading are summarized as below.

(1) Input the loading history and get the rotation range using the rainflow counting method;

(2) Calculate the $N_{f(i)}$ for corresponding loading amplitude θ_i using Eqs. (3-2)- (3-4) or Eq. (3-6);

(3) Calculate the damage accumulation using Eq. (3-7); when D reaches 1.0, the number of cycles to fracture N_f can be obtained.

The number of cycles to fracture N_f were calculated using both the regular rotation angle and the normalized one. As shown in Fig. 3-21, the calculated damage accumulation for the specimens under random cyclic loading was calculated with an acceptable error for this evaluation method.

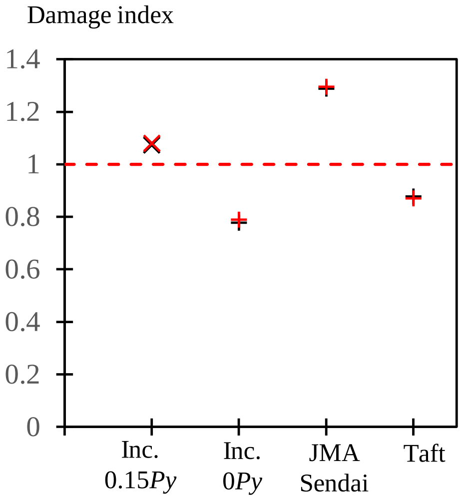

Fig. 3-21 Calculated damage index for the specimens.

3.5 Strength prediction method based on regression function

3.5.1 Definition of crack propagation in each stage

In this study, the crack propagation was monitored with photographs every several cycles. The crack length was approximately evaluated by comparing the relative position of the crack with the strain gauges and the grids. In Fig. 3-22, the width of the black tapes on the strain gauges is close to that of the grids, which is 20 mm. The crack propagation to the edge of the black tape can be clearly observed in the photographs. Four stages were defined during the whole loading process: crack initiation (stage 1) and crack propagation through the corner gauge (stage 2), middle gauge (stage 3), and the entire flange (stage 4), as illustrated in Fig. 3-22. The maximum moment of each cycle was selected to represent the strength deterioration behavior of the columns in each stage. The crack length for each stage is marked in Fig. 3-23. The photographs for each corresponding stage are shown as in Fig. 3-24.

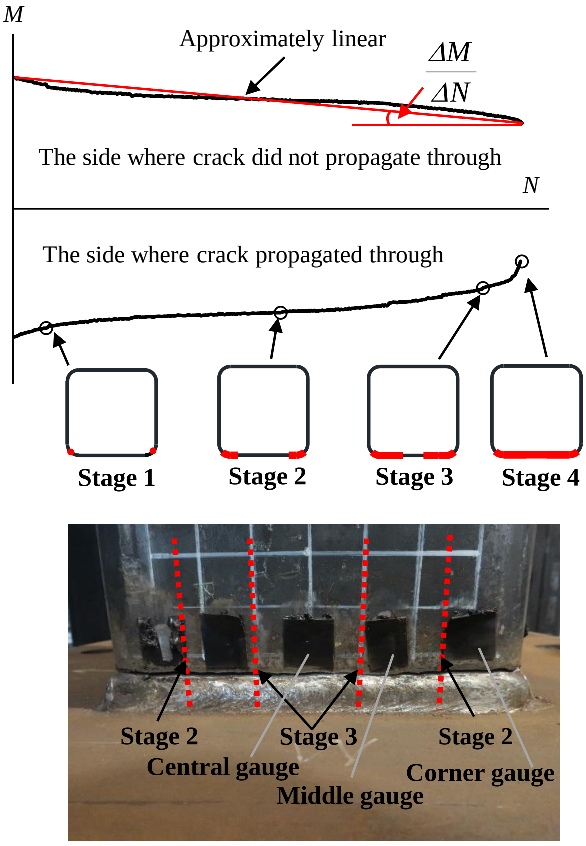

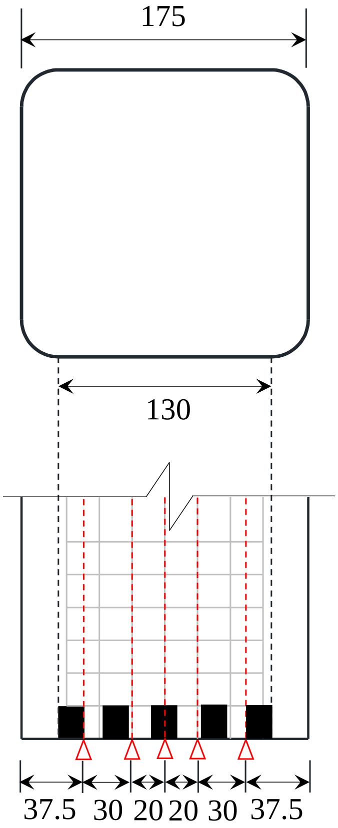

Fig. 3-22 Definition of crack propagation stage.

Fig. 3-23 Length of the crack for each stage.

(a) Stage 1

(b) Stage 2

(c) Stage 3

Fig. 3-24 Photographs for each crack propagation stage.

3.5.2 Constant amplitude loading

As discussed in Chapter 3.1, the failure of strength deterioration behaviors of steel columns due to fractures were not studied in enough detail. The strength deterioration for the specimens that failed due to crack propagation in the flange was investigated to clarify this problem. The test results revealed that the strength approximately decreased linearly with the increasing number of cycles before the crack propagated through the flange; there was a clear drop in lateral load bearing capacity during the crack propagated through the flange, as shown in Fig. 3-22. The strength deterioration rate obtained before crack propagates through was used for residual strength prediction as the number of cycles to fatigue were already predicted with high accuracy using several parameters in Chapter 3.4.

The strength deterioration rate for both sides was nearly the same before the rapid crack propagation in the flange, as shown in Fig. 3-8. During rapid crack propagation, there was a sudden change in the strength deterioration rate. The side where crack did not propagate through was selected to improve the prediction of the strength deterioration rate as the strength deterioration rate $\Delta M/\Delta N$ was almost constant during the loading process, as shown in Fig. 3-22. A relationship between the normalized strength deterioration rate and the normalized rotation angle was created to check the influence of the loading amplitude without considering the other parameters, as shown in Fig. 3-25. The regression function was calibrated subsequently as below:

$$\frac{\frac{\Delta M}{\Delta N}}{M_{pc}} = 0.00016\left(\frac{\theta}{\theta_{pc}}\right)^{4.53} \tag{3-8}$$

Good correspondence can be obtained for Eq. (3-8), where $R^2 = 0.905$. Based on the test data in this study, the effective range for the empirical regression function was $0.96 \leq \theta/\theta_{pc} \leq 2.1$, which can only be applied to specimens failing due to flange fracture.

With the regression function, the predicted deterioration trends for all the specimens can be obtained as shown in Fig. 3-8 (a)-(r) compared with the experimental ones. From the comparison, good correspondence can be obtained for most of the specimens. For specimens with moderate local buckling (Specimens C2.0_19.4_0.15_4.9 and C2.0_19.4_0.15_7.0), the predicted results were relatively smaller than the experimental ones, as shown in Fig. 3-8 (g) and (m). The fatigue life increased owing to local buckling, which caused the actual deterioration rate was smaller than the predicted ones. For these specimens, the prediction results were in the safe side. For specimens with minor local buckling (Specimens C2.0_19.4_0.15_3.0), the predicted strength deterioration trends were similar to the experimental ones.

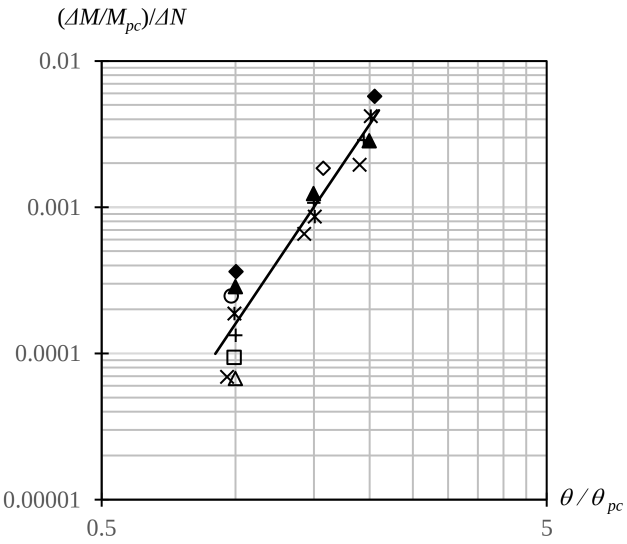

Fig. 3-25 Relationship between the normalized strength deterioration rate and the normalized rotation angle.

3.5.3 Variable amplitude loading

The rainflow counting method was used in combination with the method discussed in Chapter 3.4.4 for specimens under variable amplitude loading and obtain their rotation ranges. The strength deterioration rates $(\Delta M/\Delta N)_i$ for each loading amplitude i (θ_i) was calculated using Eq. (3-8). The strength deterioration was calculated by multiplying the number of cycles N_i and strength deterioration rates $(\Delta M/\Delta N)_i$. The total strength deterioration was then summed up, and the strength for the last cycle was obtained, as shown in Eqs. (3-9) and (3-10). The deterioration trend for the maximum loading amplitude in certain variable loading histories can be obtained by connecting the maximum strength and the one for the last set, reflecting the potential maximum lateral load resistance for each stage (within the maximum loading amplitude in the loading history). The predicted strength deterioration trends for the maximum loading amplitude were compared with the experimental results, as shown in Fig. 3-8 (s)–(v), where the envelope represents the predicted trends within acceptable error. The strength deterioration prediction method can be further applied to the hysteretic model for steel columns that failed due to flange fracture. A clear strength deterioration rule can be established for hysteretic models in future studies based on the method developed in Chapter 3.5.

$$\mathit{\Delta} M = \sum_{i=1} \left(\frac{\mathit{\Delta} M}{\mathit{\Delta} N} \right)_i \cdot N_i \tag{3-9}$$

$$M_i = M_{peak} - \mathit{\Delta} M \tag{3-10}$$

3.6 Strength prediction method based on section loss

As discussed in Chapter 3.5, strength deterioration can be observed during the loading process in this study. It is closely related to the crack propagation in the flange plate. In practice, local buckling in the columns can always play a warning role after seismic excitation. However, engineers cannot estimate the residual lateral load-bearing capacity quantitatively even when the cracks in the column end are observed, making cracks the greater potential threats to structural safety. If the strength deterioration can be evaluated quantitively by the crack propagation level, the structures can be reinforced in time. A residual strength prediction method, based on the concept of section loss in the column end, is proposed for specimens that failed due to flange fracture. The following assumptions were made based on the observed crack propagation in the specimens during the loading process:

(1) No local buckling occurred during the loading process.

(2) The whole section was in the fully plastic state, and the stress-strain relationship was considered to be the ideal elastoplastic model.

(3) The cracks initiated at the corners.

(4) The cracks propagated symmetrically in the flange and through the thickness direction of the flange.

(5) The cracks mainly propagated in the flange rather than in the web; the crack in the web can be ignored.

(6) The propagation of the cracks won’t influence the lateral load-bearing capacity on the compressive side.

In this study, the decrease in the lateral load resistance was considered to be caused by the loss of the section (i.e., the decrease in the plastic section modulus). The ratio of the residual strength (M_r) to the maximum strength (M_m) was approximately the same as the plastic moment of the cracked/uncracked section, as shown below. M_{pc}^{*} stands for the plastic moment of the cracked section, considering the axial force. The residual strength can be predicted subsequently if the plastic moment of the cracked section can be calculated. The calculation process is as follows:

$$\frac{M_r}{M_m}=\frac{M_{pc}^{*}}{M_{pc}} \tag{3-11}$$

The plastic section modulus for the cracked section was calculated first. The configuration of the cracked section is shown in Fig. 3-26. According to the design code [3-22], the neutral axis locates in the web of the section when $P/P_y \leq A_w/A$. In this study, the section was square-shaped, and the value of A_w/A was around 0.5; this ratio became larger with crack propagation. Therefore, the plastic neutral axis lies on the web for all the cases in this study. The decomposition of the moment and axial force are represented in Fig. 3-26. The position of the plastic neutral axis can be calculated subsequently.

$$(B-2t)t+2yt=(B-t-y)2t+(B-2x)t \tag{3-12}$$

$$y=\frac{B-x}{2} \tag{3-13}$$

The position for the centers of gravity of the compressive and tensile parts are calculated below. The definition for each parameter is illustrated in Fig. 3-27, where G_c and G_t are the centers of gravity of the compressive and tensile parts, respectively; C and T are the compressive and tensile resultants, respectively; and $\bar{y}_c$ and $\bar{y}_t$ are the distance from the neutral axis to the centers of gravity of the compressive and tensile parts, respectively.

$$\bar{y}_c=\frac{(B-2t)t\times(y-\frac{t}{2})+yt\times\frac{y}{2}\times 2}{(B-2t)t+2yt}=\frac{(B-2t)\times(y-\frac{t}{2})+y^2}{B-2t+2y} \tag{3-14}$$

$$\bar{y}_t = \frac{(B-t-y)t\times\frac{1}{2}(B-t-y)\times 2+(B-2x)t\times(\frac{t}{2}+B-t-y)}{(B-t-y)t\times 2+(B-2x)t} = \frac{(B-t-y)^2+(B-2x)(B-\frac{t}{2}-y)}{B-2t+2y} \tag{3-15}$$

The distance between the centers of gravity of the compressive and tensile parts can be obtained as follows:

$$\bar{y} = \bar{y}_c + \bar{y}_t \tag{3-16}$$

The plastic section modulus of the cracked section, Z_p^*, where A^* stands for the area of the cracked section, and the plastic moment of the cracked section without considering the axial force, M_p^*, are calculated as follows:

$$Z_p^* = \frac{A^*}{2}\bar{y} \tag{3-17}$$

$$M_p^* = \sigma_y Z_p^* \tag{3-18}$$

The plastic section modulus of the uncracked section, Z_p, and the plastic moment of the uncracked section without considering the axial force, M_p, can be calculated as [3-22]:

$$Z_p = Bt(B-t)+\frac{1}{2}(B-2t)^2 t \tag{3-19}$$

$$M_p = \sigma_y Z_p \tag{3-20}$$

For the column components, the influence of the axial force ratio was considered in the calculation of the lateral load resistance. The distance between the centroidal axis of the section and the plastic neutral axis (Fig. 3-26) can be calculated as follows:

$$y_0 = \frac{P}{4t\cdot\sigma_y} \tag{3-21}$$

Finally, the plastic moment, when considering the axial force for both the cracked and uncracked sections, can be obtained as follows:

$$M_{pc}^{*} = M_{p}^{*} - 2t \cdot y_0^2 \cdot \sigma_y \tag{3-22}$$

$$M_{pc} = M_{p} - 2t \cdot y_0^2 \cdot \sigma_y \tag{3-23}$$

Based on the definition of different crack propagation stages in Section 3.5.1, three different crack lengths were employed: x = 37.5, 67.5, and 87.5 mm. The residual strength for the stages of all the specimens were summarized and compared with the predicted results, as shown in Fig. 3-28. As seen in Fig. 3-28, the proposed method can predict the residual strength of specimens subjected to both constant and variable amplitude loading with an acceptable error rate. Owing to the decrease in the loading amplitude, the results from the prediction method were relatively conservative.

This method can effectively evaluate the lateral load resistance of steel columns after an earthquake. The crack propagation in the column components can not only influence the functionality of the columns but also the lateral load resistance. The lateral load resistance can only be evaluated by measuring the length of the crack with the proposed method to avoid the excessive lateral load bearing capacity loss caused by crack propagation.

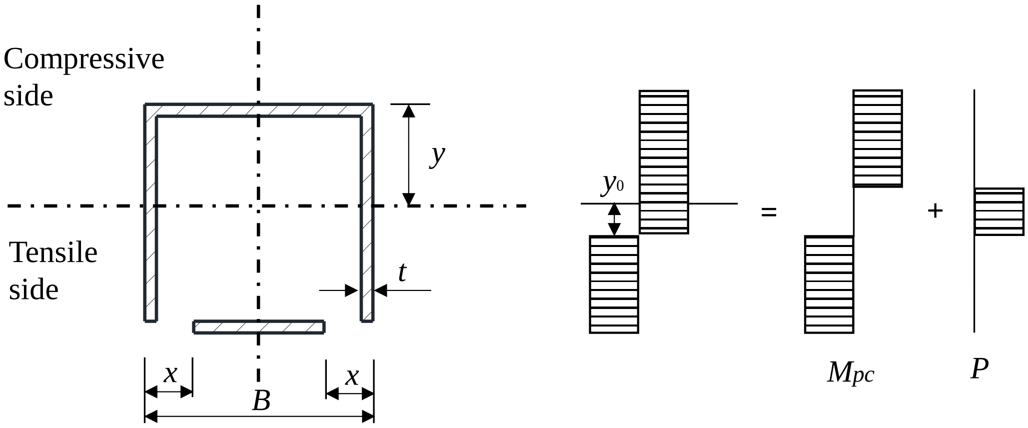

Fig. 3-26 Effective section considering axial force.

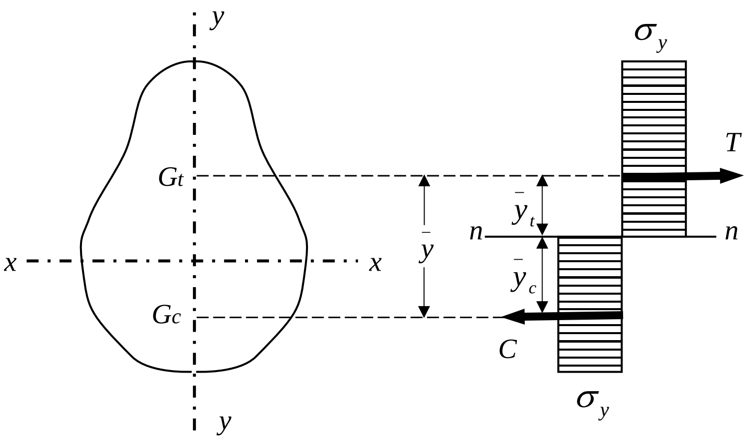

Fig. 3-27 Stress distribution and resultants of section in fully plastic status.

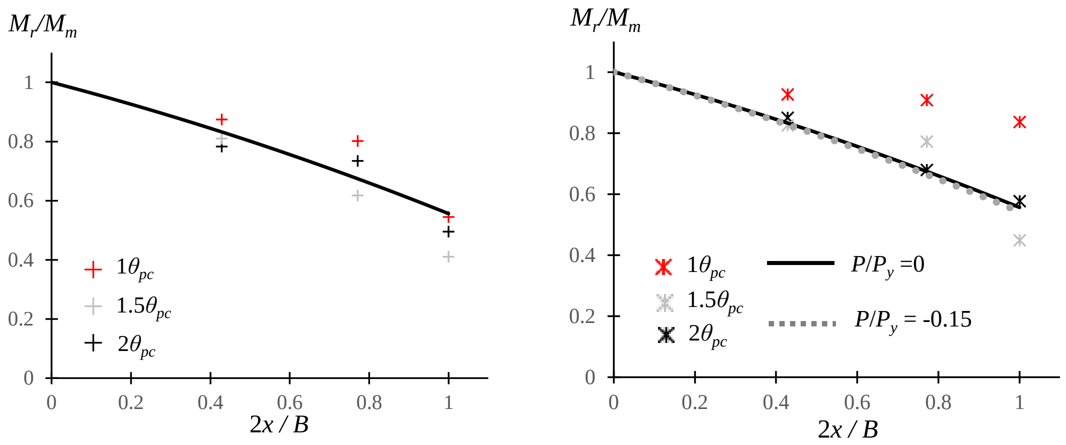

(a) B/t=19.4, P/P_y=0, L/B=4.9

(b) B/t=19.4, P/P_y=-0.15, L/B=4.9

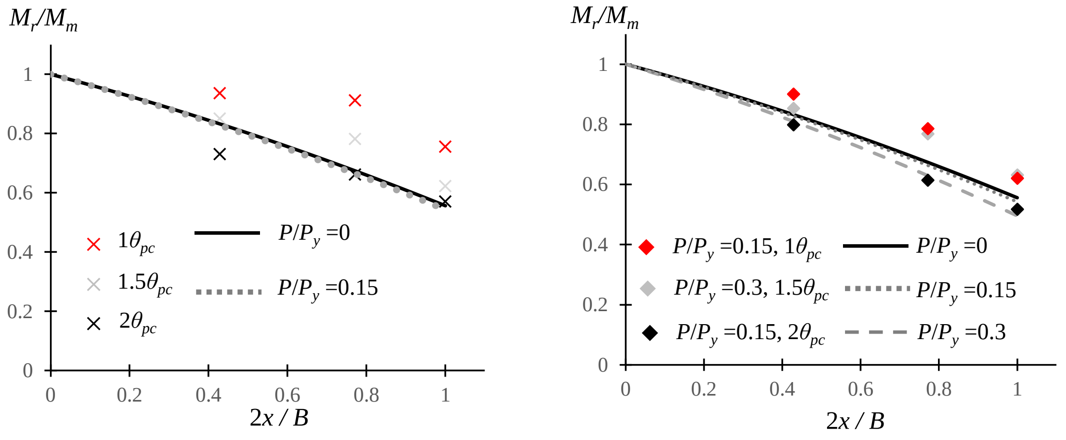

(c) B/t=19.4, P/P_y=0.15, L/B=4.9

(d) B/t=19.4, L/B=3

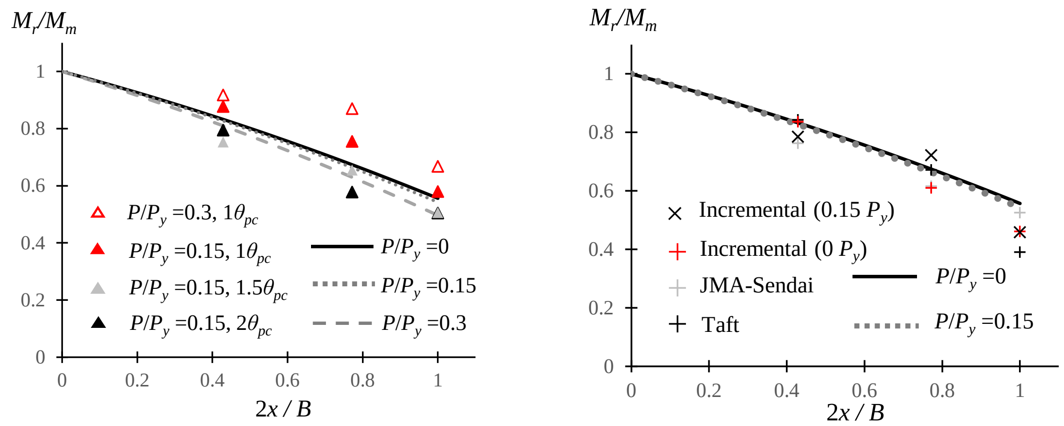

(e) *B*/*t*=19.4, *L*/*B*=7 (f) Variable amplitude loading

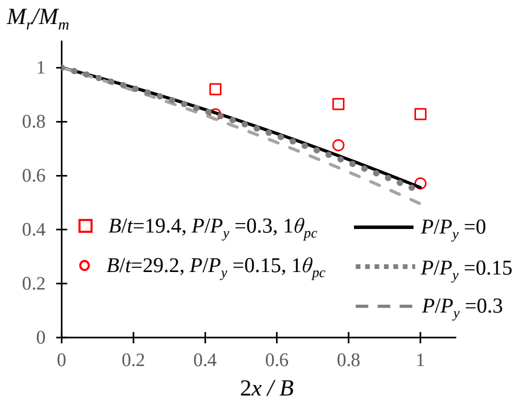

(g) Other specimens

Fig. 3-28 Comparison between the tested and predicted results.

3.7 The transformation boundaries between local buckling and flange fracture

For the SHS columns subjected to a large number of small inelastic cycles, two failure modes were clarified, i.e., local buckling (Chapter 2) and flange fracture (Chapter 3). Due to the different hysteretic behaviors owing to different failure modes, these specimens were analyzed separately. In practice, the loading history can be random and very complicated for the structural components under seismic excitation. If we want to analyze the cumulative damage and strength deterioration level for one specific SHS column with the methods proposed in Chapters 2 and 3, a method to distinguish the different failure modes has to be developed first. In other words, the failure modes transformation boundary has to be found based on the current experimental database. In this Chapter, the failure modes transformation boundary will be investigated.

The method to predict the number of cycles to the stability limit, N_{cr}, has been proposed in Chapter 2. The stability limit was considered as the boundary for excessive strength deterioration. We can consider the N_{cr} as a limit status for the specimens failed due to local buckling. In Chapter

3, the method to predict the number of cycles to flange fracture, N_f, based on the normalized rotation angle was also developed. We can consider the N_f as a limit status for the specimens failed due to flange fracture. The N_{cr} prediction method for each series of specimens is plotted together with specimens failed due to flange fracture together, as shown in Fig. 3-29. According to Fig. 3-29, when the loading amplitude decreases, the points on the N_{cr} prediction method approaches closer to the prediction curve for N_f. When the loading amplitude is smaller than the intersection point of the two curves, the failure mode changes from local buckling to flange fracture. The intersection point from the two methods can be considered as the critical status between the two failure modes.

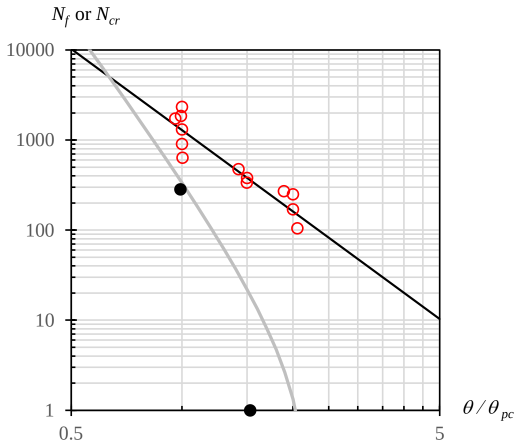

(a) 175-6-0.3P_y-4.9 (b) 175-6-0.15P_y-4.9

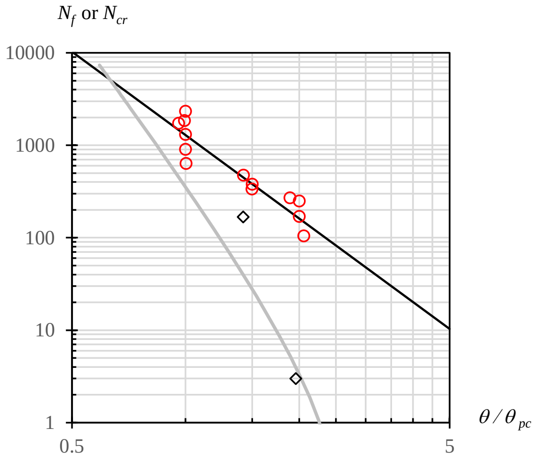

(c) 200-6-0.2P_y-4.3 (d) 175-9-0.3P_y-4.9

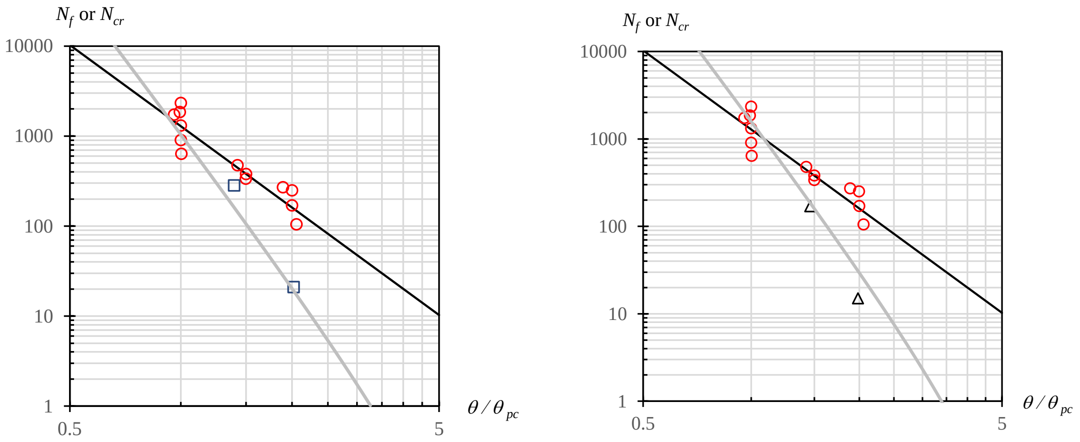

(e) 200-9-0.35P_y-4.3 (f) 175-9-0.3P_y-7

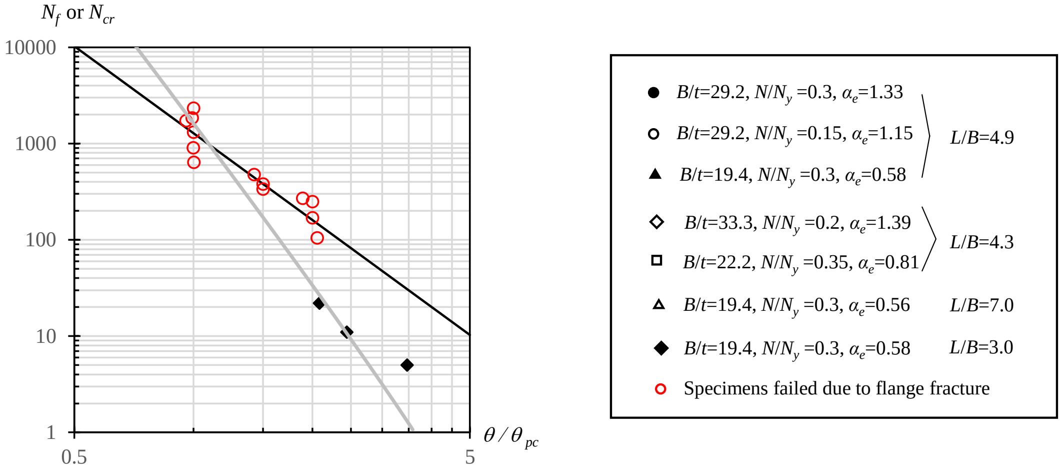

(g) 175-9-0.3P_y-3

Fig. 3-29 The relationships between N_f or N_{cr} and normalized rotation angle for each series of specimens.

The method to predict N_f (Eq. (3-6)) only depends on the normalized rotation angle θ / θ_{pc}, while there are more influential factors on the method to predict N_{cr}. Based on Eq. (2-17), N_{cr} can be represented as follows.

$$N_{cr} = \frac{\left(\frac{10.23}{\alpha_e} - 2.86\right)\left[1 - \frac{\theta}{\theta_p}\left(\frac{1}{-1.03\left(\alpha_e \bullet L / B\right) + 8.66}\right)\right]}{0.0079\left(\frac{\theta}{\theta_{pc}}\right)^{5.36}} \tag{3-24}$$

From the expression, N_{cr} is influenced by the configuration (width-to-thickness ratio and shear span ratio), and loading condition (axial force ratio and rotation angle) of the SHS column.

The normalized rotation angle is the common influential factor for both prediction methods. Therefore, the normalized rotation angle (θ / θ_{pc}) can be taken as the independent variable for the failure modes transformation boundary.

To verify the main influential factor on failure modes transformation boundary, the influence of different parameters on the N_{cr} prediction function was first investigated. The detailed information of specimens investigated in Fig. 3-30 is α_e =0.56 (B/t=22, P/P_y=0.15, σ_y=295*1.1). The independent variable is the shear span ratio L/B, i.e., L/B=3, 5 and 7. According to Fig. 3-30, the shear span ratio has minor influence on the intersection points between local buckling and fracture. When the shear span ratio increases, the value of N_{cr} slightly decreases.

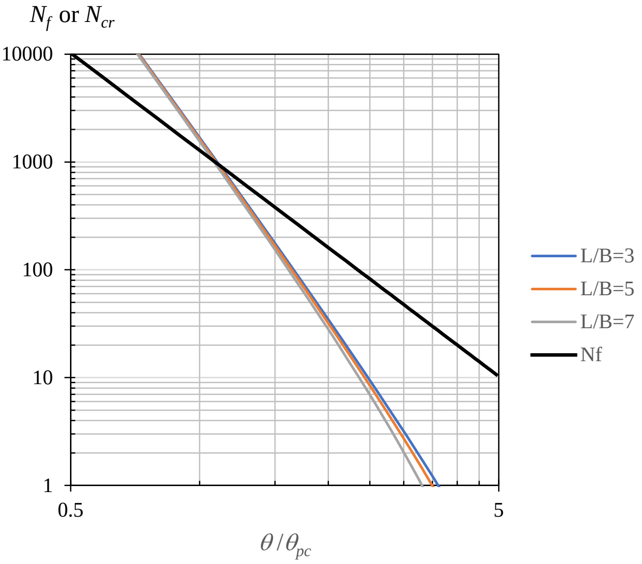

Fig. 3-30 The influence of shear span ratio on the prediction function.

The influence of shear span ratio on Eq. (3-24) has been clarified above, then the influences of axial force ratio and width-to-thickness ratio are investigated. The equivalent standardized width-to-thickness ratio, α_e, was employed to consider the parameters mentioned above. The detailed information of specimens investigated in Fig. 3-31 is L/B=5 (B/t=22, P/P_y=0.15, σ_y=295*1.1). The independent variable is the α_e. With the increase in α_e, the intersection points (the number of cycles) for different failure modes decrease. In other words, the failure mode of local buckling happens under one smaller loading amplitude with a larger α_e. The equivalent standardized width-to-thickness ratio has an unignorable influence on the boundary for different failure modes, as Fig. 3-31. With increase in the equivalent standardized width-to-thickness ratio, the boundary for different failure modes decreases. Based on the discussion above, the equivalent standardized width-to-thickness ratio can be regarded as a more critical influential factor than the shear span ratio.

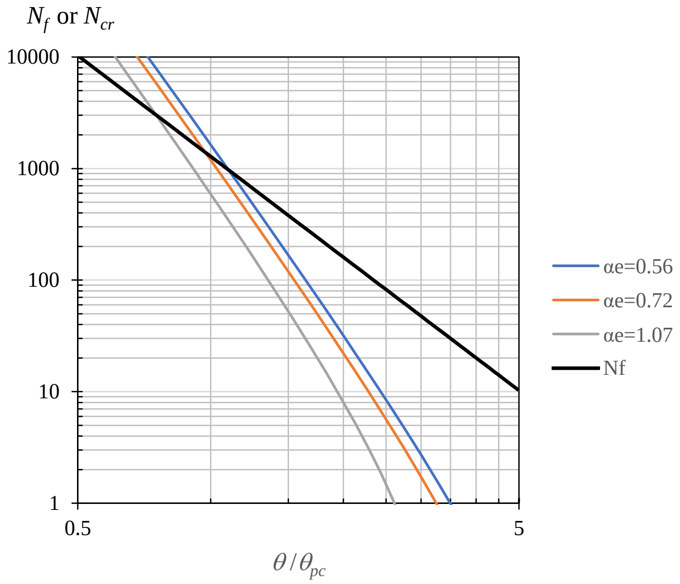

Fig. 3-31 The influence of the equivalent standardized width-to-thickness ratio on the prediction function.

Based on the discussion above, the intersection points can be calculated by combing the two prediction functions together. The failure modes transformation boundary can be obtained with a large amount of intersection points for each series of specimens, as shown in Fig. 3-32. It should be noted that the application range for the N_{cr} prediction method is $0.56 \leq \alpha_e \leq 1.39$. The transformation boundary calculation method can be only applicable to the SHS columns that locate in this effective range.

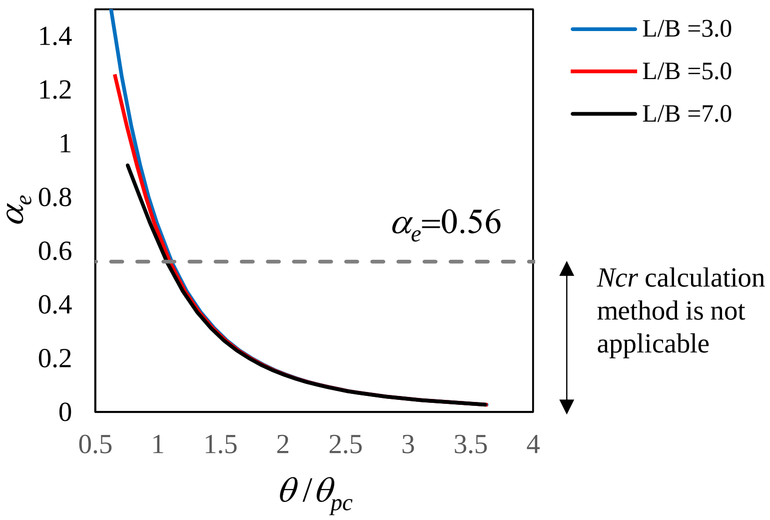

Fig. 3-32 Intersection points for specimens failed due to different failure modes.

The failure modes can be generally distinguished for the SHS columns (the equivalent standardized width-to-thickness ratio α_e from 0.56 to 1.39) with the proposed failure modes transformation boundary. However, the region is rather limited. Based on the database of the current study, we summary all the specimens and try to make a broader region to distinguish the different failure modes empirically, as shown in Fig. 3-33.

In Fig. 3-33, the red points stand for the specimens failed due to flange fracture, while the black points stand for the specimens failed due to local buckling. Boundaries of α_e=0.56 and α_e=1.39 can be developed first based on the application range mentioned above. In current study, there is no specimen fail due to flange fracture when α_e is larger than 1.15, which means the applicability of the proposed method has not been verified under this condition. Therefore, the upper limit of the boundary line is considered to be α_e=1.15 conservatively for practical use. For the specimens failed due to flange fracture, the value of the equivalent standardized width-to-thickness ratio is smaller than 0.56. Based on the test results in Chapter 3, when the loading amplitude is around $2\theta_{pc}$, minor local buckling can be observed (much smaller compared with the out-of-plane deformation in specimens failing due to local buckling, within 5mm), and the final failure mode is flange fracture. Therefore, $\theta=2\theta_{pc}$ can be considered as a conservative boundary for the specimens with small α_e. Up to now, the boundaries for the specimens fail due to flange fracture can be obtained as follows: $N_{cr}= N_f$, α_e=1.15, α_e=0.56, $\theta=2\theta_{pc}$. In Fig. 3-33, there is one point (failing due to flange fracture in experiment) locating in the region for the failure mode of local buckling (prediction method). This indicates the current prediction method can underestimate the cyclic performance of the SHS columns under some conditions, which is conservative and safe to be applied in practice.

The limitations of the failure modes transformation boundaries proposed in this study are listed as below. Due to the limited number of specimens in current study, two special cases are not considered. One case is the specimens with large equivalent standardized width-to-thickness ratio (α_e>1.15) under small amplitude loading ($\theta<\theta_{pc}$). The final failure mode is still unknown due to the lack of data support. In addition, the applicability of the proposed boundary line has to be verified in this region. The region is marked in Fig. 3-33. The other one is the specimens with small equivalent standardized width-to-thickness ratio (α_e<0.56) under relatively large amplitude loading ($\theta>2\theta_{pc}$). It is also unknown whether local buckling will happen under this loading condition when the SHS column is under small axial force ratio or with a compact section. The region is marked in Fig. 3-33. The hysteretic behaviors of the SHS columns locate in these two regions should be further investigated and clarified with tests in the future. Based on Fig. 3-33, the current failure modes distinguish method can give a relatively conservative prediction for the SHS columns under constant amplitude loading.

The specimens subjected to the variable amplitude loadings were also shown in Fig. 3-33. The largest and smallest rotation amplitudes (half of the rotation ranges obtained from rainflow method) were plotted with dashed square for each specimen. When the largest rotation amplitude exceeds the failure modes transformation boundaries many times, the specimens will surely fail due to local buckling (i.e., Specimens V_22.2_0.35_4.3, V_33.3_0.2_4.3 and Taft_22.2_0.2_4.3). If very limited number of cycles exceeded the boundaries within a small extent, the specimens will finally fail due to flange fracture (there are two cycles of $2.1\theta_{pc}$ in Specimen Sendai_19.4_0_4.9). According to Fig. 3-33, the current method can also provide a good estimation of the failure modes for the SHS columns under variable amplitude loading.

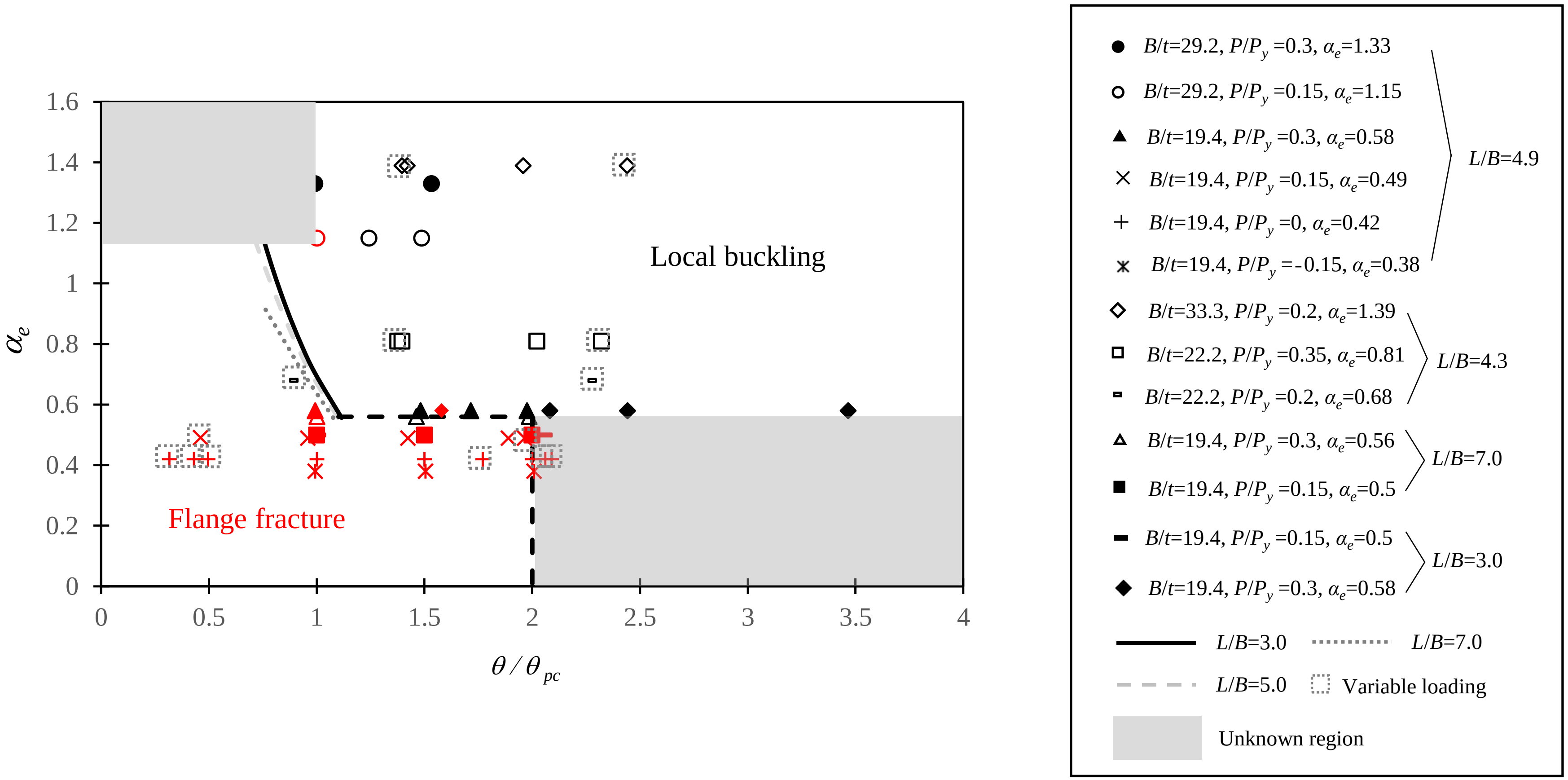

Fig. 3-33 Summary of the SHS columns failed due to different failure modes.

3.8 Summary

In this Chapter, cyclic loading tests on 22 SHS columns under small amplitude were conducted. All these specimens failed due to flange fracture. The influence of shear span ratio, axial force ratio, and loading amplitude on the LCF performance of the SHS columns was investigated and clarified. Conclusions in this Chapter can be drawn as follows.

For specimens that failed due to flange fracture under a specific loading amplitude, the axial force ratio had a minor influence on their LCF life; however, the shear span ratio had a significant effect on the N_f–θ relationship. With the decrease in the shear span ratio, the LCF life of the SHS columns decreased.

Methods to evaluate the LCF performance of the SHS columns were proposed based on the empirical regression functions for different parameters, namely the number of cycles to failure and (normalized) rotation angle, and the number of cycles to failure and strain range. These methods can be further applied to specimens under variable amplitude loading in combination with the rainflow counting method and Miner's rule; the predicted results were proved with good correspondence comparing with experimental ones.

A method to predict the strength deterioration trend was proposed based on the empirical regression function from test data (i.e., normalized strength deterioration rate and normalized rotation angle). This method can also be applied to specimens under variable amplitude loading in combination with the rainflow counting method. The deterioration trends for the lateral load-bearing capacity under maximum loading amplitude can be predicted with good accuracy. The proposed method can be applied in the future to hysteretic models for specimens that fail owing to flange fractures.

A method to predict the residual strength of columns was proposed based on the crack propagation in the column end. The corresponding derivation was based on the concept of section loss. The results of the method showed good correspondence with experimental results. This method can be directly applied in practical engineering to evaluate the residual strength of steel columns by only measuring the crack length.

The failure modes transformation boundaries (for local buckling and flange fracture) have been built for the SHS columns based on the test database in this study. The boundaries were obtained based on the concept of the stability limit and the fatigue life. With the proposed method, a conservative failure mode prediction can be obtained.

In this Chapter, great emphasis has been placed on the strength deterioration caused by LCF. According to the test results, the lateral load-bearing capacity of SHS columns will decrease even though the columns are subjected to small amplitude loadings, prompting the consideration of the lateral load resistance loss caused by LCF even though no local buckling was observed. In practice, the crack initiation and propagation in the flanges of SHS columns should always be monitored carefully to ensure the safety of the structures that they comprise.

References

[3-1] Powell GH, Allahabadi R. Seismic damage prediction by deterministic methods: Concepts and procedures. *Earthquake Engineering and Structural Dynamics*. 1988, 16(5): 719-734.

[3-2] Krawinkler H. Performance Assessment of Steel Components. *Earthquake Spectra*. 1987, 3(1): 27-41.

[3-3] Kishiki S, Lee D, Yamada S, Ishida T, Jiao Y. 2019. Low-cycle fatigue performance assessment of current Japanese steel beam-to-column connections determined by ductile fracture. *Engineering Structures*. 2019, 182: 241–50.

[3-4] Krawinkler H, Zohrei M. Cumulative damage in steel structures subjected to earthquake ground motions. *Computers & Structures*. 1983, 16: 531–41.

[3-5] Suita K, Manabe Y, Takatsuka K, Tanaka T, Tsukada T. 2012. Prediction of fracture of steel moment connection by cyclic loading with various deformation amplitude. In: 15th World Conference on Earthquake Engineering, Lisbon, Portugal.

[3-6] Takatsuka K, Suita K, Umeda T. 2017. Deformation capacity of flange-welded web-bolted moment connection under cyclic loading. In: 16th World Conference on Earthquake Engineering, Santiago, Chile.

[3-7] Ballio G, Castglioni CA. A unified approach for the design of steel structures under low and/or cycle fatigue. *Journal of Constructional Steel Research.* 1995, 34: 75-101.

[3-8] Ballio G, Calado L, Castglioni CA. Low cycle fatigue behaviour of structural steel members and connections. *Fatigue & Fracture of Engineering Materials & Structures.* 1997, 20(8): 1129-1146.

[3-9] Iyama J, Ricles JM. Prediction of fatigue life of welded beam-to-column connections under earthquake loading. *Journal of Structural Engineering*. 2009, 135(12): 1472-1480.

[3-10] Zhou H, Wang Y, Yang L, Shi Y. Seismic low-cycle fatigue evaluation of welded beam-to-column connections in steel moment frames through global-local analysis. *International Journal of Fatigue*. 2014, 64: 97-113.

[3-11] Castiglioni CA, Mouzakis HP, Carydis PG. Constant and variable amplitude cyclic behavior of welded steel beam-to-column connections. *Journal of Earthquake Engineering*. 2007, 11(6): 876-902.

[3-12] Ge H, Kang L, Tsumura Y. Extremely low-cycle fatigue tests of thick-walled steel bridge piers. *Journal of Bridge Engineering*. 2013, 18(9): 858-870.

[3-13] Tateishi K, Chen T, Hanji T. Extremely low cycle fatigue assessment method for un-stiffened cantilever steel columns. *Journal of Structural and Construction Engineering*, AIJ. 2008, 64 (2): 288-296.

[3-14] Myers AT, Kanvinde AM, Deierlein GG, Fell BV. Effect of weld details on the ductility of steel column baseplate connections. *Journal of Constructional Steel Research*. 2009, 65: 1366-1373.

[3-15] Matsuishi M, Endo T. Fatigue of metals subjected to varying stress. Japan Society of Mechanical Engineering, 1968.

[3-16] Miner MA. Cumulative damage in fatigue. *Journal of Applied Mechanics*, 1948.

[3-17] Japanese Standards Association: JIS Z 2241: Metallic materials-Tensile testing-Method of test at room temperature, 2011.

[3-18] Shimada Y, Jiao Y, Kim J, Yamada S. Effects of Strain-Rate on the Hysteretic Behavior of Structural Steels. In: 15th World Conference on Earthquake Engineering, Lisbon, Portugal; 2012.

[3-19] Tseng NT, Lee GC. Simple Plasticity Model of Two-Surface Type. *Journal of Engineering Mechanics*. 1983, 109(3): 795-810.

[3-20] Coffin LF. A study of effects of cyclic thermal stresses on a ductile metal. *Transactions of the American Society of Mechanical Engineers*. 1954, 76: 931–50.

[3-21] Manson SS. Behavior of materials under conditions of thermal stress. *Engineering Fracture Mechanics*. 1953.

[3-22] Architectural Institute of Japan, AIJ recommendations for plastic design of steel structures, 2017. (in Japanese)

Chapter 4 Conclusions and future work

4.1 Conclusions

The dissertation describes an experimental and analytical investigation on the hysteretic behaviors of SHS columns under a large number of small inelastic cycles in detail. The knowledge gap of seismic performance for SHS columns under long-duration earthquake was filled in. The following conclusions can be drawn.

In **Chapter 2**, cyclic loading tests were carried out on the SHS columns under small inelastic cycles. The hysteretic behaviors of SHS columns under this loading condition showed great differences compared with those under large amplitude loading with limited number of cycles. Furthermore, local buckling was observed after a certain number of cycles. This study confirmed that the extended skeleton curve of columns under small inelastic cycles did not correspond to the moment-rotation angle relationship of columns under monotonic loading. The influences of different parameters (i.e., width-to-thickness ratio, axial force ratio, shear span ratio and loading amplitude) on the hysteretic behaviors have been clarified. The concept of a stability limit was proposed based on the axial deformation of the flange plate in the local buckling region. For specimens under small amplitude loading, they behaved steadily before reaching the stability limit; Upon reaching the stability limit, deformation of the local buckling region of and the strength deterioration of the columns increased rapidly. A method to accurate and directly predict the stability limit value using the geometrical features, loading conditions and material property was proposed. Additionally, a method to predict the number of cycles until the stability limit is reached was also proposed, which can be applied to specimens under both constant and variable amplitude loading. The proposed concept of the stability limit and its corresponding prediction methods were further applied into the seismic analyses. The stability limit was regarded as a conservative damage evaluation index. Based on the analytical results, the stability limit can also be reached even though no strength deterioration happens, which stresses the great importance to consider this evaluation index into the further seismic analyses. Furthermore, the deterioration range of the hysteretic model for column components in the inelastic response analysis needs further modification in the future study. The residual strength of the SHS columns with local buckling can be predicted with the deformation in the flange of local buckling zone. The relationship of moment-local buckling deformation for the specimens under cyclic loading can be simply represented with that obtained from pushover test.

In **Chapter 3**, cyclic loading tests were further carried out on the SHS columns with smaller width-to-thickness ratio, under smaller axial force ratio and loading amplitude compared with those in **Chapter 2**. Flange fracture was observed in them. For specimens that failed due to flange fracture under a specific loading amplitude, the axial force ratio had a minor influence on their LCF life; however, the shear span ratio had a significant effect on the N_f–θ relationship. Methods to evaluate the LCF performance of the SHS columns were proposed based on the empirical regression functions for different parameters, namely the number of cycles to failure and (normalized) rotation angle, and the number of cycles to failure and strain range. These methods can be further applied to specimens under variable amplitude loading in combination with the rainflow counting method and Miner’s rule. A method to predict the strength deterioration trend was proposed based on the empirical regression function from test data (i.e., normalized strength deterioration rate and normalized rotation angle), which can also be applied to the SHS columns under variable amplitude loading with the rainflow counting method and Miner’s rule. A method to predict the residual strength of columns was proposed based on the crack propagation in the column end. The corresponding derivation was based on the concept of section loss. This method can be directly applied in practical engineering to evaluate the residual strength of steel columns by only measuring the crack length. The failure modes transformation boundaries have been built for the SHS columns based on the concept of stability limit and fatigue life supported by the test database in this study. With the proposed method, a conservative failure modes prediction can be obtained and the failure modes can be distinguished for SHS columns under both constant and variable amplitude loading.

Based on the research findings in this study, the following recommendations are made. For the low-rise buildings (3-story in this study), columns with large width-to-thickness ratio (*B/t*=29.4 in this study), and middle-rise buildings (6-story in this study) under single seismic wave in design level (PGV=50cm/s), it's not necessary to consider the stability limit based on the current design methods. The following cases are recommended to consider the stability limit. For the low-rise buildings, columns with more compact sections, it should be considered when single seismic input over the design level and multiple seismic inputs. For the middle-rise buildings, it should be considered when subjected to single seismic wave (long-duration earthquake) over the design level and multiple seismic inputs.

The application of the current research is briefly introduced as below. As for the practical design process, whether the stability limit will be reached for the designed buildings should be checked for the cases mentioned above to avoid the potential risks. Time-history analyses are recommended to carry out for these cases. If the buildings are designed only based on the seismic input with design level (PGV=50cm/s), reduction in the width-to-thickness ratio of the columns can effectively avoid reaching the limit status for the low-rise buildings based on the results in Chapter 2.6. Furthermore, the middle-rise buildings can be safe based on the current design method (without considering the stability limit) under the seismic input with design level. When the fatigue endurance is considered for the columns subjected to many minor earthquakes, the design of the columns should satisfy the corresponding requirements based on the fatigue life prediction methods proposed in Chapter 3.4.

After the seismic events, the estimation on the residual strength in the steel columns can be carried out quickly based on the local buckling deformation and the crack length in the column ends. The deformation can be measured manually to estimate the residual bearing capacity based on the findings in Chapter 2.7. The crack can also be measured to evaluate the residual lateral resistance of the columns based on the findings in Chapter 3.6. These methods are useful for the retrofitting work post the seismic events.

As for the structural analyses, the concept of the stability limit and the fatigue life are recommended as damage indices to evaluate the seismic performance of the steel columns in the long-duration earthquakes to avoid overestimation.

4.2 Future work

This study focused on the SHS columns that are used in low- and middle-rise buildings under long-duration earthquakes. The influences of the critical parameters, i.e., width-to-thickness ratio, axial force ratio, shear span ratio and loading amplitude, on the hysteretic behaviors have been investigated and clarified. Damage evaluation methods have been proposed for the specimens failed due to local buckling (based on deformation capacity) and flange fracture (based on fatigue life), respectively. Furthermore, the failure modes transformation boundaries were also summarized based on the experiment database. Although a large number of SHS columns were tested, there are still some limitations in this study compared with the complicated practical engineering cases. Some work needs to be further carried out in the future to supplement the insufficiencies of the current study, and they are summarized as below.

Future work 1: Taking the varying axial force into the consideration of the stability limit and the inelastic response analysis.

In this study, the specimens were carried out under constant axial load, and the stability limit was considered as the onset of the deterioration behavior under the corresponding constant axial force. During the complicated seismic event in practice, the axial force ratio in the columns always changes, which is not considered in this study. In addition, the axial load in the columns was considered as a constant value, i.e., dead load, in the infinite uniform plane model. The SHS columns under the varying axial force can be further carried out in the future to check the influence. The current stability limit prediction method should be modified based on the test data. In addition, the axial force variation should also be further considered in the inelastic response analysis occupied with the modified stability limit prediction method.

The following concepts were made by the author to predict the stability limit under varying axial force based on the current research findings for reference. For one specific rotation range (the total calculation time is t), the Miner's rule can be applied to calculate the damage in each small-time increment Δt_i in the structural inelastic response analysis, where the axial force can be considered as constant. The axial force ratio at the time increment Δt_i can be represented as P_i / P_y, and the number of cycles reaching the stability limit $N_{cr(i)}$ can be calculated. Then the total damage caused by the varying axial force in the time t period can be calculated, as shown in Fig. 4-1. It should be noted that this is only a tentative solution to the conditions considering the varying axial force. The concept has to be verified in the future study with experimental data support.

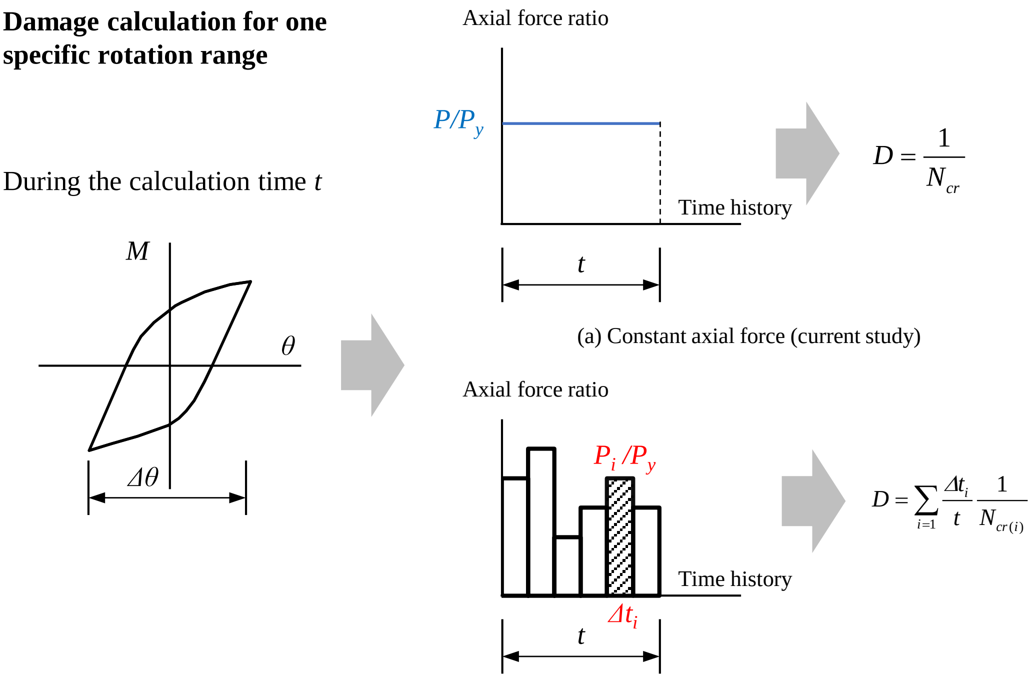

(a) Constant axial force (current study)

(b) Varying axial force (assumptions for future research)

Fig. 4-1 Concept figure for damage accumulation for specimens under constant and varying axial force.

Future work 2: The hysteretic model with strength deterioration controlled by the stability limit should be developed in the future.

With the inelastic response analysis results, the hysteretic model [4-1] proposed in the previous study was found to be unable to exhibit the strength deterioration behavior when the loading amplitude is small. This can be a relatively dangerous condition when carrying out the inelastic response analyses under long-duration earthquakes. In Chapter 2.7, the strength deterioration behavior of the SHS column was found to be closely related to the progress of the deformation in the flange of the local buckling region, δ_b. Based on the current findings, the author suggests to develop the hysteretic model based on the progress of δ_b. In this study, the progress of δ_b prior to the stability limit has been studied well, and corresponding prediction methods have already been proposed. The progress of δ_b post the stability limit should be further investigated and modelled. With the whole progress of δ_b, the strength can be obtained as well. With some appropriate assumptions (i.e., stiffness change, changing point, and target point in the model), the hysteretic model can be developed and further applied to the inelastic response analyses.

Future work 3: The cyclic softening behavior of the cold-formed steel should be investigated in depth.

In Chapters 2 and Chapter 3, before the stability limit was reached and crack initiation in the corner of the bottoms, the strength deterioration was observed for all the specimens. The phenomenon can be explained by the cyclic softening behavior of the cold-formed steel. However, the influence can be investigated quantitatively further with more coupon tests in the material level. And the results can be further applied to the numerical simulation or the analytical models (e.g., multi spring model [4-2]) for analytical work.

Future work 4: For the SHS columns failed due to flange fracture, the dependency on the welding quality and the size effect can be further investigated.

In this study, the full-penetration welds between the column ends and baseplates followed the specification [4-3]. There are also many other welding methods. The influence of the different welding methods can be taken as a parameter for further investigation. In addition, due to the limited specimens, the size effect for them were not considered in the current study, which can be further investigated and clarified in the future.

Future work 5: Investigation on the SHS columns under a large number of bi-directional small inelastic cycles.

The experiment in this study only focused on the hysteretic behaviors of the SHS columns under a large number of in-plane small inelastic cycles. However, the structures are always subjected to bi-directional seismic input in the practical engineering. What influences will be caused by the bi-directional loading pattern on the hysteretic behaviors are still unknown, which is a good topic to be investigated in the future.

Future work 6: The failure mode transformation boundaries should be further modified. Based on the concepts developed in Chapter 2 (stability limit) and Chapter 3 (fatigue life), the failure modes transformation boundaries were built in Chapter 3.7. However, due to the limited data, the calculated boundary line has a limited applicable range. There are some unknown regions due to the lack of test data support. The SHS columns locating in these regions are suggested to be further carried out to clarify the potential mechanisms.

References

[4-1] Yamada S, Ishida T, Jiao Y. Hysteretic behavior of RHS columns under random cyclic loading considering local buckling. *International Journal of Steel Structures*. 2018, 18(5):1761-1771.

[4-2] Ishida T, Yamada S, Shimada Y. Analytical model of RHS columns under random bi-directional horizontal forces. *Journal of Structural and Construction Engineering*, AIJ, 2013, 78(691):1631-1640.

[4-3] Architectural Institute of Japan: Japanese Architectural Standard Specification (JASS) 6 Steel Work, 2018

Appendix 1 Calculation methods of M_{pc} in AIJ design recommendations and K_e

The calculation method of M_{pc} (the plastic moment considering the effect of the axial force) is first introduced as below.

For the cross section under bending and compression, two different conditions exist. One condition is that the neutral axis locates in the web of the section, as shown in Fig. A.1-1. Under this condition,

$$\frac{P}{P_y} \le \frac{A_w}{A} \tag{A1-1}$$

The expression for the M_{pc} can be expressed as,

$$\frac{M_{pc}}{M_p} + \frac{A^2}{\left(4A_f + A_w\right) \cdot A_w}\left(\frac{P}{P_y}\right)^2 = 1 \tag{A1-2}$$

$$M_p = \sigma_y \cdot Z_p \tag{A1-3}$$

Where P/P_y: Axial force ratio; M_{pc}: The plastic moment considering the effect of the axial force; M_p: The plastic moment without considering the effect of the axial force; A: The whole area of the section; A_w: The whole area of the web; A_f: The area of one flange; Z_p: The plastic section modulus; σ_y is the yield stress; y_0 is the distance from the centroidal axis of the section to the plastic neutral axis (in Figs. A.1-1 and A.1-2).

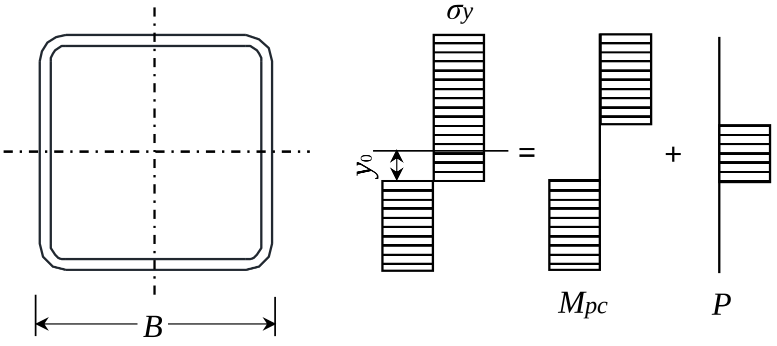

Fig. A.1-1. Neutral axis locates in the web.

The other condition is that the neutral axis locates in the flange of the section, as shown in Fig. A.1-2. Under this condition,

$$\frac{P}{P_y} > \frac{A_w}{A} \tag{A1-4}$$

The expression for the M_{pc} can be expressed as,

$$\frac{M_{pc}}{M_p} = \frac{2A}{4A_f + A_w}\left(1 - \frac{P}{P_y}\right) \tag{A1-5}$$

The definition for each quantity is the same as above.

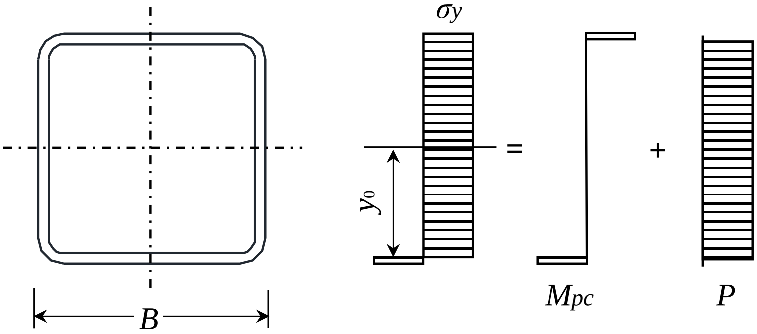

Fig. A.1-2. Neutral axis locates in the flange.

Next, the progress to calculate the elastic stiffness of the columns is listed as below. In the calculation, both the deformation caused by bending moment and shear force is considered.

The stiffness calculated with the shear force k is shown as below. The unit of k is kN/m.

$$k = \frac{1}{\frac{L^3}{3EI} + \frac{L}{GA}} \tag{A1-6}$$

Where E is the Young's modulus; G is the shear modulus; L is the length of the column; I is the area moment of inertia.

The elastic stiffness of the column (in the view of moment) can be represented as below. The unit is kN·m.

$$K_e = kL^2 \tag{A1-7}$$

Appendix 2 Information for the infinite uniform plane model

Infinite uniform plane model was used as the analytical model, as shown in Fig. A.2-1. An infinite number of plane frames with uniform size were assumed to exist in the plane model. The response of the frame can be represented by one bay of the frame owing to the uniform response for every bay. The models are designed using a plastic design method for severe earthquakes based on the Japanese design code, where a severe earthquake approximately corresponds to the PGV (peak ground velocity) =0.5m/s. The strong column-weak beam concept is applied, and column-to-beam moment ratio (M_{pc}/M_{pg}) should be greater than or equal to 1.5 according to the Building Standard Law of Japan. The length of the beams and columns are 3.5m and 7m, respectively. The column bases are exposed-type, and strong-type column bases are employed in this model, where the moment capacity ratio of column base to the column in the first-floor equals to 1.3. P-Δ effect was considered in the analyses, and 2% Rayleigh damping is used for the first and second mode. The weight per story per span is 400kN.

In this study, four different models were investigated, i.e., three 3-story models with columns having different width-to-thickness ratios (B/t=22.2, 25 and 29.4), and one six-story model. It should be noted that the width-to-thickness ratio of the columns is the only difference in the models (the beams remain the same). The basic information for the beams and columns was listed in Tables A. 2-1- A. 2-6.

The acceleration time histories of the input waves in the analyses are shown in Fig. A. 2-3.

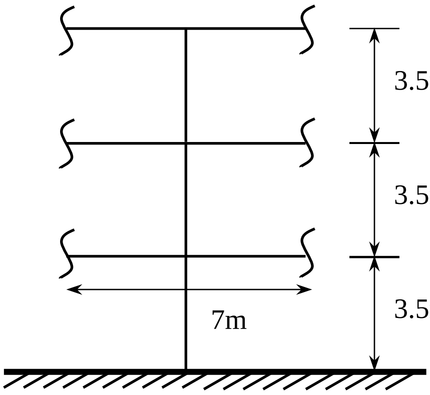

Fig. A.2-1 Layout of the 3-story steel moment-resisting frame in response analyses.

Table. A. 2-1 Detailed information for columns of the three-story model (*B/t*=29.4)

Story	Column	Steel type	Nominal yield stress [N/mm^2]	Tensile yield stress [N/mm^2]	Column-to-beam moment ratio (M_{pc}/M_{pg})
3	□-353×12	BCR295	295	400	1.5
2	□-353×12	BCR295	295	400	1.5
1	□-353×12	BCR295	295	400	1.5

Table A. 2-2 Detailed information for columns of the three-story model (*B/t*=25)

Story	Column	Steel type	Nominal yield stress [N/mm^2]	Tensile yield stress [N/mm^2]	Column-to-beam moment ratio (M_{pc}/M_{pg})
3	□-353×14.1	BCR295	295	400	1.78
2	□-353×14.1	BCR295	295	400	1.78
1	□-353×14.1	BCR295	295	400	1.78

Table A. 2-3 Detailed information for columns of the three-story model (*B/t*=22.2)

Story	Column	Steel type	Nominal yield stress [N/mm^2]	Tensile yield stress [N/mm^2]	Column-to-beam moment ratio (M_{pc}/M_{pg})
3	□-353×15.9	BCR295	295	400	2.01
2	□-353×15.9	BCR295	295	400	2.01
1	□-353×15.9	BCR295	295	400	2.01

Table A. 2-4 Detailed information for beams of the three-story model

Story	Beam	Steel type	Nominal yield stress [N/mm^2]	Tensile yield stress [N/mm^2]
3	H-493×211×8×12	SN400	235	400
2	H-493×211×8×12	SN400	235	400
1	H-493×211×8×12	SN400	235	400

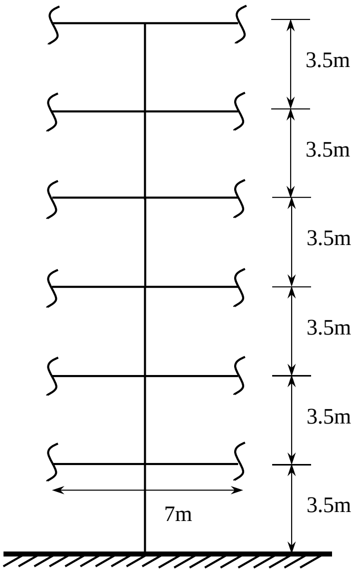

Fig. A.2-2 Layout of the 6-story steel moment-resisting frame in response analyses.

Table A. 2-5 Detailed information for columns of the six-story model

Story	Column	Steel type	Nominal yield stress [N/mm^2]	Tensile yield stress [N/mm^2]	Column-to-beam moment ratio (M_{pc}/M_{pg})
6	□-425×14	BCR295	295	400	1.5
5	□-425×14	BCR295	295	400	1.5
4	□-425×14	BCR295	295	400	1.5
3	□-470×16	BCR295	295	400	1.5
2	□-470×16	BCR295	295	400	1.5
1	□-470×16	BCR295	295	400	1.5

Table A. 2-6 Detailed information for beams of the six-story model

Story	Beam	Steel type	Nominal yield stress [N/mm^2]	Tensile yield stress [N/mm^2]
6	H-602×258×10×14	SN400	235	400
5	H-602×258×10×14	SN400	235	400
4	H-602×258×10×14	SN400	235	400
3	H-653×280×10×16	SN400	235	400
2	H-653×280×10×16	SN400	235	400
1	H-653×280×10×16	SN400	235	400

Appendix 3 Typical strength deterioration behavior for specimens under cyclic large amplitude loading

The moment-rotation angle relationship for one SHS column [1-20] under cyclic constant large amplitude loading is shown in Fig. A.3-1. The loading amplitude for the specimen under cyclic loading is larger than the rotation angle corresponding to the maximum moment of monotonic loading, θ_m. The extended skeleton curve was compared with its moment-rotation angle relationship under monotonic loading in Fig. A.3-2. The basic information for the two specimens is shown in Table A.3-1.

Table A.3-1 Basic information for the specimens

Dimension	Yield stress [N/mm^2]	Yield ratio	*B/t*	P/P_y	*L/B*	Loading history	Loading amplitude
□-125×125×4.5 (STKR400)	366	0.82	27.8	0.3	6	Monotonic	n/a
						Constant amplitude	0.028

Notes: The definitions for the quantities are the same as those in Table 2.

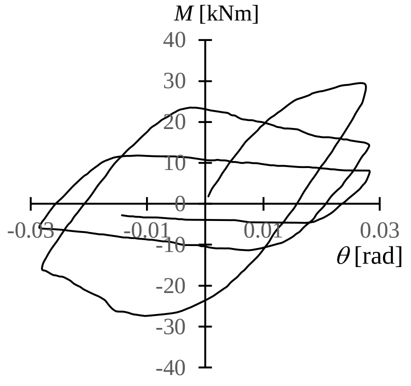

Fig. A.3-1. Moment-rotation angle relationship.

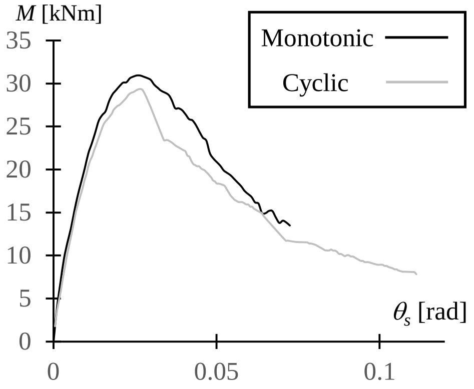

Fig. A.3-2. Comparison of the extended skeleton curve.

Appendix 4 The relationship between δ_b and θ of specimens under monotonic loading prior to the stability limit

In Chapter 2, the relationship between δ_b and θ of specimens under monotonic loading prior to the stability limit was considered to be linear. The modelling concept was built based on the following database in this study. It should be noted that the naming rule is the same as that in Chapter 2.

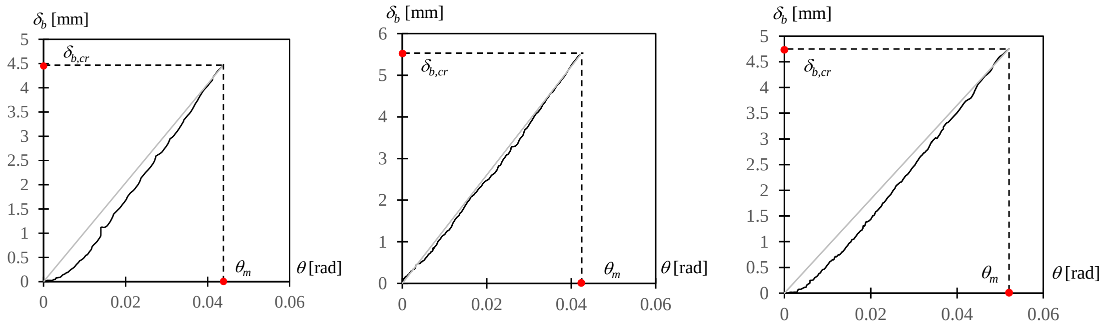

(a) M_19.4_0.3_4.9 (b) M_19.4_0.3_3 (c) M_19.4_0.3_7

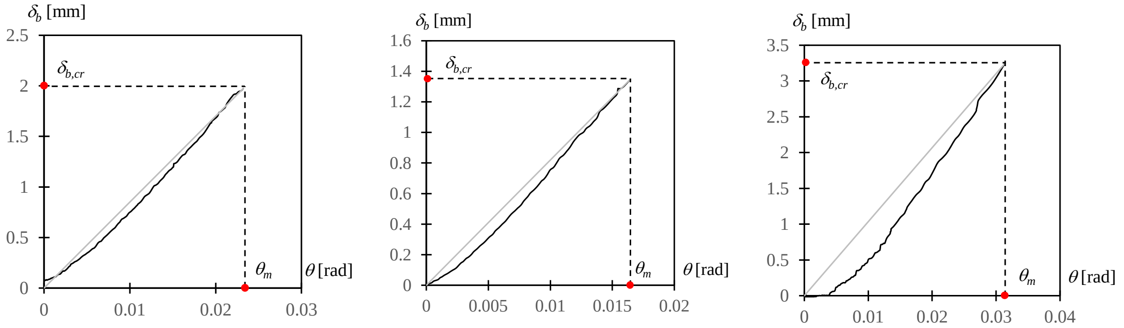

(d) M_29.2_0.15_4.9 (e) M_29.2_0.3_4.9 (f) M_22.2_0.2_4.3

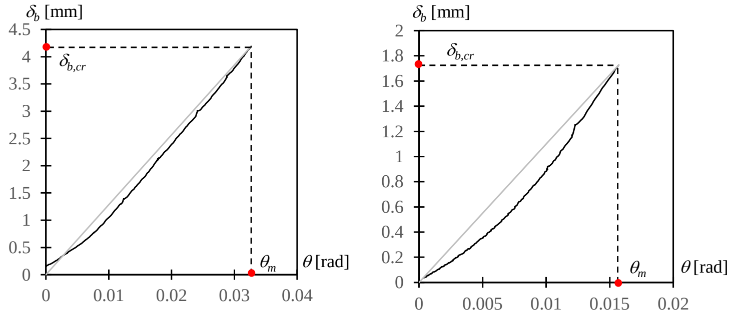

(g) M_22.2_0.35_4.3 (h) M_33.3_0.2_4.3

Fig. A.4-1the relationship between δ_b and θ of specimens under monotonic loading prior to the stability limit.

Appendix 5 The progress of the rotational part in δ_b

The modelling concept, i.e., the rotational part seems to be a constant value prior to the stability limit, was proposed based on the experimental database in this study. The progress of the rotational part in δ_b for all the specimens under constant amplitude loading was shown as below. The applicability of the assumption in the modelling concept was verified.

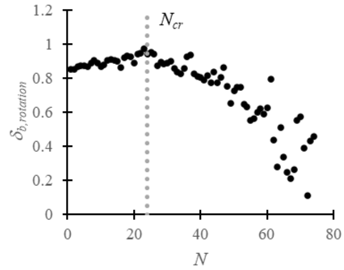

(a) C2.0_19.4_0.3_4.9

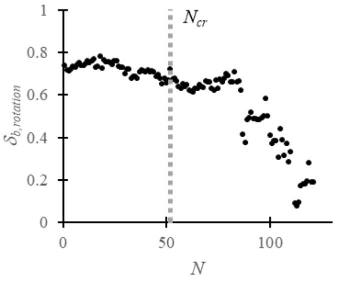

(b) C1.75_19.4_0.3_4.9

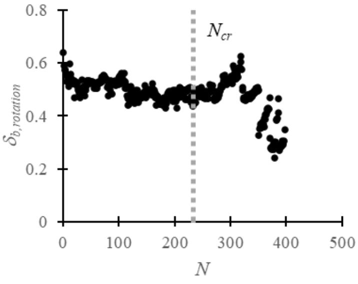

(c) C1.5_19.4_0.3_4.9

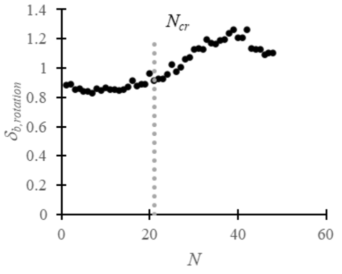

(d) C2.0_22.2_0.35_4.3

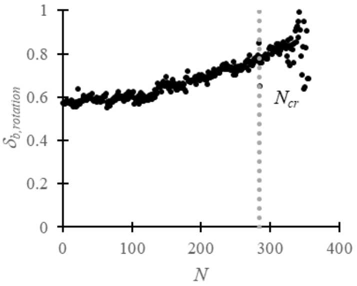

(e) C1.5_22.2_0.35_4.3

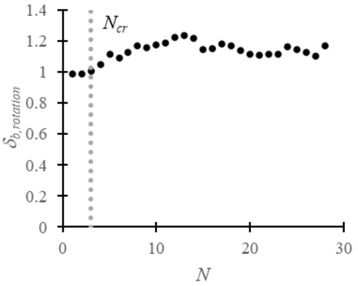

(f) C2.0_33.3_0.2_4.3

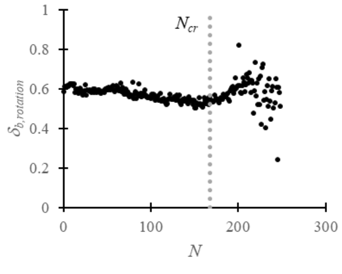

(g) C1.5_33.3_0.2_4.3

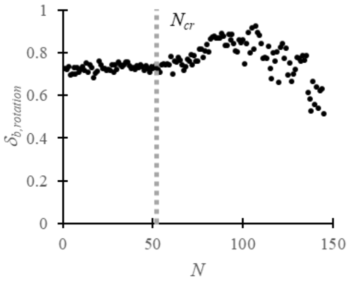

(h) C1.5_29.2_0.15_4.9

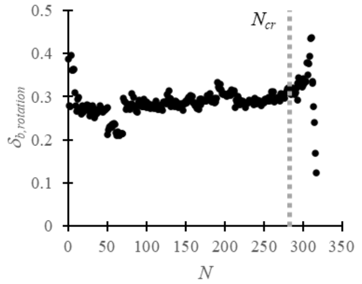

(i) C1.0_29.2_0.3_4.9

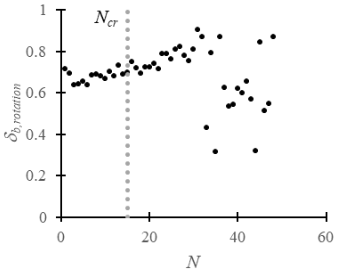

(j) C2.0_19.4_0.3_7.0

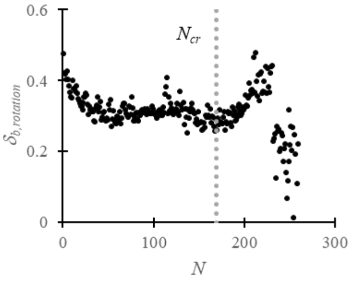

(k) C1.5_19.4_0.3_7.0

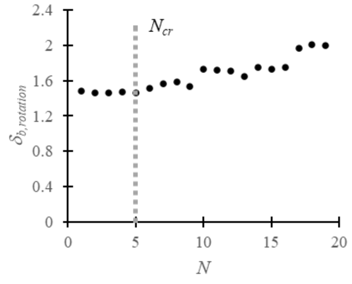

(l) C3.5_19.4_0.3_3.0

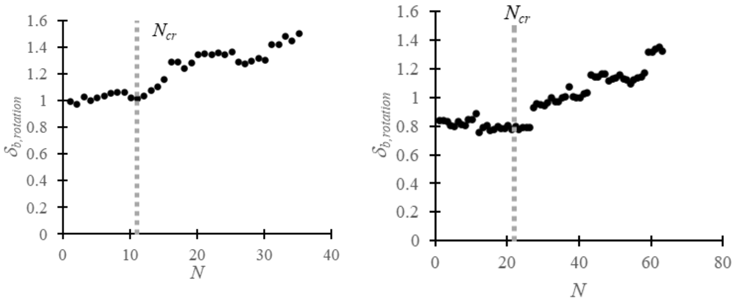

(m) C2.5_19.4_0.3_3.0 (n) C2.0_19.4_0.3_3.0

Fig. A.5-1 The progress of the rotational part in δ_b.

Appendix 6 The elastic local buckling stress for the plate with linear stress change in the longitudinal direction

The standardized width-to-thickness ratio was derived from the elastic local buckling stress for the plate. The plate is simple supported as shown in Fig. A.6-1. The small shear stress in the flange was neglected.

Local buckling deformation ω is approximately considered as

$$\omega = \delta \sin\frac{\pi x}{a} \cdot \sin\frac{\pi y}{b} \qquad \text{(A6-1)}$$

The boundary conditions can be expressed as follows

$$N_x = (1-\beta x)\sigma \qquad \text{(A6-2)}$$

$$N_{xy} = N_y = 0 \qquad \text{(A6-3)}$$

The work done by the external force can be given as below

$$\begin{aligned}\Delta T &= \frac{1}{2}\int_0^b\int_0^a \left[N_x (\frac{\partial \omega}{\partial x})^2 \right] \mathrm{d}x\mathrm{d}y \\ &= \frac{\sigma\delta^2\pi^2}{8}\frac{b}{a}\left(1-\beta\frac{a}{2}\right)\end{aligned} \qquad \text{(A6-4)}$$

Strain energy can also be obtained

$$\begin{aligned}\Delta U &= \frac{D}{2}\int_0^b\int_0^a \left\{ \left(\frac{\partial^2\omega}{\partial x^2} + \frac{\partial^2\omega}{\partial y^2} \right) - 2(1-\nu)\left[\frac{\partial^2\omega}{\partial x^2}\cdot\frac{\partial^2\omega}{\partial y^2} - (\frac{\partial^2\omega}{\partial x\partial y})^2 \right] \right\} \mathrm{d}x\mathrm{d}y \\ &= \frac{\pi^4 ab}{8} D\delta^2 \left(\frac{1}{a^2} + \frac{1}{b^2} \right)^2\end{aligned} \qquad \text{(A6-5)}$$

Where $D = \frac{Et^3}{12(1-\nu^2)}$

Based on the law of conservation of energy $\Delta T = \Delta U$, the elastic local buckling stress can be obtained as below.

$$\sigma_{cr} = \frac{k\pi^2 E}{12\left(1-\nu^2\right)}\left(\frac{t}{b}\right)^2\left(\frac{1}{1-0.5\beta a}\right) \tag{A6-6}$$

When the stress in the half wave length (x=0.5a) reached the value of $\frac{k\pi^2 E}{12\left(1-\nu^2\right)}\left(\frac{t}{b}\right)^2$ (the maximum stress point in x=0), local buckling appears.

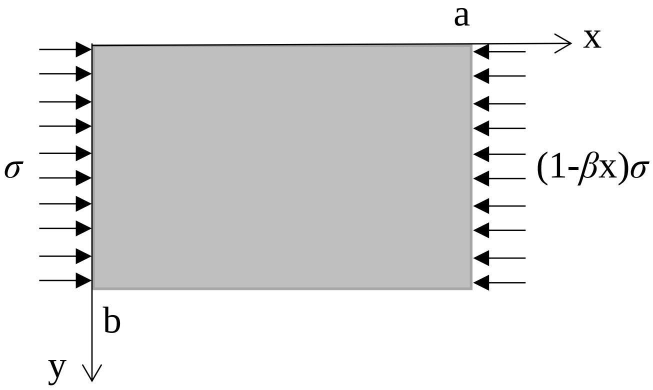

Fig. A.6-1 Plate with linear changing stress in the longitudinal direction.

Appendix 7 Prediction model considering local buckling behaviors for stub columns [2-10][2-14]

The prediction model considering local buckling for stub columns are shown in Fig. A.7-1. The definition for each parameter in the model is listed as follows.

σ_y is the yield stress of the stub column (from material test); ε_y is the elastic strain corresponding to the yield stress of the stub column; ε_u is the strain corresponding to the maximum stress of the stub column; μ_0 is the ratio of strain corresponding to the maximum stress to yield strain; α is the standardized width-to-thickness ratio, as Eq. (2-12); E is the Young's modulus; E_{d1} is the negative stiffness of the first deterioration stage; E_{d2} is the negative stiffness of the second deterioration stage; E_{d3} is the negative stiffness of the third deterioration stage; S, T and T_2 are the coefficients of the model, determining the peak strength, end of the first and second deterioration stage, respectively.

The parameters in the model can be expressed with the following functions, which was obtained from the stub column tests.

$$\mu_0 = \varepsilon_u / \varepsilon_y = 8.7/\alpha - 1.2 \quad (2.62 \geq 1/\alpha \geq 0.19) \tag{A7-1}$$

$$E_{d1}/E = -0.014\alpha^2 - 0.005 \quad (3.14 \geq 1/\alpha \geq 0.33) \tag{A7-2}$$

$$E_{d2}/E = -0.005 \quad (3.70 \geq 1/\alpha \geq 0.62) \tag{A7-3}$$

$$E_{d3}/E = -0.001 \tag{A7-4}$$

$$T/S = -0.079\alpha + 0.81 \quad (3.70 \geq 1/\alpha \geq 0.62) \tag{A7-5}$$

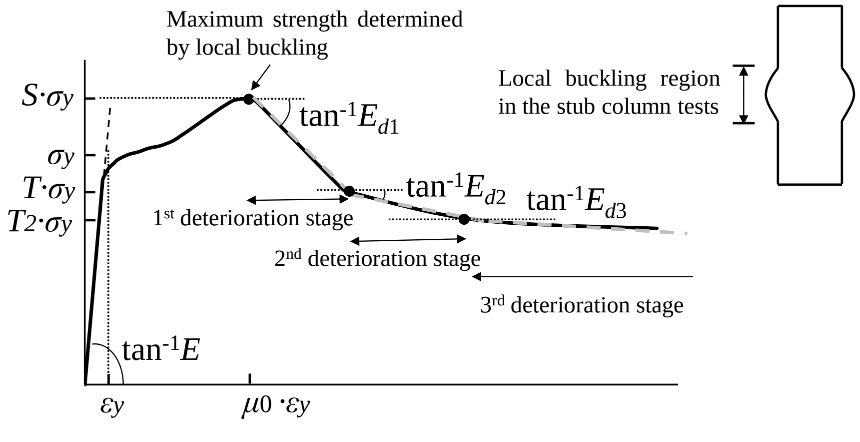

Fig. A.7-1 Stress-strain relationship of the local buckling region in stub columns.

Appendix 8 Load-deformation characteristics of steel tubes under monotonic loading [2-15]

For the SHS columns, the moment-rotation angle relationship under monotonic loading can be empirically modeled based on the previous experimental study, as shown in Fig. A.8-1. The detailed definition for each parameter in the model is shown as below.

$$p=\frac{P}{P_y} \tag{A8-1}$$

When there is a yield plateau in the material test,

$$k_p=0.03+0.04|p| \tag{A8-2}$$

When there is no yield plateau in the material test,

$$k_{p1}=\frac{1}{10(1-0.7|p|)} \tag{A8-3}$$

$$k_{p2}=\frac{1}{22(1-0.7|p|)} \tag{A8-4}$$

The approximate value of k_p can be given as,

$$k_p=\frac{\tau-1}{\frac{0.1}{k_{p1}}+\frac{\tau-1.1}{k_{p2}}} \tag{A8-5}$$

where k_p, k_{p1}, and k_{p2} are the slopes of the strength increasing part in the model in Fig. A.8-1; p is the axial force ratio. The expression of τ is obtained from the columns failed due to local buckling,

$$\tau=\frac{\tau_0 Z_{pc}(\frac{p}{\tau_0})}{Z_{pc}(p)} \tag{A8-6}$$

τ_0 equals to the larger value of Eqs. (A8-7) and (A8-8), where B/t is the width-to-thickness ratio; ε_y is the yield strain; λ is the slenderness ratio; Z_{pc} is the plastic section modulus considering the influence of the axial force; τ and τ_0 are model coefficients to determine the peak strength.

$$\tau_0 = \frac{1}{0.526 + 0.341\frac{B}{t}\sqrt{\varepsilon_y}} \tag{A8-7}$$

$$\tau_0 = 0.98 + 0.0202\left[\left(2.624\frac{B}{t}\sqrt{\varepsilon_y} - 5.79\right)^2 - 1.368\right](1.81 - \sqrt{\varepsilon_y}\lambda) \tag{A8-8}$$

The slope for the deterioration part k_d can be represented as,

$$k_d = -0.1377\left[\left(2.624\frac{B}{t}\sqrt{\varepsilon_y} + 0.4\right)^2 - 3.76\right](\sqrt{\varepsilon_y}\lambda - 0.1906)\sqrt{\varepsilon_y} \tag{A8-9}$$

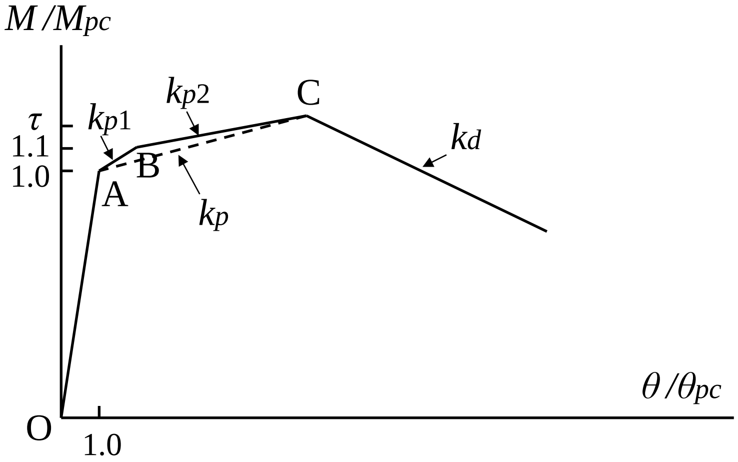

Fig. A.8-1 The deformation characteristics of steel tubes.

Appendix 9 Hysteretic model for the structural components in the analytical model

A tri-linear model was employed for the beam, as shown in Fig. A.9-1. The hysteretic curve characteristic of the beams is based on the concept of the extended skeleton curve (as mentioned in Chapter 2.), including the skeleton part, Bauschinger part, and elastic unloading part, as shown in Fig. 2-15. The skeleton part is considered to correspond to the load-deformation relationship under monotonic loading [A9-1]; the Bauschinger part is modelled based on the modelling concept in [A9-2]; the unloading part of the hysteretic curves is considered to be the same as the original elastic stiffness of the beams.

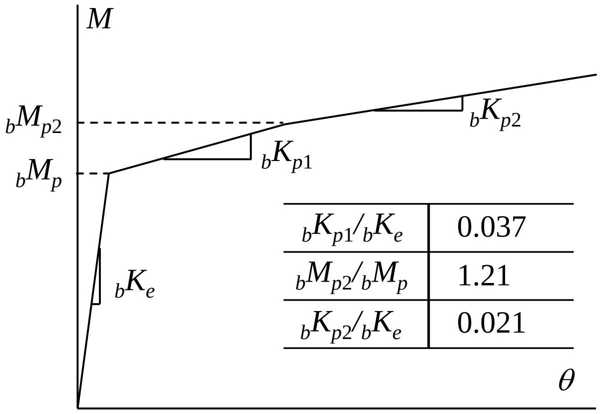

${}_bK_{p1}/{}_bK_e$	0.037
${}_bM_{p2}/{}_bM_p$	1.21
${}_bK_{p2}/{}_bK_e$	0.021

Fig. A.9-1 Tri-linear model of the beam.

A Penta-linear hysteretic model [A9-3] is employed to all the column components, as shown in Fig. A.9-2. The model was also built based on the concept of the extended skeleton curve for the steel columns under relatively large amplitude loading. The extended skeleton curve of the steel columns under cyclic loading is considered to be with similar trend to the monotonic one. Before the maximum strength, the strength increasing part is the same as the skeleton part mentioned above; after the maximum strength, the deterioration part is determined by the cumulative rotation angle, which contributed by every progression of plastic deformation. The unloading part of the hysteretic curves is considered to be the same as the original elastic stiffness of the columns as well. In the hysteretic model, the cyclic softening behavior prior to the stability limit observed in this study was not considered since the strength decrease level was limited.

For the exposed-type column base in the frame model, the hysteretic model is shown as Fig. A.9-3. The model uses a form of the slip-type model [A9-4] that considers the effect of the moment resistance from axial force (M_n) and strain hardening behavior of the anchor bolts (K_p)

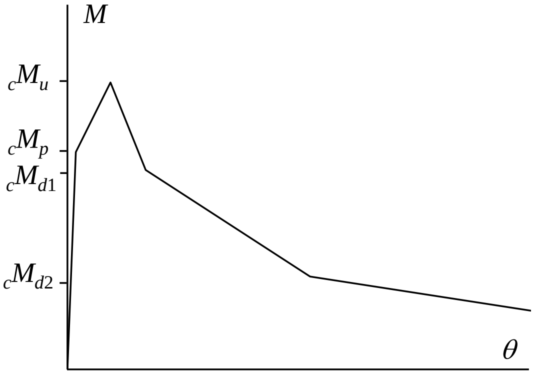

Fig. A.9-2 Penta-linear model of the column

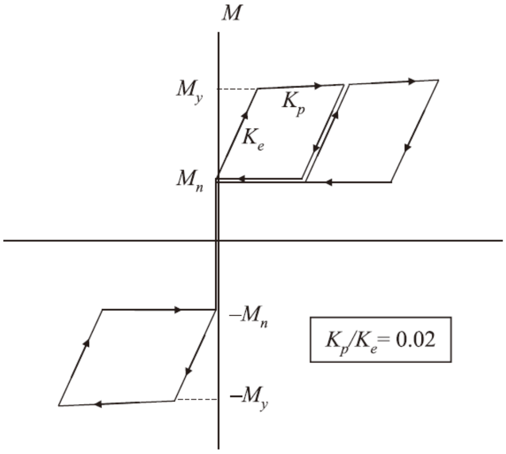

Fig. A.9-3 Slip-type model of the exposed column base

References

[A9-1] Kato B, Akiyama H, Yamanouchi H. 1973. Predictable properties of materials under incremental cyclic loading, *IABSE reports of the working commissions 13*, 119-124.

[A9-2] Akiyama H, Takahashi M. Influence of Bauschinger effect on seismic resistance of steel structures. *Journal of Structural and Construction Engineering*, AIJ. 1990, 418: 49-57. (in Japanese)

[A9-3] Yamada S, Ishida T, Jiao Y. Hysteretic behavior of RHS columns under random cyclic loading considering local buckling. *International Journal of Steel Structures*. 2018, 18(5):1761-1771.

[A9-4] Yamada S, Akiyama H, Sadamoto M. Influence of the elasto-plastic behavior of column bases with slip-type hysteresis characteristics on the ultimate earthquake resistance of multi-story steel moment frames. *Journal of Structural and Construction Engineering*, AIJ. 1997, 62, 141-147. (in Japanese)

Appendix 10 Finite element modelling for the columns

The finite element modelling work (with ABAQUS [A10-1]) was also carried out for the steel columns in this study. The details for the models and some representative results are summarized.

Shell models were established for all the specimens considering analysis precision as well as computational efficiency. Four-node shell elements, *S4R*, were employed in the models and the rigid elements were used in the top and end sections of the specimens. Since the current simulation focuses on the local buckling behavior, the mesh dependency is minor, and a mesh size of 10mm is selected for all the models to enable the calculation accuracy and efficiency. The boundary conditions were the same for all the specimens, i.e., one end was fixed and freedom in the loading direction and axial direction of the other end were relaxed, as illustrated in Fig. A.10-1. Monotonic and cyclic displacement loading histories were applied to the movable end. In the simulation, the actual thickness was adopted, which were measured before carrying out the material test.

For the material properties for the steel columns, two different materials are applied to the section, i.e., the material property of the corner and flat surface parts, respectively, as shown in Fig. A.10-2. For the elastic material property, Young's modulus of 205000MPa and possion's ratio of 0.3 are employed. The property of the flat surface part is obtained from the material coupon test in Chapter 2. The combined hardening law [A10-2] is employed and the corresponding parameters are calibrated by the ABAQUS inputting the material property as "Half cycle".

As for the corner property, the material coupon test was not carried out for these parts in this study, and it was simply assumed as a trilinear relationship (with yield stress and ultimate stress, constant strength after the ultimate stress) based on the material test database in previous studies [A10-3, A10-4]. The cold-formed affected zone is first determined. Based on material test results for different positions nearby the corner [A10-3], the curve parts (in Fig. A. 10-2) are considered to have higher yield stress, σ_y, and ultimate stress, σ_u, compared with the flat part material property. Next, the critical parameters for the trilinear relationship are determined. Based on the material test results for both corner and flat parts [A10-3], the following regular patterns can be found: The ultimate stress/ the yield stress for the corners is around 1.06 in average; the yield stress of corner part/ flat part is around 1.35 in average. With a simple assumption that the ultimate strain for different parts is the same, the critical points for the trilinear relationship can be determined subsequently, as shown in Fig. A.10-3.

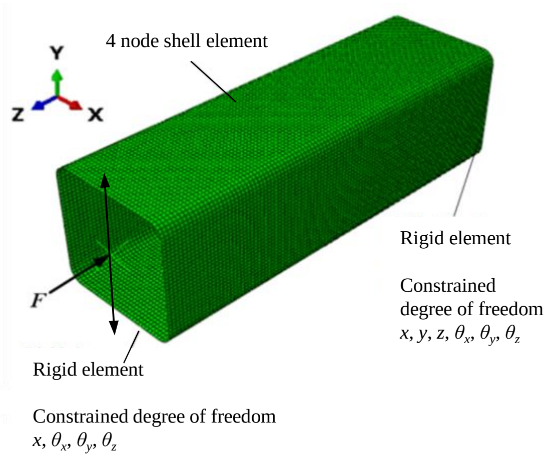

Fig. A.10-1 Finite element model in the numerical simulation

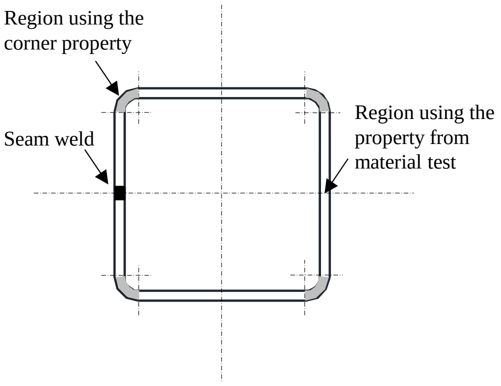

Fig. A.10-2 Assignment of the material properties in the numerical simulation

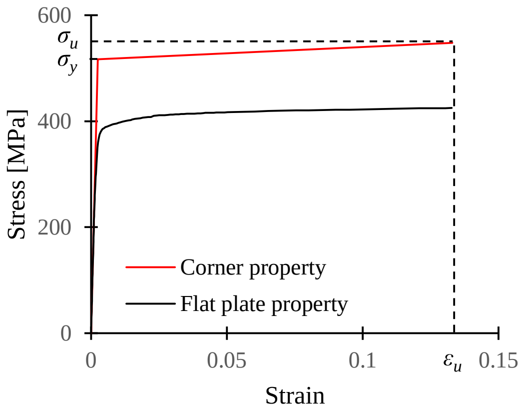

Fig. A.10-3 Material property of the flat part and corner part in the numerical simulation

The simulation for pushover tests in this study was carried out. The simulated moment-rotation angle relationships were compared with the test results and analytical results from the model in previous research [A10-5]. According to the comparison in Fig. A.10-4, the numerical simulation can give a prediction with relatively good accuracy.

The deformation in the flange of local buckling zone in the experiment was also compared with that from the numerical simulation, as shown in Fig. A.10-5. Similarly, good correspondence was shown between the experimental and numerical results. Therefore, numerical simulation can provide the skeleton curve for the proposed concept in Chapter 2.7 with good accuracy.

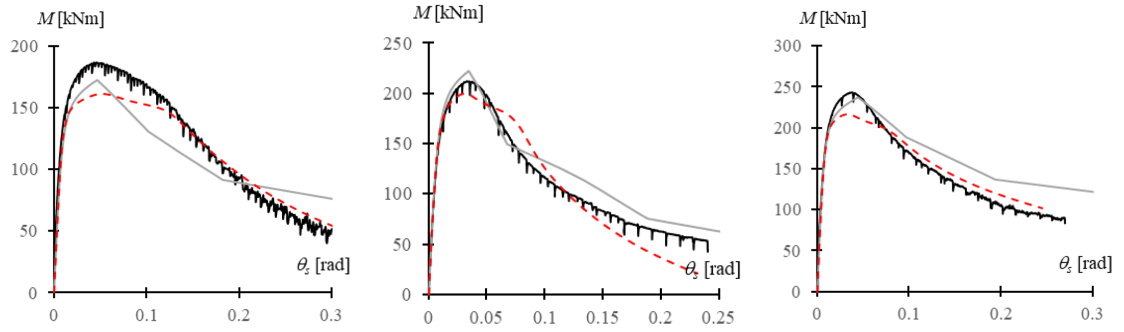

(a) M_19.4_0.3_4.9 (b) M_22.2_0.35_4.3 (c) M_33.3_0.2_4.3

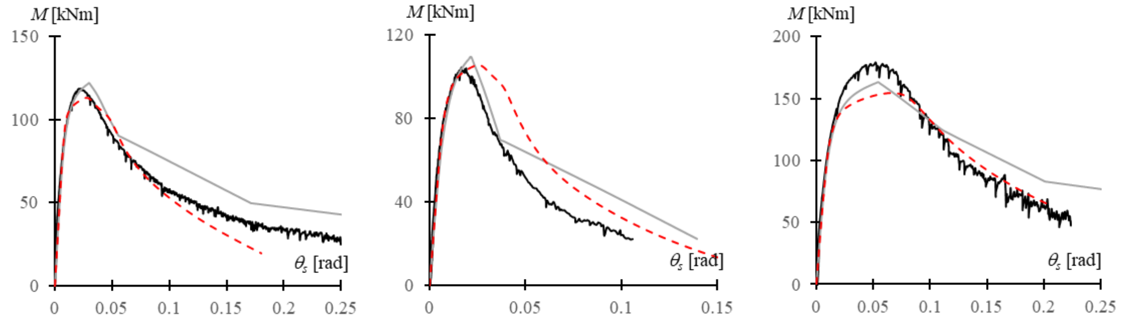

(d) M_29.2_0.15_4.9 (e) M_29.2_0.3_4.9 (f) M_19.4_0.3_7

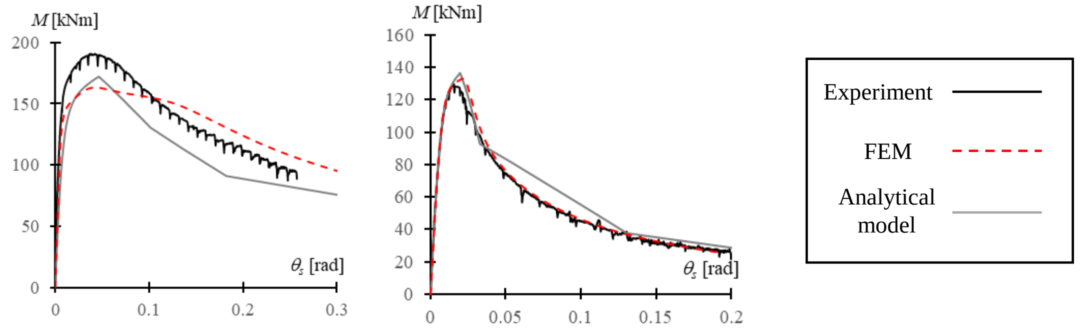

(g) M_19.4_0.3_3 (h) M_22.2_0.2_4.3

Fig. A.10-4 Moment-rotation angle relationship for SHS columns under monotonic loading (experimental, analytical and numerical results)

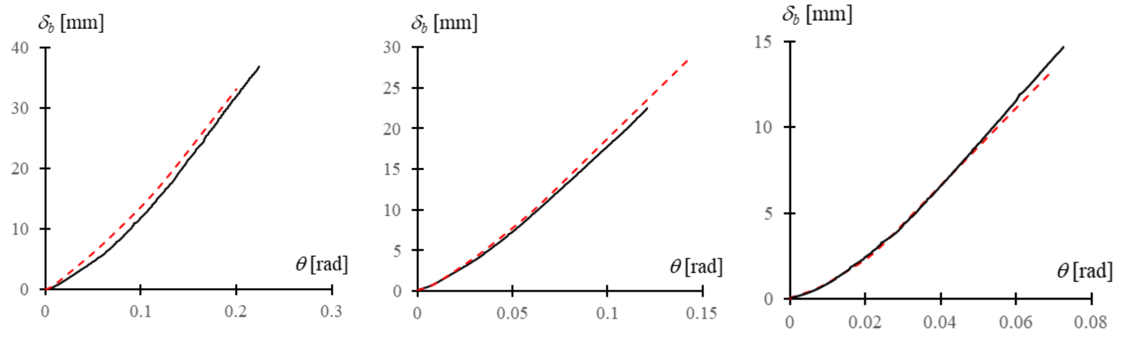

(a) M_19.4_0.3_4.9 (b) M_22.2_0.35_4.3 (c) M_33.3_0.2_4.3

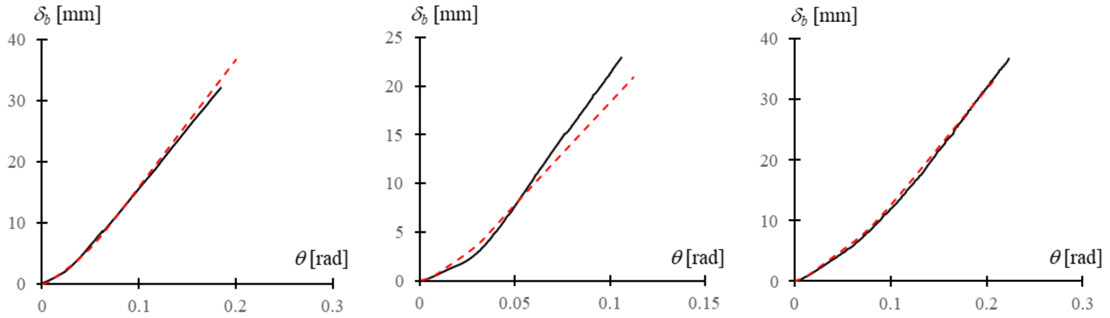

(d) M_29.2_0.15_4.9 (e) M_29.2_0.3_4.9 (f) M_19.4_0.3_7

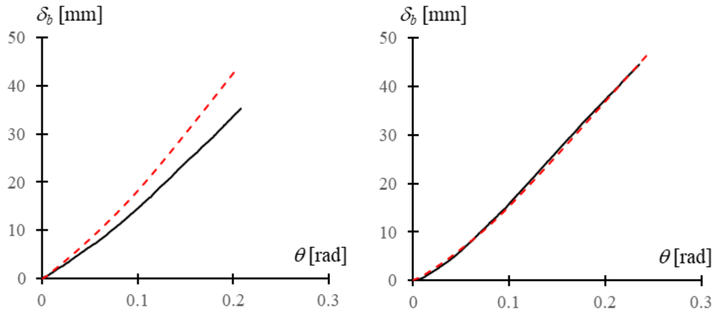

(g) M_19.4_0.3_3 (h) M_22.2_0.2_4.3

Fig. A.10-5 δ_b-rotation angle relationship for SHS columns under monotonic loading (experimental, analytical and numerical results)

References

[A10-1] Hibbitt. 2010. ABAQUS /Standard user's manual. Pawtucket (RI, USA): Karlsson & Sorensen Inc.

[A10-2] Chaboche JL. Time-independent constitutive theories for cyclic plasticity. International Journal of Plasticity. 1986, 2(2), 149-188.

[A10-3] Kuwamura H, Chiu J, Akiyama H. Experiment on the mechanical properties and their improvement of cold roll-formed steel columns. Journal of Structural and Construction Engineering, AIJ. 1993, 453: 171-180. (in Japanese)

[A10-4] Kato B, Aoki H, Kurosawa T. Plastic strain history and residual stresses locked in cold-formed square steel tubes. Journal of Structural and Construction Engineering, AIJ. 1988, 385: 39-48. (in Japanese)

[A10-5] Yamada S, Akiyama H, Kuwamura H. Post-buckling and deteriorating behavior of box-section steel members, Journal of Structural and Construction Engineering. AIJ, 1993, 444: 135-143. (in Japanese).

Appendix 11 Verification of the accuracy of strain gauge data

The accuracy of the strain gauge data was also proved with numerical simulation (FEM, ABAQUS). The simulated specimens were listed in Table. A.11-1. In the simulation, only the first 20 cycles were considered and compared.

Firstly, the hysteretic curves from the numerical simulation and the experimental results were compared. From the comparison, the numerical simulation can basically capture the cyclic behavior of the simulated specimens. The strain data were then extracted based on the discussion above. The positions, where the strain data was extracted from the ABAQUS model, were shown in Fig. A.11-2. The average strain ranges (middle three strain gauges of two sides) obtained from the experiment were also compared. From the comparison, the accuracy of simulated results is reliable.

Based on the simulation results, the strain range for the corner is much larger than the other two parts, which is the same as observed in experiment. The strain ranges for the middle and center gauges are similar to each other, where middle part is larger than the central one. In addition, the decrease in the strain range can also be observed in the numerical simulation results. With the increase in the loading amplitude, the trend becomes more obvious.

Table. A.11-1 Simulated specimens

Dimension	Specimen	B/t	P/P_y	L/B	Loading history	Loading amplitude
□-175×175×9 (BCR295)	C1.0_19.4_-0.15_4.9	19.4	-0.15	4.9	Const. amp. 1.0θ_{pc}	0.0075
	C1.5_19.4_-0.15_4.9				Const. amp. 1.5θ_{pc}	0.0113
	C2.0_19.4_-0.15_4.9				Const. amp. 2.0θ_{pc}	0.0151

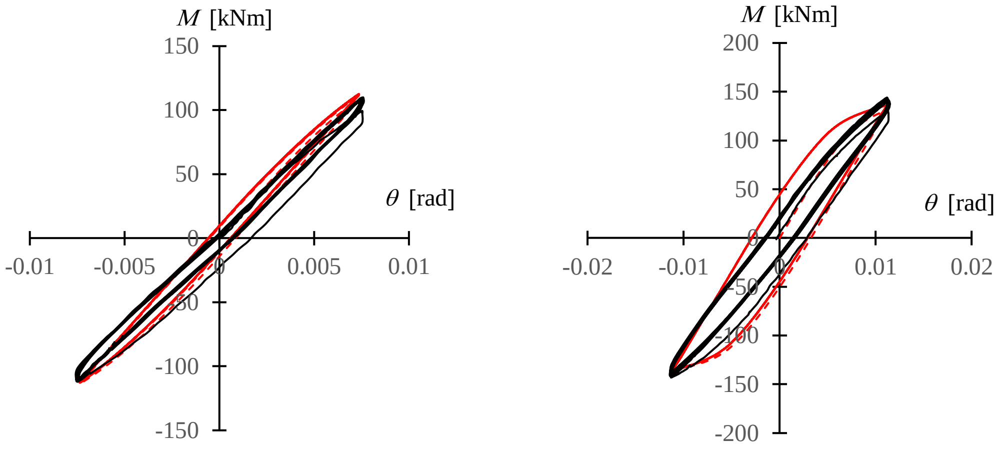

(a) C1.0_19.4_-0.15_4.9

(b) C1.5_19.4_-0.15_4.9

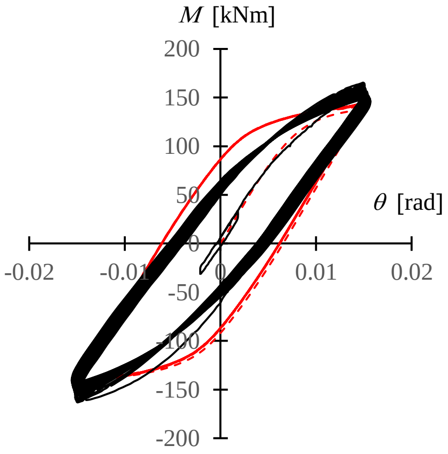

(c) C2.0_19.4_-0.15_4.9

Fig. A.11-1 Comparison between the experimental and numerical results

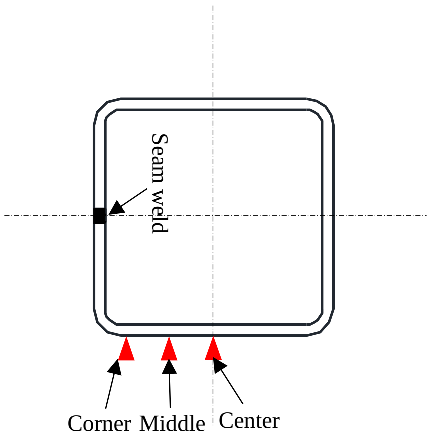

Fig. A.11-2 The position of the strain data

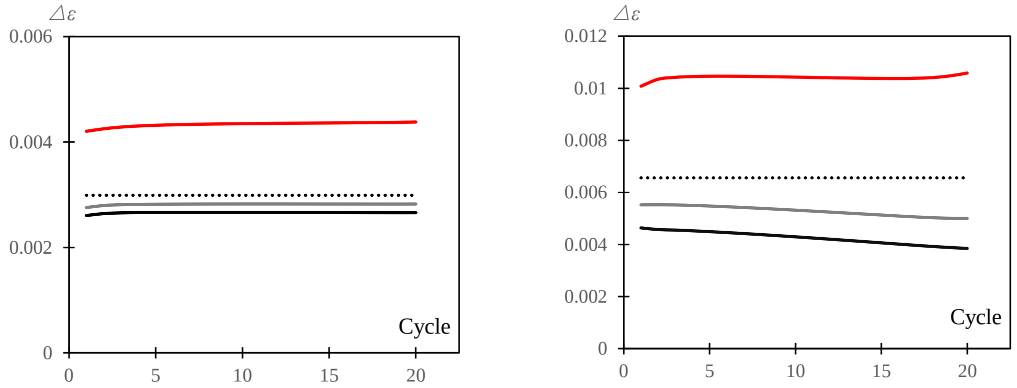

(a) C1.0_19.4_-0.15_4.9

(b) C1.5_19.4_-0.15_4.9

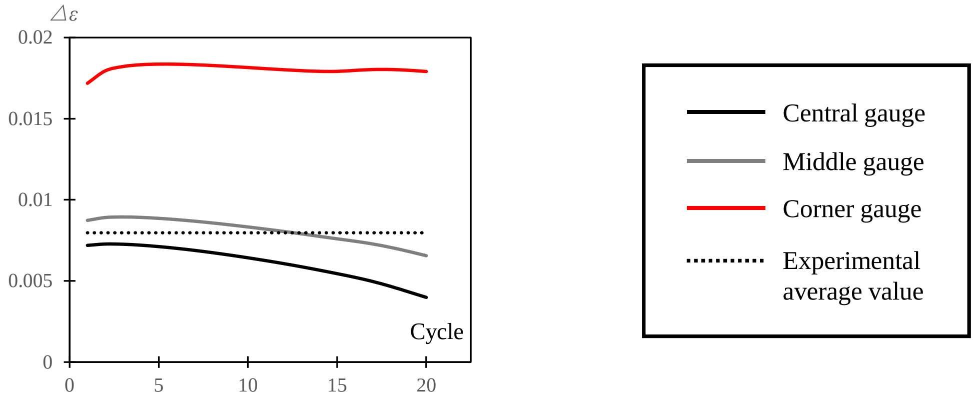

(c) C2.0_19.4_-0.15_4.9

Fig. A.11-3 Comparison between the experimental and numerical strain range

Appendix 12 The hysteretic loops of the columns and story drift in the 1st floor (prior to the stability limit)

The moment-rotation angle relationships of the SHS columns on the 1st floor (prior to the stability limit) were presented in Appendix 12. Furthermore, the time histories of the story drift of the 1st floor were shown as well, where *R* stood for the story drift of the 1st story. These relationships can help better understand the damage accumulation progress in the columns in Chapter 2.6.

For the 3-story model with the width-to-thickness of 29.4, the relationships were summarized as follows. The orders of the figures correspond to the damage evolution relationships in Chapter 2.6.2. According to the hysteretic loops, the strength deterioration began when the stability limit was reached.

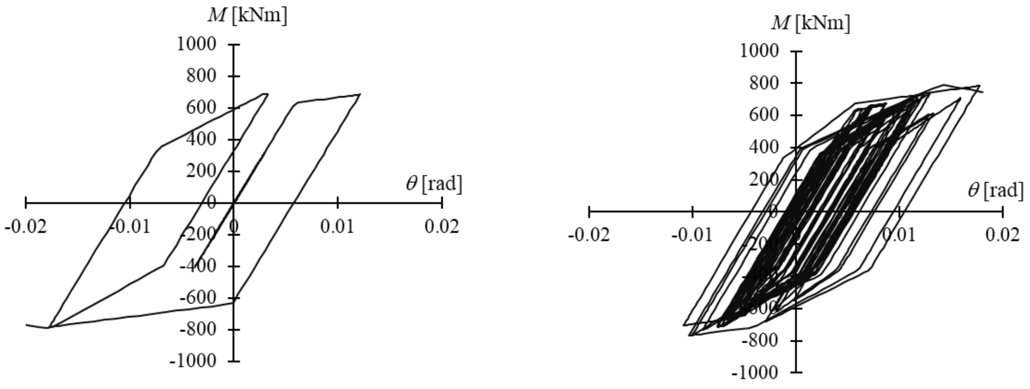

(a) Hachinohe (b) Artificial wave (CH1)

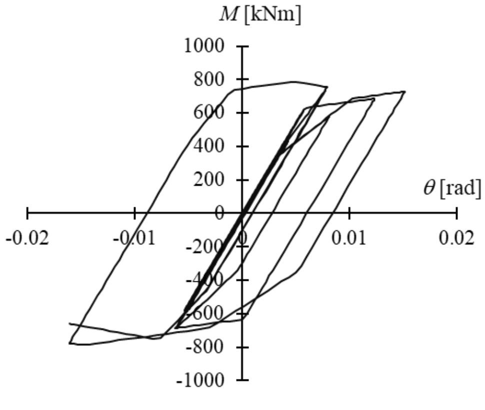

(c) Artificial wave (OS1)

Fig. A.12-1 Hysteretic loops of the columns (in 1st floor, prior to the stability limit) under single seismic excitation (PGV=50cm/s).

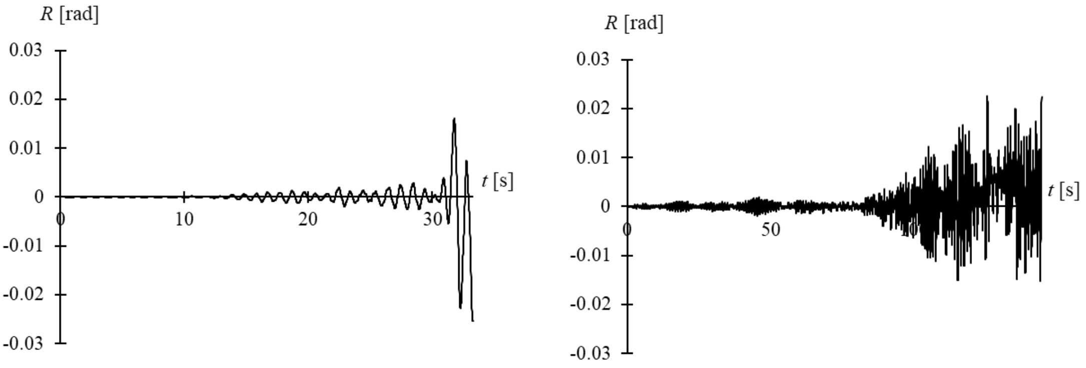

(a) Hachinohe

(b) Artificial wave (CH1)

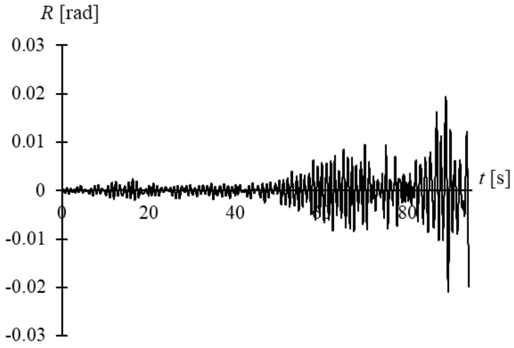

(c) Artificial wave (OS1)

Fig. A.12-2 Time history of the 1st story drift (prior to the stability limit) under single seismic excitation (PGV=50cm/s).

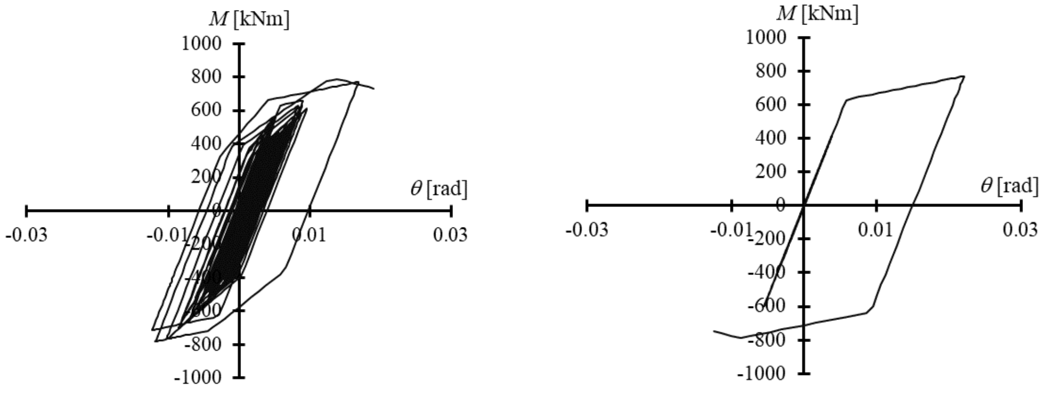

(a) JMA Sendai

(b) Hachinohe

Appendix 12 The hysteretic loops of the columns and story drift in the 1st floor (prior to the stability limit)

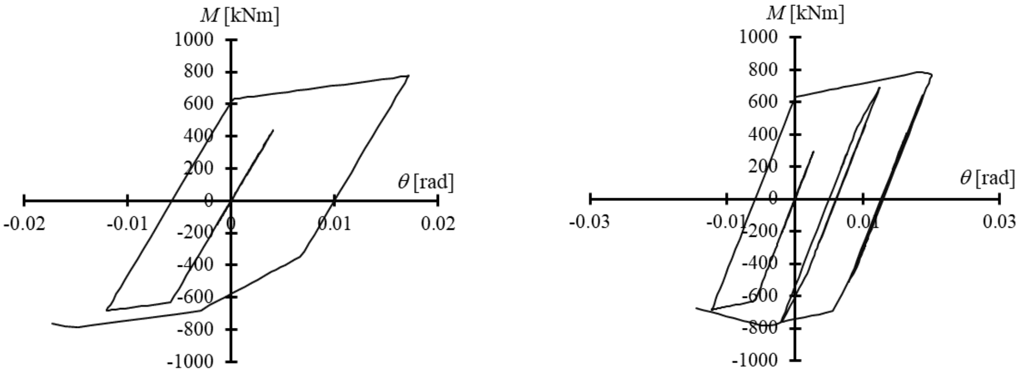

(c) El Centro

(d) Taft

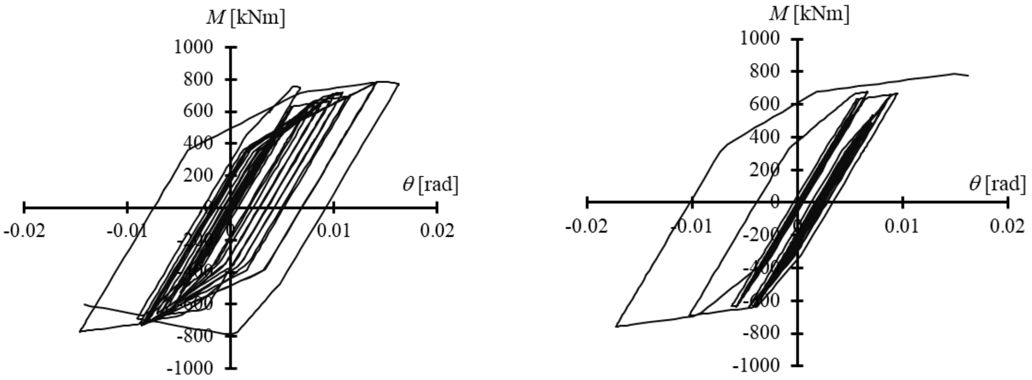

(e) Artificial wave (CH1)

(f) Artificial wave (OS1)

Fig. A.12-3 Hysteretic loops of the columns (in 1st floor, prior to the stability limit) under single seismic excitation (PGV=75cm/s).

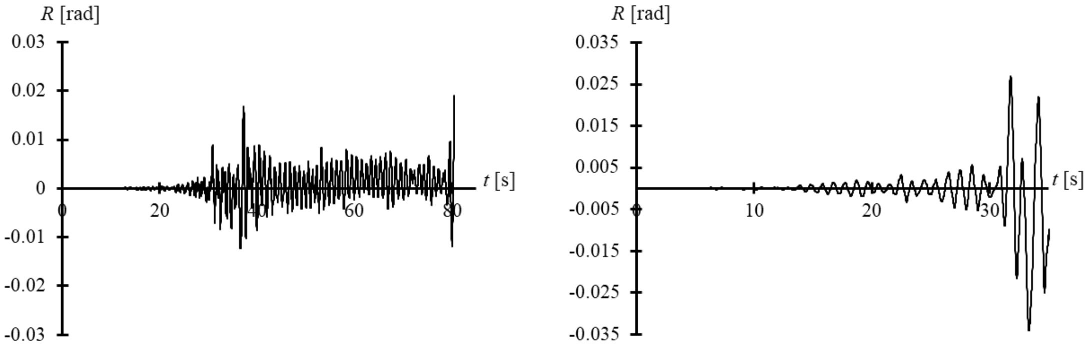

(a) JMA Sendai

(b) Hachinohe

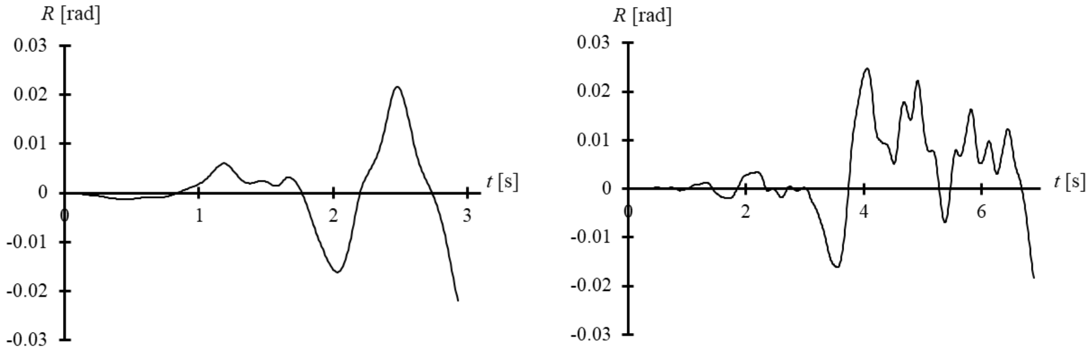

(c) El Centro

(d) Taft

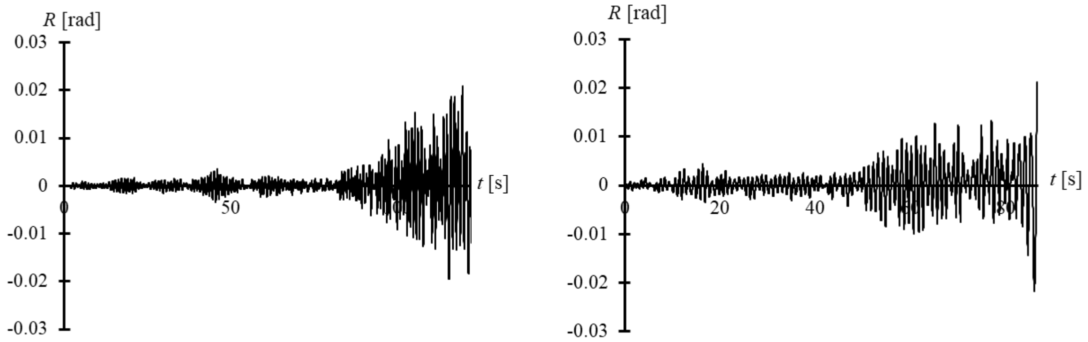

(e) Artificial wave (CH1)

(f) Artificial wave (OS1)

Fig. A.12-4 Time history of the 1st story drift (prior to the stability limit) under single seismic excitation (PGV=75cm/s).

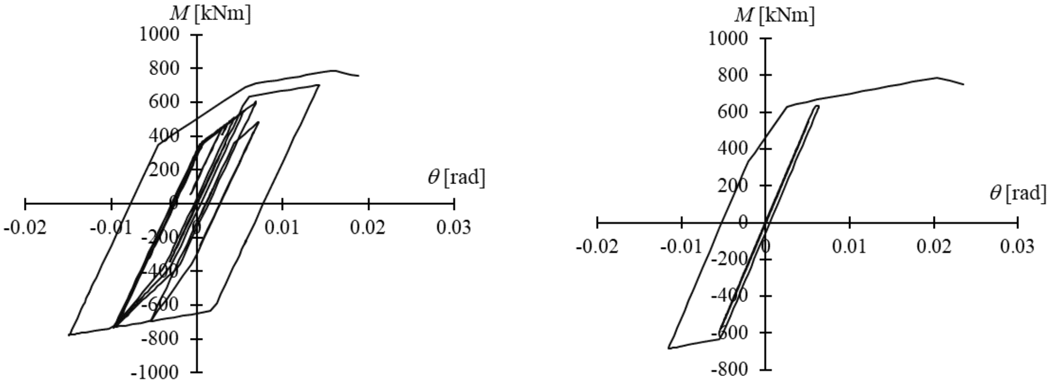

(a) JMA Sendai

(b) Hachinohe

Appendix 12 The hysteretic loops of the columns and story drift in the 1st floor (prior to the stability limit)

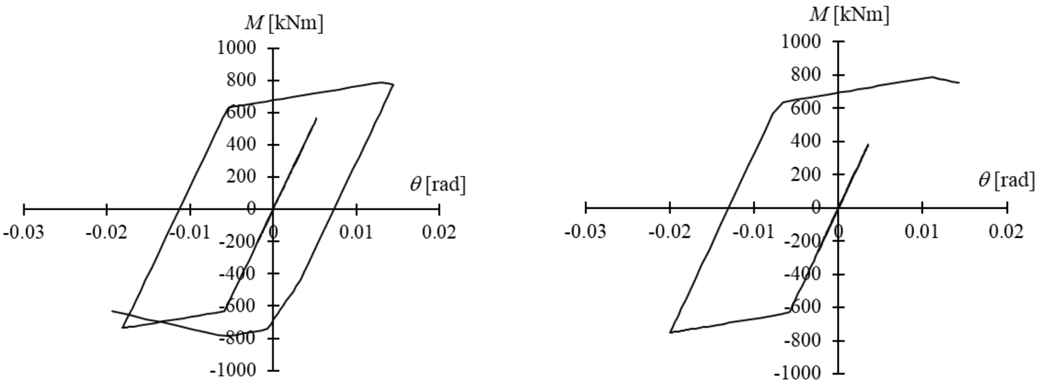

(c) El Centro

(d) Taft

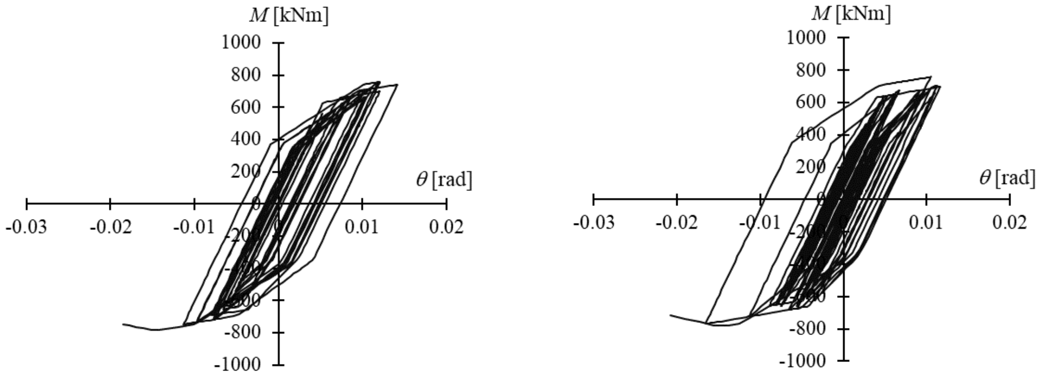

(e) Artificial wave (CH1)

(f) Artificial wave (OS1)

Fig. A.12-5 Hysteretic loops of the columns (in 1st floor, prior to the stability limit) under single seismic excitation (PGV=100cm/s).

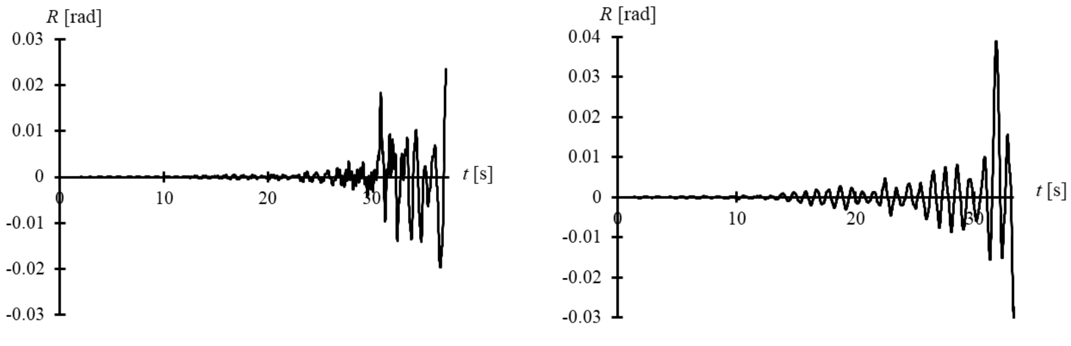

(a) JMA Sendai

(b) Hachinohe

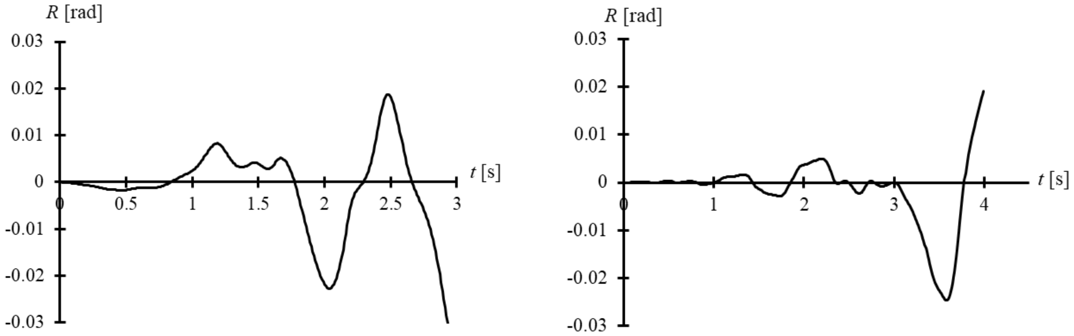

(c) El Centro

(d) Taft

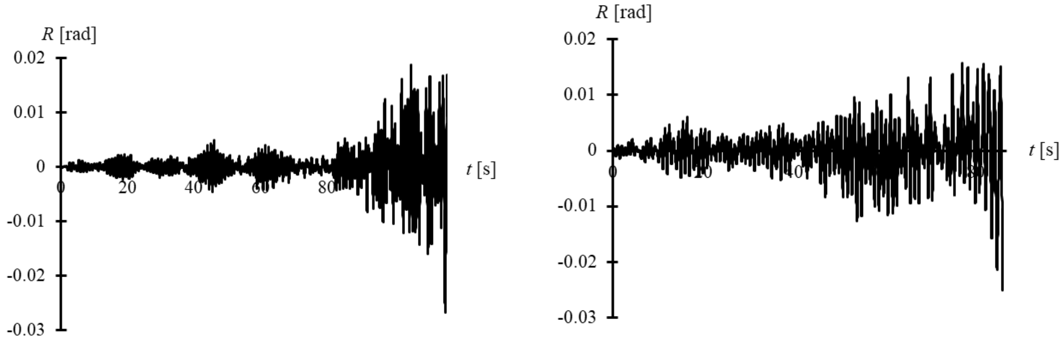

(e) Artificial wave (CH1)

(f) Artificial wave (OS1)

Fig. A.12-6 Time history of the 1st story drift (prior to the stability limit) under single seismic excitation (PGV=100cm/s).

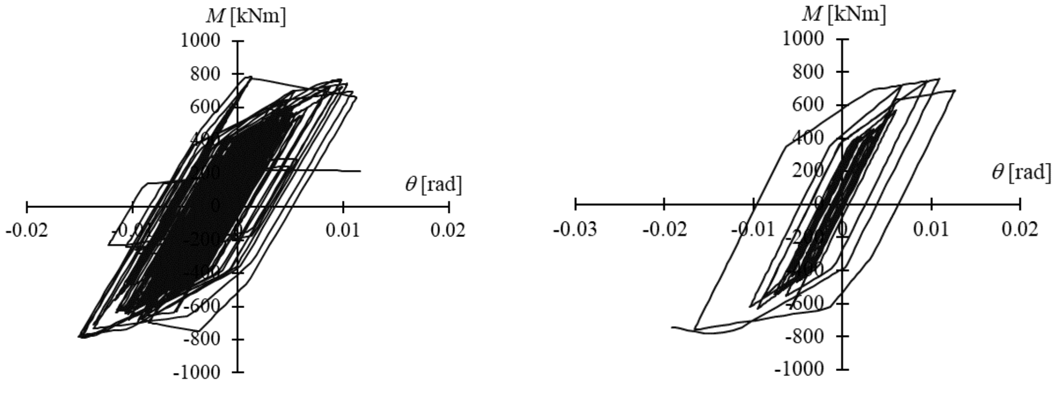

(a) JMA Sendai

(b) El Centro

Appendix 12 The hysteretic loops of the columns and story drift in the 1st floor (prior to the stability limit)

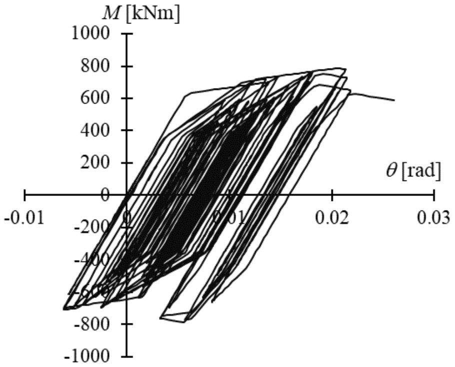

(c) Taft

Fig. A.12-7 Hysteretic loops of the columns (in 1st floor, prior to the stability limit) under multiple seismic excitations (PGV=50cm/s).

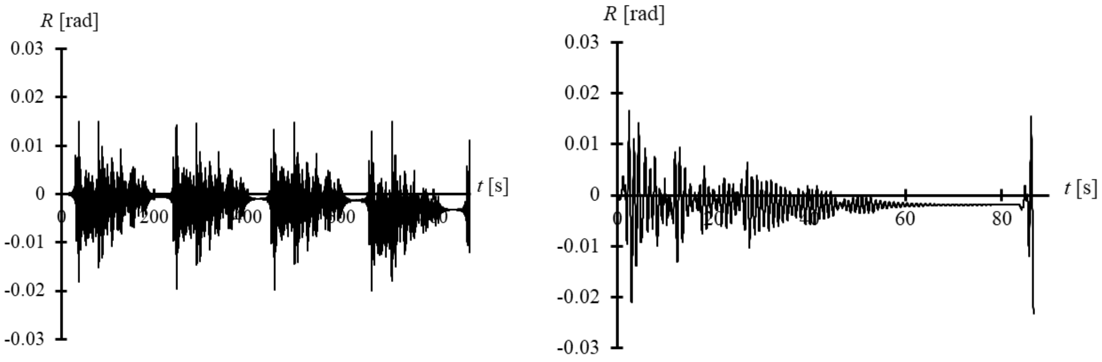

(a) JMA Sendai

(b) El Centro

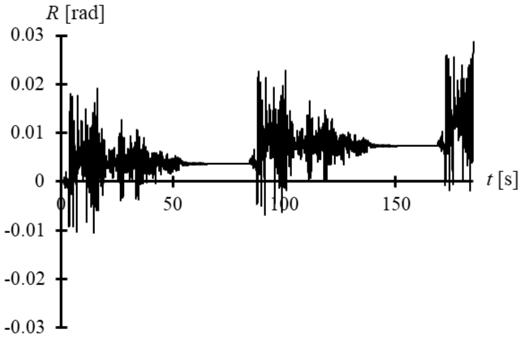

(c) Taft

Fig. A.12-8 Time history of the 1st story drift (prior to the stability limit) under multiple seismic excitations (PGV=50cm/s).

For the 6-story model with the width-to-thickness of 29.4, the relationships were summarized as follows. The orders of the figures correspond to the damage evolution relationships in Chapter 2.6.3. According to the hysteretic loops, the strength deterioration did not begin when the stability limit was reached.

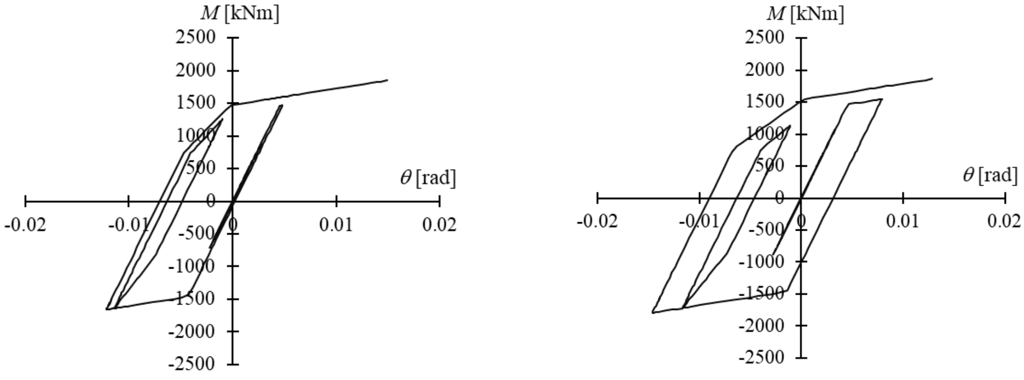

(a) Hachinohe, PGV=75cm/s (b) Hachinohe, PGV=100cm/s

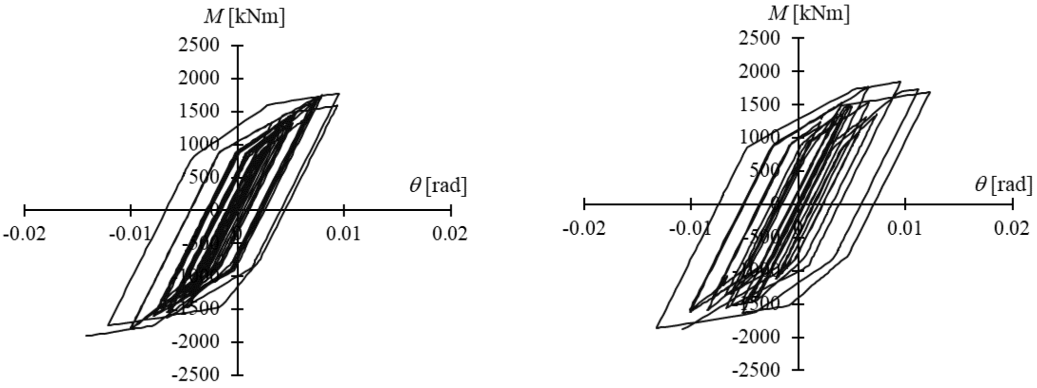

(c) Artificial wave (CH1), PGV=75cm/s (d) Artificial wave (CH1), PGV=100cm/s

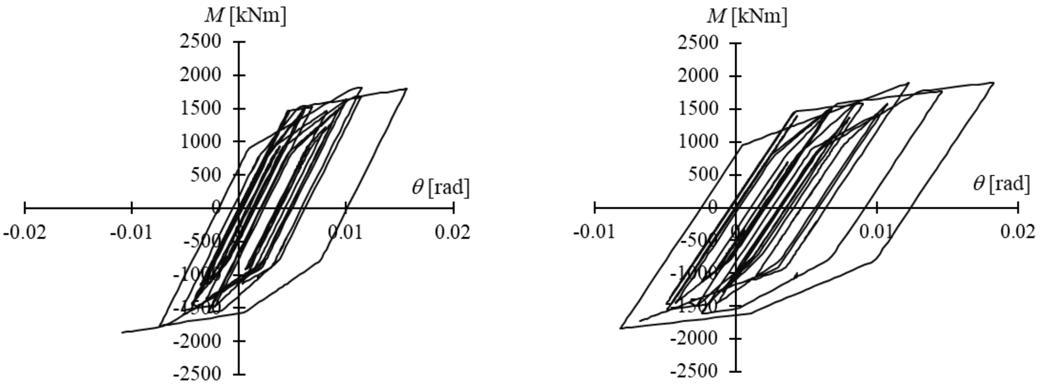

(e) Artificial wave (OS1), PGV=75cm/s (f) Artificial wave (OS1), PGV=100cm/s

Fig. A.12-9 Hysteretic loops of the columns (in 1st floor, prior to the stability limit) under single seismic excitation.

Appendix 12 The hysteretic loops of the columns and story drift in the 1st floor (prior to the stability limit)

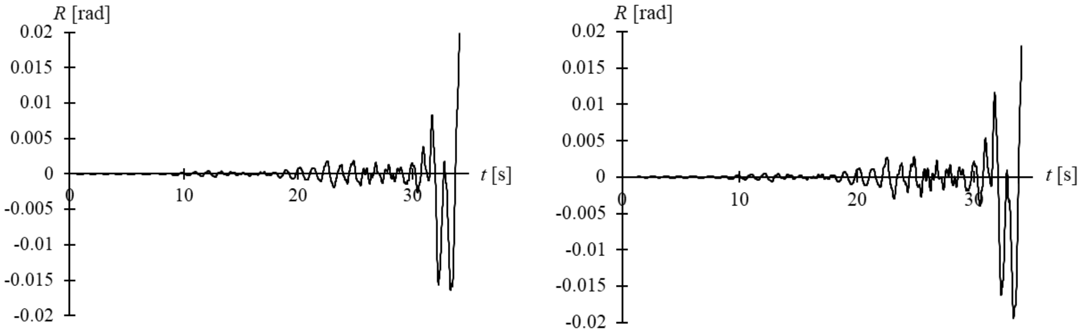

(a) Hachinohe, PGV=75cm/s (b) Hachinohe, PGV=100cm/s

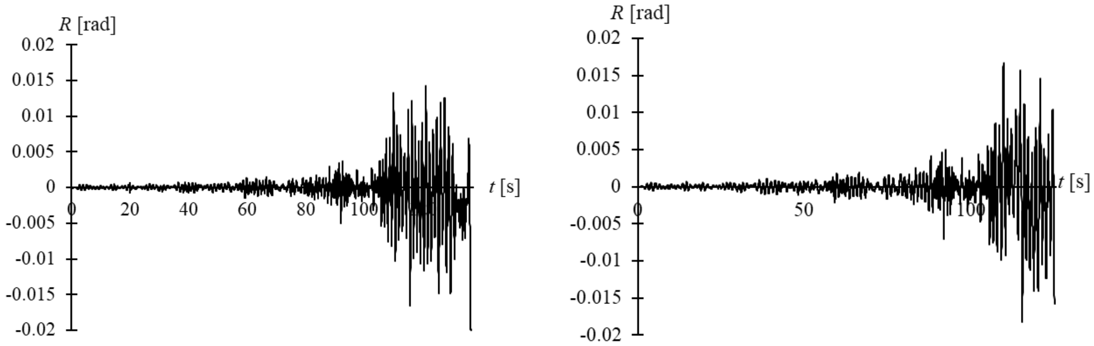

(c) Artificial wave (CH1), PGV=75cm/s (d) Artificial wave (CH1), PGV=100cm/s

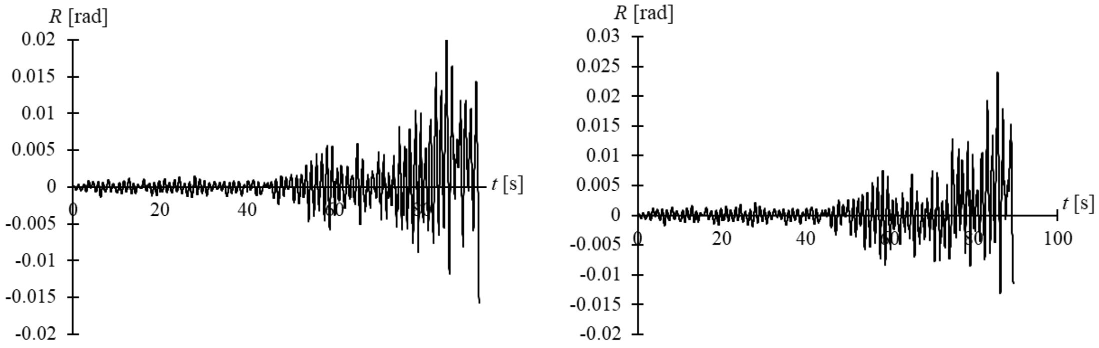

(e) Artificial wave (OS1), PGV=75cm/s (f) Artificial wave (OS1), PGV=100cm/s

Fig. A.12-10 Time history of the 1st story drift (prior to the stability limit) under single seismic excitation.

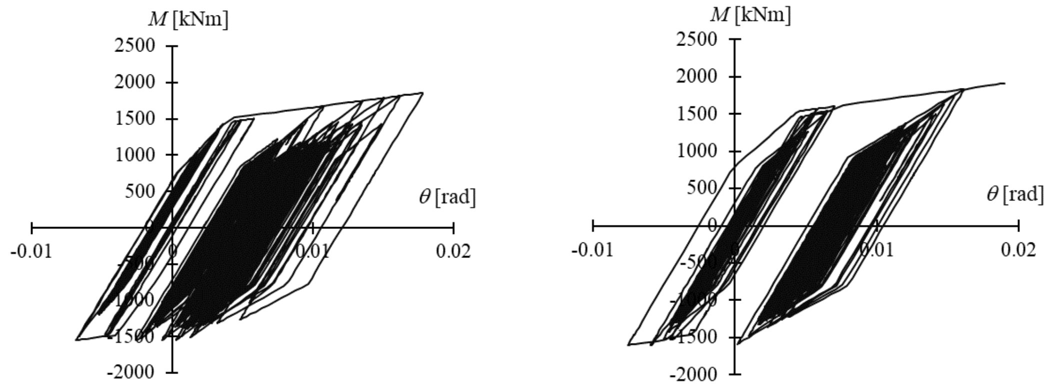

(a) JMA Sendai, PGV=75cm/s (b) JMA Sendai, PGV=100cm/s

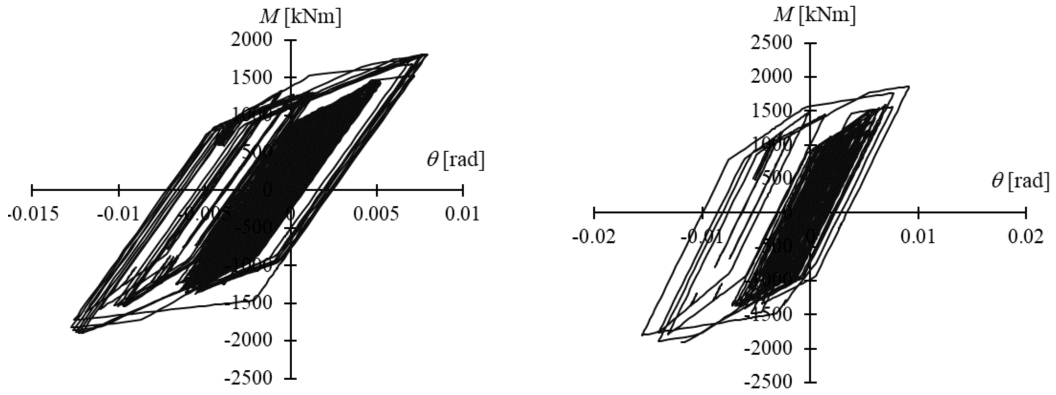

(c) El Centro, PGV=75cm/s (d) El Centro, PGV=100cm/s

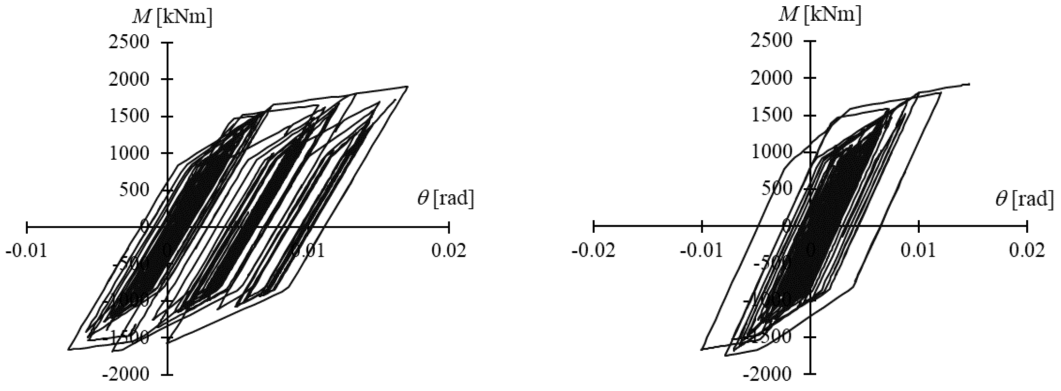

(e) Taft, PGV=75cm/s (f) Taft, PGV=100cm/s

Fig. A.12-11 Hysteretic loops of the columns (in 1st floor, prior to the stability limit) under multiple seismic excitations.

Appendix 12 The hysteretic loops of the columns and story drift in the 1st floor (prior to the stability limit)

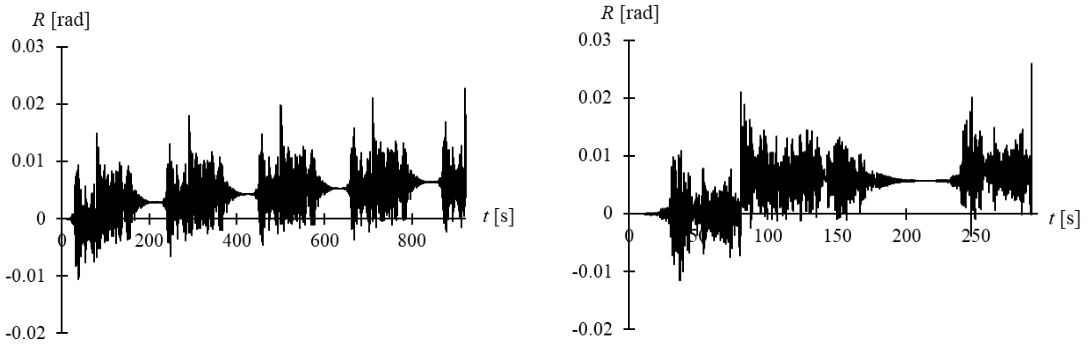

(a) JMA Sendai, PGV=75cm/s (b) JMA Sendai, PGV=100cm/s

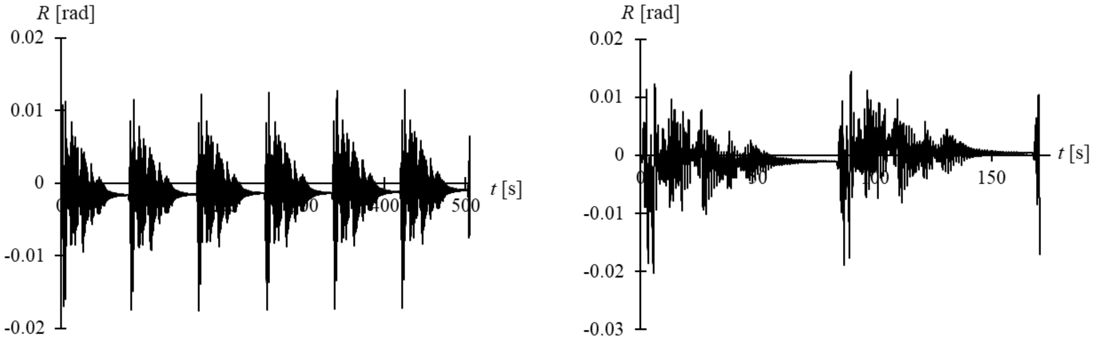

(c) El Centro, PGV=75cm/s (d) El Centro, PGV=100cm/s

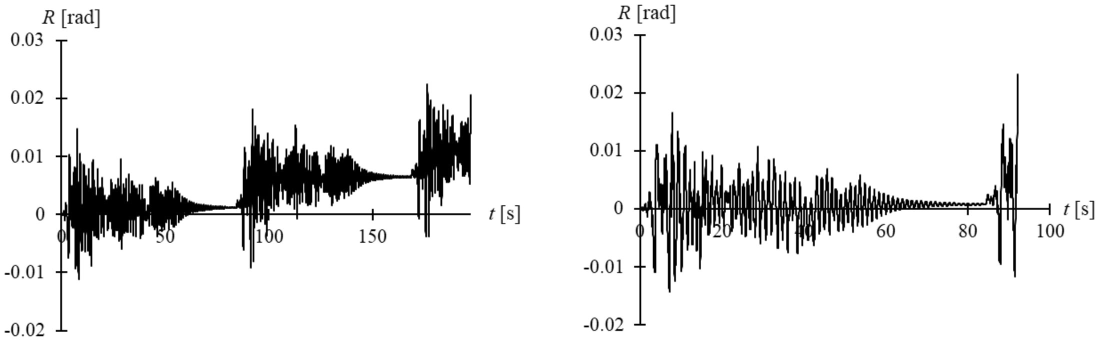

(e) Taft, PGV=75cm/s (f) Taft, PGV=100cm/s

Fig. A.12-12 Time history of the 1st story drift (prior to the stability limit) under multiple seismic excitations.

For the 3-story model with the width-to-thickness of 22.2, the relationships were summarized as follows. The orders of the figures correspond to the damage evolution relationships in Chapter 2.6.4. Similar to the cases in 6-story model, when the stability limit was reached, no strength deterioration was observed in the hysteretic loops.

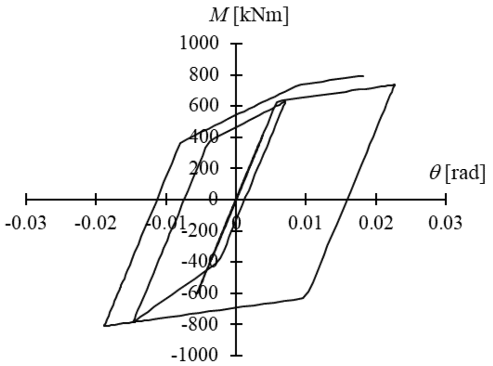

(a) Hachinohe, PGV=75cm/s

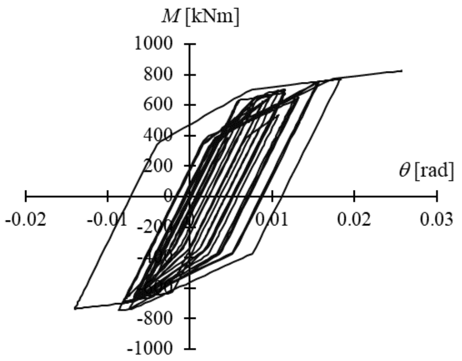

(b) Artificial wave (CH1), PGV=75cm/s

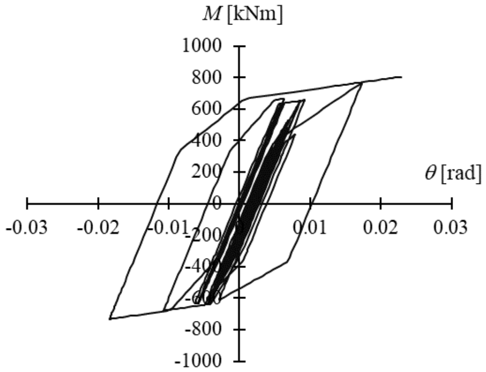

(c) Artificial wave (OS1), PGV=75cm/s

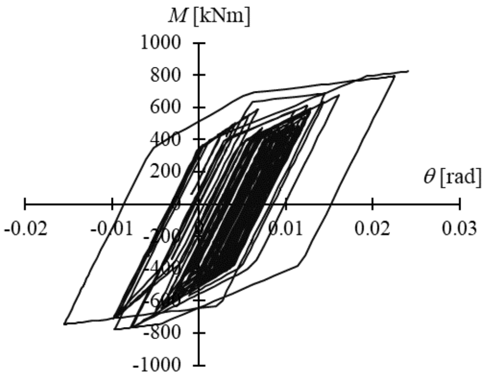

(d) JMA Sendai, PGV=100cm/s

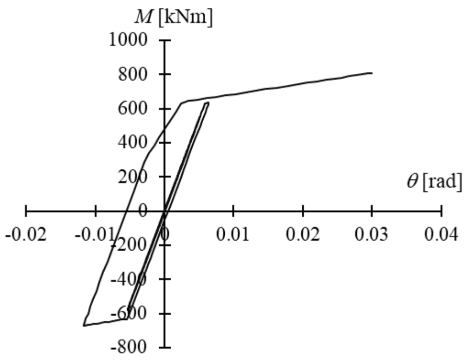

(e) Hachinohe, PGV=100cm/s

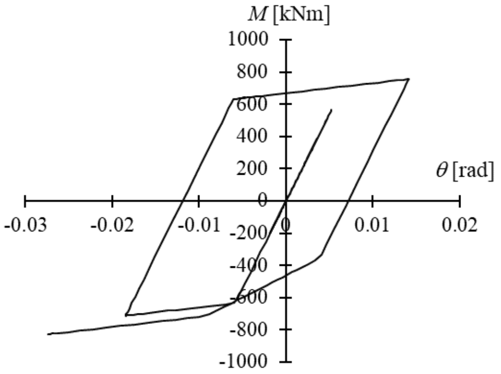

(f) El Centro, PGV=100cm/s

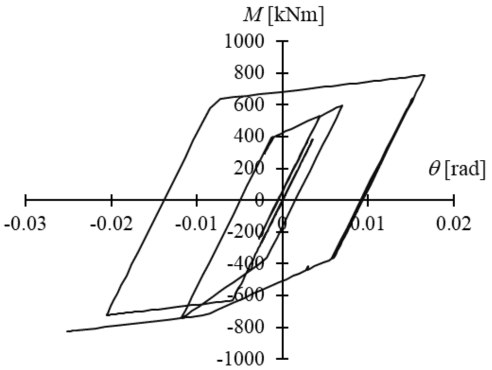

(g) Taft, PGV=100cm/s

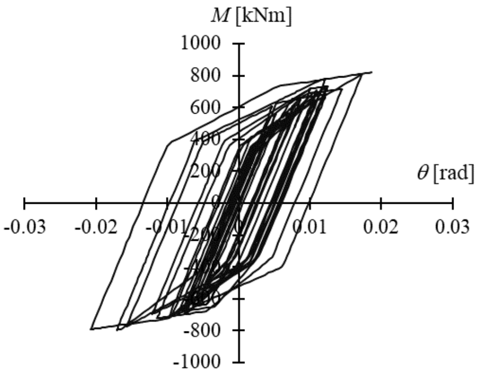

(h) Artificial wave (CH1), PGV=100cm/s

Appendix 12 The hysteretic loops of the columns and story drift in the 1st floor (prior to the stability limit)

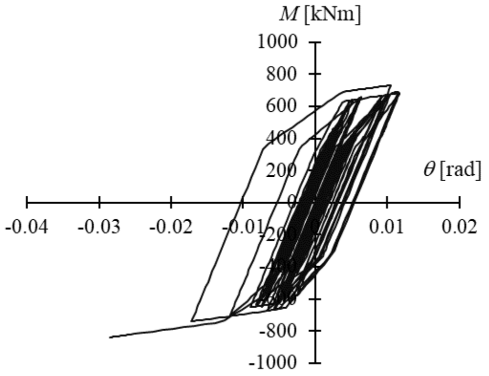

(i) Artificial wave (OS1), PGV=100cm/s

Fig. A.12-13 Hysteretic loops of the columns (in 1st floor, prior to the stability limit) under single seismic excitation.

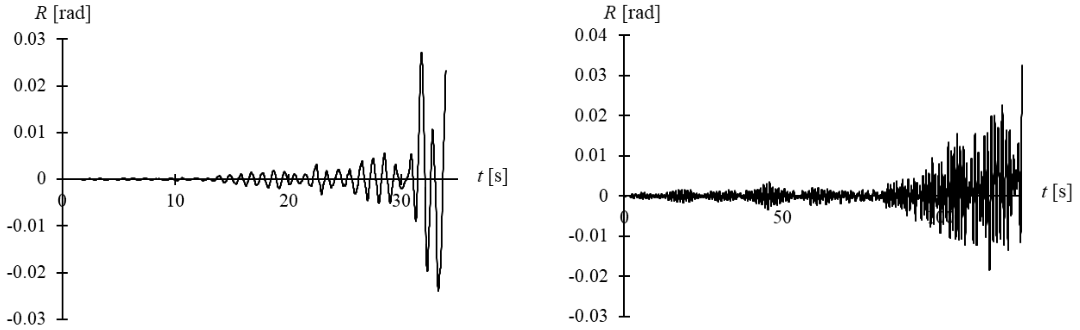

(a) Hachinohe, PGV=75cm/s
(b) Artificial wave (CH1), PGV=75cm/s

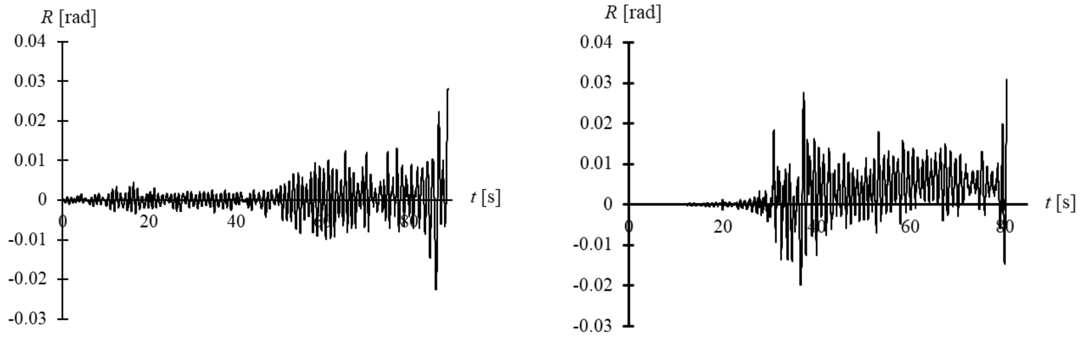

(c) Artificial wave (OS1), PGV=75cm/s
(d) JMA Sendai, PGV=100cm/s

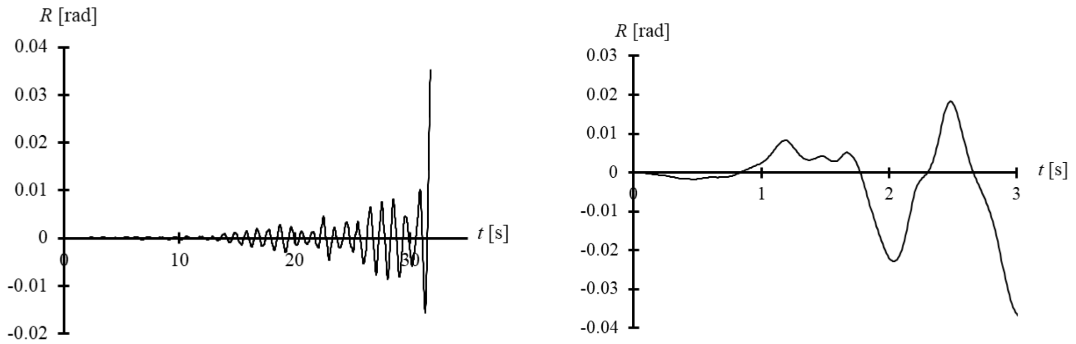

(e) Hachinohe, PGV=100cm/s
(f) El Centro, PGV=100cm/s

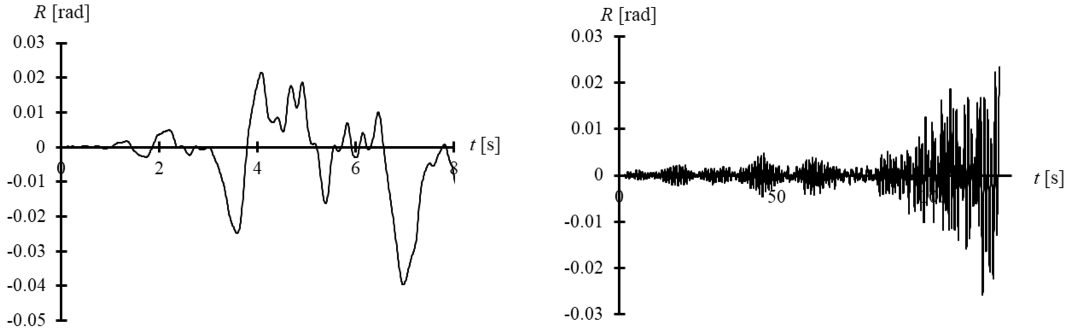

(g) Taft, PGV=100cm/s (h) Artificial wave (CH1), PGV=100cm/s

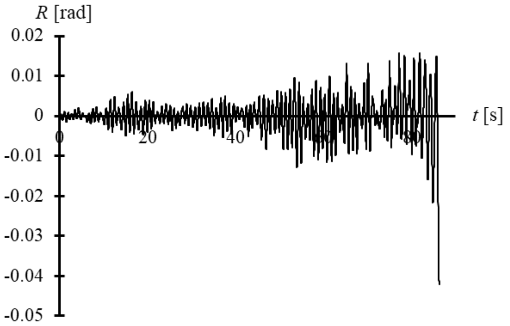

(i) Artificial wave (OS1), PGV=100cm/s

Fig. A.12-14 Time history of the 1st story drift (prior to the stability limit) under single seismic excitation.

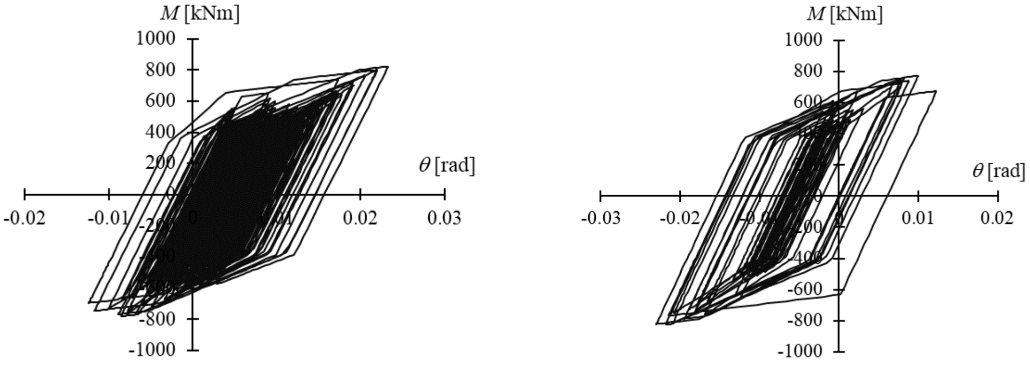

(a) JMA Sendai, PGV=75cm/s (b) Hachinohe, PGV=50cm/s

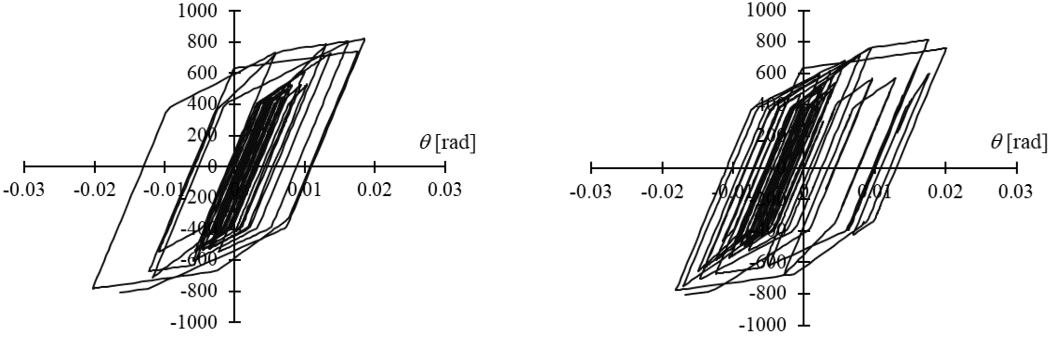

(c) El Centro, PGV=75cm/s　　(d) Taft, PGV=75cm/s

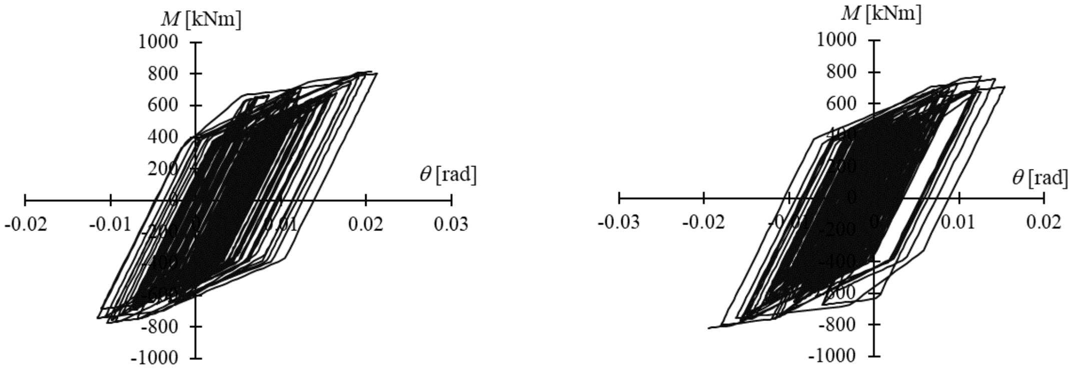

(e) Artificial wave (CH1), PGV=50cm/s　　(f) Artificial wave (OS1), PGV=50cm/s

Fig. A.12-15 Hysteretic loops of the columns (in 1st floor, prior to the stability limit) under multiple seismic excitations.

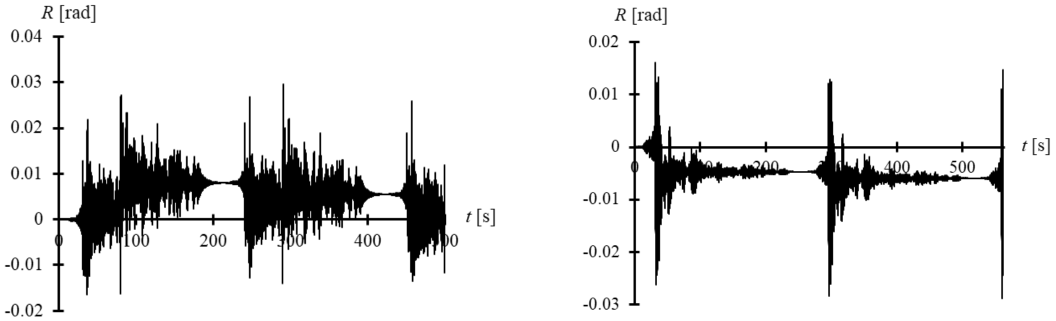

(a) JMA Sendai, PGV=75cm/s　　(b) Hachinohe, PGV=50cm/s

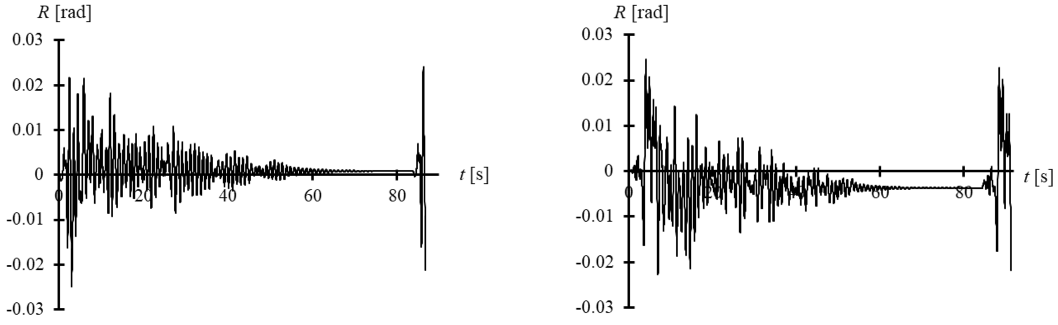

(c) El Centro, PGV=75cm/s　　(d) Taft, PGV=75cm/s

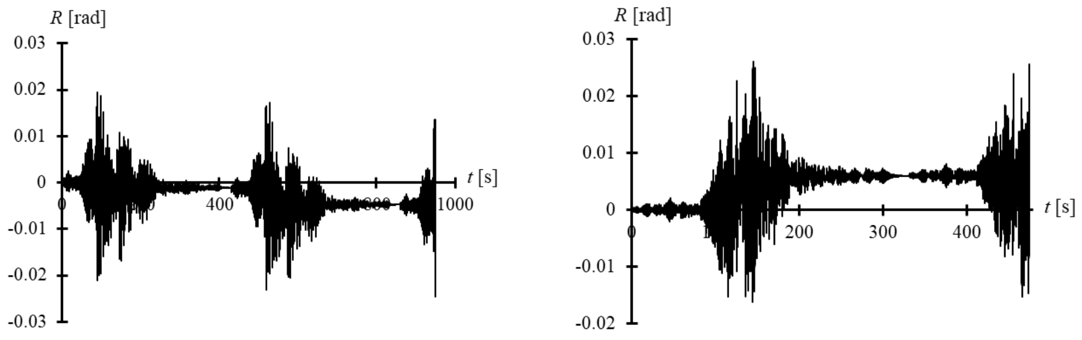

(e) Artificial wave (CH1), PGV=50cm/s (f) Artificial wave (OS1), PGV=50cm/s

Fig. A.12-16 Time history of the 1st story drift (prior to the stability limit) under multiple seismic excitations.

For the 3-story model with the width-to-thickness ratio of 25, the relationships were summarized as follows. The orders of the figures correspond to the damage evolution relationships in Chapter 2.6.5. Similar to the 3-story model with width-to-thickness ratio of 22.2, when the stability limit was reached, no strength deterioration was observed in the hysteretic loops.

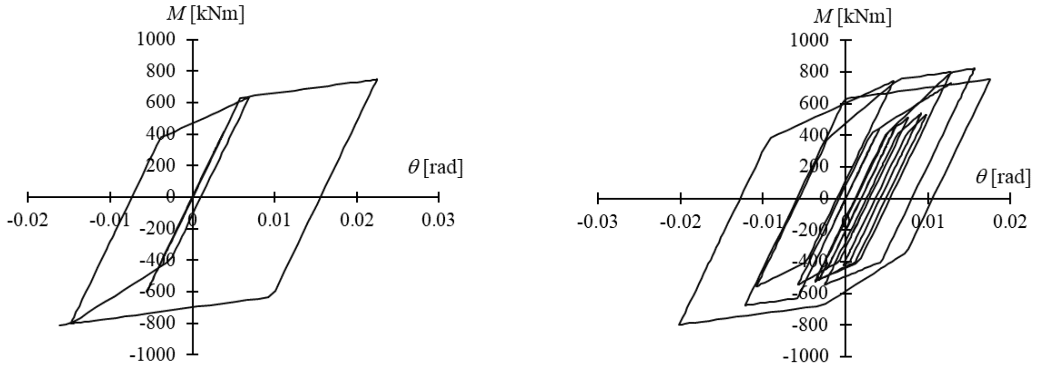

(a) Hachinohe, PGV=75cm/s (b) El Centro, PGV=75cm/s

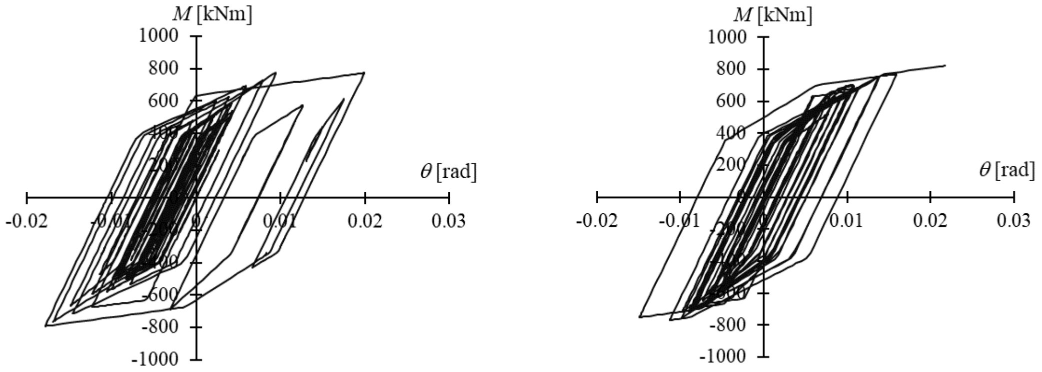

(c) Taft, PGV=75cm/s (d) Artificial wave (CH1), PGV=75cm/s

Appendix 12 The hysteretic loops of the columns and story drift in the 1st floor (prior to the stability limit)

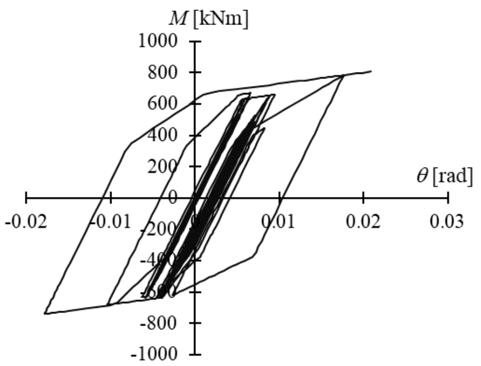

(e) Artificial wave (OS1), PGV=75cm/s

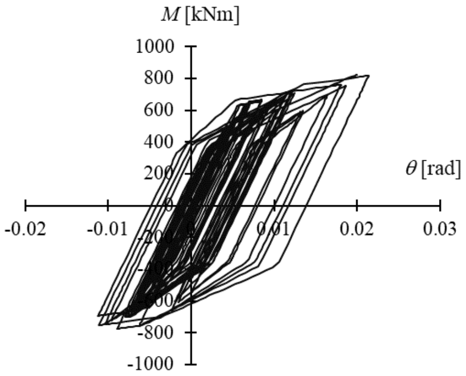

(f) Artificial wave (CH1), PGV=50cm/s

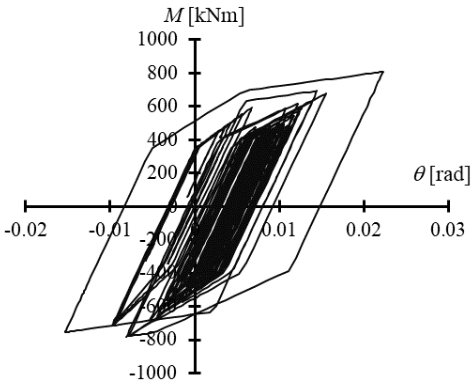

(g) JMA Sendai, PGV=100cm/s

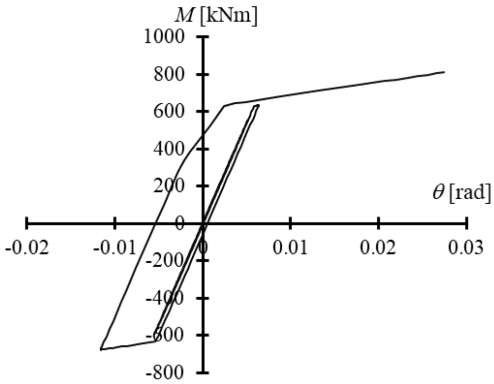

(h) Hachinohe, PGV=100cm/s

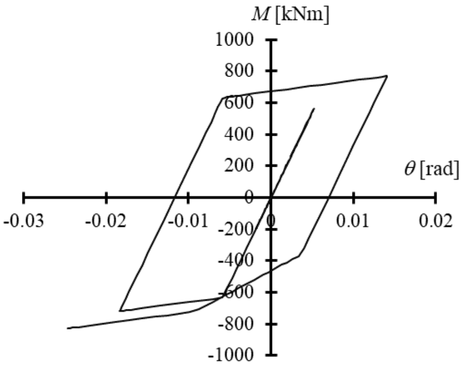

(i) El Centro, PGV=100cm/s

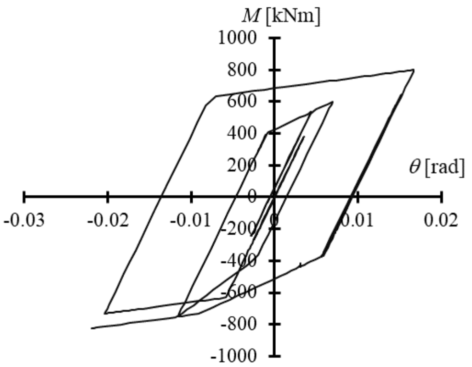

(j) Taft, PGV=100cm/s

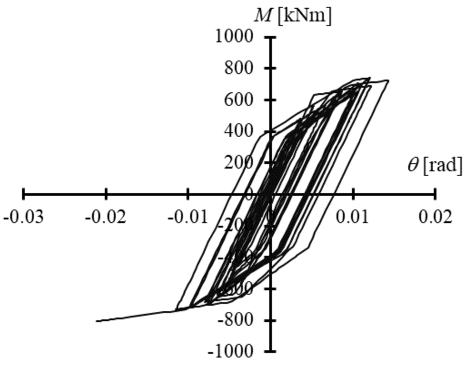

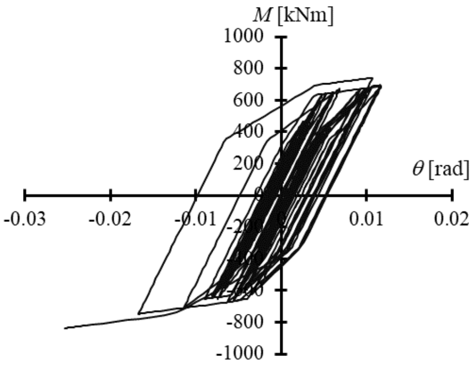

(k) Artificial wave (CH1), PGV=100cm/s (l) Artificial wave (OS1), PGV=100cm/s

Fig. A.12-17 Hysteretic loops of the columns (in 1st floor, prior to the stability limit) under single seismic excitation.

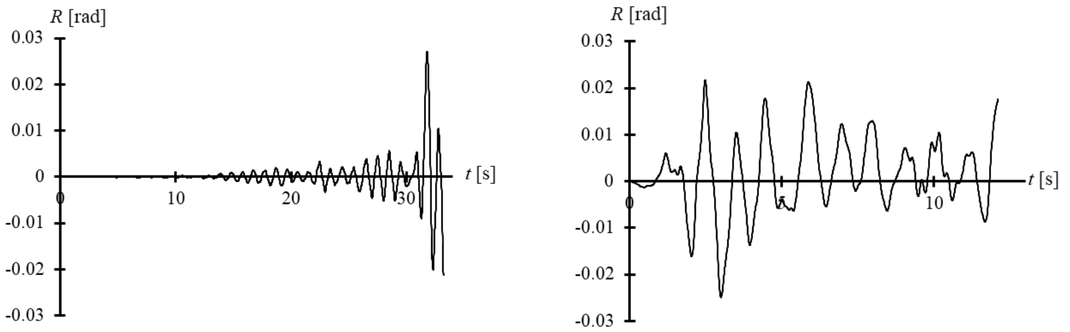

(a) Hachinohe, PGV=75cm/s (b) El Centro, PGV=75cm/s

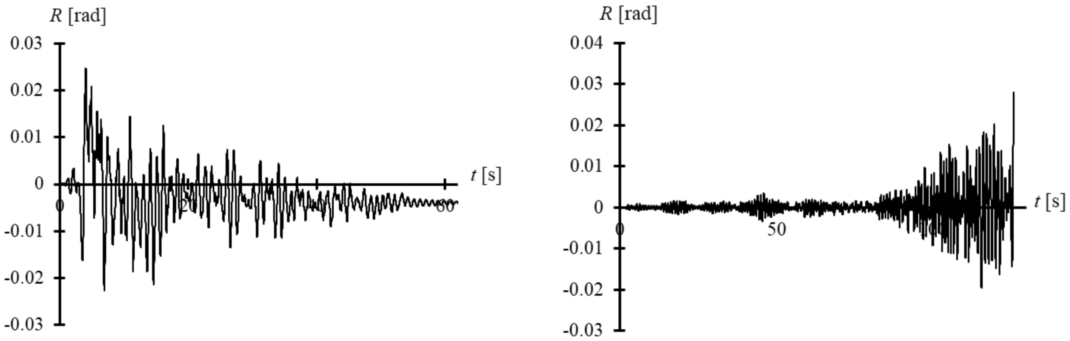

(c) Taft, PGV=75cm/s (d) Artificial wave (CH1), PGV=75cm/s

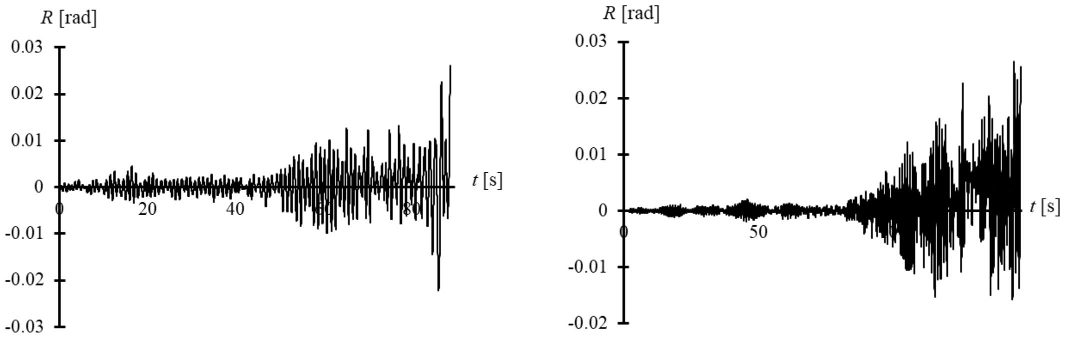

(e) Artificial wave (OS1), PGV=75cm/s (f) Artificial wave (CH1), PGV=50cm/s

Appendix 12 The hysteretic loops of the columns and story drift in the 1st floor (prior to the stability limit)

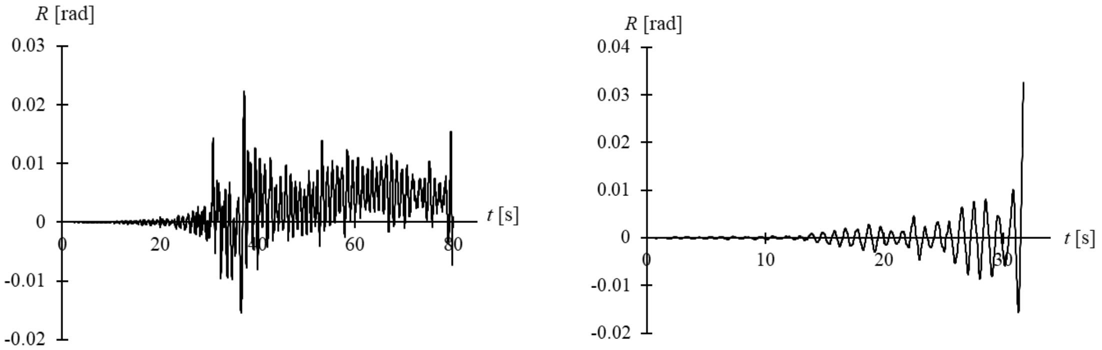

(g) JMA Sendai, PGV=100cm/s

(h) Hachinohe, PGV=100cm/s

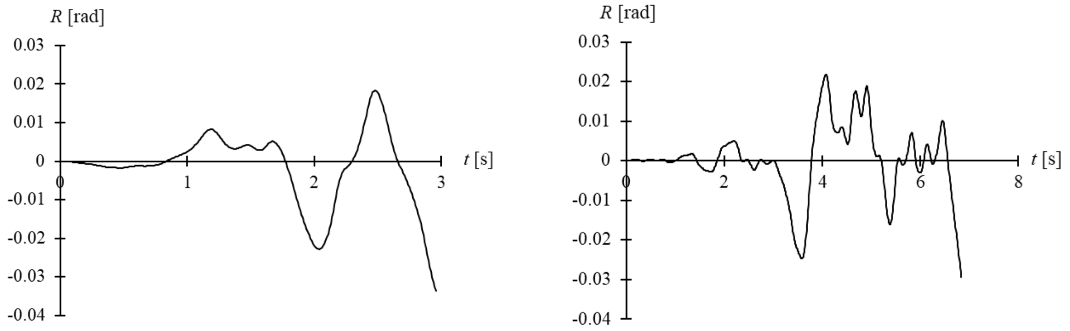

(i) El Centro, PGV=100cm/s

(j) Taft, PGV=100cm/s

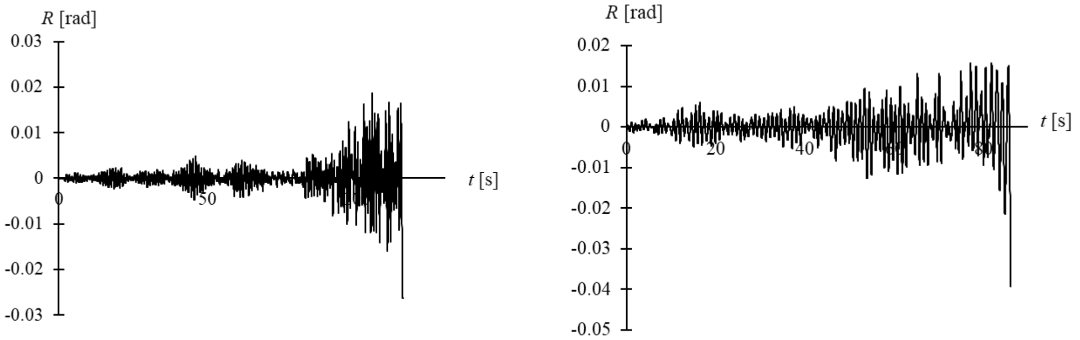

(k) Artificial wave (CH1), PGV=100cm/s

(l) Artificial wave (OS1), PGV=100cm/s

Fig. A.12-18 Time history of the 1st story drift (prior to the stability limit) under single seismic excitation.

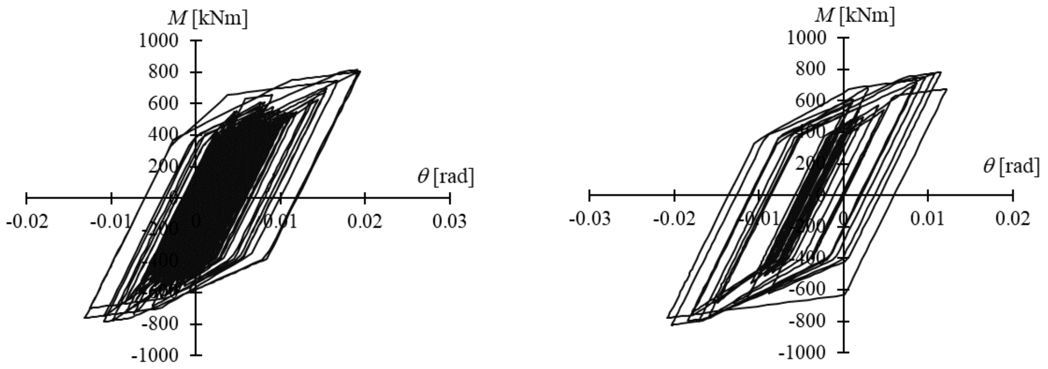

(a) JMA Sendai (PGV=75cm/s)

(b) Hachinohe (PGV=50cm/s)

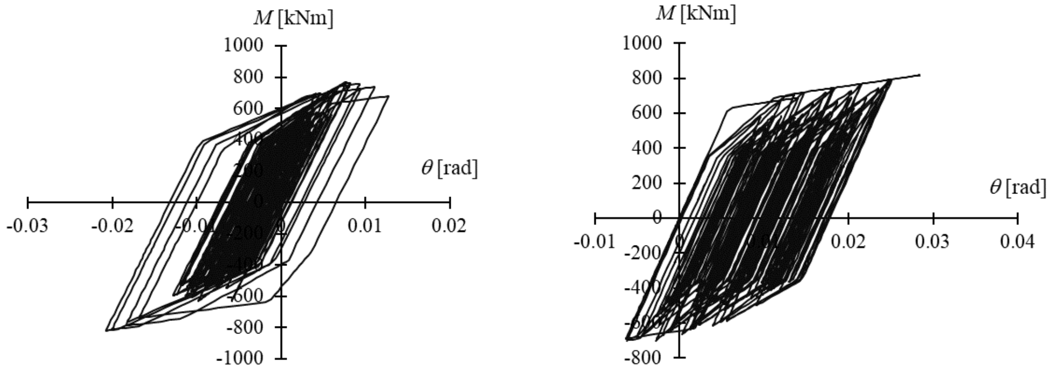

(c) El Centro (PGV=50cm/s)

(d) Taft (PGV=50cm/s)

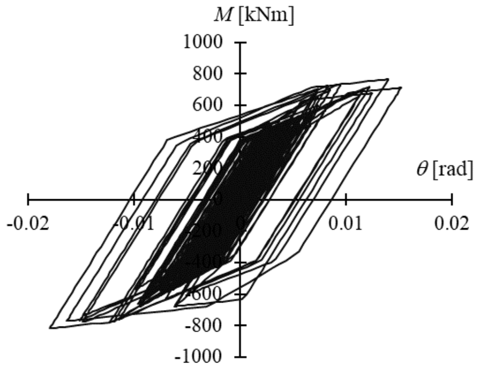

(e) Artificial wave (OS1) (PGV=50cm/s)

Fig. A.12-19 Hysteretic loops of the columns (in 1st floor, prior to the stability limit) under multiple seismic excitations.

Appendix 12 The hysteretic loops of the columns and story drift in the 1st floor (prior to the stability limit)

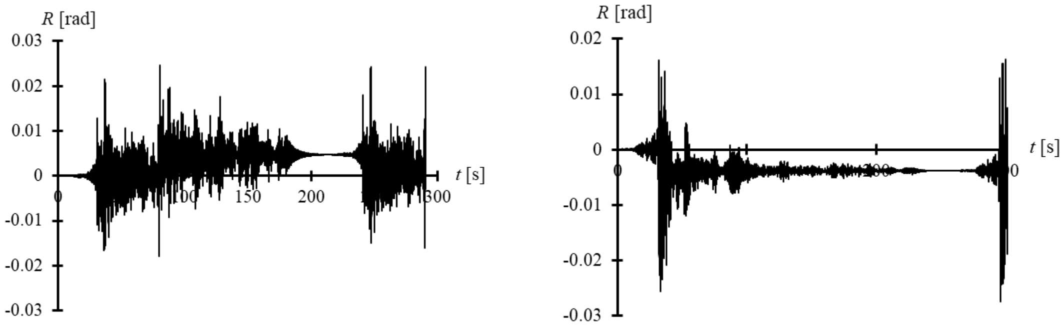

(a) JMA Sendai (PGV=75cm/s)   (b) Hachinohe (PGV=50cm/s)

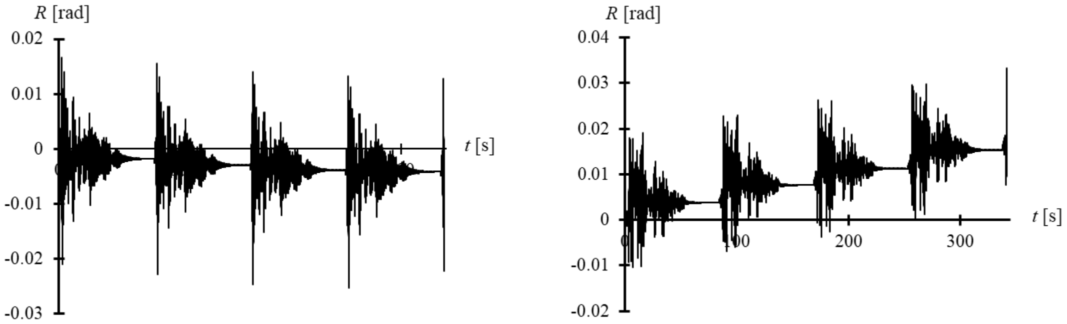

(c) El Centro (PGV=50cm/s)   (d) Taft (PGV=50cm/s)

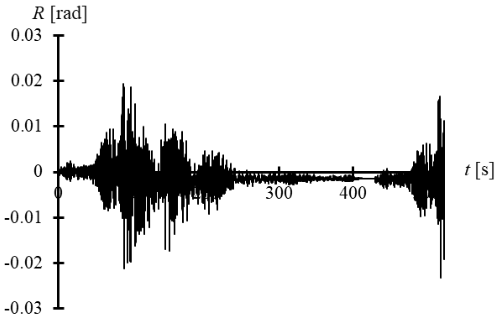

(e) Artificial wave (OS1) (PGV=50cm/s)

Fig. A.12-20 Time history of the 1st story drift (prior to the stability limit) under multiple seismic excitations.

Appendix 13 Summary of the local buckling modes for specimens in Chapter 2

The local buckling mode was summarized for each specific specimen. Furthermore, the values of the stability limit were summarized as well.

Table A.13-1 Summary of the local buckling failure modes

Lot	Dimension	Specimen	B/t	P/P_y	L/B	α_e	$\delta_{b,cr}$	Loading history	North side	South side	East side	West side
A	□-175×175×9 (BCR295)	M_19.4_0.3_7.0	19.4	0.3	7.0	0.56	4.76	Monotonic	convex	convex	na	concave
		C1.5_19.4_0.3_7.0						Const. amp. 1.5θ_{pc}	convex	convex	concave	convex
		C2.0_19.4_0.3_7.0						Const. amp. 2.0θ_{pc}	convex	convex	convex	convex
B		M_19.4_0.3_4.9	19.4	0.3	4.9	0.58	4.46	Monotonic	concave	concave	na	convex
		C1.5_19.4_0.3_4.9						Const. amp. 1.5θ_{pc}	convex	convex	convex	convex
		C1.75_19.4_0.3_4.9						Const. amp. 1.75θ_{pc}	convex	convex	convex	convex
		C2.0_19.4_0.3_4.9						Const. amp. 2.0θ_{pc}	convex	convex	convex	convex
C		M_19.4_0.3_3.0	19.4	0.3	3.0	0.58	5.50	Monotonic	concave	concave	na	convex
		C2.0_19.4_0.3_3.0						Const. amp. 2.0θ_{pc}	convex	convex	convex	convex
		C2.5_19.4_0.3_3.0						Const. amp. 2.5θ_{pc}	convex	convex	convex	convex
		C3.5_19.4_0.3_3.0						Const. amp. 3.5θ_{pc}	convex	convex	convex	convex
D	□-175×175×6 (BCR295)	M_29.2_0.15_4.9	29.2	0.15	4.9	1.15	1.97	Monotonic	convex	convex	na	concave
		C1.5_29.2_0.15_4.9						Const. amp. 1.5θ_{pc}	convex	convex	concave	concave
		M_29.2_0.3_4.9	29.2	0.3	4.9	1.33	1.35	Monotonic	convex	convex	na	concave
		C1.0_29.2_0.3_4.9						Const. amp. 1.0θ_{pc}	convex	convex	concave	concave
		C1.5_29.2_0.3_4.9						Const. amp. 1.5θ_{pc}	convex	convex	concave	concave

E	□-200×200×9 (BCR295)	M_22.2_0.35_4.3	22.2	0.35	4.3	0.81	4.19	Monotonic	convex	convex	na	concave
		C1.5_22.2_0.35_4.3						Const. amp. 1.5θ_{pc}	convex	convex	concave	concave
		C2.0_22.2_0.35_4.3						Const. amp. 2.0θ_{pc}	convex	convex	concave	concave
		V_22.2_0.35_4.3						Variable	convex	convex	convex	concave
F		M_22.2_0.2_4.3	22.2	0.2	4.3	0.68	3.96	Monotonic	convex	convex	na	concave
		Taft_22.2_0.2_4.3						Variable	convex	convex	concave	concave
G	□-200×200×6 (BCR295)	M_33.3_0.2_4.3	33.3	0.2	4.3	1.39	1.73	Monotonic	convex	convex	na	concave
		C1.5_33.3_0.2_4.3						Const. amp. 1.5θ_{pc}	convex	convex	concave	concave
		C2.0_33.3_0.2_4.3						Const. amp. 2.0θ_{pc}	convex	convex	concave	concave
		V_33.3_0.2_4.3						Variable	convex	convex	concave	concave

Notes: The West-East side is the loading direction. For the specimens under monotonic loading, the displacements were applied on the top of the columns from East to West side. α_e: The equivalent standardized width-to-thickness ratio; $\delta_{b,cr}$: The value of the stability limit.

Publications

Publications related to this study

Journal paper

Chapter 2

1) Takanori Ishida, **Yang Dong***, Shoichi Kishiki, Satoshi Yamada, Takashi Hasegawa. Cyclic behaviors of SHS columns subjected to small amplitude loading. *Engineering Structures*, 2022, 252: 113611.

Chapter 3

2) **Yang Dong**, Takanori Ishida, Shoichi Kishiki, Satoshi Yamada, Takashi Hasegawa. Cyclic behaviors of SHS columns in low cycle fatigue tests. *Journal of Earthquake Engineering*. (Under review)

Conference paper

1) **Yang Dong**, Takanori Ishida, Shoichi Kishiki, Satoshi Yamada, Takashi Hasegawa. Cyclic behaviors of SHS columns subjected to small inelastic cycles *The 11th International Symposium on Steel Structures*, Jeju, Korea, 2021.11.
2) **Yang Dong**, Takanori Ishida, Shoichi Kishiki, Satoshi Yamada, Takashi Hasegawa. Low cycle fatigue performance of SHS columns subjected to small amplitude loading, *Proceedings of Constructional Steel*, 2021, 29: 318-327.
3) **Yang Dong**, Takanori Ishida, Shunsuke Tamada, Shoichi Kishiki, Satoshi Yamada. Experimental study on deterioration behavior of SHS columns under cyclic small amplitude loading, *Proceedings of Constructional Steel*, 2020, 28: 874-882.
4) **Yang Dong**, Takanori Ishida, Shoichi Kishiki, Satoshi Yamada, Takashi Hasegawa. Cyclic behavior of SHS columns under small inelastic cycles: Part 1 Cyclic loading tests with shear span ratio of 7.0 and experiment database. *Summaries of Technical Papers of Annual Meeting (Kanto branch),* Architectural Institute of Japan, Vol. 91: pp. 165-168, 2021.3.
5) **Yang Dong**, Takanori Ishida, Shoichi Kishiki, Satoshi Yamada, Takashi Hasegawa. Cyclic behavior of SHS columns under small inelastic cycles: Part 2 Prediction of deformation capacity to the stability limit. *Summaries of Technical Papers of Annual Meeting (Kanto branch),* Architectural Institute of Japan, Vol. 91: pp. 169-172, 2021.3.

6) Takanori Ishida, **Yang Dong**, Kazumasa Mogi, Shoichi Kishiki, Satoshi Yamada, Takashi Hasegawa. Low Cycle Fatigue of SHS Columns Subjected to Small Amplitude Loading: Part 1 Test plan and summary of test results, *Summaries of Technical Papers of Annual Meeting*, Architectural Institute of Japan, pp. 823-824, 2021.9.
7) Kazumasa Mogi, **Yang Dong**, Takanori Ishida, Shoichi Kishiki, Satoshi Yamada, Takashi Hasegawa. Low Cycle Fatigue of SHS Columns Subjected to Small Amplitude Loading: Part 2 Investigation on low cycle fatigue life, *Summaries of Technical Papers of Annual Meeting*, Architectural Institute of Japan, pp. 825-826, 2021.9.
8) **Yang Dong**, Takanori Ishida, Kazumasa Mogi, Shoichi Kishiki, Satoshi Yamada, Takashi Hasegawa. Low Cycle Fatigue of SHS Columns Subjected to Small Amplitude Loading: Part 3 Investigation on strength deterioration prediction method, *Summaries of Technical Papers of Annual Meeting*, Architectural Institute of Japan, pp. 827-828, 2021.9.
9) Takanori Ishida, **Yang Dong**, Shunsuke Tamada, Shoichi Kishiki, Satoshi Yamada, Takashi Hasegawa. Cyclic behavior of SHS columns subjected to small amplitude loading: Part 1 Test plan and outline of test results, *Summaries of Technical Papers of Annual Meeting*, Architectural Institute of Japan, pp. 983-984, 2020.9.
10) **Yang Dong**, Takanori Ishida, Shunsuke Tamada, Shoichi Kishiki, Satoshi Yamada, Takashi Hasegawa. Cyclic behavior of SHS columns subjected to small amplitude loading: Part 2 Investigation of strength deterioration behavior due to local buckling, *Summaries of Technical Papers of Annual Meeting*, Architectural Institute of Japan, pp. 985-986, 2020.9.
11) Shunsuke Tamada, **Yang Dong**, Takanori Ishida, Shoichi Kishiki, Satoshi Yamada, Takashi Hasegawa. Cyclic behavior of SHS columns subjected to small amplitude loading: Part 3 Evaluation of cyclic deformation capacity, *Summaries of Technical Papers of Annual Meeting*, Architectural Institute of Japan, pp. 987-988, 2020.9.

Other publications

Journal paper

1) **Yang Dong**, Liang-Jiu Jia. Plasticity model for structural steel with Lode angle dependence. *Journal of Bridge Engineering*, 2021, 26(12): 04021087.
2) Liang-Jiu Jia, **Yang Dong**, Han-bin Ge, Kana Kondo and Ping Xiang. Experimental study on high-performance buckling-restrained braces with perforated core plates. *International Journal of Structural Stability and Dynamics*. 2019, 19: 1940004.
3) Liang-Jiu Jia, **Yang Dong**. Experiments on perforated buckling restrained braces with bending-shear deformation under compression. *Journal of Hunan University (Natural Science Edition).* 2019, 46(3): 66-73. (EI, in Chinese)
4) Liang-Jiu Jia, **Yang Dong**. Review on research and application of high-performance steel in structural engineering. *Industrial Construction*, 2016, 46(7):1-9. (CSCD/JST, in Chinese)
5) Jun-Yan Wang, Jun-Yuan Guo, Liang-Jiu Jia, Shi-Ming Chen and **Yang Dong**. Push-out tests of demountable headed stud shear connectors in steel-UHPC composite structures. *Composite Structures*, 2017, 170: 69-79.
6) Liang-Jiu Jia, Rui-Wen Li, Ping Xiang, De-Yuan Zhou and **Yang Dong**. Resilient Steel Frames Installed with Self-Centering Dual-Steel Buckling Restrained Brace. *Journal of Constructional Steel Research*, 2018: 95-104.

Conference paper

1) **Yang Dong**, Liang-Jiu Jia. Cyclic loading on cold-formed SHS stub columns. *The 16th International Symposium on Tubular Structures*. Tubular Structures XVI, 2017, 381-386.
2) **Yang Dong**, Liang-Jiu Jia. Study on plasticity model considering the Lode angle for structural steel under monotonic loading. *12th Pacific Structural Steel Conference*, Tokyo, Japan, 2019. 11.
3) Liang-Jiu Jia, **Yang Dong**. Coupling analysis of buckling and ductile fracture of square steel tube under strong earthquake. *The 17th National Symposium on Modern Structural Engineering*. 2017. (in Chinese)
4) Liang-Jiu Jia, **Yang Dong**. A newly proposed buckling restrained brace. *The 12th Sino-Japan Symposium on building structure*. 2017. (in Chinese)

5) Takanori Ishida, Kazumasa Mogi, **Yang Dong**, Shoichi Kishiki, Satoshi Yamada. Bi-directional horizontal loading test of concrete-filled square tube columns under small amplitude loading history: Part 1 Test plan, *Summaries of Technical Papers of Annual Meeting*, Architectural Institute of Japan, 2022.
6) Kazumasa Mogi, **Yang Dong**, Takanori Ishida, Shoichi Kishiki, Satoshi Yamada. Bi-directional horizontal loading test of concrete-filled square tube columns under small amplitude loading history: Part 2 Evaluation of hysteretic behavior and strength deterioration in major axis, *Summaries of Technical Papers of Annual Meeting*, Architectural Institute of Japan, 2022.
7) **Yang Dong**, Takanori Ishida, Kazumasa Mogi, Shoichi Kishiki, Satoshi Yamada. Bi-directional horizontal loading test of concrete-filled square tube columns under small amplitude loading history: Part 3 Evaluation of cyclic deterioration based on local buckling deformation, *Summaries of Technical Papers of Annual Meeting*, Architectural Institute of Japan, 2022

Acknowledgements

Time passed so rapidly when I look back after finishing the doctoral course. I can still remember my feeling of excitement and diffidence when I came to Tokyo Institute of Technology three years ago. The three years can be unforgettable and valuable in my whole life. To finish the dissertation, a lot of work has been done, including large amount of experiment, analytical work, programming and numerical simulation. I would like to express my gratitude to the people that have contributed to the current dissertation.

First of all, I would like to express my gratitude to my supervisor Professor **Shoichi Kishiki**. He always gave me the freedom to explore in the research work. He has a high attainment in making stories in the research, figures, and slides to transfer our research findings easily for understanding. I have learnt a lot on how to present the research work well. He is also creative and can always offer some good ideas and comments. He is rigorous and strict in research but always kind to students in the daily life. His enthusiasm and commitment to the research has motivated me a lot during my doctoral course.

I would like to express my gratitude to Professor **Satoshi Yamada** in the University of Tokyo. He offered me the precious chance to study in Tokyo Tech originally. He has a great knowledge in the structural engineering and earthquake engineering. He can always transform the difficult problems into easy ones. He also has a lot of good ideas and a strict timeline for the doctoral students to graduate on time. If you go astray in your research, he can always point out your mistakes and help you back on track. He is also rigorous in research and kind to students in every aspect.

I would like to express my sincere thanks to Professor **Takanori Ishida** in Yokohama National University. He supervised and discussed with me on my research during the whole doctoral course. Even though he went to Yokohama National University in early 2021, he still came to Tokyo Tech for discussion and experiment at times, which showed his responsibility to students. He offered the technical support and always taught me in a detailed and easy-understanding way. I have learnt a lot from him, including experiment design, experiment operation, modeling concept and programming. He always listened to my ideas carefully and pointed out the inefficiencies and modification points accurately. He has a high requirement for the research findings, which is helpful to the growth of the students. He has a deep understanding and great knowledge in his research field, which is very respectable.

I would like to express my gratitude to Professor **Yu Jiao** in Tokyo City University. She offered a lot of help in my daily life. Furthermore, she shared a lot of experience in Japan and made me get used to the life here quickly. She also shared the experience in the research life, which helped me to determine the future plan. She is kind and behaves as a friend of mine.

I would like to express my gratitude to Professor **Nabuhiko Tatsumi** in Aichi Institute of Technology. He used to be the assistant professor in Kishiki lab, and was responsible for the fairs related to the experiment. When I met problems or needed his help, he can always help me and solve the problems immediately, which is highly responsible for the fairs in the lab.

There are so many shining points in you, and I will always set you as my role models in the future research life. In addition, I would like to express my great gratitude to Professors **Motoyui**, **Ishihara**, **Sato** and **Nishimura** for giving the valuable advice and instructions to this dissertation. Your suggestions made the dissertation better and also pointed out the direction for the future research.

Furthermore, I am grateful for the help from Fu san, Yang san, Li kun, Zheng kun, Liu kun, Cui san in my daily life. Great appreciation to my foreign friends Randy san, Thailean san and An kun for daily life and academic discussion. Thanks for the help from Nakada san, Kurosawa san, Mogi san, and Tamada san in the experimental work. Thanks for the care and love from Endo san, Okubo san, Nagami san, and Miyamoto san in the daily life. I sincerely thank for all the members in previous Yamada lab and Kishiki lab for accompanying me in the three-year time. I wish you all to have good health and bright future. Great appreciation to Chinese Scholarship Council for financial support for my daily expenses.

Lastly, I want to express my great appreciation to my parents and family members. They always back up and encourage me during my doctoral course. They always support my decision and can offer good suggestions. This is the third time to sincerely express my gratitude to them. The last twice was in Tongji University, Shanghai, while this time is in Tokyo Tech, Tokyo. Even though many things have changed, their love never changes.

September 2022

Yang DONG